DISSERTATION

submitted to the

Combined Faculty of Mathematics, Engineering and Natural Sciences
of Heidelberg University, Germany

for the degree of

Doctor of Natural Sciences

Put forward by

THOMAS RINK

born in: Marburg
Oral examination: 16 February 2022

INVESTIGATING NEUTRINO PHYSICS WITHIN AND BEYOND THE STANDARD MODEL USING CONUS EXPERIMENTAL DATA

1st Referee: Prof. Dr. Dr. h.c. Manfred Lindner
2ndReferee: Prof. Dr. Jörg Jäckel

ABSTRACT

The observation of coherent elastic neutrino-nucleus scattering (CEνNS) opens up new possibilities for the standard model (SM) neutrino sector and beyond. As a leading reactor experiment, CONUS aims for its detection in the coherent interaction regime with antineutrinos emitted from the $3.9\,\mathrm{GW_{th}}$ reactor core of the Brokdorf nuclear power plant. The experiment makes use of four high-purity germanium detectors within a compact shield at 17 m distance. In this thesis spectral investigations of CEνNS and further neutrino interactions beyond the standard model (BSM) are performed, which are based on data collected between April 2018 and June 2019. The analysis scheme relies on signal predictions incorporating the evolution of the reactor's fuel composition and of its thermal power. The spectral analysis constrains CEνNS to contribute with $\lesssim 85$ events (90% C.L.) assuming the favored quenching parameter $k = 0.16$, which is a factor of ~ 10 above its SM prediction. BSM investigations of CEνNS and elastic neutrino-electron scattering (EνeS) yield competitive bounds for non-standard interactions (NSIs) and simplified mediator models. The energy scales of vector and tensor NSIs are individually constrained to lie above 100 GeV and 360 GeV. Universal couplings of simplified mediators can be probed down to $\sim 10^{-5}$ and $\sim 10^{-6}$ for CEνNS and EνeS, respectively. Finally, 90% C.L. limits on the neutrino's effective magnetic moment ($\mu_{\nu_e} < 7.5 \cdot 10^{-11} \mu_B$) and millicharge ($|q_{\nu_e}| < 3.3 \cdot 10^{-12} e$) are determined.

ZUSAMMENFASSUNG

Die Beobachtung von kohärenter elastischer Neutrino-Kern-Streuung (CEνNS) eröffnet neue Möglichkeiten für den Neutrinosektor des Standardmodells (SM) und darüber hinaus. Als ein führendes Reaktorexperiment strebt CONUS einen Nachweis im kohärenten Wechselwirkungsbereich mit Antineutrinos an, die vom $3{,}9\,\mathrm{GW_{th}}$-Reaktorkern des Kernkraftwerks Brokdorf emittiert werden. Das Experiment nutzt vier hochreine Germaniumdetektoren innerhalb einer kompakten Abschirmung in 17 m Entfernung. In dieser Arbeit werden spektrale Analysen von CEνNS und weiteren Neutrino-Wechselwirkungen jenseits des Standardmodells (BSM) durchgeführt, welche auf Daten basieren, die zwischen April 2018 und Juni 2019 gesammelt wurden. Das Analyseschema stützt sich auf Signalvorhersagen, welche die Entwicklung der Brennstoffzusammensetzung des Reaktors und seiner thermischen Leistung berücksichtigen. Unter Annahme des bevorzugten Quenching-Parameters $k = 0{,}16$, erlaubt die spektrale SM-Analyse ein Limit von $\lesssim 85$ CEνNS-Signalen (90% C.L.) zu bestimmen, welches sich einen Faktor ~ 10 über der SM-Vorhersage befindet. BSM-Untersuchungen von CEνNS und elastischer Neutrino-Elektron-Streuung (EνeS) ergeben kompetitive Grenzen für Nicht-Standard-Wechselwirkungen des Neutrinos (NSIs) und vereinfachte Modelle neuer Austauschteilchen. Die Energieskalen von vektoriellen und tensoriellen NSIs werden jeweils auf Werte oberhalb von 100 GeV und 360 GeV beschränkt. Universelle Kopplungen vereinfachter Austauschteilchen können bis auf $\sim 10^{-5}$ und $\sim 10^{-6}$ für CEνNS bzw. EνeS erprobt werden. Schließlich werden 90% C.L.-Grenzwerte für das effektive magnetische Moment ($\mu_{\nu_e} < 7{,}5 \cdot 10^{-11} \mu_B$) und für die Milliladung ($|q_{\nu_e}| < 3{,}3 \cdot 10^{-12} e$) des Neutrinos bestimmt.

ACKNOWLEDGMENTS

First of all, I would like to thank my PhD supervisor Prof. Dr. h.c. Manfred Lindner, who laid the foundation for my scientific career so far. From the beginning of my bachelor's thesis in your research group until today, you have given me the freedom to choose the topics that interested me the most and encouraged me to remain curious about areas that are not in my "comfort zone". Moreover, the unique opportunity to cross the boundaries between experiment and theory and to participate in and contribute (as a theorist) to relevant phases of an experimental endeavor was a rewarding experience that definitely changed my naive theoretical outlook, even if it was sometimes quite hard and tedious.

Further, I would like to thank my co-supervisors Dr. Werner Maneschg and Dr. Werner Rodejohann for their support and patience throughout the last years. You were understanding when I was occupied either by experimental, theoretical or bureaucratic obligations, but always available when I had questions or concerns. A great thanks to both of you for coming to my defense in times when duties or work became overwhelming.

I am also grateful for the opportunities to become a member of the graduate school "IMPRS-PTFS" and the research training group GRK1940 at Heidelberg University. Besides the interesting lectures and seminars, I enjoyed several retreats and interesting discussions. In that context I want to deeply thank Janette Bloch-Ditzinger, Anja Kamp, Britta Schwarz and Anja Berneiser for their support in terms of bureaucratic and organizational matters. Even if it is not always visible in daily (doctoral) life, your work forms the basis for the achievements in the context of a doctorate.

I am thankful to Prof. Dr. Jörg Jäckel for donating me his valuable time around Christmas in order to read and review this thesis. Further thanks are directed to the other members of my promotion committee, Priv.-Doz. Dr. Teresa Marrodán Undagoitia and Prof. Dr. Matthias Bartelmann, for their time and flexible calendars.

Special gratitude is directed to my experimental colleagues of the Conus Collaboration: Hannes Bonet, Aurélie Bonhomme, Christian Buck, Janina Hakenmüller, Janine Hempfling, Jakob Henrichs, Gerd Heusser, Thomas Hugle, Kai Fülber (KBR), Werner Maneschg, Herbert Strecker, Tobias Schierhuber, Josef Stauber and Roland Wink (KBR). Thank you for the pleasant working environment and your patience in dealing with the several naive theory questions I asked over the years. At this point, I want to highlight the work in cooperation with my colleague Dr. T. Hugle with whom together the analysis routines of this work were developed. I learned a lot from you and your knowledge about advanced programming techniques helped to improve and optimize the written code at several stages.

The scientific expertise of Dr. Kai Fülber (KBR), Dr. Constanze Hasterok, Dr. Stefan Schoppmann and Dr. Markus Seidl (Preussen Elektra GmbH) were quite valuable for

this work's outcome. Further, a large thank-you is also directed to the MPIK IT group, especially to Stephanie Kolb, Frank Köck and Kevin Zink for providing the technical infrastructure that allowed the intensive computations of this thesis.

Moreover, I want to emphasize the patience and stamina of Dr. Kai Schmitz and Dr. Werner Rodejohann in the context of our theory project, which was interrupted several times by my obligations in the CONUS Collaboration.

I am further grateful for the proof-reading of Ingolf Bischer, Aurélie Bonhomme, Christian Döring, Thomas Hugle, Werner Maneschg, Karsten Mosny, Mortitz Platscher, Oliver Scholer and Katharina Rink.

The great time I enjoyed in the "Partybüro" during my PhD needs to be mentioned as well. Thank you for the many interesting and passionate discussions and for moments that will be remembered: Cristina Benso, Ingolf Bischer, Christian Döring, Yannick Emonds, Thomas Hugle, Carlos Jaramillo, Kevin Max, Mortitz Platscher, Tobias Schierhuber, Oliver Scholer. The tea and coffee groups consisting of Aurélie Bonhomme, Janina Hakenmüller, Christian Döring, Veronica Pizzella and Thomas Hugle were important for maintaining the author's caffeine level. The foundations of this thesis have been laid down in studies at Heidelberg University together with Patrick Friedrich, Christoph Klein, Agnes Korcsak-Gorzo, Karsten Mosny, Felix Riexinger, Linda Shen, Sebastian Thielen and Adrian van Kan.

I also like to give thanks to the Marburg crew for accepting my regular absence in several activities within the last years, but still calling me a group member: Aline Behmenburg, Daniel Gimbel, Lars Kautzner, Matthias Muth, Yvette Maly-Muth, Julia Szabo, Lukas Wellner.

I want to sincerely thank my family for their support through my studies and this doctoral period: my sisters Lisa Sophie Rink and Theresa Laus as well as my parents Silke und Helmut Rink.

My deepest gratitude belongs to my best friend and beloved wife, Katharina Rink. Without you this work would have never been written...

Contents

List of Figures xiii

List of Tables xv

List of Abbreviations xvii

1 Introduction 1

2 Theoretical Foundations 7

- 2.1 Coherent elastic neutrino-nucleus scattering (CEνNS) . . . 7
  - 2.1.1 Scattering amplitude: from quarks to nuclei . . . 7
    - 2.1.1.1 Standard Model Lagrangian below the electroweak scale . 8
    - 2.1.1.2 Single-nucleon scattering amplitudes . . . 9
    - 2.1.1.3 From nucleons to the nucleus . . . 12
  - 2.1.2 Scattering cross section and channel properties . . . 14
  - 2.1.3 Coherence condition and nuclear form factors . . . 17
  - 2.1.4 Nuclear recoils, signal quenching and detectable energy . . . 19
- 2.2 Requirements for successful CEνNS detection . . . 20
  - 2.2.1 The neutrino source . . . 21
    - 2.2.1.1 Pion decay-at-rest neutrino sources . . . 21
    - 2.2.1.2 Nuclear reactors . . . 22
  - 2.2.2 Background in low energy threshold CEνNS experiments . . . 24
    - 2.2.2.1 Overview of different background components . . . 25
    - 2.2.2.2 Background suppression techniques . . . 28
  - 2.2.3 Detection techniques . . . 29
    - 2.2.3.1 Scintillation detectors . . . 30
    - 2.2.3.2 Semiconductor detectors . . . 30
    - 2.2.3.3 Sub-Kelvin detectors . . . 31
- 2.3 Statistical data analysis . . . 32
  - 2.3.1 Parameter estimation and maximum likelihood method . . . 32
    - 2.3.1.1 Parameter estimation . . . 32
    - 2.3.1.2 Maximum likelihood method . . . 33
    - 2.3.1.3 Maximum likelihood for binned data . . . 36
    - 2.3.1.4 Systematic uncertainties as nuisance parameters . . . 36
  - 2.3.2 Hypothesis tests . . . 37

2.3.2.1 Hypotheses and significance levels 37
2.3.2.2 Likelihood ratio test and Neyman-Pearson lemma 39
2.3.2.3 Test statistics and Wilks' theorem 40
2.3.3 Confidence intervals and limits within the maximum likelihood approach 41
2.3.4 Experimental sensitivity 42

3 Investigating coherent elastic neutrino-nucleus scattering within the Conus experiment 45
3.1 The Conus experiment 45
3.1.1 Experimental site 46
3.1.2 Conus shield design 48
3.1.3 Conus detectors 48
3.2 CEνNS prediction for the Conus experiment 50
3.2.1 Reactor antineutrino emission spectra 51
3.2.2 Quenching effects in germanium for low nuclear recoil energies . . . 58
3.2.3 Electronic response 60
3.2.4 Theoretical CEνNS prediction and contributing uncertainties . . . 63
3.3 Constraints on CEνNS in the fully coherent regime 64
3.3.1 Conus data collection 65
3.3.2 Background contributions and modeling 66
3.3.2.1 Reactor-uncorrelated background contributions 66
3.3.2.2 Reactor-correlated background contributions 67
3.3.2.3 Background modeling 68
3.3.2.4 Elastic neutrino-electron scattering (EνeS) 69
3.3.3 Statistical investigation 69
3.3.3.1 Systematic uncertainties 70
3.3.3.2 Likelihood function and implementation 71
3.3.3.3 Simulation of test statistic 73
3.3.4 First spectral CEνNS limits from the Conus experiment 74
3.3.4.1 Exemplary single-detector fit: C1R1 74
3.3.4.2 CEνNS limits from combined data sets 76
3.4 Summary and outlook 77

4 Novel constraints on neutrino physics beyond the standard model 81
4.1 Adjustments of the analysis procedure 81
4.1.1 Extension of data sets at higher energies 82
4.1.2 Background modeling and systematic uncertainties 82
4.1.3 Refined antineutrino emission spectra 84
4.1.4 Simulation of test statistic and limit determination of BSM models 86
4.2 Non-standard neutrino interactions 86
4.2.1 Effective field theory and new neutrino interactions 87
4.2.2 Vector-type interactions 89
4.2.2.1 Cross section 89
4.2.2.2 Results 90
4.2.3 Tensor-type interactions 92

4.2.3.1 Cross section . . . 92
4.2.3.2 Results . . . 93
4.3 New particle searches in a simplified model framework . . . 95
4.3.1 Foundations of simplified dark matter (DM) models . . . 95
4.3.2 Light scalar mediators . . . 97
4.3.2.1 Cross sections . . . 97
4.3.2.2 Results . . . 99
4.3.3 Light vector mediators . . . 101
4.3.3.1 Cross sections . . . 101
4.3.3.2 Results . . . 103
4.4 Neutrino magnetic moment (νMM) and millicharge (νMC) . . . 105
4.4.1 Neutrino electromagnetic properties . . . 105
4.4.2 Magnetic and electric dipole moments . . . 107
4.4.3 Electromagnetic induced EνeS: νMM and νMC . . . 110
4.4.4 Results on the effective νMM and νMC . . . 112
4.5 Summary and outlook . . . 113

5 The future of Conus and CEνNS 117
5.1 Improvements of the CONUS set-up . . . 117
5.2 Improved reactor antineutrino spectra . . . 121
5.3 Nuclear form factors . . . 123
5.4 Further BSM neutrino phenomenology . . . 124
5.4.1 Weinberg angle at low-Q value . . . 124
5.4.2 νMM and νMC via CEνNS and neutrino charge radius . . . 125
5.4.3 Sterile neutrino searches . . . 128
5.4.4 New Fermions and Dark matter . . . 129
5.5 The future of CEνNS investigations . . . 130
5.5.1 Advantages of different target materials . . . 131
5.5.2 Complementarity in CEνNS searches . . . 131
5.5.3 Neutrino astronomy . . . 132
5.6 Summary . . . 133

6 Conclusions 135

Appendices 141
A CEνNS fundamentals . . . 141
B Additional tools for maximum likelihood methods . . . 147
C Supplementary plots . . . 151
D Monte Carlo simulation of the test statistic . . . 157

Disclaimer 163

Bibliography 165

List of Figures

Fig. 1.1: Comparison of different neutrino interactions 4

Fig. 2.1: Feynman diagram of the CEνNS process 15
Fig. 2.2: CEνNS cross section for different neutrino energies and target materials 16
Fig. 2.3: Spectra of neutrino sources applied in current CEνNS experiments . . 22
Fig. 2.4: Overview of potential CEνNS detection techniques 29
Fig. 2.5: Likelihood contour around minimum and error determination 35
Fig. 2.6: Illustration of a hypothesis test 38

Fig. 3.1: Conus location inside the Brokdorf nuclear power plant 47
Fig. 3.2: CONUS shield design and detectors 49
Fig. 3.3: Reactor thermal power during the first two data collection periods . . 52
Fig. 3.4: Full reactor antineutrino emission spectrum for C1R1 55
Fig. 3.5: Spectral contribution of E_ν to the obtained CEνNS events 59
Fig. 3.6: Expected CEνNS count rates for C1R1 in dependence of E_{thr} and k . 61
Fig. 3.7: Exemplary single-detector fit for C1R1 75
Fig. 3.8: Confidence levels (1-p) of CEνNS counts and s-parameters for C1R1 75
Fig. 3.9: Upper limits on CEνNS events 77

Fig. 4.1: Signal expectation and allowed regions for vector NSIs 91
Fig. 4.2: Signal expectation and allowed regions for tensor NSIs 94
Fig. 4.3: Signal expectation and exclusion limits for light scalar mediators . . . 100
Fig. 4.4: Signal expectation and exclusion limits for light vector mediators . . 104
Fig. 4.5: νMM- and νMC-EνeS signal expectation for C1R1 111
Fig. 4.6: Example fit of combined νMM investigation for C1R1 112

Fig. 5.1: Quenching factor measurement of the Conus Collaboration 119
Fig. 5.2: New reactor antineutrino spectrum and CEνNS sensitivity to $\sin^2\theta_W$ 123
Fig. 5.3: Conus sensitivity to sterile neutrinos and new fermions 129

Fig. C.1: Logarithmic reactor antineutrino spectrum for C1R1 151
Fig. C.2: Signal uncertainties induced by the reactor antineutrino spectrum . . 152
Fig. C.3: Reactor thermal power of extended data sets 152
Fig. C.4: Overview of quenching factor measurements 153
Fig. C.5: CEνNS event spectrum in dependence of quenching 153
Fig. C.6: Ionization energy spectrum of detector C2 154

Fig. C.7: Background suppression capability of the CONUS shield 155
Fig. C.8: CONUS background model and its composition 156

List of Tables

Tab. 2.1: Overview of weak NC couplings constants for all SM fermions 9
Tab. 2.2: Coherence condition for potential CEνNS detector materials 18
Tab. 2.3: Detection requirements at different neutrino sources 19

Tab. 3.1: Active detector masses of the CONUS detectors 50
Tab. 3.2: Average fission fractions of the main fission isotopes 53
Tab. 3.3: General information about the four main fission isotopes 53
Tab. 3.4: Average thermal powers and corresponding reduced reactor fluxes . . 56
Tab. 3.5: Relevant quantities of the CONUS antineutrino emission spectra . . 64
Tab. 3.6: Detector exposures and ROIs used within the SM analysis 65
Tab. 3.7: Likelihood fit parameters with uncertainties of the SM analysis . . . 71

Tab. 4.1: Detector exposures and ROIs used in the BSM analyses 83
Tab. 4.2: Nuisance parameters with uncertainties of the BSM analyses 85

Tab. 5.1: CEνNS events and significance projections for Conus and Conus-100 120

Tab. 6.1: Summarized findings of this work 136

List of Abbreviations

$0\nu\beta\beta$ neutrinoless double beta decay

BAU baryon asymmetry of the universe

BNB Booster Neutrino Beam

BSM Beyond the Standard Model

C.L. confidence level

CC charged-current

CCD charge-coupled device

CDF cumulative distribution function

CEνNS coherent elastic neutrino-nucleus scattering

CI confidence interval

CM center-of-mass

CMB cosmic microwave background

CONUS **CO**herent elastic **N**eutrino-n**U**cleus **S**cattering

DAQ data acquisition

DD direct detection

DM dark matter

DOF degree of freedom

EFT effective field theory

EνeS elastic neutrino-electron scattering

EOM equation of motion

ESS European Spallation Neutron Source

EW	electroweak
GNI	general neutrino interaction
HMM	Huber-Mueller model
HPGe	high-purity germanium
IBD	inverse beta decay
ID	indirect detection
KBR	Kernkraftwerk Brokdorf (Germany)
LAr	liquid argon
LFV	lepton flavor violation
LHC	Large Hadron Collider
LNV	lepton number violation
LXe	liquid xenon
MC	Monte Carlo
ML	maximum likelihood
MLF	Material and Life Science Experimental Facility
MPIK	Max-Planck-Institut für Kernphysik, Heidelberg (Germany)
MSSM	Minimal Supersymmetric Standard Model
m w.e.	meters of water equivalent
NC	neutral-current
ν**MC**	neutrino millicharge
ν**MM**	neutrino magnetic moment
NP	New Physics
NSI	non-standard (neutrino) interaction
PDF	probability density function
π-**DAR**	pion decay-at-rest

PMT photomultiplier tube

PSD pulse-shape discrimination

PWR pressurized water reactor

QCD quantum chromodynamics

QED quantum electrodynamics

QF quenching factor

QM quantum mechanics

RAA reactor antineutrino anomaly

RMS root mean square

ROI region of interest

SM Standard Model of Particle Physics

SNS Spallation Neutron Source

SSB spontaneous symmetry breaking

VEV vacuum expectation value

WIMP weakly interacting massive particle

Chapter 1

Introduction

It is fascinating and also slightly disturbing that fundamental properties of the second most abundant particle of our Universe, the neutrino, still provide mysteries with the ability of questioning our knowledge gained from decades-long investigations. However, looking at the history of neutrino research, unanswered questions and at first irritating experimental results have been quite the rule rather than the exception, cf. Ref. [1, 2]. Accepting this and acknowledging the developments both in experimental and theoretical areas lets one appreciate the impressive journey neutrino physics has undertaken within the last century.

Postulated by W. Pauli in 1930 as a stopgap in order to explain the continuous beta decay emission spectrum [3], neutrino physics flourished from a theoretical idea, which was never expected to be measured, to an independent and highly active research field that, up to now, accumulated four Nobel prices [4]. While W. Pauli assumed it to be a massive but electrically neutral particle, E. Fermi [5] and F. Perrin [6] established the neutrino to be massless. Its elusive character as very weakly interacting particle caused experimental physics to take over two decades to proof its existence [7, 8]. Only by using a nuclear reactor as powerful antineutrino source and large target masses it was possible for Reines and Cowan to claim its first detection via inverse beta decay (IBD) in 1956. The observation of solar neutrinos by the Homestake experiment [9] another two decades later, was a further milestone for neutrino physics although the lack of expected events triggered new discussions, i.e. the so-called solar neutrino problem [10]. Potential solutions were also discussed in context of new neutrino properties and interactions, cf. Refs. [11–13]. The problem was finally solved by measurements of the experiments SNO [14] and Super-Kamiokande [15, 16] which proved the existence of neutrino flavor conversion during their propagation (neutrino oscillations) [17–19]. The picture got complete by inclusion of the Mikheyev-Smirnov-Wolfenstein (MSW) effect for high energy neutrinos, i.e. enhanced flavor conversions due to resonant neutrino interaction with matter [20, 21]. The implication that neutrinos exhibit tiny masses is the first concrete hint that the Standard Model of Particle Physics (SM) is incomplete! After years of investigations most of the parameters that underlie neutrino oscillations have been determined, i.e. the three angles within their mixing matrix θ_{12}, θ_{23}, θ_{13} and their mass squared differences Δm^2_{21}, $|\Delta m^2_{32}|$, while the unknown sign of the latter still allows for different mass orderings among the three detected neutrinos [22]. Upcoming experiments are likely to determine this ordering and might test for a non-zero phase within the neutrino mixing matrix (lepton CP violation).

However, we are still far away from understanding the neutrinos' full nature. Simple questions like the origin of their masses and why neutrinos are much lighter than all other SM fermions are yet not answered. Even whether neutrinos are Dirac or Majorana fermions, which would have strong phenomenological consequences like lepton number violation (LNV), remains unclear.

Neutrinos and their interactions play important roles in several physics branches and connect a wide range of physical scales, from the largest scales of cosmology to the smallest scales of nuclear and particle physics. They take part in primordial [23] as well as stellar nucleosynthesis [24, 25] and could affect the formation of large-scale structures [26]. Moreover, they might even be related to the creation of the observed baryon asymmetry of the universe (BAU) [27] and thus basically to our entire existence. Their weak interacting nature allows to obtain insights of far cosmological distances and from extreme environments, like supernova explosions [28–30], the interior of stars [31, 32] or even black holes [33]. Especially in the later stages of stellar evolution, neutrino emission is the primary energy loss mechanism and coherently enhanced momentum transfer from neutrinos to nuclei is important in blowing off outer matter layers of stars [28, 34].

Neutrino mass, as *the* concrete indicator for the existence of Beyond the Standard Model (BSM) physics, might also be related to other unanswered questions of particle physics. Therefore, it is not surprising that neutrinos and their properties are discussed in various contexts, e.g. in connection to the BAU via leptogenesis [35–37], dark matter (DM) [38–40], the flavor problem as well as gauge unification [41, 42] or even extra dimensions [43]. Further, neutrinos have been considered as a solution to the muon anomalous magnetic moment [44], an observed tension in determinations of the Hubble parameter H_0 [45, 46] as well as a recently detected excess in measurements of the XENON1T experiment [47]. From a theoretical perspective, there exists a large number of models capable of explaining neutrino masses, cf. Ref. [48, Section 9], and corresponding predictions such as new neutrino interactions or additional neutrino properties can be used to test them.

Although approached from various directions, the SM so far withstands all experimental tests and thus remains the most successful and consistent framework to describe particle interactions, except neutrino masses of course. Due to the lack of smocking gun signatures for distinct BSM models, e.g. the Minimal Supersymmetric Standard Model (MSSM), phenomenologists nowadays tend to rely on more model-independent frameworks. For example, effective field theories (EFTs) as well as so-called simplified models have become popular in order to test interaction channels on more general grounds.

All these points make neutrino interactions and their properties an interesting field of study. In particular, in the absence of clear evidence for certain BSM physics, neutrinos remain the only guiding principle towards a more complete understanding of nature. Over the years a broad neutrino research program developed with experiments tackling the yet unknown neutrino parameters, i.e. their fermionic nature and mass hierarchy through neutrinoless double beta decay ($0\nu\beta\beta$) (GERDA [49], LEGEND [50], Majorana Demonstrator [51], even future DM experiments like XENONnT [52]...), the absolute neutrino mass scale (ECHO [53], KATRIN [54], Project8 [55]...), leptonic CP violation and mass hierarchy (DUNE [56], Hyper-K [57], JUNO [58]...). Further, experiments have been set up to test the existence of sterile neutrinos (PROSPECT [59], STEREO [60], ...). In astronomical context, several telescopes that rely on neutrino detection have been built or are in consideration

(Antares [61], IceCube [62], KM3NeT [63], Rno-G [64]...), and together with light and gravitational waves they opened the era of multi-messenger astronomy [65]. In any case, the neutrino's weak coupling to other SM particles pushes the applied technologies to their boundaries. Therefore, large detector masses or instrumented volumes are still a general feature of neutrino experiments until recently.

Developments in the last decades have reached a status where the detection of coherent elastic neutrino-nucleus scattering (CEνNS) has become possible for several detector technologies. CEνNS is a SM channel that has been predicted shortly after the discovery of the Z boson as a new weak neutral-current (NC) interaction by D. Freeman in 1974 [28, 34, 66, 67]. As illustrated in Fig. 1.1, its coherent nature, reflected by its scaling with the squared neutron number of the target nucleus, renders it the strongest known neutrino interaction, which is about two and four orders of magnitude stronger than IBD and elastic neutrino-electron scattering (EνeS), respectively. Hence, via CEνNS neutrinos may be detected with kg-size detectors and high event rates! The difficulty, however, lies in the corresponding observable, i.e. (very small) nuclear recoils, which is why it remained undetected for over forty years. In 2017 and subsequently in 2021 the Coherent Collaboration reported first observations with a Spallation Neutron Source (SNS) at the Oak Ridge National Laboratory by using a CsI(Na) [68] and a liquid argon (LAr) detector [69], respectively. The strongest CEνNS limits from a reactor site so far have been reported by the **CO**herent elastic **N**eutrino-n**U**cleus **S**cattering (CONUS) experiment [70]. Likewise further attempts close to nuclear reactors have been established: Connie [71], Miner [72], Ncc-1701 at Dresden-II [73], Neon [74], ν-cleus [75], νGen [76], Red-100 [77], Ricochet [78] and Texono [79]. Thus, CEνNS is approached with the full repertoire of modern detection technologies and various target materials, i.e. charge-coupled device (CCD) sensors [80], cryogenic calorimeters [81], high-purity germanium (HPGe) crystals [82], liquid noble gas detectors [83] as well as scintillating crystals [84].

This newly accessible interaction channel is not only interesting to confirm SM neutrino interactions. It is additionally linked to a rich neutrino phenomenology in both, SM and BSM context. In principle, important (CEνNS) applications like reactor monitoring and controlling of nuclear non-proliferation might become possible in the future [85–87].

While so far no deviations from its SM prediction have been observed, CEνNS already stimulated various BSM studies [88–92]. Within the SM context, it allows to determine the neutron density distribution of the target nucleus [93–96]. Although only mildly depending on the Weinberg angle $\sin^2\theta_W$, measurements in the MeV-regime are possible as well [97–100]. Moreover, as a NC it provides the opportunity to be threshold-free and sensitive to all neutrino flavors. Thus, flavor-blind neutrino detection (in contrast to IBD measurements) of certain sources can be done, e.g. of reactor, solar or supernova (anti)neutrinos. In particular, the future generation of DM direct detection (DD) experiments is going to probe the so-called neutrino floor [101–104], i.e. an irreducible background for DM DD experiments by coherent interaction of atmospheric, solar and (diffuse) supernova neutrinos. First investigations of high-energy solar neutrinos will become possible already with the next generation of experiments, especially of neutrinos from ^{8}B decays [104–106]. Thus, the sun itself is likely to become a source for future (SM and BSM) CEνNS investigations [107–110].

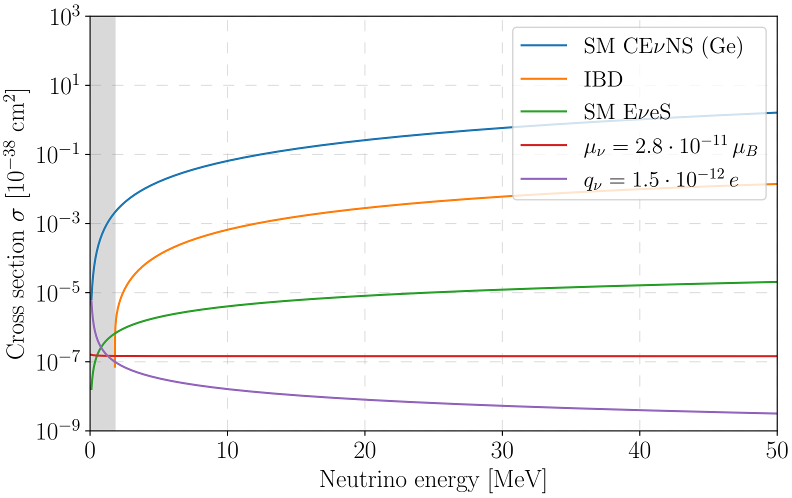

Figure 1.1.: Comparison of different SM and BSM neutrino interactions. Assuming a germanium target, the total CEνNS cross section exceeds the ones of IBD and EνeS by two and four orders of magnitude, respectively. The IBD threshold energy $E_{IBD}^{\mathrm{min}} = 1.806\,\mathrm{MeV}$ [149] is indicated in gray. Further, we indicate cross sections of EνeS induced by an effective νMM as well as an effective νMC. For both we assume the current best limits given by Ref. [150] and Ref. [151].

In the general context of BSM neutrino physics, CEνNS is interesting for testing new non-standard (neutrino) interactions (NSIs) among neutrinos and quarks [111–117]. Neutrino electromagnetic properties, in particular a neutrino magnetic moment (νMM), can be studied in two-fold way, either directly via CEνNS or via EνeS, and benefit from the low backgrounds and low thresholds of CEνNS-measuring experiments [118–122]. Both interactions are in principle induced by a finite νMM. This is especially interesting as the Xenon1T Collaboration [47] reported an excess in the energy region of $[2, 3]\,\mathrm{keV}$, that could, among others solutions, be explained by a νMM slightly below its current best limits. Although being in tension with astrophysical constraints [123–125], CEνNS measuring devices with low threshold energy could shed light on this matter. Further, searches for light mediators can be conducted via CEνNS [92, 126–128]. In particular, spectral distortions in the recoil energy spectrum could hint for new light scalars [129–131] or light vectors [132–134]. In this spirit, CEνNS measurements might contribute to axion-like particle [131] and dark photon searches [135, 136]. Investigations of new fermions [137, 138] have been discussed as well as CEνNS searches for eV-mass sterile neutrinos [139–143], which could explain the observed reactor antineutrino anomaly (RAA) [144–146]. Of course, DM investigation might also profit from this new interaction channel [126, 147, 148].

This work deals with spectral investigations of CEνNS and related BSM phenomena of the first two data collection periods conducted by the CONUS experiment from April 2018 to June 2019. CONUS uses four kg-size HPGe detectors in an elaborated shield design and is located at 17 m-distance to the 3.9 $\mathrm{GW_{th}}$-single-unit pressurized water reactor (PWR) core of the commercial nuclear power in Brokdorf (Germany). Besides a flux orders of magnitude larger than pion decay-at-rest (π-DAR) sources, the energy of reactor antineutrinos allows a CEνNS detection in the fully coherent regime. Thus, the cross section receives no reduction by nuclear form factors, which quantify the transition from scattering off a point-like object. However, this advantage comes at the price of having lower nuclear recoils, which are even harder to detect. CEνNS at a reactor site represents a complementary approach to measurements at π-DAR sources and provides further possibilities for νMM or sterile neutrino searches as well as for reactor investigations. A spectral analysis of SM CEνNS is performed with data obtained in the first two data collection periods. Subsequently, BSM models that are commonly investigated in the context of CEνNS, such as NSIs of vector- and tensor-type as well as simplified mediator models for light scalar and vector particles, are tested. EνeS induced within the latter framework is searched for with data sets at slightly higher energies. In addition, these data sets are used to deduce constraints on electromagnetic properties of the neutrino, i.e. a finite νMM and with it, a limit on the neutrino millicharge (νMC). Future aspects of the CONUS experiment as well as opportunities of CEνNS related to further measurements are discussed as well.

This thesis has been carried out in the context of the CONUS experiment which searches for CEνNS and BSM physics. The findings presented in this work are the result of a long-lasting process in which the author himself already contributed with first sensitivity studies during and after his bachelor's thesis and accompanied the experiment's design and development phase in parallel to his master's studies. Further, the author had the opportunity to visit the experimental site while contributing to the commissioning process.

This work is structured in the following way:
In Chapter 2, we introduce the fundamentals of CEνNS and the performed analysis method, whereby we approach the topic from theoretical and experimental perspective. The interaction's characteristics are highlighted and the experimental challenges are pointed out, after which we lay down the statistical essentials of the performed investigations. The first spectral analysis of the CONUS experiment is content of Chapter 3. Here, the ingredients underlying a realistic signal prediction are illustrated and the analysis scheme that is applied throughout this work is described, before we present collaborative effort in setting the best CEνNS limits from a reactor-based experiment so far. Chapter 4 covers subsequent analyses of potential BSM signatures of the collected CONUS data sets. With a refined analysis method, NSIs of vector- and tensor-type, simplified mediator model of light scalar and vector particles in addition to electromagnetic neutrino properties (effective νMM and νMC) are investigated. Afterwards, a discussion about further opportunities of CEνNS within CONUS and in the future is given in Chapter 5. Improvements of the CONUS set-up and further investigation possibilities are illustrated, while CEνNS measurements are also discussed in terms of their complementarity among each other and to further physics branches. In the end, we put our findings into context and conclude with Chapter 6. Formal and technical aspects of this work and supplementary material are collected in several appendices.

Chapter 2

Theoretical Foundations

The first investigation of CEνNS at a reactor site as well as subsequent analyses in the context of BSM neutrino phenomenology require a broad range of topics, ranging from experimental prerequisites necessary for its detection, over knowledge about statistical inference to its theoretical modifications in the context of BSM physics. This chapter provides an overview into the individual topics, starting with the derivation of the CEνNS cross section. Afterwards, the subject is illuminated from the experimental side and developments recently discussed as detection possibilities are introduced. In the end, we close with statistical data analyses and present techniques that are used throughout this work.

2.1 Coherent elastic neutrino-nucleus scattering

At first we start with a derivation of the CEνNS cross section from the SM Lagrangian, while we introduce additional knowledge needed for its extensions. Subsequently, we elaborate on the channel's characteristic properties, i.e. its coherent nature, and further, quantify experimental requirements for its detection. This section is mainly based is knowledge presented in Refs. [28, 115, 152–154].

2.1.1 Scattering amplitude: from quarks to nuclei

In (high-energy) particle physics, interactions are commonly defined at the most fundamental level we know today, i.e. leptons, quarks and bosons. Altogether they constitute the so-called Standard Model of Particle Physics defined by the corresponding Lagrangian [152, Chapter 7]. Hence, BSM physics of new particles and new interactions are usually introduced at the same level. Since the energy scale of CEνNS is well below the scale of quark confinement, the relevant degrees of freedom (DOFs) are not quarks but nuclei. Therefore, we have to understand how one obtains the interaction cross section at hadron or nucleus level from a theory that is formulated at quark level. In doing so, we also introduce expressions that are relevant in the context of new BSM neutrino interactions, cf. Ch. 4.

2.1.1.1 Standard Model Lagrangian below the electroweak scale

We start with the SM Lagrangian after spontaneous symmetry breaking (SSB) and focus only on the Gauge and Higgs sector, while choosing unitary gauge, i.e. $\phi \to \frac{1}{\sqrt{2}}\begin{pmatrix}0 & h+\nu\end{pmatrix}^T$ [152, Chapter 7.2.2]. After the symmetry breaking of $SU(2)_L \times U(1)_Y \to U(1)_{em}$, the corresponding weak and hypercharge gauge bosons acquire mass through the kinetic term of the Higgs boson, which takes the form

$$\mathcal{L}_\phi \supset (D_\mu\phi)^\dagger(D^\mu\phi) = \frac{1}{2}(0\ \ \nu)\left[\frac{g}{2}\tau^i W^i_\mu + \frac{g'}{2}B_\mu\right]^2\begin{pmatrix}0\\ \nu\end{pmatrix} + \text{h-terms}\,, \tag{2.1}$$

with the Pauli matrices $\tau^i\,, i=1,2,3$ and the $SU(2)_L$ and hypercharge couplings g and g', respectively. While the weak charged-current (CC) mediators $W^\pm = \frac{1}{\sqrt{2}}\left(W^1 \mp iW^2\right)$ obtain similar masses, the weak NC mediator becomes a mixed state of the $SU(2)_L$ and $U(1)_Y$ bosons, i.e. $Z \equiv -\sin\theta_W B + \cos\theta_W W^3$, which in addition acquires a different mass. The corresponding gauge boson masses are defined according to[1]

$$M_W^2 W^{+\mu}W^-_\mu + \frac{M_Z^2}{2}Z^\mu Z_\mu \equiv \frac{g^2\nu^2}{4}W^{+\mu}W^-_\mu + \frac{1}{2}\left(g^2+g'^2\right)\frac{\nu^2}{4}\left[\frac{-g'B_\mu + gW^3_\mu}{\sqrt{g^2+g'^2}}\right]^2\,, \tag{2.2}$$

and the weak mixing angle θ_W[2] is obtained from a combination of the couplings g and g',

$$\sin\theta_W = \frac{g'}{\sqrt{g^2+g'^2}}\,, \qquad \cos\theta_W = \frac{g}{\sqrt{g^2+g'^2}}\,. \tag{2.3}$$

In addition to the massive neutral gauge boson Z, there is a massless one associated with the electromagnetic interaction $U(1)_{em}$, i.e. the photon $A = \cos\theta_\theta B + \sin\theta_W W^3$. All in all, after SSB the (tree-level) gauge boson masses are given by

$$m_W = \frac{g\,\nu}{2}\,, \qquad m_Z = \frac{\sqrt{g^2+g'^2}\,\nu}{2} = \frac{m_W}{\cos\theta_W}\,, \qquad m_A = 0\,, \tag{2.4}$$

with $\nu \simeq 246\,\text{GeV}$ being the vacuum expectation value (VEV) of the Higgs boson.

For CEνNS only the NC interactions is relevant, which are obtained from the fermion and Yukawa part of the SM Lagrangian [152, Chapter 7.2.2], yielding

$$\mathcal{L}_\Psi + \mathcal{L}_{\text{Yuk}} \supset -eJ^\mu_Q A_\mu - \frac{g}{2\cos\theta_W}J^\mu_Z Z_\mu\,, \tag{2.5}$$

with the elementary charge being defined as $e \equiv g\sin\theta_W$. The corresponding currents are

---

[1] Equation (2.2) is a direct consequence of Eq. (2.1) under application of $\tau^i W^i_\mu = \tau^3 W^3_\mu + \sqrt{2}\tau^+ W^+_\mu + \sqrt{2}\tau^- W^-_\mu$ with $\tau^\pm = \frac{1}{\sqrt{2}}\left(\tau^1 \mp i\tau^2\right)$.

[2] Throughout this work, we will use the terms *Weinberg angle* or *weak mixing angle* as synonyms for any expression containing θ_W, i.e. $\sin^{(2)}\theta_W$ and $\cos^{(2)}\theta_W$.

fermions	charge	vector coupling g_V	axial-vector coupling g_A
ν_e, ν_μ, ν_τ	0	$\frac{1}{2}$	$\frac{1}{2}$
e, μ, τ	-1	$-\frac{1}{2} + 2\sin^2\theta_W$	$-\frac{1}{2}$
u, c, t	$\frac{2}{3}$	$\frac{1}{2} - \frac{4}{3}\sin^2\theta_W$	$\frac{1}{2}$
d, s, b	$-\frac{1}{3}$	$-\frac{1}{2} + \frac{2}{3}\sin^2\theta_W$	$-\frac{1}{2}$

Table 2.1.: Overview of weak neutral-current coupling constants for all SM fermions.

defined according to

$$J^\mu_Q = \sum_r q_r \bar{\psi}_r \gamma^\mu \psi_r \,, \qquad\qquad J^\mu_Z = \sum_r \bar{\psi}_r \gamma^\mu \left(g^r_V - g^r_A \gamma^5 \right) \psi_r \,, \tag{2.6}$$

where r runs over all fermion species. Further, q represents the electric charge of the fermion (generation) and the vector and axial-vector couplings of the NC are given by

$$g^r_V = t^3_{rL} - 2q_r \sin^2\theta_W q_r \qquad\qquad g^r_A = t^3_{rL} \,, \tag{2.7}$$

with t^3_{rL} being the value of the weak isospin's third component. An overview of all SM fermion couplings is given in Tab. 2.1.

In the limit of small momentum transfer, i.e. $q^2 \ll m_Z^2$, the weak gauge bosons can only exist as virtual particles, whose propagator is dominated by the mediator mass such that the weak NC part reduces to an effective "four-fermion" interaction with coupling strength given by the Fermi constant G_F,

$$\mathcal{L}^{\text{NC}}_{eff} = -\frac{G_F}{\sqrt{2}} J^\mu_Z J_{Z\mu} \,, \qquad \text{with} \quad \frac{G_F}{\sqrt{2}} = \frac{g^2}{8m_W^2} = \frac{1}{2\nu^2} \,. \tag{2.8}$$

This is the classical example of an EFT, where the physics at a given scale $q^2 \ll m_Z^2$ is given in terms of the relevant DOFs and higher-dimensional (non-renormalizable) operators. The (Wilson) coefficients are experimentally determined or calculated from the underlying (UV) theory. More details about the effective NC interaction, especially how one determines Eq. (2.8) is given in App. A.1.

2.1.1.2 Single-nucleon scattering amplitudes

Now we derive the scattering amplitude for CEνNS, while following closely derivations in the context of DM DD summarized in Ref. [154]. Since we later deal with scalar and vector modifications of CEνNS, we will only focus on these aspects. For the derivation of the CEνNS cross section we assume the nucleus to be a spin-0 particle for simplicity.

For the first step in the calculation of the CEνNS amplitude $\mathcal{M}_{\text{CE}\nu\text{NS}}$, the hadronic matrix elements of gluon and quark operators are needed, with which one can calculate the individual scattering amplitudes of neutrino-nucleon scattering. We follow the convention of Ref. [154] and define the neutrino-nucleon scattering amplitude $\mathcal{M}_{\nu N}$ in relation to the corresponding scattering matrix $S_{\nu \mathrm{N}} = \langle \nu', N' | \nu, N \rangle + (2\pi)^4 \delta^{(4)}(p + k - p' - k')\, i\mathcal{M}_{\nu \mathrm{N}}$, with k, k' being the initial and final momenta of the nucleon and p, p' being the respective expressions for the (anti)neutrino. The first term represents no scattering at all and is irrelevant for the following considerations. We further define the shorthand notation $|N\rangle \equiv |N(\boldsymbol{k}, r)\rangle$ with $N \in \{p, n\}$ for the nucleon state vector with momentum k and spin r and imply operator matrix elements always to be evaluated at the origin. For spinors, we apply the same notation, i.e. $u_N \equiv u_N(\boldsymbol{k}, r)$ for a spinor with momentum k and spin r.

Here, we consider the following two Lagrangians which will serve as basic examples for SM and BSM CEνNS interactions,

$$\mathcal{L}_I = c_{q,g} \mathcal{O}_\nu(x) \mathcal{O}_{q,g}(x)\,, \qquad \mathcal{L}_{II} = \mathcal{O}_\nu(x) S(x) + \mathcal{O}_q(x) S(x)\,, \tag{2.9}$$

with the operators $\mathcal{O}_\nu$ and $\mathcal{O}_{q,g}$ being constructed from neutrino and quark/gluon fields, respectively. $S(x)$ represents a scalar mediator that couples neutrinos to quarks. Lagrangian $\mathcal{L}_I$ describes an effective interaction between neutrinos and quarks where the mediating DOF is much heavier than the energy scale under consideration, i.e. $q^2 \ll M^2$, which could be in its simplest form the four-fermion interaction of Eq. (2.8). A propagating scalar particle that mediates between neutrinos and quarks could, for instance, take the form of $\mathcal{L}_{II}$. Note that the individual mass dimension of operators and couplings depends on the underlying Lorentz structure of the corresponding quantities.

To calculate the individual scattering processes one uses the perturbative expansion of the scattering matrix. The contact interaction of $\mathcal{L}_I$ is already obtained at first order in perturbation theory while the tree-level scalar interaction of $\mathcal{L}_{II}$ is gained at second order. Then, the corresponding scattering amplitudes separate into matrix elements for the neutrino and nucleon current and are given by [154, Section E]

$$\mathcal{M}_I = \langle \nu' | \, \mathcal{O}_\nu \, | \nu \rangle \, c_q \, \langle N' | \, \mathcal{O}_{q,g} \, | N \rangle \,, \tag{2.10}$$

$$\mathcal{M}_{II} = - \langle \nu' | \, \mathcal{O}_\nu \, | \nu \rangle \, \frac{1}{q^2 - m_S^2} \, \langle N' | \, \mathcal{O}_q \, | N \rangle \,, \tag{2.11}$$

with N representing either protons or neutron $N \in \{p, n\}$ and a scalar mediator of mass m_S. While the evaluation of neutrino matrix elements is usually straightforward, the step from quarks to the nucleons is more involved and is explained in the following. The quark or gluon matrix elements appearing in both amplitudes are usually parameterized in terms of nucleon-spinor-bilinears

$$\langle N' | \, \mathcal{O}_{q,g} \, | N \rangle = \sum_\Gamma F_\Gamma^N(q^2) \bar{u}'_N \Gamma(q, K) u_N \,, \tag{2.12}$$

with the spinor matrices Γ being generally dependent on the two momenta $q = k' - k$ and $K = k + k'$, while one can express the (operator-specific) form factors $F_\Gamma^N(q^2)$ as functions of q^2 only. A summary of potential Lorentz bilinears (in the context of DM DD) can be found in Ref. [155]. Since we are only interested in color and electrically neutral, hermitian and flavor-diagonal Lorentz bilinears for $\mathcal{O}_{q,g}$ we restrict ourselves to combinations that contain the 16 matrices $\Gamma = I_4, i\gamma^5, \gamma^\mu, i\gamma^5\gamma^\mu, \sigma^{\mu\nu}$ for $\mu, \nu = 1, ..., 4$.

Now, we want to explicitly state two single-nucleon matrix elements, i.e. for scalar and the vector couplings. Since we are interested in the coherent regime where the momentum transfer is very small, we also elaborate on the meaning of form factors at $q^2 = 0$.

The operators that form a scalar quark bilinear are

$$\mathcal{O}_q = \bar{q}q \,, \qquad \mathcal{O}_g = \frac{\alpha_s}{12\pi} G^{a,\mu\nu} G^a_{\mu\nu} \,, \tag{2.13}$$

with $G^{a,\mu\nu}$ being the quantum chromodynamics (QCD) field strength tensors and α_s being the strong coupling constant. Following the convention of Eq. (2.12), the corresponding hadronic matrix elements imply form factors $F_S^{q/g,N}(q^2)$ which are real functions only depending on the momentum transfer q^2. Expressions of these matrix elements can be derived by evaluating the trace of the QCD energy-momentum tensor at zero momentum transfer,[3] which yields the nucleon mass [157, 158]

$$m_N \langle N'|\, \bar{N}N \,|N\rangle = \langle N'|\, \Theta^\mu_\mu \,|N\rangle \;, \quad \text{with} \quad \Theta^\mu_\mu = \sum_{q=u,d,s} m_q \bar{q}q - \frac{9\alpha_s}{8\pi} G^{a,\mu\nu} G^a_{\mu\nu} \,, \tag{2.14}$$

with $N \in \{p, n\}$ representing the proton and the neutron, respectively. In this expression heavier quarks $q_h = \{c, b, t\}$ are already integrated out since they only contribute through gluon lines, e.g. via triangle diagrams. With this, the desired expressions for the hadronic matrix elements can be linked with the (light) quark and gluon contribution to the nucleon mass[4]

$$f^{(N)}_{Tq} \equiv \frac{\langle N'|\, m_q \bar{q}q \,|N\rangle}{2m_N^2} = \frac{m_q}{m_N} F_S^{q,N}(0) \,, \quad f^{(N)}_{TG} \equiv 1 - \sum_{q=u,d,s} f^{(N)}_{Tq} = -\frac{27}{2} \frac{F^{g,N}(0)}{m_N} \,, \tag{2.15}$$

where $f^{(N)}_{Tq}$ and $f^{(N)}_{TG}$ represent the (light) quark and gluon contribution to the nucleon mass, respectively. The individual terms are either determined via lattice QCD calculations or pion-nucleus scattering [159]. A summary of values is presented in Table 4 of Ref. [156]. With this knowledge, a scalar-quark coupling $c_q \bar{q}q$ can be described through an effective scalar-nucleon coupling $S\bar{N}N$ with coefficient

$$c_N = \sum_{q=u,d,s} c_q \frac{m_N}{m_q} f^{(N)}_{Tq} + \frac{2}{27} f^{(N)}_{TG} \left(\sum_{q=c,b,t} c_q \frac{m_N}{m_q} - c_q \frac{m_N}{\Lambda} \right) \,, \tag{2.16}$$

where the last part reflects a scalar-gluon coupling that is induced by a quark loop and Λ is associated with the mass of the loop particle.

Now we draw our attention to nuclear matrix elements of vector operators like

$$\mathcal{O}_q = V^\mu_q \equiv \bar{q}\gamma^\mu q \,, \tag{2.17}$$

---

[3] The QCD energy-momentum tensor under application of the individual equations of motion (EOMs) is given by $\Theta^\mu_\mu = \sum_q m_q \bar{q}q + \frac{\beta(\alpha_s)}{4\alpha_s} G^{a\mu\nu} G_{\mu\nu a}$. Substituting the heavier quark contributions with $m_q \bar{q}q \to -\frac{\alpha_s}{12\alpha} G^{a\mu\nu} G_{\mu\nu a}$ for $q \in \{c, b, t\}$ at lowest order in α_s [156, Appendix B] and applying the beta function $\beta(\alpha_s) = -(11 - \frac{2}{3} N_f) \frac{\alpha_s^2}{2\pi} + \mathcal{O}(\alpha_s^3)$ for $N_f = 6$ [154, Section E.2] leads to the stated expression.

[4] In literature, definitions of $f^{(N)}_{Tq}$ with only a factor of m_N in the denominator can be found, e.g. in Ref. [156, Section E.2]. As pointed out there, this difference is due to a different normalization of the state vectors, i.e. exchange $|N\rangle \leftrightarrow \frac{1}{\sqrt{2m_N}} |N\rangle$ for a nucleon at rest.

which can generally be parameterized according to [160, Section 6.2]

$$\langle N'| V_q^\mu |N\rangle = \bar{u}'_N \left(F_1^{q,N}(q^2)\gamma^\mu + F_2^{q,N}(q^2)\frac{i\sigma^{\mu\nu}q_\nu}{2m_N} \right) u_N \,, \tag{2.18}$$

with V_q^μ being hermitian and the so-called Dirac and Pauli form factors $F_1^{q,N}(q^2)$ and $F_2^{q,N}(q^2)$, respectively. When the heavy quarks c, b, t are neglected, QCD exhibits an approximate $U(3)$ flavor symmetry in the limit of equal light quark masses, i.e. $m_u \sim m_d \sim m_s$, which is valid at 25%-level [152, Chapter 5.1]. Neglecting quantum electrodynamics (QED)[5] is valid under the approximation of nucleon structures to be insensitive to electric charge. Assuming this unbroken $U(3)$ flavor symmetry, the corresponding nine vector currents are conserved $\mathcal{V}_\mu^a = \bar{f}\gamma_\mu T^a f$, with $f \equiv (u,\ d,\ s)^T$ and T^a for $a = 1, ..., 9$ being the nine generators of $U(3) = U(1) \times SU(3)$. For all currents, corresponding matrix elements similar to Eq. (2.18) can be constructed, each with its on form factors $F_{1,2}^{a,N}$. Further, the diagonal operators $T^{0,3,8}$ induce relations among light quark currents. After some algebra, cf. Ref. [154, Chapter E.4], and under the assumption of isospin symmetry[6] one obtains the following form factor relations

$$F_i^{u,p}(q^2) = F_i^{d,n}(q^2) = 2F_i^p(q^2) + F_i^n(q^2) + F_i^{s,N}(q^2)\,, \tag{2.19}$$

$$F_i^{d,p}(q^2) = F_i^{u,n}(q^2) = F_i^p(q^2) + 2F_i^n(q^2) + F_i^{s,N}(q^2)\,, \tag{2.20}$$

$$F_i^{s,p}(q^2) = F^{s,n}(q^2) \equiv F_i^{s,N}(q^2)\,, \tag{2.21}$$

where F_i^N represents the form factor of the whole nucleon. As we are in the context of CEνNS mainly interested in the coherent regime, thus very small q^2, we can set $q^2 \to 0$. In such a case, the individual vector currents related to the form factors F_1 simply measure the nucleon's quark content, while the form factors F_2 yield the proton and neutron anomalous magnetic moments in units of the nuclear magneton $\hat{\mu}_N$, i.e.

$$F_1^{u,p}(0) = 2\,, \quad F_1^{d,p}(0) = 1\,, \quad F_1^{s,p}(0) = 0\,, \quad F_2^p(0) = \kappa_p\,, \quad F_2^n(0) = \kappa_n\,. \tag{2.22}$$

Further, the small momentum transfer in CEνNS implies $q^\mu/m_N \ll 1$ such that neglecting the terms including the form factors F_2 is a valid approximation.

Of course, there are pure pseudoscalar and axial vector operators as well, i.e. for $\mathcal{O}_q = \bar{q}i\gamma^5 q$ and $\mathcal{O}_q = \bar{q}\gamma^\mu\gamma^5 q$. However, since we focus only on spin-0 nuclei as targets within the main analysis of Ch. 3 and, further, only consider BSM extensions of scalar- and vector-type, we will not cover them here and, instead, refer to the literature, cf. Refs. [1, 154, 161].

2.1.1.3 From nucleons to the nucleus

The step from single-nucleon matrix elements to the full nuclear response is quite complex and involves many-body interactions, especially when the nucleon matrix elements of the considered operators involve a certain spin structure, cf. Ref. [154, Chapter G]. In the coherent regime, the (nuclear) charge operator is the leading contribution to the

---

[5] This could source additional symmetry breaking due to different up-type and down-type quark charges.

[6] Isospin symmetry implies $\langle p'| V_q^\mu |p\rangle = \langle n'| V_q^\mu |n\rangle$ for $q \in \{u, d, s\}$.

nuclear response since it is the only one that is fully coherent. Additional semi-coherent contributions related to spin-orbit corrections or axial-vector operators may exhibit some enhancements through interference with the charge operator, cf. Ref. [161]. However, at approximate zero momentum transfer such factors either vanish or stay finite and can be ignored when focusing on the fully coherent regime.

Further, in the context of CEνNS the (anti)neutrino is usually such low in energy that internal structure cannot be resolved. Similar to DD of DM (except the neutrino being relativistic), we assume that the matrix elements of nucleon-level operators with nuclear states are encoded in nuclear form factors, whose computation relies on the underlying nuclear physics, i.e. a model of bound nucleons inside a nucleus [162, Section 4].

In what follows we show a heuristic derivation of the leading contribution to CEνNS scattering amplitude, i.e. the vector part, by closely following Ref. [115]. The underlying assumptions are a spinless nucleus, such that parity is (at least statistically) conserved, a spherical and equal distribution of nucleons[7] and energies that guarantee a coherent interaction, i.e. $q^2 \to 0$, between the neutrino and the nucleus. In doing so, the corresponding cross section is derived at zero momentum transfer and multiplied with a form factor that takes into account deviations from scattering of a point-like nucleus [163].

Thus, by ignoring the axial-vector part of the NC interaction with the nucleus, cf. Eq. (2.6), the Z boson simply behaves as a massive photon that couples to the charge g_V^q for $q \in \{u, d\}$. From the previous section we know that vector currents in the limit of zero momentum transfer basically probe the content of valence quarks. Thus, for the nucleon matrix element of the NC interaction, cf. Eq. (2.18), at zero momentum transfer, we obtain

$$\langle N'| J^{\mu}_{\text{vNC}} |N\rangle = \begin{cases} 2g_V^u \langle p'| \bar{u}\gamma^{\mu} u |p\rangle + g_V^d \langle p'| \bar{d}\gamma^{\mu} d |p\rangle \ , & \text{for} \quad N = p\,, \\ g_V^u \langle n'| \bar{d}\gamma^{\mu} d |n\rangle + 2g_V^d \langle n'| \bar{d}\gamma^{\mu} d |n\rangle \ , & \text{for} \quad N = n\,. \end{cases} \tag{2.23}$$

The matrix element for the whole nucleus is then obtained via summation of the contributions of the individual nucleons with the addition of a form factor that takes into account the deviation from scattering off a point-like object. Since we assume the nucleus to be a spinless object, analogies can be drawn from scalar QED [115, 153], where the scalar-photon interaction vertex is momentum dependent [164, Chapter 9]. Taking all this into account one receives for the NC matrix element of the nucleus A the following expression

$$\begin{aligned} \langle A(k')| J^{\mu}_{\text{vNC}} |A(k)\rangle &= (k+k')^{\mu} F(q^2) \left[\sum_p \left(2g_V^u + g_V^d \right) + \sum_n \left(g_V^u + 2g_V^d \right) \right] \\ &\equiv (k+k')^{\mu} F(q^2) \left[Z g_V^p + N g_V^n \right] \ , \end{aligned} \tag{2.24}$$

with the nuclear form factor $F(q^2)$ depending on the momentum transfer $q^2 = (k' - k)^2$

---

[7] As Ref. [115] has pointed out, even for a spinless nucleus, the number of spin-up and spin-down quarks of a certain flavor might not be exactly the same as well as the distribution of protons and neutrons could be aspherical. However, for larger atomic numbers this is a valid approximation and, furthermore, the impact of unpaired quark spins and occurring spin-flips becomes negligible.

and the vector-like nucleon couplings

$$g_V^p = \frac{1}{2} - 2\sin^2\theta_W \,, \qquad\qquad g_V^n = -\frac{1}{2} \,. \tag{2.25}$$

One further defines the weak nuclear charge according to

$$Q_W = \frac{1}{2}\left[(1-4\sin^2\theta_W)Z - N\right] \,. \tag{2.26}$$

2.1.2 Scattering cross section and channel properties

Next, we can derive the actual CEνNS matrix element for the process given in Fig. 2.1. The general matrix element $i\mathcal{M}\left(\nu(p) + A(k) \rightarrow \nu(p') + A(k')\right)$ is obtained by simple application of tree-level Feynman rules, cf. Fig. 2.1,

$$\begin{aligned} i\mathcal{M} &= \langle \nu(p')|\, J^\mu_{\mathrm{vNC}}\, |\nu(p)\rangle \frac{-ig}{2\cos\theta_W} \frac{-i\left(g_{\mu\nu} - \frac{q_\mu q_\nu}{m_Z^2}\right)}{q^2 - m_Z^2} \frac{-ig}{2\cos\theta_W} \langle A(k')|\, J^\nu_{\mathrm{vNC}}\, |A(k)\rangle \\ &\simeq i\frac{g^2 g_{\mu\nu}}{4\cos^2\theta_W m_Z^2} \langle \nu(p')|\, J^\mu_{\mathrm{vNC}}\, |\nu(p)\rangle \langle A(k')|\, J^\nu_{\mathrm{vNC}}\, |A(k)\rangle \,, \end{aligned} \tag{2.27}$$

where we simplified the Z boson propagator under the assumption of $q^2 \ll M_Z^2$, as we did to obtain Eq. (2.8). Inserting the neutrino current in analogy to Eq. (2.6), the definition of the Fermi constant of Eq. (2.8) and the gauge boson masses given by Eq. (2.4) as well as the matrix element of the nucleus current in Eq. (2.24), one obtains the effective matrix element of CEνNS with antineutrinos

$$i\mathcal{M} = i\frac{G_F}{\sqrt{2}} Q_W F(q^2) g_L^\nu (k+k')_\mu \bar{v}^s(p)\gamma^\mu(1-\gamma^5)v^{s'}(p') \,, \tag{2.28}$$

with the momentum transfer of the scattering process given by the Mandelstam variable $q^2 = t = (k-k')^2$, the helicities of initial and final state neutrinos s, s' and their coupling to the vector component of the Z boson $g_L^\nu = \frac{1}{2}$.

For the neutrino, the full $V - A$ coupling structure of the Z boson is considered, while we neglected axial vector coupling to the nucleus A, cf. Sec. 2.1.1.3. Squaring and summing over the initial and final neutrino helicities yields the *squared matrix element*

$$|\mathcal{M}|^2 = \sum_{s,s'} |i\mathcal{M}|^2 = 32 G_F^2 Q_W^2 F^2(q^2) (g_L^\nu)^2 m_A^2 E_\nu^2 \left(1 - \frac{T_A}{E_\nu} - \frac{m_A T_A}{2E_\nu^2}\right) \,, \tag{2.29}$$

with the nucleus' weak charge Q_W, the nuclear form factor $F(q^2)$, the neutrino energy E_ν and the nuclear recoil energy in the lab frame T_A. The associated momentum transfer mediated by the process is given by $t = q^2 = -2m_A T_A$. The explicit derivation of the squared matrix element is given in App. A.2.2. Recall that the whole nucleus is assumed to be a spinless object throughout this calculation. Assuming it to be a spin-$\frac{1}{2}$ object, results in the replacement $(p_2 + k_2)^\mu \rightarrow \bar{u}^{r'}(k_2)\gamma^\mu u^r(p_2)$ with r, r' being the initial and final helicities of the nucleus spinors. However, the obtained final expression equals the result of the calculation with a spinless nucleus up to a small (kinematic) correction that is usually

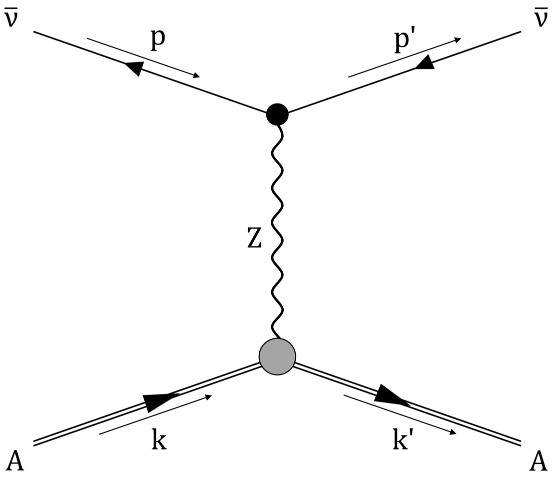

Figure 2.1.: Feynman diagram of the CEνNS process $\bar{\nu}(p) + A(k) \rightarrow \bar{\nu}(p') + A(k')$. Since CONUS will detect CEνNS with reactor antineutrinos, we derive the cross section under consideration of reactor antineutrinos. However, ignoring axial vector couplings yields a similar expression as for the case of neutrinos.

negligible.[8] This is in line with the general assumption that the nucleon spins (almost) cancel among each other. Furthermore, the nucleus is considered to be a point-like object whose internal (nucleon) status cannot be probed/resolved with coherently interacting (anti)neutrinos. In addition, exchanging antineutrinos with neutrinos yields the same squared matrix element because of the assumption of a parity-conserving nucleus. However, matrix elements for neutrinos and antineutrinos would be different if the axial-vector contribution in J^{μ}_{NC} would have been considered.

The nuclear recoil energy T_A in the lab frame depends on the scattering angle θ (between initial and final neutrino momenta) and is given by

$$T_A = \frac{2 m_A E_\nu^2 \cos^2\theta}{(m_A^2 + E_\nu)^2 - E_\nu^2 \cos^2\theta} \xrightarrow{\theta \to 0} \frac{2E_\nu^2}{m_A + 2E_\nu}\,, \tag{2.30}$$

where the last step yields the expression for a maximal nuclear recoil $T_A^{\max}$. For instance, CEνNS off a heavy nucleus with $m_A \sim 100\,\mathrm{GeV}$ at a reactor site, i.e. $E_\nu \lesssim 10\,\mathrm{MeV}$, leads to nuclear recoil energies below $\mathcal{O}(1)\,\mathrm{keV}$.

Adjusting the cross section for general $2 \rightarrow 2$ scattering for lab frame kinematics, cf. App. A.2.2, and inserting the squared matrix element of Eq. (2.29) yields the desired expression of the CEνNS cross section,

$$\frac{d\sigma}{dT_A}(T_A, E_\nu) = \frac{G_F^2}{4\pi} Q_W^2 m_A \left(1 - \frac{m_A T_A}{2E_\nu^2}\right) F^2(q^2)\,, \tag{2.31}$$

where we have already inserted the left-handed neutrino coupling $(g_L^\nu)^2 = \frac{1}{4}$ and ignored

---

[8] To obtain the corrections for a spin-$\frac{1}{2}$, simply replace $\left(1 - \frac{T_A}{E_\nu} - \frac{m_A T_A}{2E_\nu^2}\right)$ with $\left(1 - \frac{T_A}{E_\nu} - \frac{m_A T_A}{2E_\nu^2} + \frac{T_A^2}{2E_\nu^2}\right)$, cf. Ref. [115].

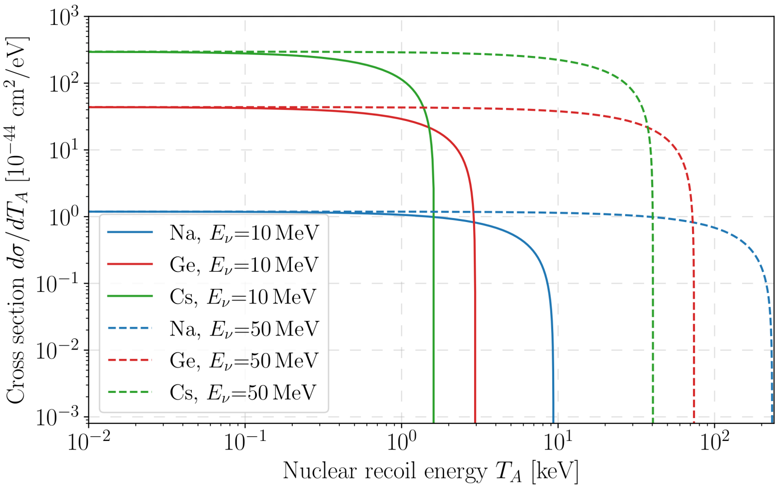

Figure 2.2.: CEνNS cross section for different neutrino energies and target materials. Its characteristic scaling with the squared neutron number leads to large cross sections for heavy elements. However, the maximum recoil energy is suppressed at the same time. This “push-pull” situation needs to be solved for CEνNS detection.

the (T_A/E_ν)-term in the bracket since it is would be negligible anyway. The corresponding momentum transfer is given by $q^2 = -2m_AT_A$. Note that the dependence on the proton number of the nuclear weak charge in Eq. (2.26) nearly cancels, such that the CEνNS cross section scales approximately with the squared neutron number.

An alternative expression of the differential cross section in terms of the lab frame scattering angle is given in Eq. (A.18). The total CEνNS cross section is given by integrating over the nuclear recoil energy T_A [67][9]

$$\sigma \approx \frac{G_F^2 N^2}{4\pi} E_\nu^2 \simeq 0.42 \cdot 10^{-44} N^2 \left(\frac{E_\nu}{1\,\mathrm{MeV}}\right) \mathrm{cm}^2 \,. \tag{2.32}$$

Although the axial vector contribution has been ignored in the previous derivation, Equation (2.31) is accurate enough for the analyses in this work. However, the full CEνNS cross section is given by [111, 165]

$$\frac{d\sigma}{dT_A} = \frac{G_F^2 m_A}{2\pi}\left[(G_V+G_A)^2 + (G_V-G_A)^2\left(1-\frac{T_A}{E_\nu}\right)^2 - \left(G_V^2-G_A^2\right)\frac{m_AT_A}{E_\nu^2}\right] , \tag{2.33}$$

with the vector and axial-vector $G_V = F_pZg_V^p + F_nNg_V^n$ and $G_A = F_p\Delta Zg_A^p + F_n\Delta Ng_A^n$, respectively. Further, with F_x being the form factor and $g_{V,A}^x$ the (axial) vector coupling to protons and neutrons, i.e. $q \in \{p, n\}$, and ΔZ and ΔN the number of unpaired proton and neutrons spins, i.e. the differences between nucleons with spin-up and spin-down configuration. Equation (2.31) is recovered by assuming the (T_A/E_ν)-term to be negligible

---

[9] Starting from Eq. (2.31), the nuclear recoil energy T_A is integrated from 0 to $T_A^{\max} \approx \frac{2E_\nu^2}{m_A}$. The approximation is valid as the (T_A/E_ν)-term in Eq. (2.29) is negligible.

as well as setting $g_V^p \to 0$ and ignoring the nucleus spin [165].

After the derivation of the CEνNS cross section, we want to emphasis the main features of this reaction channel [67]: First, a general characteristic is the coherent enhancement of the cross section, i.e. its scaling with the squared neutron number, which, in combination with the quadratic dependence on the neutrino energy E_ν, renders it to be larger than any other neutrino interaction channel, cf. Fig. 1.1. Second, in contrast to IBD there is no kinematic threshold which is of special interest for reactor antineutrino investigations since detection of antineutrinos below the IBD threshold of $E_{IBD}^{\text{min}} = 1.806\,\text{MeV}$ becomes in principle feasible [87]. A third advantage of this reaction channel is its flavor-blind nature, thus, it is equally sensitive to all neutrino flavors and of special advantage if the source neutrino composition is not known. However, all these benefits come with the drawback of having to detect very low nuclear recoil energies, i.e. impacts with recoil energies of $\mathcal{O}(\text{keV})$ and below.

2.1.3 Coherence condition and nuclear form factors

Now, we elaborate on the circumstances that need to be guaranteed for this characteristic enhancement to appear and discuss the role of the nuclear form factor in Eq. (2.31). In doing so, we follow considerations of Ref. [28], introduce form factors according to Ref. [166] and finally discuss their application in the context of CEνNS.

The coherent enhancement appearing in the CEνNS cross section is a beautiful example of coherence appearing in quantum mechanics (QM). Thus, it is based on the superposition principle, when the individual scattering amplitudes of neutrino-nucleon scattering are indistinguishable. Assuming the neutrino to scatter elastically off a composite object that consists of n individual constituents, i.e. nucleons at given positions x_i with $i = 1, .., n$, the scattering amplitude from an incident neutrino with momentum $\boldsymbol{p}$ to an outgoing neutrino with momentum $\boldsymbol{p'}$ is given by the sum of individual contributions[10]

$$\mathcal{A}(\boldsymbol{p'}, \boldsymbol{p}) = \sum_{i=1}^{n} A_i(\boldsymbol{p'}, \boldsymbol{p}) e^{i(\boldsymbol{p'} - \boldsymbol{p})\boldsymbol{x}_i} \,, \tag{2.34}$$

where the individual amplitudes A_i are weighted with a phase factor that incorporates the relative phases among the scatterings. The corresponding differential cross section scales with $|\mathcal{A}(\boldsymbol{p'}, \boldsymbol{p})|^2$. Further, the momentum transfer is given by $\boldsymbol{q} = \boldsymbol{p'} - \boldsymbol{p}$ and one defines the size of the composite object as $R = \max_{i,j} |\boldsymbol{x}_i - \boldsymbol{x}_j|$.

In the case of $qR \ll 1$, the individual phase factors are negligible and all amplitudes add up coherently $\frac{d\sigma}{d\Omega} \simeq N^2 |\tilde{\mathcal{A}}(\boldsymbol{p'}, \boldsymbol{p})|^2$ with the average amplitude $\tilde{\mathcal{A}}(\boldsymbol{p'}, \boldsymbol{p}) = \mathcal{A}/n$. If there are several constituents, i.e. protons and neutrons with different spin configurations, there might be cancellations among the individual scattering amplitudes. Otherwise, the cross section scales with the squared number of scattering centers. On the other hand, for $qR \sim 1$ the relative phase factor becomes important and contributions from the individual amplitudes might cancel each other and, thus, reduce the overall scattering

---

[10] Here, we neglect multiple scatterings. Further, assuming the constituents at defined locations x_j is not relevant as the argumentation can be generalized to a full QM treatment. A necessary condition is that the considered quantum states must not change, i.e. through spin-flip or charge exchange, otherwise amplitudes do not add up in a coherent manner.

Element	N	r_A [fm]	$E_\nu^{\max}$ [MeV]	$T_A^{\max}$ [keV]
Na	12	3.6	27.7	71.5
Si	14	3.8	25.9	51.3
Ar	22	4.4	23.1	28.5
Ge	38/40/42	5.2	18.9	10.5
I	74	6.3	15.7	4.16
Xe	75/77/78	6.4	15.5	3.93
Cs	78	6.4	15.4	3.85

Table 2.2.: Coherence condition for potential CEνNS detector materials with their neutron number N (three most abundant isotopes) and approximate nucleus radius $r_A \simeq 1.25 \cdot \sqrt[3]{N+Z}\,\text{fm}$. The maximally allowed neutrino energies $E_\nu^{\max} \sim (2r_A)^{-1}$ that is needed to fulfill a coherent interactions as well as the resulting maximal nuclear recoil energy $T_A^{\max}$ are estimated, cf. Eq. (2.30).

amplitude. The condition $qR \ll 1$ can be expressed more intuitively: If the wavelength of the mediating particle is larger than the target size, the individual amplitudes add up coherently. However, in Ref. [154, Section C] is was pointed out that the above condition for a mediator's wavelength is only meaningful if one-particle exchanges are considered. For intermediate particles in loops this condition is not required, but occurring loop factors lead to suppression of higher order contributions.

In the fully coherent regime, the target nucleus behaves like a point-like object. To account for the finite extent of some (nuclear) charge distribution, usually form factors are introduced which take into account the phase differences between the contributions of scattered wave packages. In the case of non-relativistic electromagnetic electron-proton scattering, one can show, for instance cf. Ref. [166, Chapter 7.3], that the matrix element $\mathcal{M}$ separates into the matrix element of point-like scattering times the form factor $F(\boldsymbol{q}^2)$,

$$\mathcal{M}_{fi} \to \mathcal{M}_{fi}^{\text{point}} F(\boldsymbol{q}^2)\,, \qquad \text{with } F(\boldsymbol{q}^2) = \int \rho(\boldsymbol{r}) e^{i\boldsymbol{q}\cdot\boldsymbol{r}} d^3\boldsymbol{r}\,. \tag{2.35}$$

$\mathcal{M}_{fi}^{\text{point}}$ represents the matrix element for scattering off a point-like charge Q and $F(\boldsymbol{q}^2)$ is the Fourier transform of a (normalized) charge distribution $\rho(\boldsymbol{r})$. In the coherent regime, i.e. for mediator wavelengths larger than the charge distribution, $\boldsymbol{q}\cdot\boldsymbol{r} \sim 0$, the form factors equals approximately unity and, thus, the charge distribution appears to be point-like. For a wavelength much smaller than the charge distribution, rapid oscillations in the phase factors occur such that the overall quantity tends to zero, i.e. $F(\boldsymbol{q}^2 \to \infty) = 0$. However, in the case of relativistic kinematics the interpretation of Form factors is more involved due to their dependence on the corresponding four-vector $Q^2 \equiv -q^2 = -(p'-p)^2$. In the limit of small momentum transfer $Q^2 \ll 4m_A^2$, which is fulfilled in the case of CEνNS, the time-like component becomes small such that $Q^2 \approx \boldsymbol{q}^2$ and the interpretation of the form factor as Fourier transform of the underlying weak charge distribution is restored, cf. Ref. [166, Section 7.5].

Neutrino source	Target	$T_A^{\max}$ [keV]	$E\,(\mathrm{QF} \in \{0.1, 0.15, 0.2\})$ [keV]
Nuclear reactor (10 MeV)	Na	9.33	0.93 / 1.40 / 1.87
	Si	7.64	0.76 / 1.15 / 1.53
	Ar	5.37	0.54 / 0.81 / 1.07
	Ge	2.96	0.30 / 0.44 / 0.59
	I	1.69	0.17 / 0.25 / 0.34
	Xe	1.64	0.16 / 0.25 / 0.33
	Cs	1.62	0.16 / 0.24 / 0.32
π-DAR source (50 MeV)	Na	232.4	23.2 / 34.9 / 46.5
	Si	190.4	19.0 / 28.6 / 38.1
	Ar	134.0	13.4 / 20.1 / 26.8
	Ge	73.8	7.38 / 11.1 / 14.8
	I	42.3	4.23 / 6.34 / 8.45
	Xe	40.9	4.09 / 6.13 / 8.17
	Cs	40.4	4.04 / 6.03 / 8.07

Table 2.3.: Detection requirements at different neutrino sources given for potential target materials. Values are given for two typical sources that are used in the context of CEνNS investigations, i.e. nuclear reactors and π-DAR sources, while assuming neutrino energies E_ν at the higher ends of the individual emission spectra. The maximal expected nuclear recoil energy $T_{\mathrm{A}}^{\max}$, cf. Eq. 2.30, and the corresponding detectable energy E assuming energy-independent quenching factors (QFs) $\mathrm{QF} \in \{0.1, 0.15, 0.20\}$ are calculated, whereby the value are chosen for illustrative purposes and do not necessarily represent quenching within the chosen materials.

2.1.4 Nuclear recoils, signal quenching and detectable energy

Finally, we take a more quantitative look onto the CEνNS cross section. For this, we select several target materials as examples and check their requirements for a potential detection at reactors and π-DAR sources, respectively.

When comparing the expression of the CEνNS cross section and the corresponding observable, the (maximal) recoil energy T_A, one recognizes a "push-pull" situation in terms of ideal target isotope selection. While the cross section of Eq. (2.31) scales approximately with the squared neutron number, the maximal nuclear recoil energy in Eq. (2.30) scales inversely proportional with the atomic number of the target material, i.e. $T \propto (Z+N)^{-1}$. Hence for a fixed neutrino energy E_ν, enhancing the cross section by selecting heavier nuclei (with higher neutron number), the observable is lowered at the same time. As a consequence, target materials with intermediate atomic numbers are a good compromise since they represent a certain trade-off between coherent enhancement and detection possibility.

In addition, to initially guarantee this enhancement, (anti)neutrinos within *the right energy range* have to fulfill the coherence condition $qR \ll 1$, with R being the maximal nucleon distance, cf. Ref. [28], which we assume to be the nuclear diameter, thus twice its radius $R \sim 2r_A$. Table 2.2 shows a selection of target materials that are already used or at least under consideration for CEνNS detection. Besides the approximate nuclear diameter d, the maximal neutrino energy $E_\nu^{\max}$ that allows for a coherent interaction as well as the corresponding maximal nuclear recoil energy $T_A^{\max}$ are shown, ordered according to the elements' neutron number. The neutrino energies indicate that at a reactor site CEνNS might be detected with full coherence for most of the accessible neutrino energies, cf. Sec. 2.2.1. From the maximal recoil energies $T_A^{\max}$, one can derive specifications a potential detector should satisfy in order to achieve a successful detection.

A nuclear recoil that is stored in the detector after a CEνNS event cannot directly be measured. Hence, secondary processes like ionization or scintillation need to be used. Unfortunately, this stored energy is not only converted into detectable signals but also lost in dissipative processes such that only a fraction of the initial energy is actually measured. The conversion from stored nuclear recoil energy T_A to detectable (heat or ionization) energy E is called signal quenching and the corresponding energy ratio E/T_A is referred to as quenching factor (QF) [167].[11] As a consequence signal quenching imposes even stronger requirements on the detector's energy threshold. In Tab. 2.3, we list the maximum nuclear recoil energy $T_A^{\max}$, cf. Eq. (2.30), expected from an experiment using a common target materials close to a nuclear reactor and a π-DAR source, respectively. To roughly illustrate the effect of quenching, we estimate the detectable energy after signal quenching for a selection of QFs that are currently discussed in the context of germanium detectors [168, 169].[12] The values indicate threshold requirements that detectors of the individual target material and at the corresponding source have to fulfill for a potential CEνNS detection. In the next section, the individual experimental requirements for a CEνNS-measuring device are discussed in detail. However, for the CONUS analyses of Ch. 3 and Ch. 4 the estimates for a germanium detector at a reactor site are relevant.

2.2 Requirements for successful CEνNS detection

A successful CEνNS detection has taken about forty years since its prediction, and not without any reason. As with any other endeavor in the history of neutrino physics, experimental efforts were pushed to their boundaries, but detecting keV-energy nuclear recoils has been an unsolved issue for a long time [66, 68]. In general, there are three main obstacles any CEνNS-measuring experiment has to overcome, namely

- an intense and controllable neutrino source,
- lowest possible background levels,
- a very low-threshold detection technology for nuclear recoils.

---

[11] In the literature, the difference between nuclear recoil energy and ionization energy (in terms of electron equivalents) is sometimes indicated by subscripts at the energy unit, eV_{nr} and eV_{ee}, respectively. Since we are mainly interested in the detectable energy, whenever not explicitly stated, the unit electron volt refers to ionization energy in the detector context.

[12] Note that signal quenching is complex and depends, among others, on the used target material, detection technology and on the nuclear recoil [170]. However, for the illustrative purposes at this point, we ignore all these subtleties.

These three ingredients are necessary to ensure the detection of small nuclear recoil energies with high interaction probability and clear signal significance. In what follows, we give a short overview of potential candidates that exist in each topic. Moreover, we show which kind of solutions already exist or are currently discussed in the CEνNS community.

2.2.1 The neutrino source

In Nature, there is a plethora of potential neutrino sources, ranging from cosmological over astronomical to artificial (human-made) sources, cf. Ref. [171]. But not every source, however appealing, is appropriate since it has to be in agreement with the overall experimental design. A neutrino source appropriate for the investigation of neutrino interactions has to guarantee an intense neutrino flux, whose spectral shape is to be known precisely [172]. Especially important in the context of CEνNS are neutrino energies high enough to allow a detection of low nuclear recoils, cf. Eq. (2.30). For practical purposes, a controllable and stoppable neutrino source is usually preferred as it is helpful in terms of background discrimination. Possibilities suitable for CEνNS investigations are neutrinos originating from pion decays at a SNS [173] or from nuclear reactors [174]. More recently, new approaches making use of artificial sources have been discussed [175]. In what follows we shortly introduce individual characteristics of the two recently applied neutrino source: π-DAR sources and nuclear reactors.

2.2.1.1 Pion decay-at-rest neutrino sources

The SNS at the Oak Ridge National Laboratory provides an integrated neutrino flux of $4.3 \cdot 10^7\,\mathrm{cm}^{-2}\,\mathrm{s}^{-1}$ at 20 m-distance and is currently the strongest π-DAR neutrino source. This renders it a perfect facility for various SM and BSM CEνNS investigations [173, 176]. Since the emitted neutrinos reach energies up to 53 MeV, the nuclear recoils result in high detectable energies, which are in the reach of today's low-threshold detectors, cf. Tab. 2.3. The SNS's neutrino spectrum consists of three different neutrino flavors ν_μ, ν_e, $\bar{\nu}_\mu$ reflecting the different emission processes: a pion-decay-at-rest and a subsequent decay of the emitted muon. The facility's neutrons are created by the interaction of an intense proton beam with a dense mercury target. As byproducts of this collision, mesons such as pions, are produced and stopped in the high-density target while neutrinos are emitted in subsequent decays, i.e. pion and muon decays. The overall neutrino spectrum is well-known since major particle emission takes place in decay-at-rest processes where the kinematics are known and the flavor content is entirely determined from π^+ decays. Within the mercury target almost all π mesons are stopped. While the π^- fraction is captured in mercury, the remaining π^+ mesons decay at rest according to $\pi^+ \to \mu^+ + \nu_\mu$ and leaving the emitted muon neutrinos with a monochromatic energy of 30 MeV. Within a few μs (with $T_{1/2} = 2.2\,\mu\mathrm{s}$), electron neutrinos ν_e and muon antineutrinos $\bar{\nu}_\mu$ are emitted with energies up to 52.6 MeV. The muon's three-body-decay results in a continuous spectrum of the latter two neutrino species. Further, the proton beam energy guarantees only a small contamination from decay-in-flight pions. The left plot in Fig. 2.3 shows a π-DAR neutrino simulation of mono-energetic 1 GeV-proton incident on mercury target. The (prompt) monoenergetic 30 MeV peak of muon neutrinos from pion decays is the dominant contribution to the whole emission spectrum. The continuous energies of electron neutrinos

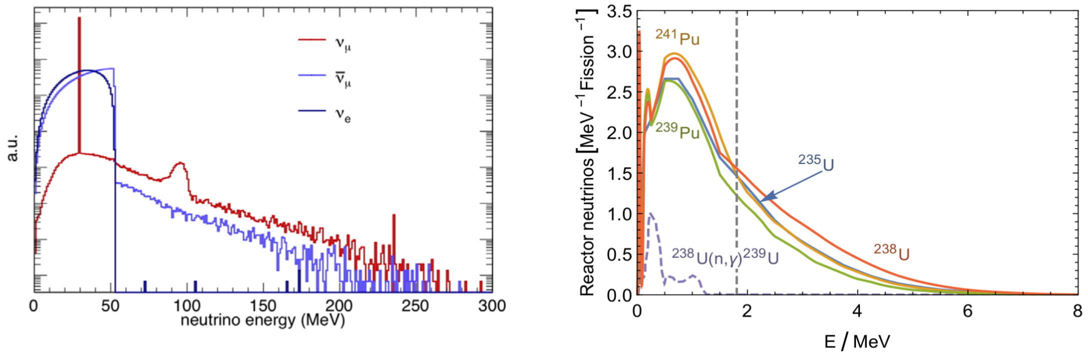

Figure 2.3.: **Left:** Simulated neutrino spectrum of the SNS at Oak Ridge National Laboratory. The peak in muon-neutrinos comes from (prompt) π^+ decays at rest, while the continuous spectrum of muon antineutrinos and electron neutrinos are created by the delayed three-body muon decay within a few μs later. Figure is taken from Ref. [181]. **Right:** Reactor antineutrino spectrum of the four main fission isotopes responsible for antineutrino emission. The threshold of IBD is indicated by a vertical dashed line. The low energy contribution due to neutron capture $^{238}\mathrm{U}(n,\gamma)^{239}\mathrm{U}$ is rescaled by a factor of 1/20. Figure is taken from Ref. [171].

and muon antineutrinos reflect the underlying kinematics of muon decays and reach up to about 50 MeV. Other contribution, e.g. from pion-decays-in-flight are negligible.

The beam pulse structure with collision frequency of 60 Hz is beneficial for background discrimination, such that rejection factors of 10^{-3}-10^{-4} are achievable [177]. In principle, beam-related high-energy neutrons can mimic a CEνNS signal, so-called neutron-induced neutrinos, and spoil potential measurement, but appropriate shielding and an off-axis location of the experimental set-up helped to mitigate this issue.

Besides the SNS in Oak Ridge, there are additional beam facilities for potential future CEνNS investigation. For example, the Booster Neutrino Beam (BNB) at Fermilab, which might be operated at slightly smaller neutrino fluxes, is already in consideration [178]. Further, the J-PARC Material and Life Science Experimental Facility (MLF) spallation neutron source in Japan uses a proton beam with higher energies which increases the concentration of neutrinos from non-decay-at-rest processes and thus, exhibits a more complex neutrino emission spectrum [179]. The physics potential of the European Spallation Neutron Source (ESS) in its capabilities of CEνNS investigations has already been studied in Ref. [180].[13]

2.2.1.2 Nuclear reactors

Nuclear fission reactors provide an intense and controllable flux of low-energy antineutrinos which emit $\sim 4\%$ of their produced energy in form of MeV-scale neutrinos that have been created in decays of nuclear fission products. Reactors have been involved in the first

---

[13] A summary of potential π-DAR neutrino facilities with their individual specification is given in Tab. 1 of Ref. [173].

experimental neutrino detection by Cowan and Reines [7, 8] and, since then, antineutrinos from nuclear fission have been widely applied in investigations of neutrino interactions and properties [174, 182, 183]. In PWRs, which are mainly used for commercial purposes, 99.9% of the energy produced in nuclear reactor cores originates from fissions of only four isotopes: ^{235}U, ^{239}Pu, ^{238}U, ^{241}Pu. Their fraction among all occurring fissions, from now on referred to as "fission fractions", varies with time but is on average given of about 55%, 32%, 7%, 6% [171]. Electron antineutrinos are emitted in beta decays of neutron-rich nuclei that appear in the individual fission chains. Hence, a reactor's antineutrino emission varies with the composition of the underlying fission fragments of the four main isotopes.[14] During a PWR cycle, ^{235}U is depleted and plutonium is bred, while the fraction of ^{238}U fission remains approximately constant at about 10%. As the resulting antineutrino spectra of the four main isotopes are different in shape and magnitude, the total reactor emission spectrum changes over a reactor burn-up cycle, i.e. the per-fission contribution of ^{235}U is about 45% higher than the one of ^{241}Pu and about 60% lower than contributions of ^{238}U. Thus, over a reactor cycle of about 550 d the overall effect in the expected IBD count rate can be of about 10%, cf. Ref. [185].

All in all, an average six neutrinos are emitted per fission with a total energy of about 200 MeV [186]. Below the IBD threshold, neutron captures of ^{238}U lead to a subsequent decay of the created ^{239}U, usually written as $^{238}\mathrm{U}(n,\gamma)^{239}\mathrm{U}$, which in turn contributes additional 1.2 antineutrinos, cf. Ref. [186, 187]. This leads to a powerful antineutrino emission of about $2 \cdot 10^{20}\,\mathrm{GW}^{-1}\,\mathrm{s}^{-1}$, which makes nuclear reactors the most powerful human-made neutrino source on Earth. Although their (electric and thermal) power is frequently monitored and compared with detailed simulation, a prediction of the expected reactor spectrum is more involved. The right plot in Fig. 2.3 illustrates the typical shape of antineutrino emission spectra in terms of the four main isotopes. About 75% of the antineutrino emission occurs at energies below 1.8 MeV and is thus inaccessible to IBD. Moreover, this part is more reactor-specific as it subject to neutron capture of long-lived fission fractions, whose abundances depend on the neutron flux in the reactor core as well as the expose to it. Consequently, only 25% of a reactor's total antineutrino emission occurs at energies above the IBD threshold, cf. the right plot of Fig. 2.3.

The so-called ab-initio approach (or summation method) tries to determine the individual antineutrino fission spectra by summing contributions from all beta decay branches of all fission fragments [118, 187, 188]. In such way, recent methods sum up hundred of branches [187] to determine the final aggregation of antineutrinos that are emitted from the isotope or the reactor in general. Although straightforward, several obstacles in the procedure lead to large uncertainties in flux and spectrum. Fission yields, branching ratios and endpoint energies of the decays are sometimes, especially in the case of short-lived fragments, not well know and, thus, need to be estimated. Further, the beta spectrum of about 30% of the involved transitions are attributed to so-called first forbidden transitions, whose calculations are more difficult and noticeable different from allowed transition.

---

[14] The subsequent beta decays responsible for the actual antineutrino emission do not proceed instantaneously as the corresponding states exhibit finite lifetimes. At the beginning of a fission cycle a certain time is needed for the isotopes to reach steady equilibrium, i.e. higher energies require shorter time intervals. Thus, the same applies to the resulting antineutrino spectrum. Here, we neglect effects of reactor burn-up and cool-down and directly assume equilibrated decay states. Effect of non-equilibrium reactor fluxes are for instance discussed in Ref. [184].

Additional smaller corrections arise for example from radiative and nuclear finite size contributions who might also depend in the transition, cf. Ref. [185]. In the end, these systematic uncertainties and correction add to overall model uncertainties of $10 - 20\%$.

A complementary approach, the so-called conversion method, is to use experimentally determined beta decay spectra of the isotopes of interest. Besides small corrections, which take into account that spectra have not reached full equilibrium, such electron emission spectra already reflect the aggregation of all fission yields and branching ratios. In the general procedure, the determined electron spectrum is fitted with a set of up to 30 virtual branches with an assumed spectral shape. Ignoring nuclear recoil energies, the electron spectrum can in principle be converted into the corresponding electron antineutrino spectrum due to energy conservation. Experimental determinations of the individual isotope spectra have been done in the past, i.e. Refs. [189–191] for thermal neutron fissions and Ref. [192] for fast fission and provided corresponding antineutrino spectra.

Finally, there are direct measurements of antineutrino spectra at reactor-site that have been recorded via IBD interactions [149, 193]. The collaborations of Daya Bay [194, 195] and RENO [196] applied unfolding techniques to deliver data-based reactor spectra that are free from experiment-specific features, e.g. efficiencies and resolutions. In this context, CEνNS might be an interesting option as it allows, in principle, measurements of a reactor's spectrum below the IBD threshold [87], cf. Sec. 5.2.

However, two anomalies appear when these directly measured IBD spectra are compared to theoretical predictions, i.e. the RAA and the so-called "reactor bump" [197]. The first is related to an observed neutrino flux deficit of 6.5%, which could be related to uncertainties underlying the theoretical predictions or the existence of a fourth sterile neutrino, cf. Sec. 5.2 and Sec. 5.4.3. The later refers to a shape distortion (compared to theoretical predictions) above 4 MeV [198, 199], which might be explained by contributions of certain fission isotopes, cf. Sec. 5.2.

All in all, nuclear fission reactors are a favorable choice in the quest of measuring CEνNS as they exhibit huge antineutrino fluxes. The emitted antineutrino energy is below 10 MeV and, thus, safely in the coherent regime of CEνNS for currently discussed detector materials, cf. Tab. 2.2. Nuclear reactors are generally well-monitored and duty cycles of about one year allow regular acquisition of pure reactor OFF time. However, these outages, in which the reactor is maintained and the core loaded with new fuel elements, are with a duration of about one month per year short in comparison to normal operation.

2.2.2 Background in low energy threshold CEνNS experiments

We now address the second issue a reactor or π-DAR-based CEνNS experiment has to overcome: low-level background at shallow depths. To understand how this is achieved with the CONUS set-up, a general introduction into backgrounds of low-energy rare-event experiments is given in the following. This section is mainly based on the review of Refs. [200, 201]. For more details and quantitative expressions, the author refers the inclined reader to Ref. [202].

2.2.2.1 Overview of different background components

Low background levels are in general necessary for any rare-event search. With increasing sensitivity of modern experiments, the experimental requirements on background events are pushed further. Since the expected number of physics events is only of a few counts per day or year, the experimental reach is often limited by background events. Thus, discrimination of potential signal from background events and electronic noise becomes crucial.

The very broad term “background” summarizes events that cover a wide range of energies (keV up to GeV), involve different particle types (α, β, γ, neutrons, etc.) and originate from various interactions (electron/nuclear recoils, hadronic interactions, neutron production). To distinguish physics signals from unwanted background, several methods can be applied depending on the actual experimental design. For example, these can be reduction of external and internal radiation (shielding, materials selection and surface cleaning), event-by-event selection (active tagging) or utilizing characteristic signal features (pulse-shape discrimination (PSD)). Usually, the expected signal rates are limited by experimental parameters and economic reasoning such that compromises between a clear event signature, experimental design, data collection and financial budget have to be found. Simulation techniques have become popular practice to estimate an experiment’s expected background level in order to check requirements on background rejection, components’ internal radiopurity and cosmic radiation, cf. Refs. [202, 203].

In general, the background of low-event experiments can be grouped into the following categories on which we discuss further below: environmental radioactivity, intrinsic material contamination of detector components, airborne activity (radon and it progenies), cosmic rays as well as neutrons from natural fission and (α,n) reactions.

Environmental radioactivity Radionuclides present in nature can be generally grouped into three categories: primordial, cosmogenic and anthropogenic origin. During their (and subsequent daughter) decay, gamma radiation is emitted, which generally needs consideration in rare-event searches. The naturally occurring (long-lived) radioisotopes ^{238}U, ^{232}Th ad ^{40}K are the dominant contributors with largely varying local concentration. Direct cosmic ray gamma radiation at ground level only contributes a small portion, i.e. $\leq 1\%$.

At surface or near-surface environments, the activity of daughter nuclides can deviate from the activity of their parent nuclides due to physical and chemical processes.

The most important cosmic ray-produced radionuclides in the atmosphere are ^{7}Be, ^{10}Be, ^{14}C. Although cosmogenic radionuclides only reach permille-level activity of primordial radionuclides in the upper soil layers, these isotopes require attention when the applied detector technology contains them, e.g. in the case of scintillators (C, H, Be, Cl) and (liquid) gas detectors (via the cosmogenically produced isotopes ^{37,39,42}Ar).

Anthropogenic radioactivity originates above ground from nuclear tests and operation of nuclear power plants that have added the radionuclides ^{3}H, ^{14}C, ^{90}Sr and ^{137}Cs to the atmosphere. Especially, the nuclear accidents of Chernobyl and Fukushima have resulted in large surface contamination with ^{137}Cs [204]. Further, ^{85}Kr that is released in the atmosphere by nuclear reactors and nuclear fuel re-processing facilities might be problematic as it is highly solvable in organic materials.

Radioimpurities in detectors and shield material Radioimpurities due to environmental radioactivity can be found in manufactured products as well, and therefore also in detector components and shield materials or attached to their surfaces. As a consequence, components for rare-event purposes have to be specially treated previous to and during their processing and manufacturing stages. Thus, dedicated material selection, monitoring for acceptable contamination levels and minimizing contact with other materials and the environment are crucial to guarantee low background rates in the final experiment. A general guideline is, for example, that electron detecting experiments, e.g. for $0\nu\beta\beta$ and IBD, are more limited by intrinsic radioactivity, while nuclear recoil detection, e.g. in CEνNS and DM experiments, is more likely to be limited by neutrons originating from radioactive decay-induced nuclear reactions [200, Section 36.6.3]. Refined materials seem to be more radiopure than their natural form, although this depends highly on the individual manufacturing steps. Further, semiconducting materials like Si and Ge profited from industrial developments and are among the cleanest materials available. Plastic material or liquid hydrocarbons are more demanding since most of them consist of C, H and O and thus incorporate ^{3}H and ^{14}C. If refined, e.g. by distillation methods, they can become very radiopure.

Special care must be given to electronic components, e.g. resistors, capacitors, etc., since their components often carry high radioimpurities.

For shielding purposes, lead turns out to be an almost ideal shielding material due to its high atomic number, acceptable costs and material properties. Its low interaction probability with neutrons and cosmic rays, also in terms of radionuclide production, renders it perfect for rare-event searches. However, its intrinsic radioactivity might not be negligible mainly because of ^{210}Pb and its daughter nuclides ^{210}Bi and ^{210}Po. Due to the 22-year-long half life of ^{210}Pb, low-uranium ores or lead that has been produced several half lives ago are preferred.

During an experiment's commissioning surface contamination can occur through dust or contact with other materials. Thus, components are stored in sealed bags and the whole assembly might be done in an enclosed environment, i.e. under clean-room conditions; also to reduce radon deposition. The most demanding low-rate experiments require material screening of all components, detailed understanding of the radioactivity at experimental site, usually gained with sophisticated simulations and the whole repertoire of radiation detection instruments to achieve their desired background specifications.

Radon and it progenies Airborne radioactivity is an issue during an experiment's commissioning but also during its operation. Especially, the noble gas and α-emitter ^{222}Rn, which originates from ^{238}U, is released from surface soil and found everywhere in the atmosphere. Its typical values of $10 - 100\,\mathrm{mBq\,L^{-1}}$ outdoors or $100 -$ few $1000\,\mathrm{mBq\,L^{-1}}$ [200, Section 36.6.4] and its half life of 3.8 d renders it the strongest source of airborne radioactivity. The radionuclide ^{220}Rn, originating from the thorium series, has a much shorter half-life of 55.6 s and decays within its host material leaving its daughter materials immobile. Further, there is ^{219}Rn of the actinium series with a half-life of 3.96 s, which is negligible in most low background considerations.

Generally, the airborne radon concentration depends on the barometric pressure and shows daily as well as seasonal variation. It is highly solvent in water and organic solvents and, as a consequence, lowest concentrated above oceans.

Direct radon progenies are either free or attached to aerosols. Further, radon deposition is strongly enhanced on electrostatically charged surfaces, i.e. on glas or plastic. An established practice to protect a device against radon is to encase the whole system with metallic radon-tight foil and apply a small overpressure of old compressed air or (purified) nitrogen. This should expel incorporated radon and prevents further influx from cracks or small openings.

For electron detection, radon itself is not harmful but its progenies ^{214}Pb, ^{214}Bi, ^{210}Bi emit energetic beta and gamma radiation. On the contrary, recoils of α particles from radon decays might become problematic in the case of nuclear recoil detection.

Cosmic ray-induced background Cosmic ray particles cannot only create radionuclides by activation of experimental materials but also directly contribute background events. The Earth's atmosphere is permanently hit by primary cosmic ray particle (90% protons, 9% α and 1% heavier particles), whose interactions generate secondary particles ($\pi^{\pm}$, p^{+}, $e^{\pm}$, n, $\mu^{\pm}$) which penetrate the atmosphere further. At sea level, the relative intensity of $\pi^{\pm}$: p^{+}: $e^{\pm}$: n : $\mu^{\pm}$ is $1 : 13 : 340 : 480 : 1420$ with $1.34 \cdot 10^{-5}\,\mathrm{cm}^{-2}\,\mathrm{s}^{-1}$ for charged pions [200, Section 36.6.5]. Charged pions and protons contribute to cosmogenic production only in the first few 10 $\mathrm{g/cm}^2$ of material below rock surface, while electrons and protons are generally absorbed by overburden of the experimental building. Thus, only muons and neutrons are harmful for low-event background searches. In general, cosmic neutrons loose their energy via inelastic scattering before they are typically captured or decay. Neutron production in high-Z materials is strongly enhanced, i.e. via capture of negative muons, photonuclear reactions and photofission of photons associated with fast neutrons. This makes tertiary neutrons the dominant background contribution in massive Pb shield already below a few meters of water equivalent (m w.e.). Fission and (α, n)-derived neutrons become important only below a few 100 m w.e. [201, Section 3].

Muons, in contrary, are attenuated on longer scales ($2\,\mathrm{kg\,cm}^{-2}$) by several kinds of interactions, i.e. ionization, pair production, bremsstrahlung and nuclear interaction [201, Section 3]. Besides direct production of background events, cosmic rays might contribute indirectly higher radiation levels through cosmogenic production of radionuclides in detector components. Especially, hadronic components can induce radioactivity levels that exceeds contamination of primordial components at sea level and becomes important for intermediate-Z materials like copper and iron, where short-lived radionuclides, e.g. ^{56,58,60}Co, might spoil desired background levels. Muons also contribute to radioisotope production as they produce energetic showers of proton, neutrons and pions, which can extend over several cubic meters (mostly in forward direction). Neutrons on the other side can activate components through nuclear desintigration, capture of negative muons, (α, n) reactions and natural fission. To avoid high cosmogenic activation, detector components and material should be stored above ground only for manufacturing and transport.

Next to it, the production of cosmic neutrons can directly induce background events via inelastic scattering or radiative capture in shielding or detector material which renders them an important source of low-energy background. They are even more problematic as sufficiently energetic neutron might fake weakly interacting massive particle (WIMP) or neutrino recoils in elastic scattering. At an overburden of 15 m w.e., secondary neutrons are already filtered out and tertiary neutrons created by muons become the dominate background component. Especially, high-Z shielding used to suppress external gamma radiation can be a source for cosmogenic tertiary neutrons. Depending on the experiment and its overburden, additional neutron absorbers, e.g. borated polyethylene, might be an option to effectively reduce tertiary neutrons.

Direct interactions of muons are almost exclusively of electromagnetic origin with the transversed medium. Their deceleration happens in small fractions of their primary energy and creates energetic showers of electrons, positions and gamma rays, direct electron pair production and *bremsstrahlung*. The small energy loss in combination with a relativistically enlarged decay time allows large penetration depth into the Earth's crust. At rest, muons either decay under emission of another shower or if negatively charged, they are captured by a nucleus which results in emission of further neutrons or photonuclear disintegration of the entire nucleus.

2.2.2.2 Background suppression techniques

After the discussion of individual background sources, we summarize which techniques are available to suppress or avoid events induced by cosmic rays or from radioactive decays. All of them are applied within the context of the CONUS experiment.

Shielding The ideal shield against external gamma radiation at sea-level is made out of low-activity lead. Since lead with low ^{210}Pb contamination is rare, an onion-like structure with increasing radiopurity towards the detector chamber is a valid possibility, whereas the radiopurity level of the inner layers is determined by the muon flux, whether or not a veto system is used and the overall background specifications. The individual lead layer must not be too thick, otherwise muon-induced components and secondary neutrons begin dominating the background spectrum which cannot be further suppressed with additional lead layers. At very low muon flux, either by more effective veto counters or larger amount of overburden, electrolytically produced copper proved to be superior as inner shield since its higher radiopurity balances the lower self-absorption for *bremsstrahlung* induced by secondary charged particles. Measures against radon aggregation should be established to avoid rising background levels due to radon diffusion. In solid-state detector-shield configurations, boil-off nitrogen is typically used to mitigate airborne radon.

Radioassay techniques and material treatment Material screening and selection as well as proper storage is a key ingredient for low-background experiments. Spectroscopy with germanium detectors has proven beneficial for screening purposes as they are sensitive to all types of radiation and exhibit high radiopurity [205]. With them the detection of typical environmental radioimpurities is possible at the sub-mBq kg^{-1}-level. Low-energy contamination, e.g. from ^{3}H and ^{14}C can be measured with liquid scintillators as well. Additional methods are α counting, neutron activation analysis, and mass spectrometry. Especially, α counters are useful devices for measuring radon levels at storage locations or during the experiment's runtime. Not only selection of radiopure materials is important, also processing and manufacturing can increase surface contamination. Thus, surface cleaning might be necessary afterwards.

Active background discrimination techniques Further background reduction can be achieved by application of active discrimination techniques. Such methods can be

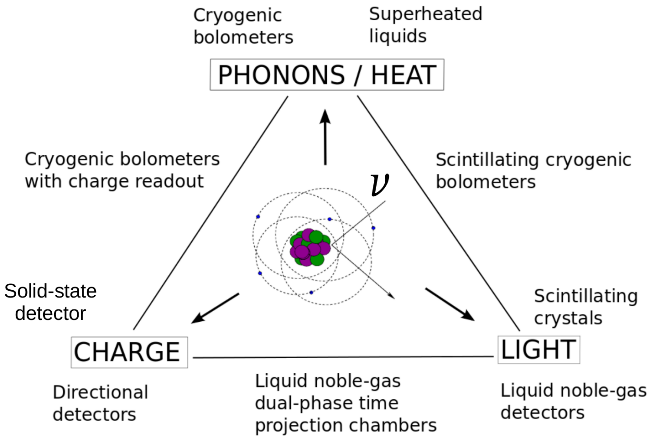

Figure 2.4.: Overview of detection signals and techniques that can be used for CEνNS and DM DD experiments. Since DM-nucleus scattering and CEνNS are similar in nature and share (very roughly) same energy ranges, similar detection technologies can be applied. Picture taken from Ref. [207] and adapted for our aim of measuring CEνNS.

anticoincidence veto systems (muon-induced events), detector-detector coincidence (decays, scatter sequences), signal pattern identification (PSD) or multiple detection mechanism. A general rule for the selection of active components is that as long as radiopurity is an issue for active shielding techniques, passive shielding is a preferred choice because of fewer construction constraints, easier screening possibilities and long time stability [201, Section 4.3]. Since experiments looking for CEνNS are most likely to be performed at shallow depth, cosmic ray muons and corresponding neutrons will be an issue. As the distribution angle of muons grows steeper with growing overburden (at sea level $\sin\varphi$ with φ being the azimuthal angel), an active muon veto system encapsulating the whole detector is a necessary choice. Plastic and liquid scintillators have proven to be more effective at sea level and shallow depth than gas counters, while they further reduce background events from secondary neutrons.

2.2.3 Detection techniques

In the last section of this experimental introduction, we address technologies that can be used to detect CEνNS. They can be grouped according to the signal type that a potential interaction might leave in the detector, e.g. heat/phonons, charge and light or combinations of the latter, cf. Fig. 2.4. Since (WIMP) DM-nucleus interactions and CEνNS are similar in nature and share approximately the same recoil energies, both investigations have to fulfill similar experimental requirements and thus we can take advantage of this complementarity. We mainly focus on technologies that are already applied in experiments or planned in upcoming CEνNS investigations, while we select representatives for each of the available signal types. This section is based on Refs. [200, 206, 207].

2.2.3.1 Scintillation detectors

Scintillation detectors exhibit a simple working principle and experience common application in particle physics. While particles cross the scintillating medium, they transfer energy to the material's atoms or molecules and excite them to short-lived states. After a certain period of time, these states return to their ground states under emission of photons, which are detected by photodetectors. Although the efficiency of light emission after excitation of typical scintillation material range from $10-15\%$, appropriate photodetectors with high photon counting and collection efficiency, e.g. photomultiplier tubes (PMTs), allow for efficient particle detection [208]. Scintillators can be separated into two main groups: organic and inorganic media. Organic scintillators have the advantage that they are widely used in several forms, i.e. as plastic, liquid or crystalline, and can be customized to any geometry and application. Inorganic scintillators are mainly applied in crystalline structures with the advantage of having higher densities and higher atomic numbers than their organic counterpart. This is advantageous when high stopping power of the incident particle or radiation is needed. Higher light yields are obtained with inorganic scintillators as well.

In DM investigations with scintillation detectors, usually NaI(Tl) and CsI(Tl) crystals are used due to the advantages of inorganic components. In such crystals, inhomogeneities, such as thallium, are added on purpose to modify the scintillator's properties. In the case of NaI(Tl) and CsI(Tl), thallium increases the total light yield and shifts the wavelength of the pure crystal. Further, the energy resolution can be improved and lower thresholds are achieved.

Since scintillation light is emitted almost isotropic, no particle discrimination or position reconstruction is possible. Besides multiple-hit rejection, active background suppression techniques are valid choices to reduce background events. An example for the application of pure scintillation detectors in DM searches is the DAMA/LIBRE experiment where a NaI(Tl) crystal has been used [209]. Further, the first CEνNS detection was achieved with a CsI(Na) crystal with a mass of 14 kg [68]. Instead of thallium, sodium has been used to reduce the scintillator's de-excitation times and allow an operation at shallow depth.[15] Another, proposal exists that pursues CEνNS detection with NaI(Tl), i.e. NEON [74].

2.2.3.2 Semiconductor detectors

Semiconductor detectors use the characteristic band structure of semiconducting materials for particle or radiation detection. Among the various possibilities, crystalline silicon and germanium are among the most commonly applied detectors while the overall detection principle remains the same.

When ionizing radiation or energetic particles pass through the detector medium, they create electron-hole pairs that are collected via an electric field and further processed by appropriate electronics. The advantage of semiconductors is that the energy needed for the creation of an electron-hole pair is quite small, i.e. 2.96 eV (at 77 K) for germanium and 3.81 eV (at 77 K) for silicon [211]. The remaining energy released into the detector medium is available for ionization events which is beneficial for the detector's resolution.

---

[15] Otherwise, frequent cosmic ray interactions would contribute a continuum of light emissions and spoil the desired detector specifications, cf. Ref. [210].

Thus, semiconducting crystals exhibit excellent energy resolution, e.g. 2.4% at 5.9 keV, 0.41% at 122 keV [212, Table 3.2], 0.15% at 1.3 MeV [211, Section 10.7.3], which also qualifies them best for material screening purposes [205]. Moreover, they are capable of reaching sub-keV detection thresholds and generally show a high degree of purity, i.e. $< 10^{10}$ atoms cm^{-3} [211]. A high density (5.2 and 2.3 g cm^{-3} for germanium and silicon, respectively) which results in a large stopping power as well as compact size and fast response time are further characteristics of this detector type.

However, semiconductors usually require cooling during operation to suppress thermal noise. This is commonly done with liquid nitrogen at 77 K. The ionization signal generally allows no direct discrimination between signal and background although PSD enables the rejection of specific background events [213–216]. The circumstance that the noise level scales with crystal size due to the diode's increasing capacitance is not beneficial for low-energy investigations since it implies that the limiting factor could be the detector itself.

In a pure semiconductor the number of holes equals on average the number of electrons. Modification of charge carriers is achieved by introduction of impurities, the so-called doping, in the crystal structure which perturbs the semiconductor's band structure and generally exists in two variants: In n-type doped semiconductors elements like arsenic, phosphorous or antimony are used to create an excess in electrons in the material. P-type doped semiconductors incorporate elements like boron, gallium and indium that absorb electrons and create an excess of holes within the crystal. Both detector types differ, among other, in the position of anode and cathode and the location and thickness of their dead layer, a layer of decreased detection efficiency. P-type semiconductors have their dead layer around the crystal's top and lateral surface which is beneficial in shielding against external α and β particles.

HPGe detectors have been widely applied in particle physics for radiation detection and, further, solved as target material for DM and various neutrino experiments. For instance, the experiments CoGeNT [214] and CDEX [217] used them in their DM searches. Many neutrino experiments applied these technology in searches for $0\nu\beta\beta$, e.g. Majorana Demonstrator [51] and GERDA [49], or investigations of finite νMMs, such as TEXONO [218] and GEMMA [186]. Because of this experimental history it is not surprising that semiconductors are also considered in attempts to measure CEνNS: CONNIE [71], CONUS [82], MINER [219], NCC-1701 at DRESDEN-II [73], νGEN [76], TEXONO [220].

2.2.3.3 Sub-Kelvin detectors

Sub-Kelvin detectors use primarily phonon excitation within a crystal to detect scattering events. These bosonic quasiparticles arise in the conversion of a scatterer's kinetic energy to a crystal lattice and have typical energy scales of a few meV, much lower than energies of light quanta or charge carries in other detectors. Since these detectors are generally operated at sub-Kelvin temperatures they benefit from reduced thermal noise, lower material specific heat and thermal conductivity. As a consequence, very low detection thresholds and excellent energy resolution can be achieved. In combination with other signals, e.g. light or charges, discrimination between nuclear and electronic recoils becomes possible since the energy transfer into detectable signals differ between these processes.

An interaction within the detector medium deposits energy which is subsequently dissipated in the crystal by nuclei and electron collisions. These processes create phonons, i.e. crystal excitation, which can by detected in the following whereby two different categories are distinguished: thermal and athermal phonons. Thermal phonons are measured via the induced temperature rise in equilibrium detectors and insensitive to the processes that are involved in reaching thermal equilibrium. Athermal phonons, on the other side, carry information about an energy deposition and its position and appear as prompt signals or excitations of the material.

Cryogenic devices are usually limited to kg-crystal size and thermally coupled to a heat reservoir of constant sub-Kelvin temperature, i.e. $10 - 100\,\mathrm{mK}$, while temperature sensors monitor the crystal's thermal behavior.

In DM searches, thermal phonons in combination with ionization signal are used in the EDELWEISS-III experiment [221], while athermal phonons are measured in combination with scintillation light in CRESST-II [222] and with charge signals in SuperCDMS [223]. Cryogenic detectors have been further applied in sensitive beta decay measurement to determine the absolute neutrino masses, i.e. in the ECHo experiment [53], or searches for $0\nu\beta\beta$ like in the CUORE experiment [224]. For CEνNS investigations they are considered in the experimental approaches of ν-clues [81] and RICOCHET [78].

2.3 Statistical data analysis

The main parts of this work are dedicated to the analysis of data provided by the CONUS experiment, either in the context of the first spectral (SM) CEνNS analysis [70] or in the context of a follow-up BSM investigation [225]. Here, we introduce the basic ingredients that are needed for the following investigations, such as the maximum likelihood method, hypothesis tests and confidence intervals (CIs). The following section is based on the content of Refs. [226–229].

2.3.1 Parameter estimation and maximum likelihood method

In this part we summarize the concept of parameter estimation via maximum likelihood (ML) methods. Next to general properties of estimators and likelihood functions, the treatment of systematic uncertainties is covered, which should enable the reader to comprehend the construction of likelihood functions used in the analysis of Ch. 3 and 4.

2.3.1.1 Parameter estimation

One of the core tools within statistics is the deduction of information from an experimental measurement about a certain observable x that is subject to statistical fluctuations. The observable can be understood as a random variable, which is distributed according to a certain probability density function (PDF), while the so-called sample space is spanned by all possible values that x might occupy. An experiment that performs n measurements can be understood as a single n-dimensional vector $\boldsymbol{x} = (x_1, ..., x_n)$, whose entries x_i have been drawn from the underlying PDF. Usually, the vector $\boldsymbol{x}$ is referred to as a sample of size n. Generally, it is assumed that the individual observations are independent from each other and that they are distributed according to the same PDF $f(x_i)$. In such cases the sample's joint PDF is simply given by the product of the individual PDFs, thus $f_{\text{sample}}(x_1, ..., x_n) = \prod_{i=1}^{n} f(x_i)$. In reality, one often encounters the situation in which an experiment has provided n measurements of a random variable x, or equivalently the sample $\boldsymbol{x}$, while the explicit form of the underlying PDF remains unknown. More explicitly, one is usually interested in properties, e.g. unknown parameters $\boldsymbol{\theta} = (\theta_1, ..., \theta_m)$, of a hypothesized PDF $f(\boldsymbol{x}; \boldsymbol{\theta})$ that are to be inferred on the basis of available observations $\boldsymbol{x}$. A function that depends only on the sample $\boldsymbol{x}$ is called a statistic, while it is referred to as an estimator when it is used to infer some properties of the PDF. Further, the evaluation of an estimator with a certain sample is called an estimate, which we indicate with a hat.[16]

The main properties of an useful estimator are consistency, bias and efficiency. Consistency means that an estimator $\hat{\theta}$ should converge, in terms of probability, to the parameter's true value θ. Bias quantifies an estimator's average deviation from the true value θ, i.e. $b[\hat{\theta}] = \langle \hat{\theta} - \theta \rangle = \langle \hat{\theta} \rangle - \theta$. Thus, an unbiased estimators exhibits $b[\hat{\theta}] = 0$. Finally, the property "efficiency" refers to the estimator's variance and will be covered in the context of likelihood properties in the next section. Examples for familiar estimators are the sample mean $\bar{x} = \sum_{i=1}^{n} x_i$ or the sample variance $s^2 = \frac{1}{n-1} \sum_{i=1}^{n} (x_i - \bar{x})^2$.

2.3.1.2 Maximum likelihood method

Now we want to focus on a more advanced technique to estimate unknown parameters from a given data sample of size n, i.e. the ML method. In doing so, we assume a random variable x that is distributed according to a PDF $f(x_i; \boldsymbol{\theta})$ with m unknown parameters $\boldsymbol{\theta} = (\theta_1, ..., \theta_m)$. The unknown parameters might represent model parameters such as coupling constants or particle masses or could take into account experimental effects, e.g. detector efficiency and resolution, that have to be determined from the data sample.

Assuming the individual observations to be independent of each other and to rely on the same underlying PDF, the overall probability for the x_i to lie within an infinitesimal interval is given by

$$\text{probability for } x_i \text{ in } [x_i, x_i + dx_i] \ \forall \ i = \prod_{i=1}^{n} f(x_i; \boldsymbol{\theta}) dx_i \,. \tag{2.36}$$

The product in this expression implies that the probability is maximal if the assumed PDFs are correct and the corresponding parameter values $\boldsymbol{\theta}$ are close to their true values. Since the dx_i are independent of any parameters, the same is true for the so-called likelihood function which is nothing but the product of the individual PDFs, $\mathcal{L}(\boldsymbol{\theta}) = \prod_{i=1}^{n} f(x_i; \boldsymbol{\theta})$.

Thus, the likelihood function is a function of the unknown parameter θ_j, while the sample points x_i remain fixed. Since the likelihood function becomes extremal when the parameters θ_j are close to their true values, the corresponding ML estimators $\hat{\theta}_j$ are

---

[16] For obvious reasons, the whole procedure of estimating parameter from a given data sample $\boldsymbol{x}$ is called parameter fitting.

defined as the solutions to the equations,[17]

$$\frac{\partial \mathcal{L}}{\partial \theta_j} = 0, \quad j = 1, .., m \,. \tag{2.37}$$

In the case of several maxima, the global maximum is chosen. ML estimators are consistent and have a bias that, however, vanishes for a very large number of measurements, the so-called *large sample limit*. Further, they are said to be efficient in the large sample limit as they exhibit the smallest variance of all possible consistent estimators [228], which holds up to the point where the extent of the sample space explicitly depends on the estimated parameter.

Another useful feature of the ML approach is its invariance under variable transformations. It can be shown that the ML estimator of some function $a(\theta)$ is simply obtained by evaluating it with the parameter estimator $\hat{\theta}$, i.e. $\hat{a} = a(\hat{\theta})$. Unbiased estimators do not necessarily remain unbiased under transformations, but for large enough sample sizes this can be usually assumed [227, Chaper 6.2].

Analytic maximization of likelihood functions is only possible in a few simple cases, e.g. for an exponential PDF, so usually numerical methods are applied to find the ML estimators. In practice, $-2\log\mathcal{L}$ is usually considered instead of $\mathcal{L}$ which is equivalent due to the logarithm's monotonically increasing property. Thus, the parameter values that maximize $\mathcal{L}$ also maximize $\log\mathcal{L}$ [227, Section 6.2]. Moreover, the logarithm converts the product of several PDFs, e.g. a product of exponentials in the Gaussian or Poissonian case, into a sum of simple terms. Further, the minus sign turns the maximization into a minimization procedure which is numerically more stable, while the factor of 2 plays a role in the determination of errors from likelihood contours.

Variance of maximum likelihood estimators Since the estimator on a parameter $\boldsymbol{\theta}$ is a function of the data sample $\boldsymbol{x}$, it is expected to fluctuate under repetitions of the same experiment. Thus, one usually gives an additional statement about the estimator's variance, i.e. *parameter* = *value* ± *error*. This means that the estimator of the true parameter is *value* which fluctuates according to a distribution with standard deviation of *error*.[18] Analytic calculation of the estimator's variance is only possible for specific PDFs, e.g. an exponential distribution [227, Chapter 6.2]. Therefore a general method of assessing the estimator's distribution is by using Monte Carlo (MC) techniques. In doing so, a large number of experimental outcomes is simulated, while each time the ML estimates are calculated. Finally, the estimator's variance is determined from the obtained distribution of estimates. The estimates of the observed data are usually applied as true parameters in the MC simulation.

For reason of completeness, we mention the so-called Rao-Cramér-Frechet or information inequality, cf. Ref. [227, Chapter 6.6], with which an estimate of (the inverse of) the covariance matrix can be derived for an unbiased estimator and a sufficiently large data sample [229, Chapter 40.2.2]. Basically, the likelihood function's second derivatives are

---

[17] Of course, $\mathcal{L}(\boldsymbol{\theta})$ has to be differentiable in the parameters $\theta_1, ..., \theta_m$ and the maximum must not lie at the boundary of the parameter range.

[18] Strictly speaking, this is only true for cases where the estimator is distributed according to a Gaussian distribution. However, in the large sample limit it can be shown that ML estimators actually follow a Gaussian PDF [227, Chapter 6.3].

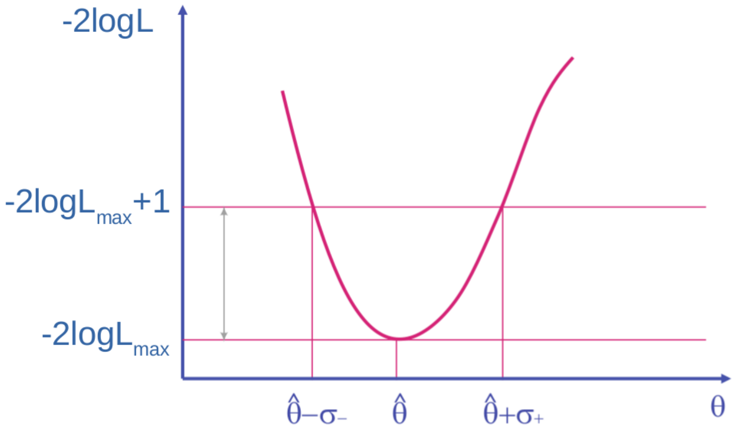

Figure 2.5.: Values of the likelihood function $-2\log\mathcal{L}$ around its best-fit $\hat{\theta}$. The corresponding errors are obtained by determining the parameter θ for which the likelihood function increases by one unit. Again, this underlines the benefit of multiplying the likelihood function with the factor of -2. The figure it taken from Ref. [231] and adapted to our conventions.

evaluated at the best estimates $\hat{\boldsymbol{\theta}}$ which is the conventional way of estimating the covariance matrix $V_{ij} = \mathrm{cov}[\hat{\theta}_i, \hat{\theta}_j]$ in numerical routines, e.g. the minuit package [230], which we also use throughout this work.

An intuitive understanding of how variances of ML estimators are obtained via a graphical illustration can be drawn from the following consideration: Assuming a single parameter and Taylor-expanding the log-likelihood function around the ML estimate $\hat{\theta}$, one obtains

$$\log\mathcal{L}(\theta) = \log\mathcal{L}(\hat{\theta}) + \left[\frac{\partial\mathcal{L}}{\partial\theta}\right]\Bigg|_{\theta=\hat{\theta}}(\theta-\hat{\theta}) + \frac{1}{2!}\left[\frac{\partial^2\mathcal{L}}{\partial\theta^2}\right]\Bigg|_{\theta=\hat{\theta}}(\theta-\hat{\theta})^2 + \mathcal{O}(\theta^3)\,. \tag{2.38}$$

Since $\hat{\theta}$ maximizes the likelihood by definition, $\log\mathcal{L}(\hat{\theta}) = \log\mathcal{L}_{\text{max}}$, the first derivative vanishes. Applying the Rao-Cramér-Frechet inequality in the single-parameter case and ignoring higher order terms, yields then, cf. Ref. [227, Chapter 6.7],

$$\log\mathcal{L}(\theta) = \log\mathcal{L}_{\text{max}} - \frac{(\theta-\hat{\theta})^2}{2\sigma^2_{\hat{\theta}}}\,, \tag{2.39}$$

where one can directly infer that the log-likelihood value decreases by $1/2$ from its maximum when parameter θ changes by one standard deviation from its ML estimate. This now justifies the former multiplication with a factor of 2 since $-2\log\mathcal{L}(\theta)$ then increases by 1 under 1σ-change of $\hat{\theta}$. This behavior is illustrated in Fig. 2.5 as well. Note that the log-likelihood contour is not necessarily parabolic; only in the large sample limit this is a valid approximation. Additionally, correlated estimators in the case of several parameters, imply the likelihood value to decrease by more than $1/2$ (equivalently by more than 1 for $-2\log\mathcal{L}(\theta)$) under 1σ-changes [227, Chapter 6.8].

2.3.1.3 Maximum likelihood for binned data

Throughout this work we apply ML methods to very large data samples, such that computing the log-likelihood function becomes numerically intensive, among others because of summing logarithms of PDFs for all data points x_i. Generally speaking, we have a large number of observations n_{tot} of a random variable x that is distributed according to a PDF $f(x;\boldsymbol{\theta})$ from which we want to obtain estimates from a certain number of parameters $\boldsymbol{\theta} = (\theta_1, ..., \theta_m)$. A solution is to make a histogram with entries $\boldsymbol{n} = (n_1, ..., n_N)$ in N bins, where each bin is assumed to be independent from any other bin.

Then, such a histogram can be interpreted to be a single measurement of a N-dimensional vector that is drawn from a joint PDF given by a multinomial distribution.

In many experiments the total number of entries n_{tot} fluctuates as well. Therefore, it is assumed to be a random variable that is distributed according to a Poisson distribution of mean ν_{tot}. In such cases one usually refers to an extended (binned) ML approach and the joint PDF is then multiplied with the corresponding Poisson distribution,

$$f_{\text{joint}}(\boldsymbol{n};\boldsymbol{\nu}) = \frac{\nu_{\text{tot}}^{n_{\text{tot}}} e^{\nu_{\text{tot}}}}{n_{\text{tot}}!} \frac{n_{\text{tot}}!}{n_1! ... n_N!} \left(\frac{\nu_1}{n_{\text{tot}}}\right)^{n_1} ... \left(\frac{\nu_N}{n_{\text{tot}}}\right)^{n_N} = \prod_{i=1}^{N} \frac{\nu_i^{n_i} e^{-\nu_i}}{n_i!}\,, \tag{2.40}$$

where the ν_i represent the expectation values of the corresponding bin i and in the last step $\nu_{\text{tot}} = \sum_{i=1}^{N} \nu_i$ and $n_{\text{tot}} = \sum_{i=1}^{N} n_i$ has been used. Hence, the joint PDF is similar to the case where each bin entry is an independent Poisson variable n_i with mean ν_i. The extended binned likelihood function, which is obtained by taking the logarithm as well as dropping additive, constant terms, is then given by

$$\log \mathcal{L}(\nu_{\text{tot}};\boldsymbol{\theta}) = -\nu_{\text{tot}} + \sum_{i=1}^{N} n_i \log \nu_i(\nu_{\text{tot}};\boldsymbol{\theta})\,. \tag{2.41}$$

In the limit of very small bin size this expression approaches the extended likelihood function without binning. Note that bins with just a few or no entries are in general no problem! Within the approach (even in the unbinned case), one distinguishes between two cases: If there is no (functional) relation between the total number of events and the unknown parameters, one obtains as estimates $\hat{\nu}_{\text{tot}} = \nu_{\text{tot}}$ in addition to the results of the usual likelihood approach $\hat{\boldsymbol{\theta}}$. On the contrary, if the total number of events is a function of the unknown parameters, the variances of the estimators $\hat{\boldsymbol{\theta}}$ are generally reduced because of the additional information provided by the total number of events n_{tot}.

Although ML methods are generally a powerful tool for parameter estimation, they do not (directly) allow for a test of overall goodness-of-fit. In App. B.1, a short overview of how to judge a parameter fit via a ML method is given.

2.3.1.4 Systematic uncertainties as nuisance parameters

Within a parameter estimation procedure, one might determine, next to the explicit quantities of interest, further parameters that are related either to the underlying PDFs, the experimental set-up or the signal prediction. Such parameters are usually called nuisance parameters as they are not necessarily relevant for the scientific question but might be required to incorporate a detector's response (efficiency and resolution), background yields, event shapes or generally to improve the underlying signal model, which can rely on further parameters. They are also relevant in the implementation of systematic uncertainties with so-called pull terms, cf. Ref. [228, Section 5.6] and Ref. [229, Chapter 40.2.2.2]. Their addition to the likelihood function generally allows for more freedom in the estimating process and, therefore, results in increased statistical uncertainties for the parameters of interest. To reduce the impact of this nuisance parameters, their values can be constrained with independent control measurements, e.g. knowledge from other experiments. Such external information is incorporated under assumption of a certain PDF, e.g. a Gaussian distribution.

For the nuisance parameter $\boldsymbol{\nu}$ and two random variables $\boldsymbol{x}$ and $\boldsymbol{y}$ that are distributed according to given PDFs, $f(\boldsymbol{x};\boldsymbol{\theta},\boldsymbol{\nu})$ and $g(\boldsymbol{y};\boldsymbol{\nu})$ respectively, one obtains the (profile) likelihood function by simple multiplication of both PDFs

$$\mathcal{L}(\boldsymbol{\theta},\boldsymbol{\nu}) = f(\boldsymbol{x};\boldsymbol{\theta},\boldsymbol{\nu})g(\boldsymbol{y};\boldsymbol{\nu})\,. \tag{2.42}$$

In maximizing the likelihood function for both parameters, information about $\boldsymbol{\nu}$ that might be incorporated in a measurement of $\boldsymbol{y}$, is then entering also the determination of $\boldsymbol{\theta}$ via measurements of $\boldsymbol{x}$. Note that within a MC simulation, both experiment have to be simulated under assumptions of fixed values for both parameters $\boldsymbol{\theta}$ and $\boldsymbol{\nu}$.

2.3.2 Hypothesis tests

In this section, we give an overview of statistical hypothesis testing with special emphasis on topics relevant for particle physics investigations, i.e. the distinction of potential (new) physics events from other less-relevant (physical) background events. For instance, in Section 3 the signal of interest is CEνNS itself, which is to be distinguished from background events. In Section 4 potential modifications or additional signals from BSM physics are foregrounded while the SM prediction of CEνNS is considered as background.

2.3.2.1 Hypotheses and significance levels

In a hypothesis test, one generally wants to quantify how well a certain statement, i.e. a hypothesis for a theory model, agrees with an observation of a random variable x. The statement under consideration is usually referred to as null hypothesis H_0, which for example provides a certain PDF for the random variable x. If the corresponding PDF $f(\boldsymbol{x})$ is uniquely defined, H_0 is called a simple hypothesis, while it is called a composite hypothesis, if the PDF $f(x;\boldsymbol{\theta})$ depends on further parameters $\boldsymbol{\theta}$ that are to be determined from the data. Generally, H_0 has to be tested against several alternative hypotheses $H_1, H_2, ...$, where each is associated with its own PDF $f(x|H_1), f(x|H_2)...$.

In (new) signal searches as well as in the present work, H_0 is usually the background-only hypothesis, while H_1 represents the hypothesis for a (new) signal in addition to background events. In order to investigate the agreement between the performed measurement, i.e. between the data sample $\boldsymbol{x}$, and the hypotheses under consideration, one uses a so-called test statistic $t(\boldsymbol{x})$ as a measure of disagreement. It can be either the original data itself, a multidimensional vector of lower dimension or just a single number. Examples for the

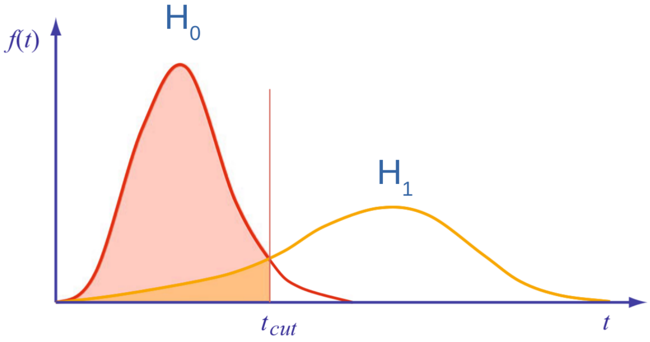

Figure 2.6.: Illustration of a hypothesis test. The PDFs corresponding to the signal hypothesis $g(t|H_1)$ and the null hypothesis $g(t|H_0)$ are illustrated. The null hypothesis H_0 is rejected if the observed test statistic $t(\boldsymbol{x})$ is observed above t_{cut}, vice versa H_0 is excepted for $t(\boldsymbol{x}) < t_{\mathrm{cut}}$. The figure it taken from Ref. [231] and adapted to our conventions.

latter can be a certain number of particles, a ratio of likelihood values or a p-value.

Each of the considered hypotheses is assumed to yield a certain PDF for the test statistic, $g(t|H_0), g(t|H_1), \ldots$. In the course of the test, the compatibility between the observed data and the hypotheses is judged by defining a so-called critical region (or alternatively acceptance regions) for the individual hypothesis. For instance, if the test statistic $t(\boldsymbol{x})$ of a given data set lies within the critical/acceptance region of H_0, the null hypothesis is rejected/accepted. The critical region for a hypothesis, e.g. H_0, is usually defined by a critical value t_{cut} that fulfills a certain probability under the assumption of hypothesis H_0. Correspondingly, a misidentification probability β can be determined considering the test hypothesis H_1 to be valid. Both quantities are illustrated in Fig. 2.6 and are defined as follows

$$\alpha = \int_{t_{\mathrm{cut}}}^{\infty} g(t|H_0)dt\,, \qquad \beta = \int_{-\infty}^{t_{\mathrm{cut}}} g(t|H_1)dt\,. \tag{2.43}$$

Basically, the significance level α is nothing but the probability to reject H_0, if H_0 is true, which is commonly referred to as either error of the first kind, or false positive. The opposite case of accepting H_0 although it is false, and thus rejecting the alternative hypothesis H_1 is called either error of the second kind or false negative. Further, the discrimination power of a test is defined as $1-\beta$. Thus, in practice one defines a certain significance level α or misidentification probability β and subsequently determines the corresponding value of t_{cut}. For $t(\boldsymbol{x}) < t_{\mathrm{cut}}$, one accepts H_0 and rejects H_1, while for $t(\boldsymbol{x}) > t_{\mathrm{cut}}$ H_0 is rejected an H_1 accepted, cf. Fig. 2.6. The often stated p-value is the probability of obtaining a test statistic at least as exceeding as the observed value. Examples of a hypothesis test in the context of particle selection can be found in Refs. [227, 228]. In the context of signal discovery, the rejection of the background-only hypothesis is only one step. Plausibility of the signal and compatibility with the observed data are further criteria as well as a comparison with the expected significance for a potential signal [232].

2.3.2.2 Likelihood ratio test and Neyman-Pearson lemma

The definition of acceptance and rejection regions is illustrative in the case of a scalar test statistic, as displayed in Fig. 2.6, while for a multidimensional test statistic $\boldsymbol{t} = (t_1, ..., t_m)$ this task might be quite complex. For such purposes the Neyman-Pearson lemma [233] is helpful and beneficial in improving a test's power. It states that for two simple test hypothesis H_0, H_1 and a fixed significance level α, the critical region with the highest power $1 - \beta$ (equivalently the lowest misidentifiaction probability) is the region of $\boldsymbol{t}$-space for which the likelihood ratio $g(\boldsymbol{t}|H_1)/g(\boldsymbol{t}|H_0)$ is larger than a constant c_α that is determined by the desired significance level α. Moreover, the test with the above criterion on the rejection region for a multidimensional test statistic $\boldsymbol{t}$ is equivalent to a test that relies on the one-dimensional ratio of the above PDFs. In practice, one is usually interested in the construction of a scalar test statistic out of the measured quantities $\boldsymbol{x} = (x_1, ..., x_n)$. A straightforward way is using the hypotheses' PDFs and construct the so-called likelihood ratio

$$\lambda_{\boldsymbol{x}} = \frac{f(\boldsymbol{x}|H_1)}{f(\boldsymbol{x}|H_0)} = \frac{\mathcal{L}(\boldsymbol{x}|H_1)}{\mathcal{L}(\boldsymbol{x}|H_0)} > c_\alpha \,. \tag{2.44}$$

However, one requires knowledge about the PDFs $f(\boldsymbol{x}|H_{0,1})$ or equivalently the likelihood functions $\mathcal{L}(\boldsymbol{x}|H_{0,1})$. Therefore, one usually applies MC techniques to determine the full test statistic $\lambda_{\boldsymbol{x}}$. For situations in which the number of simulated events becomes numerically too intensive, one makes use of other techniques such as the Fisher discriminant function, artificial neural networks, boosted decision trees and many more, for which we want to refer to the literature [227–229]. In this work, we have chosen to use MC simulations in order to obtain the corresponding test statistics.

If the tested model includes additional nuisance parameters $\boldsymbol{\nu}$, then generally the p-value of parameters $\boldsymbol{\theta}$, which might be used for hypothesis discrimination, also depends on these nuisance parameters, i.e. $p_{\boldsymbol{\theta}}(\boldsymbol{\nu}) = \int_{q_{\boldsymbol{\theta},\mathrm{obs}}}^{\infty} f(q_{\boldsymbol{\theta}}; \boldsymbol{\theta}, \boldsymbol{\nu})\, dq_{\boldsymbol{\theta}}$. Thus, strictly speaking the hypothesis for certain parameters $\boldsymbol{\theta}$ can only be rejected if the p-value drops below a defined significance α for *all* possible values of the nuisance parameters $\boldsymbol{\nu}$. A solution to this subtlety is by using the so-called *profile likelihood ratio* [234], in which approximate independence of the test statistic's PDF from any nuisance parameters is achieved,

$$\lambda(\boldsymbol{\theta}) = \frac{\mathcal{L}(\boldsymbol{x}; \boldsymbol{\theta}, \hat{\hat{\boldsymbol{\nu}}}(\boldsymbol{\theta}))}{\mathcal{L}(\boldsymbol{x}; \hat{\boldsymbol{\theta}}, \hat{\boldsymbol{\nu}})} \,, \tag{2.45}$$

where the parameters $\boldsymbol{\theta}$ and $\boldsymbol{\nu}$ are fitted simultaneously in the denominator, while in the numerator $\boldsymbol{\theta}$ is fixed and $\hat{\hat{\boldsymbol{\nu}}}(\boldsymbol{\theta})$ is the best-fit value for fixed $\boldsymbol{\theta}$. According to Eq. (2.45), $\lambda \sim 1$ represents good agreement between data and the assumed value of θ, while $\lambda \gg 1$ indicates strong disagreement between the underlying hypothesis and the analyzed data. A useful feature is that $-2 \log \lambda(\boldsymbol{\theta})$ follows approximately a χ^2 distribution in the large sample limit independent of the explicit values of the nuisance parameters $\boldsymbol{\nu}$. However, for finite data samples some general dependence of the p-value on the nuisance parameters $\boldsymbol{\nu}$ might remain.

2.3.2.3 Test statistics and Wilks' theorem

As mentioned before, MC techniques might help to simulate the expected test statistic λ at the cost of being numerically quite intensive for more involved analyses. In this subsection, we introduce a theorem that simplifies the determination of a test statistic and subsequently list approximate sampling distributions for the test statistic of Eq. (2.45). For simplicity, we now assume an investigation that tries to determine a certain signal strength μ, for instance in a Poisson counting experiment with mean $\mu\, s + b$, with s being the number of signal counts and b the respective background. However, the following considerations can be generalized to any parameter of the involved PDFs.

Wilks' theorem In the large sample limit, the log-likelihood ratio of two nested hypotheses H_0 and H_1, i.e. a hypothesis' parameter space is a subset of the other,[19] Wilks' theorem [235] states that the test statistic λ is distributed according to a χ^2 distribution whose DOF equals the difference of dimensionalities between both hypotheses' parameter sets, Θ_0 and Θ_1, respectively.[20] Thus, the logarithm of the profile likelihood ratio of Eq. (2.45) in the large sample limit is given by

$$t_\theta = -2\ln\lambda(\theta) \sim \chi^2_r\,, \tag{2.46}$$

with $\theta = 0$ representing the null hypothesis H_0 and $\theta \geq 0$ the alternative hypothesis H_1 as well as r being the difference of their dimensionalities. Recall that $\lambda \sim 1$ represents a good agreement between data and the assumed value of θ and, thus, higher values of t_θ imply increasing deviation between data and the assumed value of θ as well. Further, the level of disagreement can be quantified by the p-value $p_\theta = \int_{t_{\theta,\mathrm{cut}}}^{\infty} g(t_\theta|\theta)\, dt_\theta$. Thus, for more complex cases, Wilks' theorem provides a convenient alternative to MC simulations that might require large computation times.

Variations of test statistics Depending on the hypothesis test one pursues to perform, the test statistic has to be adapted. For example, the test statistic of Eq. (2.46), allows estimates on the potential signal strength $\hat{\mu}$ to be higher or lower than the hypothesized value μ, i.e. one speaks of a so-called two-sided test statistic and a determination of CIs is possible. Usually, one assumes that new processes increase the expected number of events, i.e. $\mu \geq 0$, such that one is interested in claiming a discovery at first. Hence, the background-only ($\mu = 0$) hypothesis has to be rejected. Alternatively, one might be interested in setting an upper limit. The corresponding test statistics are given by

$$q_0 = \begin{cases} -2\ln\lambda(0)\,, & \hat{\mu} \geq 0\,, \\ 0\,, & \hat{\mu} < 0\,, \end{cases} \tag{2.47}$$

$$q_\mu = \begin{cases} -2\ln\lambda(\mu)\,, & \hat{\mu} \leq \mu\,, \\ 0\,, & \hat{\mu} > \mu\,, \end{cases} \tag{2.48}$$

where q_0 is the quantity used for a discovery test (rejection of $\mu = 0$) and q_μ the test statistic for an upper limit. Since usually only upward fluctuations are considered, q_0

---

[19] Mathematically: For $\Theta_{0,1}$ being the parameter sets associated to $H_{0,1}$, both hypotheses are called nested if $\Theta_0 \subseteq \Theta_1$ or vice versa.

[20] Here, we recite the form of Wilks' theorem as given in Ref. [228]. For the original theorem, we refer to Wilks' original publication of Ref. [235].

only regards discrepancies between data and the null hypothesis for $\hat{\mu} \geq 0$ (downward fluctuations are ignored). The test statistic q_μ only takes into account data for $\hat{\mu} \leq \mu$ since upward fluctuations are not considered less compatible. Since both statistics only consider estimates that extend into one direction, they are referred to as one-sided test statistics.

Approximate sampling distributions In order to discriminate between any hypotheses, one requires the PDF of the considered test statistics. i.e. $f(q_0|0)$ for a discovery test or $f(q_\mu|\mu)$ for the determination of an upper limit. In the large sample limit, one can show that the most general distribution of the test statistic, i.e. the underlying signal strength of the data μ' being different than the one that is tested, follows a non-central χ^2 distribution, cf. Ref. [232]. For the case where the signal strength coincides with the tested one, $\mu' = \mu$, a χ^2 distribution according to Wilks' theorem is retrieved. Following the same argument, one can show that the PDF of the two one-sided test statistics, Eq. (2.47) and Eq. (2.48), exhibit the form

$$f(q_x|x) = \frac{1}{2}\delta(x) + \frac{1}{2}\chi_1^2(x)\,, \tag{2.49}$$

with $x = 0$ for a test of a positive signal and $x = \mu$ for a test of an upper limit. Here, the δ distribution at the origin represents the probability region that has been ignored by manually setting $q = 0$ in Eq. (2.47) and Eq. (2.48).

2.3.3 Confidence intervals and limits within the maximum likelihood approach

In particle physics, one usually searches for a signal or a new effect that corresponds to a certain parameter in the investigation to be non-zero. If the data analysis implies the corresponding parameter to deviate significantly from zero, then its best-estimate as well as a certain CI is reported. On the other side, if the obtained parameter estimate is still consistent with zero, an upper limit at a certain confidence level (C.L.) is quoted. In particle physics, one usually quotes the central value of a parameter if it is certain with a probability that corresponds to at least 3σ, otherwise the convention is to publish limits with 90% or 95% certainty [228]. Standardized methods, e.g. from Ref. [236], exist how to construct such confidence intervals and for the Gaussian case even simpler expression can be found, cf. App. B.2.

Now, we want to show a way of obtaining CIs within the ML framework. This can be done by either using the likelihood function itself or by likelihood ratios equivalent to the ones applied in hypothesis tests. While the first possibility is explained in App. B.3, we show how to determine C.L.s by using a likelihood ratio in the following.

For the determination of CIs with significance level $1-\alpha$ it is possible to use a hypothesis test for a certain parameter value assumed to be true. In such cases, one constructs a test for all potential values of interest and excludes all values for which the test would be rejected for a given α or below. All remaining values of the parameters of interest then form the CI at given significance $1-\alpha$. Moreover, if the critical region of the test is defined via a certain p-value $p_\theta \leq \alpha$, then the interval's endpoints might be determined by solving $p_\theta = \alpha$ for the parameter under consideration. Reference [237] proposed the construction of a CI based on a defined likelihood ratio, e.g. $\lambda(\theta) = \mathcal{L}(\boldsymbol{x};\boldsymbol{\theta})/\mathcal{L}(\boldsymbol{x};\hat{\boldsymbol{\theta}})$, which allows a smooth transition from two-sided (symmetric) confidence intervals to one-sided ones as it is the case of a limit determination. Using the profile likelihood ratio of Eq. (2.45), nuisance parameters can be incorporated as well. As mentioned earlier, parameters are only excluded if they are rejected for all involved nuisance parameters $\boldsymbol{\nu}$. Thus, if the p-value is used for the construction of CI, one has to use the profiled values of nuisance parameters $\boldsymbol{\nu} = \hat{\hat{\boldsymbol{\nu}}}(\boldsymbol{\theta})$ to ensure correct coverage of the obtained intervals.

Finally, we list p-values for the test statistics that we introduced so far, i.e. Eqs. (2.46), (2.47) and (2.48). For a two-sided test statistic t_μ that approximately follows a χ^2 distribution in the large sample limit, the p-value p_μ and corresponding significance Z_μ of an assumed signal strength μ is obtained via

$$p_\mu = 2\left(1 - \Phi(\sqrt{t_\mu})\right) , \qquad Z_\mu = \Phi^{-1}(2\Phi(\sqrt{t_\mu}) - 1) , \tag{2.50}$$

with Φ^{-1} being the cumulative distribution function (CDF) of the standard Gaussian. Signal strengths μ with p-values below a fixed value of α are excluded and the endpoints of the obtained interval are given by[21]

$$\mu_{\mathrm{up,lo}} = \hat{\mu} \pm \sigma \Phi^{-1}\left(1 - \frac{\alpha}{2}\right) . \tag{2.51}$$

All parameters that lie out of this range are said to be excluded at C.L. of $1 - \alpha$. Similar expressions can also be found for the one-sided test statistics of Eqs. (2.47) and (2.48), i.e.

$$p_x = 1 - \Phi(\sqrt{q_x}) , \qquad Z_x = \Phi^{-1}(1 - p_x) = \sqrt{q_x} , \tag{2.52}$$

with $x = 0$ representing the expression for a test of a positive signal and $x = \mu$ being the one for a test of the given upper limit. For the latter the corresponding upper limit is given by $\mu_{\mathrm{up}} = \hat{\mu} + \sigma\Phi^{-1}(1 - \alpha)$. Hence, parameter values with a p-value below α are excluded at C.L. of $1 - \alpha$.

2.3.4 Experimental sensitivity

Often it is useful to know the experimental sensitivity of the apparatus at hand either in terms of its capabilities in rejecting the background-only hypothesis or in establishing CIs on non-zero quantities.[22] It can be used to optimize the device's specification or within data analysis may help to identify statistical fluctuations or systematic deviations, i.e. a limit significantly below the expected background might indicate a strong downward fluctuation or an incorrect background description. Within the Frequentist approach, the experimental sensitivity is usually characterized by the expected (mean or median) p-value p_μ, equivalently the significance Z_μ, of certain hypotheses of interest. For a discovery test one usually quotes the median significance Z_0, assuming the signal to be present at its nominal rate ($\mu = 1$). Sensitivities on exclusion limits are usually calculated by generating data with $\mu = 0$ and stating the median significance of an assumed parameter value, e.g. $\mu = 1$. It is convention to state the median of the obtained significance values as they are functions of the used data and undergo fluctuations according to an underlying sampling

---

[21] Actually, the standard deviation has a certain dependence on the assumed signal strength μ [232]. Due to this dependence, in practice one usually determines the parameter value which yields $p_\mu = \alpha$.

[22] This section summarizes Ref. [238, Chapter 40.5].

distribution. This PDF $f(Z_\mu|\mu')$ depends on the assumed value of the parameter μ' which is not necessarily the same as the parameter value that is tested. Therefore one considers the outcome of several parameter values of μ' and combines them via median averaging, $\mathrm{med}[p_\mu|\mu'] = 1 - \Phi(\mathrm{med}[Z_\mu|\mu'])$.

For example, one may test a Poisson counting experiment that measures the variable n with mean $\mu s + b$ and standard deviation $\sigma = \sqrt{\mu s + b}$ for its capabilities of rejecting the background-only hypothesis $\mu = 0$. This can be done by using Eq. (2.48) with test statistic $\lambda(0) = \mathcal{L}(0)/\mathcal{L}(\hat{\mu})$ and the likelihood function $\mathcal{L}(\mu) = \frac{(\mu s+b)^n}{n!}\exp(-(\mu s + b))$. With Eq. (2.52) and the ML estimator $\hat{\mu} = (n-b)/s$, one obtains an expression for the normal and expected significance Z_0 and $\mathrm{med}[Z_0|\mu = 1]$, respectively,

$$Z_0 = \begin{cases} \sqrt{2\left(n \ln \frac{n}{b} + b - n\right)}\,, & n > b\,, \\ 0\,, & n \leq b\,, \end{cases} \qquad \mathrm{med}[Z_0|\mu = 1] = \frac{s}{\sqrt{b}}\left(1 + \mathcal{O}\left(\frac{s}{b}\right)\right)\,, \tag{2.53}$$

where $n \approx E[n|\mu = 1] = s + b$ is used in the median average. The first term of the right expression is usually called “figure-of-merit” $s/\sqrt{b}$ and only valid for $s \ll b$.

Sensitivities of more complicated cases are obtained via the corresponding p-value p_μ that allows the determination of a significance or an upper limit. In this procedure, different parameter values of μ' are assumed in the generation of data. The underlying sampling distribution for the p-value may be obtained by the usage of MC techniques or large-sample approximation, cf. Sec. 2.3.2.3 or Ref. [232].

For the aim of measuring a certain signal as accurately as possible, one is interested in minimizing the expected standard deviation of the best-estimate $\hat{\sigma}_{\hat{\mu}}$. For a simple Poisson counting experiments, the ML estimator $\hat{\mu}$ exhibits for $\mu = 1$ a variance of

$$V[\hat{\mu}] = V\left[\frac{n-b}{s}\right] = \frac{s+b}{s^2}\,. \tag{2.54}$$

Further, the quantity $s/\sqrt{s+b}$ is the expected significance for rejecting s events under assumption of an absent signal and can also be used to improve upper limit investigations on s.

CHAPTER 3

INVESTIGATING COHERENT ELASTIC NEUTRINO-NUCLEUS SCATTERING WITHIN THE CONUS EXPERIMENT

This chapter deals with the experimental effort of measuring CEνNS at a reactor site within the CONUS experiment. After an introduction of how the CONUS approach satisfies the three experimental requirements discussed in Sec. 2.2, we introduce the components of the analysis chain that led to the experiment's CEνNS spectral fit results [70]. While the experimental aspects like background modeling and data processing have been discussed in great detail in the PhD thesis of our colleague Dr. Janina Hakenmüller [239] as well as in several publications [82, 240], we keep this brief and refer to the stated literature. Here we focus more on the compilation of the antineutrino reactor spectra and the corresponding realistic signal predictions, which are among the author's main contributions. Further, a phenomenologically oriented analysis routine is described in detail, before the world's best constraints on CEνNS at a reactor site are presented [70].

3.1 The CONUS experiment

The CONUS experiment aims at the detection of CEνNS in HPGe detectors with electron antineutrinos emitted from a nuclear reactor. To fulfill the strict background conditions at shallow depth, a compact and sophisticated shield design is needed. The experimental set-up has been developed at Max-Planck-Institut für Kernphysik, Heidelberg (Germany) (MPIK), cf. Ref. [241], and assembled and commissioned close to the core of the commercial nuclear power plant in Brokdorf (Germany) in the beginning of 2018. Data collection started with the reactor outage, i.e. periods where the reactor is shut down for fuel reloading and maintenance, in April 2018. Since then the experiment has been operated and provided data from several reactor ON and OFF periods as well as intermediate optimization phases, cf. Ref. [239, Table 1.1] and Fig. 3.3 as well as Tab. 3.6. However, the collection of reactor OFF data is limited to the reactor outages which appear in roughly annual cycles and last about a month per year. First (world's best) CEνNS limits from a reactor site have been reported in autumn of 2020, while data taking with improved experimental conditions and a new data acquisition (DAQ) system is continued. After the reactor's shutdown by the end of 2021, further data collection of reactor OFF time is expected to further improve the obtained results.

3.1.1 Experimental site

The CONUS set-up is sited at the commercial nuclear power plant in Brokdorf (Germany) and is operated by the Preussen Electra GmbH [242].[1] It started operation in October 1986 and is going to be shut down 31st December 2021 in the context of Germany's energy transition towards renewable energy ("Energiewende") [243]. The reactor building houses a single-unit, PWR that is able to provide a thermal power of up to 3.9 GW which is among the strongest nuclear power plants worldwide with a gross electric power of 1.48 GW. The core itself contains 193 fuel assemblies with an active zone length of 3.9 m which in total yields an uranium mass of about 103 tonnes. The provided thermal power is monitored by three independent methods: thermal balance in the secondary heat circuit (absolute value), ex-core instrumentation (ionization chambers and proportional counters in the core shield's concrete) and the in-core instrumentation ("self-powered neutron detectors" and "aeroball measuring system", relative power values at certain positions in the core), cf. Ref. [240, Sections 3]. In addition, a reactor core simulation that relies on several data, e.g. temperatures, thermal power and control rod positions, is able to provide a full 3D assessment of the relative power distribution inside the reactor core. Information about the thermal power and the fuel evolution of the most relevant isotopes, extracted from the core simulation, are accessible to the CONUS Collaboration and used as time-averaged quantities in this analysis.

More concretely, the CONUS is located in room A-408 inside KBR's safety containment which provides basic infrastructure for experimental execution like electricity and cold air ventilation that keeps the temperature at stable levels. The distance to the reactor core's center is 17.1 m with a slight offset (~ 25 cm) in vertical direction from its central point. This relatively short distance to an intense electron antineutrino source allows fluxes of $\sim 2.3 \cdot 10^{13}\,\mathrm{cm}^{-2}\,\mathrm{s}^{-1}$ at the experimental site that can still be approximated as emitted from a point-like source. The location of the whole CONUS device within the reactor building and the experimental site is illustrated in Fig. 3.1. Although rather close to the reactor core, room A-408 is accessible at any time. It is partially located under the plant's spent fuel water pool and fully under an additional pond used for loading spent fuel storing casks prior to shipment. The building's concrete and steel structures provide an overburden of 10-45 m w.e., depending on angular directions (θ, φ). Thus, on average an overburden of 24 m w.e. is obtained.

However, operation within a nuclear power plant comes with some boundary condition. For reasons of reactor safety, robustness against earthquakes is to be ensured and the usage of flammable materials and cryogenic liquids is prohibited. In addition, stable and autonomous operation must be ensured since remote control is not possible. In terms of background, one has to deal with intrinsic and potential reactor backgrounds as well as local dust contamination and airborne radiation.

---

[1] The German name of the Brokdorf nuclear power plant is Kernkraftwerk Brokdorf (Germany) and in the following, we refer to it by using its German abbreviation KBR.

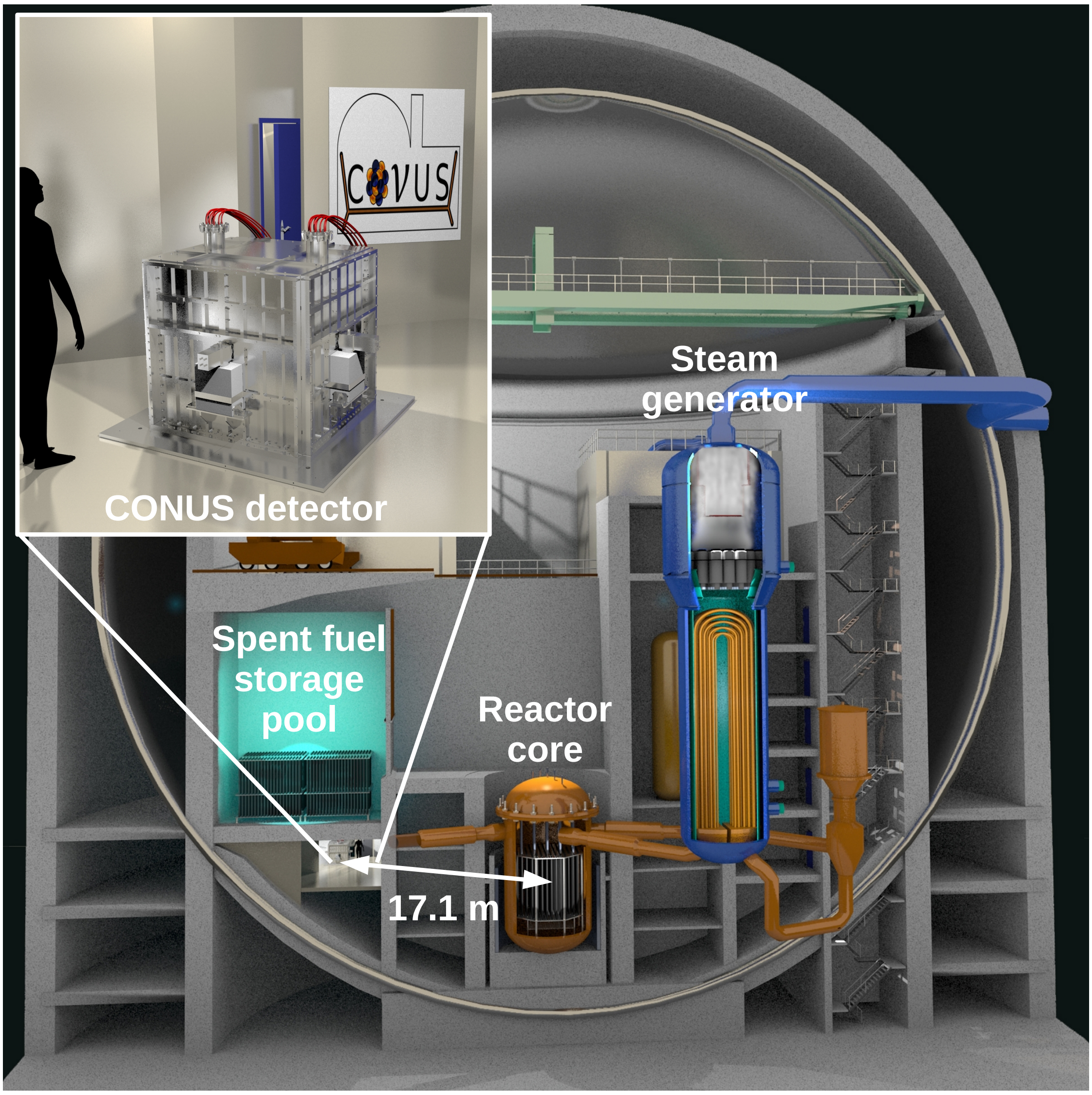

Figure 3.1.: Location of the CONUS detector in the building of the Brokdorf nuclear power plant. The set-up is located under the spent fuel storage pool at 17.1 m distance to the 3.9 GW (thermal power) reactor core, while its vertical position approximately coincides with the reactor core center. Room A-408 is illustrated in the enlarged image. The set-up's steel cage houses the four HPGe detectors that are embedded by layers of lead bricks and pure as well as borated polyethylene plates which form the passive shield against external radiation and other background sources. An active muon anticoincidence (muon veto) system consisting of plastic scintillator plates equipped with PMTs is contained as well. The picture is published in Ref. [225] by courtesy of G. Vogt (MPIK).

3.1.2 CONUS shield design

The advanced shield design of CONUS results from the decades-long experience of MPIK [201] and is based on the highly sensitive germanium spectrometer GIOVE which is used for material screening applications at shallow depth [205]. The CONUS shield exhibits an onion-like structure of different components, cf. left plot of Fig. 3.2. Five layers of lead bricks with increasing radiopurity towards the detector chamber, resulting in a thickness of in total 25 cm, are used to shield against exterior gamma radiation. Lead is advantageous compared to copper because of its stronger self-absorption and thus reduces more efficiently muon-induced bremsstrahlung at low energies. Attention was paid to the innermost layer being especially radiopure, i.e. ^{210}Pb activity $< 1.1\,\mathrm{Bq\ kg^{-1}}$. The lead alone already allows a background suppression of about 2-3 orders of magnitude. Further, layers of pure and borated polyethylene are incorporated to moderate and capture neutrons both from the experimental environment and muon-induced ones in lead, respectively. In addition to these passive components, an active muon anticoincidence (muon veto) system, i.e. plastic scintillator plates with PMTs, is installed to suppress muon-induced backgrounds and moderate neutrons in addition. With it, another order of magnitude in background suppression is achieved, cf. Fig. C.7. The construction is enclosed by a steel cage that ensures earthquake safety and helps in preventing radon migration into the detector chamber. With a volume of $1.65\,\mathrm{m}^3$ and a total mass of 11 tonnes, the whole set-up is extremely compact, cf. Fig. 3.1.

All in all a background suppression of about 4 orders of magnitude is achieved, compared to the case of having no shield at all [244]. However, at shallow depth several background components might spoil a CEνNS detection. The shield's capabilities of background suppression have been both tested at MPIK and KBR, while the dominating contribution at both sites are events induced by cosmic ray muons inside the shield or the surrounding material [70].

3.1.3 CONUS detectors

To detect CEνNS with HPGe detectors within a nuclear power plant several requirements have to be fulfilled. At first, high crystal masses are preferred to increase the expected signal and minimize the number of read-out electronics. Low intrinsic noise levels are aimed to ensure (pulser) resolutions, i.e. below 85 eV. At such resolutions, low energy thresholds, i.e. below 300 eV, can be achieved which are crucial for a signal discovery. Further, minimal cosmic activation levels of the used germanium diode as well as usage of low background materials, e.g. for the cryostat, are desired to reach lowest possible background levels. A special requirement due to the experimental location is the usage of electrically powered cryocooler, since cooling with liquid noble gases is generally prohibited. In addition, boundary conditions related to the CONUS shield have to be satisfied, e.g. longer cryostat arm lengths in order for the detector to fit into the shield construction.

In the end, four p-type point-contact HPGe detectors with an active mass of (3.73 ± 0.02) kg have been developed in collaboration with Mirion Lingolsheim [245], cf. Ref. [82]. They are operated in the temperature range of $78 - 88\,\mathrm{K}$.

Generally, the detectors can be divided into three main components: the HPGe diode itself, the cryostat that contains it and the electrical cryocooler which maintains stable

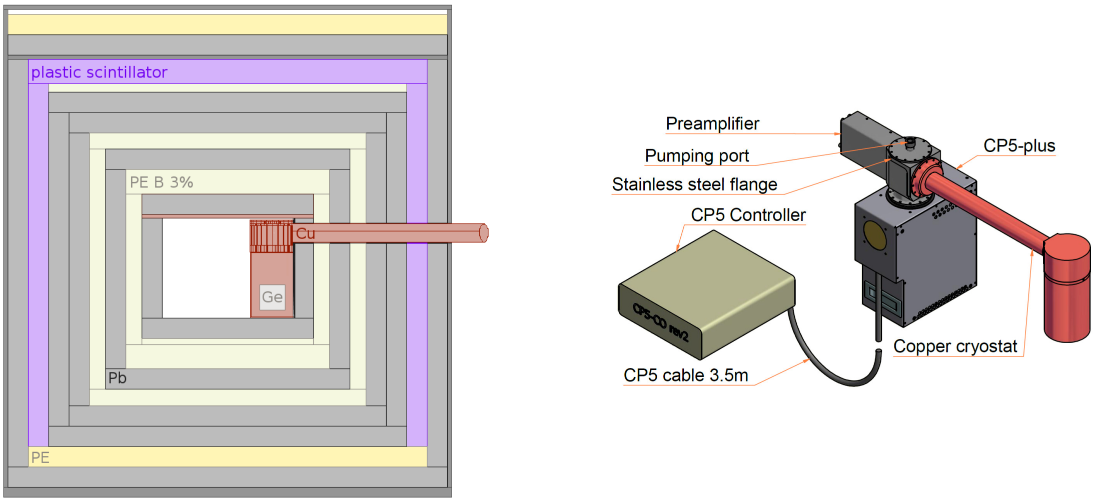

Figure 3.2.: **Left:** Onion-like structure of the CONUS shield with its individual components described in the text. The position of the germanium detector inside the copper cryostat is illustrated as well. The shielding scheme is published in Ref. [240] and provided by courtesy of Dr. J. Hakenmüller. **Right:** Detector design of the CONUS detectors with the HPGe diode located in the copper cryostat. The detector operating temperature is maintained by the electric cryocooler CP5-plus and adjustable with the wired remote controller. The picture is used in Ref. [82] and provided by courtesy of Mirion Lingolsheim [245].

operation temperatures. For the HPGe diodes four new crystals with a mass of $\sim 1\,\mathrm{kg}$ where used. After proper manufacturing, the crystals exhibit a lithium-diffused n^+-layer around their surface which is partially dead (dead layer) and semi-active (transition layer), while the bottom is fully passivated (passivation layer) except for the boron-implanted p^+-contact. A detector's active volume is defined as the volume that provides normal detection signals, i.e. the volume without dead and transition layer. The transition layer is important in the generation of so-called "slow pulses" which are related to energy depositions of particles with small absorption length, e.g. from electron or low energy photons, that are stopped in its interior. The resulting charge release diffuses slowly to the active zone where they are transported and read-out at the contacts. Such signals exhibit relatively large signal rise times and contribute background events at low energy. A full characterization of the CONUS detectors and their layer structure can be found in Ref. [82], while the active masses needed for the analysis are listed in Tab. 3.1.

The HPGe diodes are contained and cooled in cryostats, which are made of radiopure electrolytically produced copper. A long cooling arm, i.e. $> 40\,\mathrm{cm}$ in length, is required due to the shield extension. The electric cryocooler is a pulse tube cooler that requires no maintenance and avoids any flammable materials. It allows detector operations up to 40°C and adjustments of the diode temperatures, i.e. to optimize the detector's energy resolution, via an external power controller. Shock mounts and a vibration cancellation system further help to reduce potential noise events. An illustration of the detector design is depicted in the Fig 3.2.

Detector	Active mass [g]	Active volume [%]
C1	936 ± 10	94 ± 1
C2	947 ± 10	95 ± 1
C3	936 ± 10	94 ± 1
C4	907 ± 10	91 ± 1

Table 3.1.: Active detector masses and volumes of the CONUS detectors according to Ref. [82]. These values are implemented in our analysis through the detector mass pull-terms, cf. Sec. 2.3.1.4, in order to incorporate the uncertainties on the individual detector masses.

All used materials underwent careful material selection and underground storage to guarantee lowest possible background levels, especially in the case of components that are located within the shield close to the HPGe diode. Overground storage of the diodes is reduced to a minimum and tracked carefully in order to monitor cosmogenic activation by fast secondary neutrons. This is especially relevant for the isotopes ^{68}Ge, ^{65}Zn and ^{3}H. Background contributions of further isotopes, i.e. ^{57,58,60}Co, ^{55}Fe, ^{54}Mn, are quantified by MC simulations [244]. Further, electronics read-out circuits were adopted to low energy purposes, i.e. low loss dielectrics and ultra-low radioactive background materials. For the overall signal readout, the digital signal analyzer LYNX [246] is used. It proved suitable for low energy application due to its high trigger rates and sensitivity to small energies as well as long-term stability. More details can be found in the dedicated CONUS detector publication of Ref. [82]. During operation at KBR, artifacts were found in the data sets of detector C4. Therefore data sets obtained from this detector are not considered throughout this work. The same applies to the RUN-2 data set of detector C2 due to incompatible DAQ settings between reactor ON and reactor OFF periods.

3.2 CEνNS prediction for the CONUS experiment

Now, we outline the path towards a realistic signal prediction for the introduced experimental framework. The underlying reactor model as well as the effect of signal quenching on the expected event rates is explained. In contrast to Sec. 2.1.4 where generic values are chosen, we focus here concretely on the CONUS set-up and chose a more realistic description of energy-dependent quenching. Subsequently, the obtained expectation is equipped with realistic detector responses. In the end, we summarize how the final signal expectation for the first CONUS spectral fit analysis is determined and give an overview of the underlying uncertainties.

3.2.1 Reactor antineutrino emission spectra

A reactor's antineutrino emission spectrum at an experimental site located at distance L to a single-core unit can be described according to, cf. Refs. [185, 186, 194],

$$\phi(E_\nu) = \frac{1}{4\pi L^2} \frac{P_{\mathrm{th}}}{\sum_i \alpha_i E_i} \sum_i \alpha_i \left(\frac{dN_i}{dE_\nu}\right), \quad i = {}^{235}\mathrm{U},\, {}^{238}\mathrm{U},\, {}^{239}\mathrm{Pu},\, {}^{241}\mathrm{Pu}\,. \tag{3.1}$$

The E_i represent the energy released per fission of isotope i, P_{th} is the reactor's thermal power and the quantities α_i describe the relative fraction of isotope i among all fissions. The whole spectral shape information is incorporated in the cumulative electron antineutrino spectrum normalized per fission (dN_i/dE_ν). The application of Eq. 3.1 assumes that long-lived fission fragments that do not decay in equilibrium, i.e. antineutrinos from radioactive spent fuel elements, are either negligible or have been corrected for (or tested via MC simulation [240]). Generally, one only assumes a dependence on the individual nuclear properties of the fission isotope and subsequent fission fragments created via thermal neutron fission in the case of ^{235}U, ^{239}Pu, ^{241}Pu, and fast fission in the case of ^{238}U [185].[2]

Since the first quantities in Eq. 3.1 are usually known, either from external measurements or from reactor operation, we separate them from the spectral dependence in Eq. 3.1,

$$\phi(E_\nu) \equiv \phi^*(E_\nu) \cdot \sum_i \alpha_i \left(\frac{dN_i}{dE_\nu}\right), \tag{3.2}$$

where $\phi^*(E_\nu)$ incorporates all these multiplicative quantities and is referred to as "reduced reactor flux". The individual isotope spectra (dN_i/dE_ν) can be obtained in different ways via ab-initio calculations, conversion methods or direct measurements, cf. Sec. 2.2.1.2. More refined versions apply additional knowledge from available databases and/or incorporate further corrections, i.e. Refs. [247, 248]. The so-called Huber-Mueller model (HMM) is a widely used reference reactor model and a combination of Refs. [247, 248], where the thermal fission spectra are taken from the conversion methods of Ref. [248] and the fast neutron fission spectrum is gained from the refined ab-initio approach of Ref. [247]. Uncertainties of this method arise from the experimental measurements themselves, corrections to individual beta decay branches, e.g. finite nuclear size and radiative corrections as well as first forbidden decays, cf. Ref. [185, Section 3]. Overall uncertainties of about 5% are obtained with these methods [183].

In the following, we want to address the individual components and illustrate how they concur in the antineutrino spectra expected at the CONUS site.

Reactor thermal power As mentioned in Sec. 3.1.1, the absolute reactor thermal power is measured via the heat balance in the plant's secondary circuit with the mass flow of feedwater contributing the dominating uncertainty. The in-core instrumentation (at certain positions within the core) provides (via extrapolations) a three-dimensional map of relative power distributions inside the reactor core. During usual operation, thermal power values

---

[2] To be accurate, the individual fission fragment yields might further depend on the energy shape of the incident neutron flux which we neglect as well.

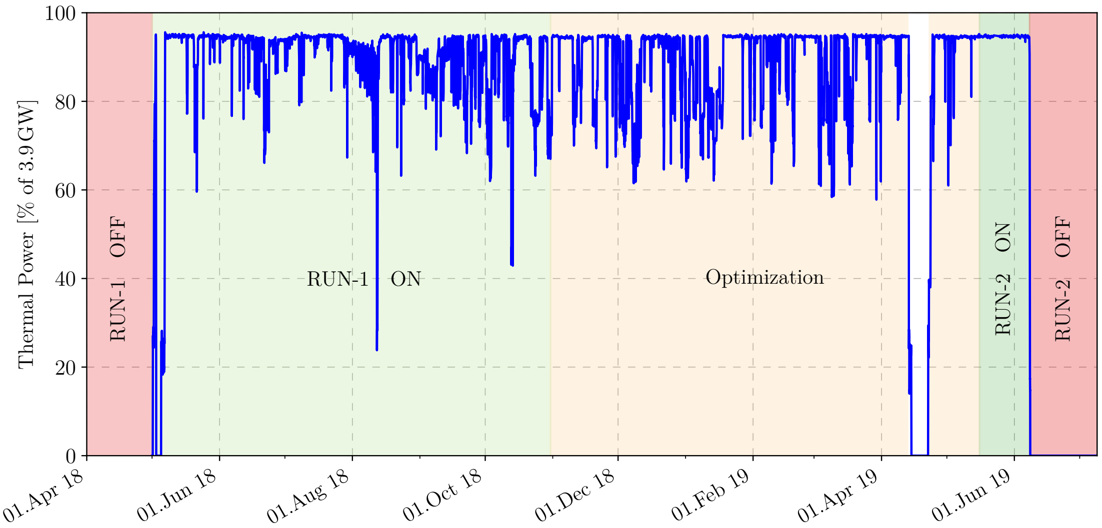

Figure 3.3.: Reactor thermal power P_{th} for the first two CONUS data collection periods. Reactor simulation data provided by courtesy of Dr. K. Fülber (Preussen Electra GmbH).

from both are used to regularly calibrate the reactor core simulation POWERTRAX [249], which provides in-time monitoring of all relevant reactor core information. Information is usually provided in two-hour intervals and in shorter intervals whenever strong power gradients appear, e.g. at reactor ramp up or shut down. The time-averaged thermal powers of the first two CONUS data collection periods are shown in Fig. 3.3.

The general CONUS data collection time is subject to periods which are not considered for physics data analysis, e.g. optimization times or intervals of unstable environmental conditions. These periods deviate for the four CONUS detectors and lead to detector-specific data collection periods that also affect the associated average reactor power. Hence, due to the provided thermal power information we are able to calculated individual detector-specific time-averaged power values with the provided reactor powers, cf. Tab. 3.4. The simulation uncertainties are assumed to be of minor importance such that the absolute thermal power is identified as dominating uncertainty [240, 250]. Hence, an overall uncertainty of $\Delta P_{\mathrm{th}} = 2.3\%$ is assumed for the reactor thermal power provided by KBR.

Fission fractions and energy release per fission The fission fractions of the four main isotopes (^{235}U, ^{238}U, ^{239}Pu, ^{241}Pu) are needed to calculate the average energy release per fission $\bar{E} = \sum_i \alpha_i E_i$ as well as to weight the individual antineutrino emission spectra (dN_i/dE_ν), cf. Eq. 3.1. Generally, these values are determined by the fuel composition of the reactor core and, since the fuel composition changes with time, are thus itself time-dependent. Fortunately, this values can be extracted from the reactor simulation data of each reactor cycle and used to determine detector-specific time-averaged fission fractions, cf. Tab. 3.2.

Analysis	Data set	^{235}U [%]	^{238}U [%]	^{239}Pu [%]	^{241}Pu [%]
SM	C1R1	60.3	7.1	27.0	5.4
	C2R1	63.8	7.1	24.2	4.9
	C3R1	57.2	7.2	29.7	6.0
	C1R2	45.0	7.3	38.4	9.3
	C3R2	45.0	7.3	38.4	9.3
BSM + νMM (extended)	C1R1	56.8	7.2	29.9	6.1
	C2R1	56.9	7.2	29.8	6.1
	C3R1	56.8	7.2	29.9	6.1
νMM (extended)	C1R2	45.0	7.3	38.4	9.3
	C3R2	45.0	7.3	38.4	9.3

Table 3.2.: Average fission fractions of the four isotopes that are relevant for the antineutrino emission. These listed values are time-averaged in the individual detector data collection periods. We label the CONUS data sets in the following convention: *Detector* + *Run*. For example, the data set of detector C1 in the first run is labeled C1R1. We already list values that are used in the BSM analyses for completeness. The fission fractions rely on different data collection periods that result e.g. from varying exposures or higher energy regions as in the case of EνeS. Data provided by courtesy of M. Seidl (Preussen Electra GmbH; extraction from reactor simulation) and processed by C. Buck (MPIK; calculation of detector-specific fission fractions).

Isotope	$\langle E_\nu \rangle$ [MeV] [251]	E_i [MeV] [251]	N_i^ν [fission^{-1}] [186]
^{235}U	9.06 ± 0.13	202.36 ± 0.26	6.12
^{238}U	10.85 ± 0.39	205.99 ± 0.52	7.11
^{239}Pu	7.41 ± 0.18	211.12 ± 0.34	5.53
^{241}Pu	8.42 ± 0.12	214.26 ± 0.33	6.36
fuel average	8.65	206.0	6.03

Table 3.3.: General information about the four main fission isotopes: average energy carried away by the antineutrinos $\langle E_\nu \rangle$, energy release per fission E_i as well as the average antineutrino emission per isotope fission (integrated over all neutrino energies). In the last row, we list the fuel-averages of these values, where we assume a typical fuel composition of a PWR: (^{235}U, ^{238}U, ^{239}Pu, ^{241}Pu) = (0.561, 0.076, 0.307, 0.056), cf. Ref. [194]. The average number of neutrinos per fission is added with another contribution of 1.2 particles per fission, which originates from neutron captures of ^{238}U [187], such that one arrives at the conventionally stated value of 7.2 antineutrinos per fission [186].

The estimation of corresponding errors is a bit more involved as the individual isotopes are correlated among each other. Fortunately, we can use in our estimation several results from the literature, both as input as well as cross-checks for the correct order of magnitude. Reference [194] provided correlation coefficients α_{corr} which we assume to be typical for any PWR, thus also for our case at KBR. Further, a detailed investigation of uncertainties in antineutrino production at nuclear reactors has been performed by Ref. [250]. According to their findings, the combined uncertainties of fission fractions are at the level of $\mathcal{O}(1)\%$, while Ref. [194] reported their uncertainties to be $\lesssim 5\%$. Moreover, the uncertainty on the expected reactor antineutrino flux was estimated for the Daya Bay experiments to be below 1% [252].

In estimating the error for the individual (averaged) fission fractions, we determined standard deviations from typical PWR values stated in the literature, e.g. from Refs. [194, 250, 253], under the assumption of identical fuel composition and similar reactor cycles and operation. The obtained values are slightly larger than the $\mathcal{O}(1)\%$ uncertainties of Ref. [250], but by all means conservative. The final covariance matrix for our fission fractions is then given by

$$\begin{aligned}\alpha_{\mathrm{cov}} &= \Delta\alpha^T\ \alpha_{\mathrm{corr}}\ \Delta\alpha \\ &= \begin{pmatrix} 0.036 & 0.01 & 0.026 & 0.01 \end{pmatrix} \begin{pmatrix} 1 & -0.22 & -0.53 & -0.18 \\ -0.22 & 1 & 0.18 & 0.26 \\ -0.53 & 0.18 & 1 & 0.49 \\ -0.18 & 0.26 & 0.49 & 1 \end{pmatrix} \begin{pmatrix} 0.036 \\ 0.01 \\ 0.026 \\ 0.01 \end{pmatrix} .\end{aligned} \tag{3.3}$$

Further ingredients are the individual energy releases E_i which are needed in order to calculate the average energy release per fission $\bar{E}$. In our model we apply improved calculations of Ref. [251], which are given in Tab. 3.3 with additional information of the individual fission isotopes. Using a typical PWR fuel composition, the average energy release per fission is about 206 MeV, which is of course expected to change with varying fuel composition.

Reduced reactor fluxes and reactor spectra For the calculation of reduced reactor fluxes as well as for the compilation of detector-specific reactor spectra, we use the time-averaged values of the fission fractions (Tab. 3.2) and the thermal reactor powers (Tab. 3.4), respectively. The obtained results are listed in Tab. 3.4 and illustrated in Fig. 3.4 as well as in App. C.1 for data collection period C1R1. Since the time-averaged fission fractions do not vary much, the spectral variations among the individual spectra are less relevant for the moment. Therefore, the spectra of data collection periods C1R1 is chosen as a representative here.

The uncertainties of the reduced reactor fluxes are determined via MC sampling, in which we draw values from (multidimensional) Gaussian distributions. These are given by corresponding mean value(s) and standard deviation/covariance matrix. One dimensional Gaussian distributions are assumed for the thermal reactor powers (Tab. 3.4 + 2.3% uncertainty), the experiment's distance to the reactor core ($L = 17.1 \pm 0.1\,\mathrm{m}$) and the individual energy releases per fission (Tab. 3.3). The correlation among fission fractions are considered by drawing from a multidimensional Gaussian distribution with covariance matrix of Eq. (3.3) and mean values according to Tab. 3.2. The obtained distribution of

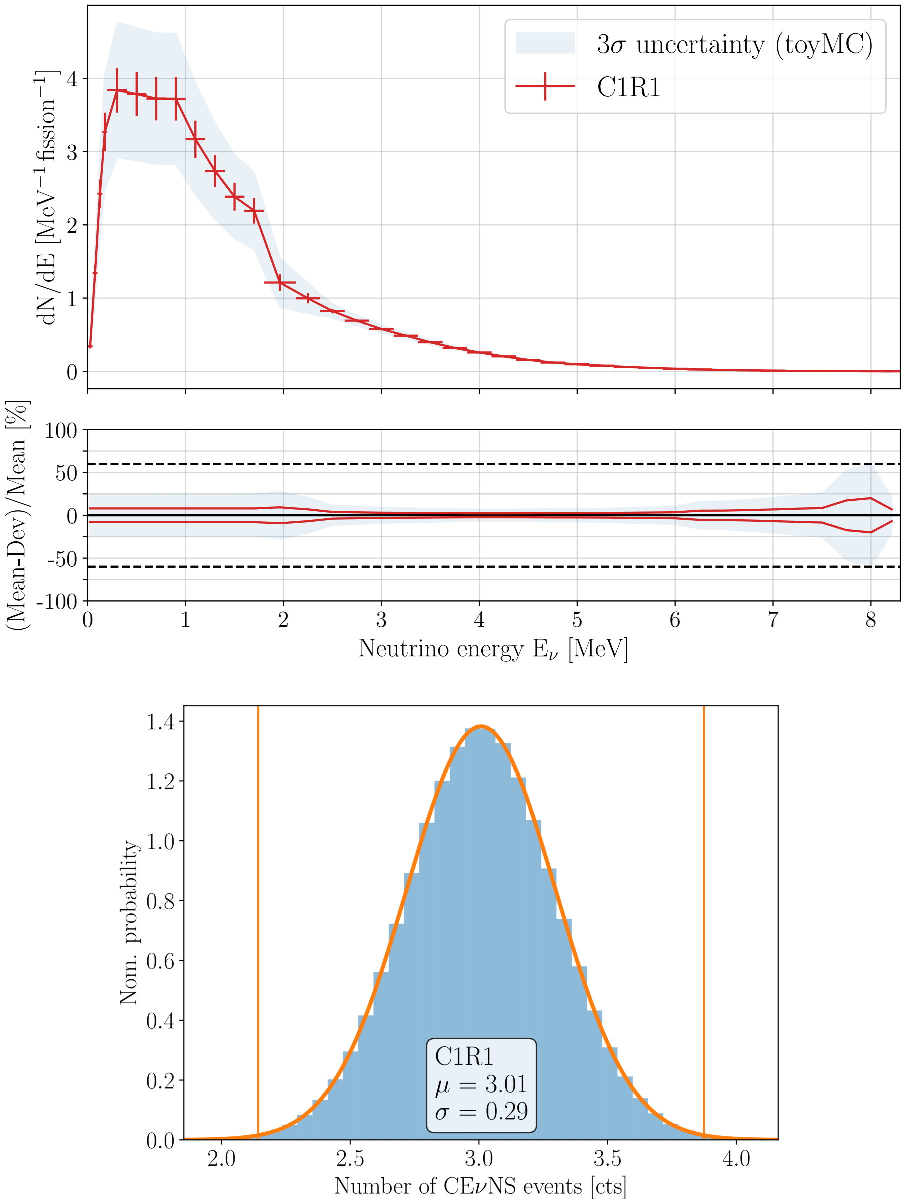

Figure 3.4.: **Top:** Full reactor antineutrino emission spectrum (dN/dE_ν) for data collection period C1R1. In the CEνNS analysis, only HMM spectra within $[1.8, 8.3]$ MeV are considered, while for the BSM analyses of Ch. 4 additional ab-initio spectra are added below 1.8 MeV, cf. Sec. 4.1. For the HMM part, individual bin uncertainties given by the diagonal entries of the refined covariance matrix are used, while for the low-energy part 10%-uncertainties are assumed. The uncertainty band is obtained by sampling reactor spectra, with the underlying distribution being determined by the spectral values and the covariance matrix. A spectrum in logarithmic scale that illustrates the effects at higher energies can be found in App. C.1 **Bottom:** Impact of spectral uncertainties on the expected SM CEνNS signal for C1R1. Uncertainties are determined from a Gaussian fit to the signal distribution obtained via sampling of reactor spectra and subsequent calculation of the resulting CEνNS events. Corresponding plots for the other data collection periods can be found in App. C.1 as well.

Analysis	Data set	$\bar{P}_{\text{th}}$	Φ^* $[10^{12}\,\text{fission}\,\text{cm}^{-2}\,\text{s}^{-1}]$
SM	C1R1	92.33	2.97 ± 0.10
	C2R1	92.70	2.99 ± 0.10
	C3R1	88.79	2.86 ± 0.09
	C1R2	94.69	3.03 ± 0.10
	C3R2	94.69	3.03 ± 0.10
BSM + νMM	C1R1	89.88	2.89 ± 0.09
(extended)	C2R1	90.12	2.90 ± 0.10
	C3R1	90.10	2.90 ± 0.10
νMM	C1R2	94.69	3.03 ± 0.10
(extended)	C3R2	94.69	3.03 ± 0.10

Table 3.4.: Average thermal powers and corresponding reduced reactor fluxes for the individual data collection periods. The latter are obtained via MC sampling of all reactor-related quantities in Eq. (3.1), i.e. the distance to the core L, the fission fractions α_i, the isotope-specific energy release per fission E_i and the reactor thermal powers $\bar{P}_{\text{th}}$.

reduced fluxes is fitted by a Gaussian function whose best-fit values are listed in the last column of Tab. 3.4.

Starting point for the CONUS antineutrino spectra is the HMM, i.e. ^{235}U, ^{239}Pu, ^{241}Pu from Ref. [248] and ^{238}U from Ref. [247] which gives the number of neutrinos emitted per MeV neutrino energy in an energy range of $1.875 - 8.125\,\text{MeV}$. We interpolate this spectra with a linear spline and extrapolate to higher energies, up to the point where the first isotope interpolation reaches zero in order to stay conservative about the spectrum at higher energies. This happens for ^{235}U at an energy of 8.3 MeV. In addition, these spectra are extrapolated to lower energies in order to fit the energy binning of Ref. [194] for reasons that will become clear below. In the next step the isotope spectra are added up according to their detector- and run-specific fission fractions, cf. Eq. (3.1). We further account for the "reactor-bump", an increase in the IBD-measured antineutrino spectra observed at energies $\sim 6\,\text{MeV}$, by using the correction values provided by Ref. [194]. At this point, we remark that these corrections factors are (strictly speaking) only true for the fission fractions that underlie Ref. [194], i.e. (56.1%, 7.6%, 30.7%, 5.6%) for the isotopes (^{235}U, ^{238}U, ^{239}Pu, ^{241}Pu). Comparing these values to the ones underlying the CONUS data collection periods, cf. Tab. 3.2, one identifies main differences in the isotopes ^{235}U and ^{239}Pu in RUN-1 of the present analysis with maximal deviation of 8%. RUN-2 exhibits stronger deviation but is less important for the analysis due to its smaller exposure. In general, we assume this fission fraction correction to be of minor importance. However, our approach represents a good compromise between the consideration of detector-specific fission fractions on the one side and the incorporation of the reactor-bump observed by

IBD experiments on the other side. Recap that only 25% of the total reactor antineutrino emission occurs at energies above 1.8 MeV, cf. Sec. 2.2.1.2. In the next paragraph we show that this is no problem in the present investigation since CEνNS is mainly sensitive to the highest neutrino energies. Caution is advised when EνeS is considered, cf. Sec. 4.1.3.

Further, we use the covariance matrix provided by Ref. [194] in order to account for the bin-to-bin correlation of the obtained spectra, when we investigate the impact of shape variation on the expected number of CEνNS events. Again, deviations between the fission fractions of Ref. [194] and the ones provided by the KBR simulation are neglected at the level of this investigation. Since the provided covariance matrix is deduced from spectral measurements via the detection of IBD, it still incorporates the corresponding cross section, cf. Ref. [194]. Therefore, we have to divide it by the IBD cross section which we adapt from Ref. [149]. To match the binning of the covariance matrix, we interpolate and evaluate the first bin of the compiled CONUS spectra at the corresponding bin center. We keep the full uncertainty of the last energy bin (ranging in the Daya Bay spectrum from 8.125 − 12 MeV) to account for the sensitivity of CEνNS towards higher neutrino energies in order to stay conservative.

With all these information at hand, we are able to assemble the reactor antineutrino emission spectra for the CONUS data sets, which consists of the reduced reactor fluxes (Tab. 3.4) and the spectral distribution, which is obtained by summing the individual isotope spectra according to the underlying fission fractions and multiplication with corresponding bump-correction factors. The spectral distribution including the reactor-bump is illustrated for data collection period C1R1 in the upper plot of Fig. 3.4. We indicated an uncertainty band by sampling antineutrino spectra from the underlying covariance matrix (the shown band corresponds to a 3σ variation in each bin). In our analysis, the reactor antineutrino spectra are used to weight the CEνNS cross section with the number of neutrinos emitted from the reactor,

$$\frac{d\bar{\sigma}}{dT_A}(T_A) = \int_{E_{\text{min}}}^{E_{\text{max}}} dE_\nu \left(\frac{dN}{dE_\nu}(E_\nu)\right)\left(\frac{d\sigma}{dT_A}(T_A, E_\nu)\right) , \tag{3.4}$$

with (dN/dE_ν) being now the fully assembled reactor antineutrino spectra, for example of Fig. 3.4. Note that the minimal energy E_{min} is obtained by inversion of Eq. (2.30),

$$E_{\text{min}} = \frac{T_A}{2}\left(1 + \sqrt{1 + \frac{2m_A}{T_A}}\right) , \tag{3.5}$$

while at a reactor site the maximal neutrino energy is assumed to be $E_{\text{max}} \lesssim 10\,\text{MeV}$.

The influence of spectral uncertainties was estimated by sampling reactor spectra a multi-dimensional Gaussian distribution and calculating the impact on the expected number of events. The obtained distributions are again fitted with a Gaussian whose standard deviation gives an estimation of the uncertainty. As evident from the example of C1R1 in the lower plot of Fig. 3.4, spectral variations can have an impact of up to 10% on the signal's prediction, cf. App. C.1 for the other data collection periods. The reactor spectra indicated by orange lines (3σ variations) are selected for tests of spectral sensitivity in order to circumvent a fit of the whole spectrum. Although being the more precise way this would lead to a large increase in computation time, which is unnecessary when spectral sensitivity is not guaranteed.

CEνNS sensitivity to neutrino energy In the end, we clarify which part of the deduced reactor antineutrino spectra contributes the most to the expected number of CEνNS events. As clear from simple scattering kinematics, incident neutrino energy E_ν and resulting recoil energy T_A are linked, cf. Eq. (2.30) and Eq. (3.5) respectively. Hence, the spectral sensitivity of the expected number of events depends also on the obtained energy threshold of the used detectors, since lower detectable energies allow to probe lower incident neutrino energies. However, the situation is a bit more complex due to signal quenching, a topic discussed in the next section. At the moment we are only interested in the sensitivity to antineutrino energies assuming a certain energy threshold (and quenching factors).

To analyze it, the number of CEνNS events for the individual bin values of the CONUS antineutrino spectra are calculated and the corresponding contribution to the total number of events is determined. Our results are shown in Fig. 3.5 for detector C1R1 including all detector-specific contributions, e.g. detector response, lifetime and reduced flux. It is evident that the effect of signal quenching generally leads to higher event rates for larger k-parameters. Further, one recognizes that CEνNS is mainly sensitive to higher neutrino energies which unfortunately also exhibit the largest uncertainties.[3] From a different viewpoint, CEνNS can be used as a flavor-independent tool to measure (or at least constrain) the high energetic part of a reactor's antineutrino emission spectrum. This, however, requires a signal with a sufficient level of statistics since antineutrino emission at these energies is already quite low, as evident from the assembled reactor antineutrino spectra, cf. Fig. 3.4.

3.2.2 Quenching effects in germanium for low nuclear recoil energies

Now that we have antineutrino emission spectra at hand, we continue the path towards a realistic CEνNS prediction by incorporating more detection-specific corrections. Before actual detector-specific responses are applied, the conversion of nuclear recoil energy T_A to the actual detectable energy E, i.e. ionization energy in the case of semiconductor detector, needs to be quantified. This is done via the so-called QF, cf. Sec. 2.1.4. So far, we only assumed constant, energy-independent quenching. However, in reality the matter is more involved and depends on several aspects, e.g. the target material or the nuclear recoil energy itself. Further impacts of detector temperature and electric field in the detector's interior are under discussion, cf. Ref. [254].

In our investigation, we apply an energy-dependent description of the quenching factor based on the so-called Lindhard model [168, 255].

---

[3] This analysis is already carried out with reactor antineutrino spectra that are attributed with simulated spectra at neutrino energies below $\sim 1.8\,\text{MeV}$, cf. Chapter 4. This part becomes crucial when EνeS is considered. The low energy part of the spectrum is irrelevant for CEνNS as the calculated spectral distributions in Fig. 3.5 reveal.

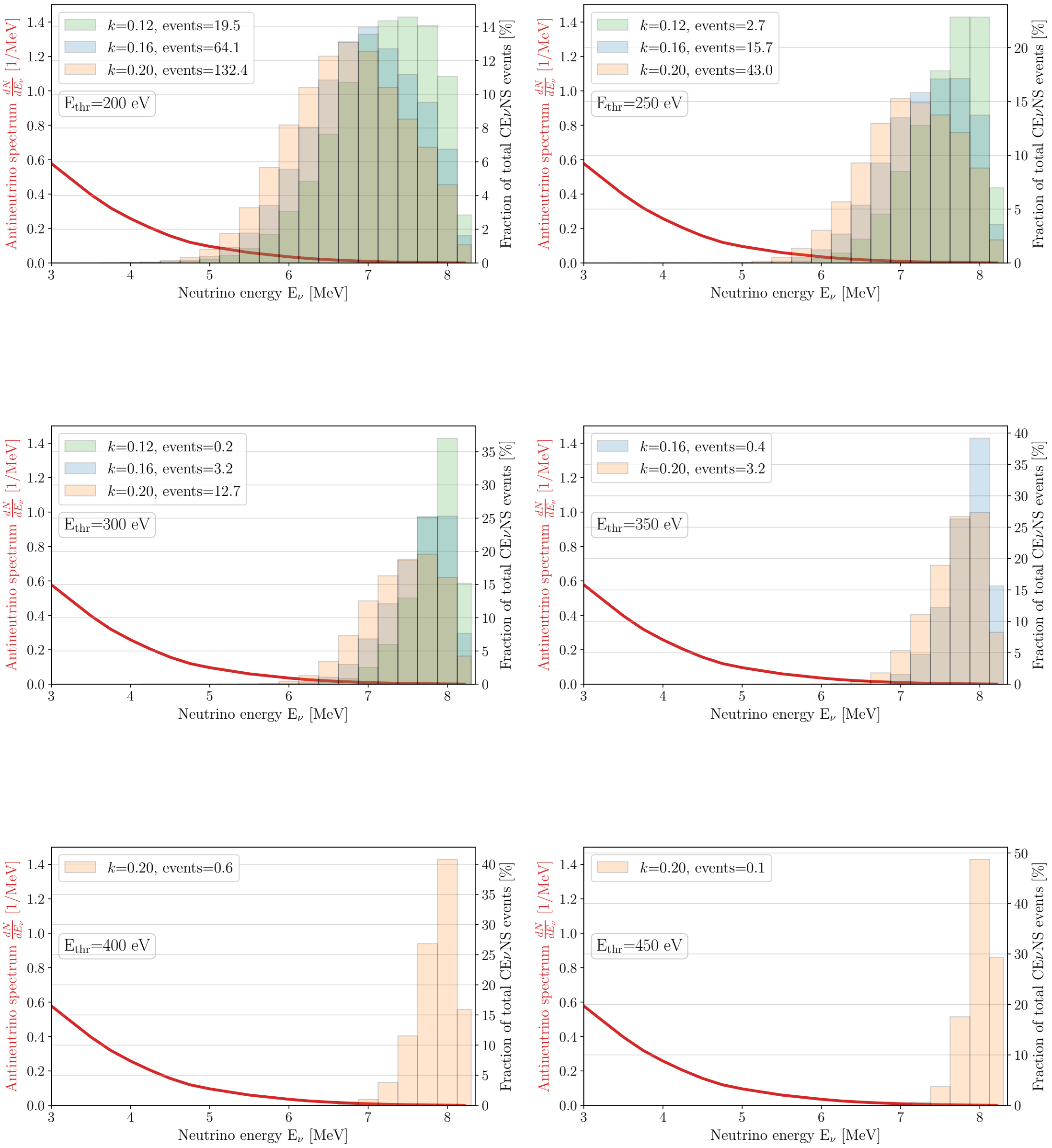

Figure 3.5.: Spectral contribution of the neutrino energy E_ν to the obtained number of CEνNS events for different quenching parameter k in dependence of the assumed minimal detectable energy, i.e. the energy threshold. The given values correspond to realistic predictions for data collection period C1R1 and are calculated with the corresponding CONUS antineutrino spectrum.

It is a semi-empirical description of radiation effects in matter that is widely used,

$$\mathrm{QF}(\epsilon) = \frac{k \cdot g(\epsilon)}{1 + k \cdot g(\epsilon)}\,, \tag{3.6a}$$

$$g(\epsilon) = 3\epsilon^{0.15} + 0.7\epsilon^{0.6} + \epsilon\,, \tag{3.6b}$$

$$\epsilon = 11.5 Z^{-7/3} T_A\,. \tag{3.6c}$$

Here, the k-parameter is almost equal to the QF for $T_A \sim 1\,\mathrm{keV}$. We apply a refined version of this model, which is extended with an (adiabatic) correction factor [256],

$$F_{\mathrm{AC}} = 1 - e^{-T_A/\xi}\,, \tag{3.7}$$

and use the recently measured values by Ref. [169], in particular the best-fit value $\xi = 160$. However, for simplicity we assume the thickness of the dead and passivation layers to be negligible, such that we can ignore the charge collection efficiency used in Ref. [169]. Since the quenching effect is still subject of recent investigation and has remained quite unknown at lowest nuclear recoil energies until just recently, cf. Figs. in Refs. [168, 169], we keep it as an explicit parameter throughout our investigations, i.e. we perform our analysis for fixed k-values within a reasonable range, cf. App. C.3.

To implement the modified Lindhard description, we perform a variable transform from recoil energies T_A to ionization energy E by following Ref. [170],

$$\frac{d\bar{\sigma}}{dE}(E) = \left(\mathrm{QF}^{-1}(E) + E \cdot \left(\frac{d}{dE}\mathrm{QF}^{-1}\right)(E)\right) \frac{d\bar{\sigma}}{dT_A}(\mathrm{QF}^{-1}(E) \cdot E)\,, \tag{3.8}$$

with $\mathrm{QF}^{-1}(E)$ being the inverse quenching factor of Eq. (3.6) in terms of the detectable energy E with its dependence on the k-parameter implicitly assumed.

The impact of the quenching effect on the expected number of CEνNS counts in dependence of the k-parameter and the minimal detection threshold is shown in Fig. 3.6 using the example of detector C1R1 with all experimental responses already considered. A realistic (optimistic) energy threshold of $E_{\mathrm{thr}} = 300\,(270)\,\mathrm{eV}$ and with recent indications for the k-parameter to be $k = 0.16$ [257], one expects $10\,(30)\,\mathrm{kg}^{-1}\,\mathrm{yr}^{-1}$. With realistic background levels of $\mathcal{O}(10)\,\mathrm{kg}^{-1}\,\mathrm{d}^{-1}$, signal-to-noise levels of $3\,(8) \cdot 10^{-3}$ can be obtained. Thus, a precise measurement of the QF is needed in order to give appropriate theoretical predictions of CEνNS in the SM context. It might further affect BSM investigations that search for potential modifications of the expected CEνNS signal [258]. Furthermore, the effect of quenching on the CEνNS event spectrum of C1R1 is shown for different k-parameters in App. C.4.

3.2.3 Electronic response

For a realistic signal prediction, we have to incorporate the detector-specific responses which have been investigated at MPIK as well as KBR and published in Ref. [82]. Here, we assume properties like detector energy scale and resolution as well as detection efficiencies as being exact, while in the analyses below uncertainties for some of these characteristics are taken into account. Hence, for the (theoretical) signal prediction these (experimental)

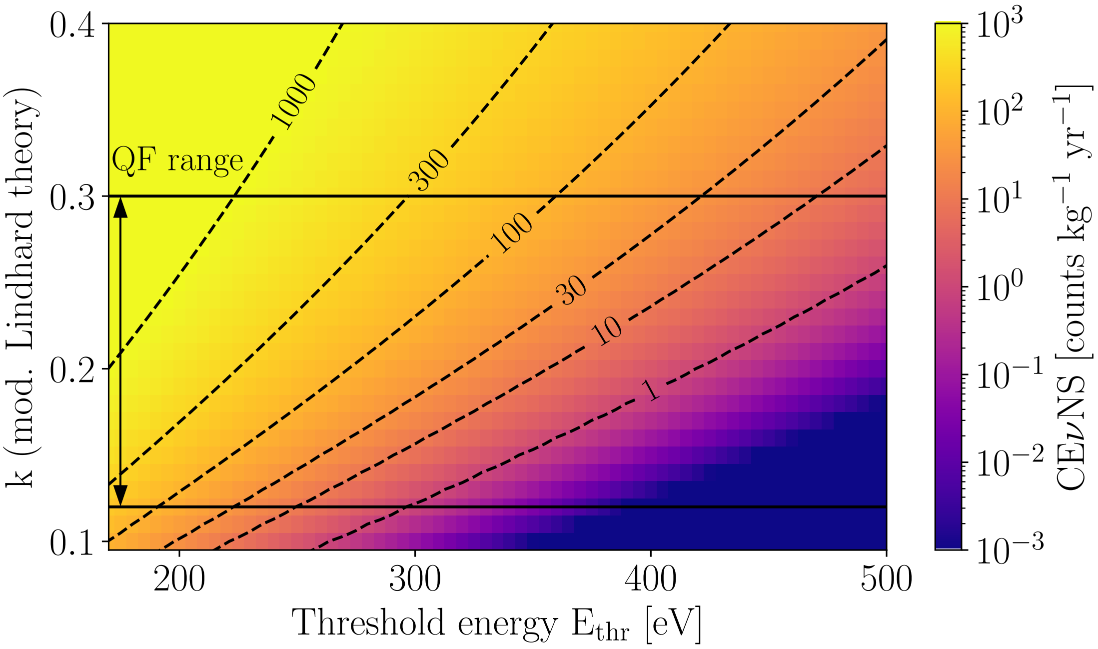

Figure 3.6.: Expected CEνNS count rates for detector C1R1 in dependence of its minimal threshold energy E_{thr} and the k-parameter of the applied modified Lindhard model, cf. Eqs. (3.6). Black horizontal lines indicate QFs that have been reported in literature. The figure has been published in Ref. [82].

quantities are not attributed with any uncertainty. Three detector properties are of main relevance for our prediction: the detector's energy scale calibration, its energy resolution and efficiencies introduced by the DAQ or the muon veto system.[4]

Energy scale calibration The energy scale, i.e. the mapping between DAQ detection channels and energy values, for the collected data is set by selecting points of known energy and an assumption of how the DAQ's read-out channels are mapped to these energies, e.g. a linear relation. Furthermore, linearity of the energy scale can be verified with pulser scans. At higher energy ($\gtrsim 50\,\mathrm{keV}$), usually external radiation of well-known sources is used, e.g. ^{241}Am, ^{133}Ba, ^{57}Co, ^{228}Th. However, at lower energies, especially the ones relevant for CEνNS, electromagnetic radiation cannot penetrate the detector's interior. A solution is to use the detector's intrinsic radiation, i.e. x-rays from radioactive decays occurring inside the HPGe crystal. Well suited for germanium, are x-ray lines that correspond to binding energies of K- (9.0, 9.7 and 10.4 keV) and L-shells (1.1, 1.2, 1.3 keV) from ^{65}Zn, ^{68}Ga, ^{68}Ge+^{71}Ge, in particular since the intensities of the weaker L-shells can be derived from K-shell decays and well-known K/L-ratios, cf. Ref. [82, Table 7]. We refer to App. C.5, where the situation is illustrated in an ionization energy spectrum of detector C2. These isotopes are permanently created by comic activation, e.g. through hadronic components. Although the CONUS shield design is able to suppress hadronic

---

[4] When we refer to efficiency from now on, we mean the (combined) efficiencies related to detector dead times induced by both the DAQ and the muon veto.

cosmic rays by several orders of magnitude, the intense cosmic muon flux at shallow depth creates MeV-neutrons which induce the isotope ^{71}Ge related to this lines. This steady-state background production, potentially harmful for CEνNS detection, is advantageous in terms of energy calibration and contributes ~ 15 counts $\mathrm{kg}^{-1}\,\mathrm{d}^{-1}$ to the background level of all detectors. For the CONUS detectors linearity of the energy scale is confirmed with an energy calibration exhibiting an uncertainty of $10-20\,\mathrm{eV}$ [82, Section 5.2].

Energy resolution The energy resolution of a detector can be determined directly via the FWHM of known and prominent lines or externally via the usage of known (preferable mono-energetic) x- and/or gamma ray sources. The injection of artificially generated pulses directly enables gathering information on the noise induced by the experimental environment or the used electronics. This procedure is quite independent of detector characteristics which might depend on the applied source. The design specifications of pulser signal resolutions to be below 85 eV are confirmed at both MPIK and KBR. Further, the pulser resolution have been determined in dependence of the energy.

In our theoretical signal prediction, energy resolution is taken into account by a convolution of the expected signal with a Gaussian of width σ. Hereby, the width $\sigma(E) = \mathrm{FWHM}(E)/2.355$ is considered to be energy-dependent as confirmed by x- and γ-ray lines at different energies. The latter is parameterized by the following functional form

$$\mathrm{FWHM}(E) = p_0 + 2.355\sqrt{p_1 \cdot 2.96 \cdot 10^{-3}(E - p_2)}\,, \tag{3.9}$$

with the detectable energy E given in keV and $p_{0,1,2}$ being detector-specific coefficients determined before experimental operation. In our analysis, the discrete convolution is performed via matrix multiplication with a so-called Toeplitz matrix, which is due to the non-constant width in our case much faster than the usual Fast-Fourier transform algorithm [259, 260].

Detection efficiency For the CONUS set-up (applying the Lynx DAQ), generally two types of detection efficiency are relevant, which are related to dead times induced by the DAQ and the muon veto, respectively. The first type is caused by the DAQ's processing time of detected events and influenced by the amount of triggered noise and physical events. For the CONUS detectors, the related efficiency usually drops for physical events below 200 eV, while already at energies below 350 eV electronic noise events are present next to physical events. The detection efficiency has been determined by pulser scans at different energies and fitted with a Gaussian CDF, cf. Ref. [82, Figure 12]. In RUN-2, for example, efficiencies of $\epsilon > 99\%$ down to $\sim 200\,\mathrm{eV}$ are observed such that we can safely approximate them with unity in the region of interest (ROI). RUN-1 exhibits efficiencies higher then 95% above 200 eV, which we account for by implementing the determined efficiency curves. For more details can be found in Ref. [82, Section 5.4].

The second type of efficiency is caused by the muon veto system, which interrupts data collection whenever a cosmic muon is detected in the shield's polyethylene plates. It has been noted that gamma rays from ^{16}N decays in a near cooling circuit affect the muon-veto's trigger rate, such that we distinguish efficiencies for reactor ON (94.2%) and reactor OFF (96.5%) periods. Both efficiencies are multiplied with the expected signal spectrum.

3.2.4 Theoretical CEνNS prediction and contributing uncertainties

Now that we have illustrated the individual steps towards a realistic signal prediction, we summarize how the final values used in the data analysis of the next section are calculated. In addition, we also list all uncertainties that are incorporated on the "prediction errors" which we assign to our results.

To obtain a realistic signal prediction for a certain CONUS detector, we have to average the CEνNS cross section (Eq. (2.31)) with the corresponding antineutrino reactor spectrum (Eq. (3.4)). As a next step, the effect of signal quenching that we describe via a modified version of the Lindhard model (Eqs. (3.6)) is taken into account (Eq. (3.8)), before we apply the individual detector responses to the flux-averaged and quenched cross section (Sec. 3.2.3). Finally, multiplying the obtained expression with further multiplicative quantities like detector runtime t (Tab. 3.6), reduced reactor flux Φ^* (Tab. 3.4) and the number of target nuclei N^{Ge},[5] allows to calculate the number of CEνNS events in a certain energy bin,

$$N_x^{\mathrm{CE\nu NS}}(E_i) = t_x \cdot \Phi_x^* \cdot N^{\mathrm{Ge}}(m_x)\Delta E_x \left(\frac{d\sigma}{dE}\right)_x (E_i)\,, \tag{3.10}$$

with ΔE_x being the detector bin width and the indices i and x indicating the bin number and the considered detector, respectively.

We start with the CEνNS cross section that includes a form factor, whose consideration depends on the energy of the (anti)neutrino source. At lowest momentum transfer the form factor in the CEνNS cross section of Eq. (2.31) can be approximated with unity, e.g. in the case of reactor antineutrinos, which we assume in what follows and further neglect corresponding uncertainties. The situation is different for neutrinos with higher energies, e.g. from a π-DAR source, where a form factor is needed in order to account for partial losses in coherence. As we have seen in Sec. 2.1.3, the actual form factor depends on the underlying charge distribution and is, therefore, model-dependent. The authors of Ref. [261] investigated the impact of uncertainties that came along with the three commonly selected parameterizations listed in App. A.3 and concluded them to be only relevant for $q \gtrsim 20\,\mathrm{MeV}$. Hence, they are negligible in the context of reactor or solar (anti)neutrinos. Further, they state form factor uncertainties to be at the percentage-level and generally to be independent of the applied parameterization.

Since the Weinberg angle at low energy is quite uncertain (compared to measurements at the Z-pole) and CEνNS provides a certain (however mild) sensitivity to it, we account for corresponding uncertainties, i.e. we use $\sin^2\theta_W = 0.2384 \pm 0.0046$ (MeV energy) taken from Ref. [262]. Further uncertainties on quantities in the CEνNS cross section are assumed to be of minor importance.

Uncertainties underlying the CONUS antineutrino emission spectra are among the most important ones, as they influence both the signal's absolute magnitude as well as its

---

[5] The number of scattering targets is given by $N(m) = \frac{m}{M}N_A$, with the detector active mass m (cf. Tab. 3.1), the target material's molar mass M and the Avogadro constant N_A.

Contribution	Value(s)	Uncertainty
thermal power	Tab. 3.4	$\Delta P = 2.3\%$
energy release per fission	Tab. 3.3	Tab. 3.3
distance to reactor core	$L = 17.1\,\mathrm{m}$	$\Delta L = 0.1\,\mathrm{m}$
fission fractions	Tab. 3.2	Eq. (3.3)
reduced fluxes	Tab. 3.4	Tab. 3.4
spectral shape	e.g. Fig. 3.4	Ref. [194]

Table 3.5.: Overview of relevant quantities that underlie the CONUS antineutrino reactor spectra and their uncertainties. Within our parameterization of Eq. (3.1), they separate into the reduced reactor fluxes or the spectral shape. Uncertainties of these quantities migrate to corresponding uncertainties on the theoretical signal prediction.

shape. Recall the signal's sensitivity towards higher neutrino energies, which unfortunately are also the most uncertain ones, cf. Fig. 3.5. A summary of all uncertainties that are incorporated in the theoretical signal prediction is given in Tab. 3.5.

Since the signal prediction is highly sensitive to the value of the k-parameter, cf. Fig. 3.6, that is still subject of large uncertainties [168, 169], we leave it explicit in our calculations and analyses. Last but not least, uncertainties of the number of scattering targets, cf. Eq. (3.10), are deduced from the uncertainties of the detector active masses, cf. Tab. 3.1, while we assume uncertainties of detector runtimes to be negligible.

In summary, all considerations of the section allow us to make realistic and specifically adjusted CEνNS predictions for all data collection periods that are analyzed in the following. The obtained events spectra are additionally used as inputs for the CEνNS analysis scheme of Dr. Janina Hakenmüller. Through a detailed assessment of the underlying uncertainties, we are able to provide theoretical errors to our assumptions. These values are used to confront the outcome of the statistical data analysis with a realistic signal expectation, cf. Fig. 3.9.

3.3 Constraints on CEνNS in the fully coherent regime

After a general introduction of the CONUS set-up and an illustration of how a CEνNS signal prediction is obtained, we are prepared to cover the spectral analysis of the first two CONUS data collection periods that is published in Ref. [70]. Characteristics of the collected data sets are presented as well as an overview of the applied background prediction provided by Dr. Janina Hakenmüller [239] is given. The experimental characteristics with their uncertainties were provided by the CONUS Collaboration, while the core analysis team consisting of Dr. Janina Hakenmüller, Dr. Thomas Hugle and the author himself, independently developed two analysis schemes that were mutually checked on a regular

Analysis	Data set	On [kg d]	Off [kg d]	ROI [keV]
SM	C1R1	96.7	13.8	0.296 - 0.75
	C2R1	14.6	13.4	0.311 - 1.00
	C3R1	97.5	10.4	0.333 - 1.00
	C1R2	19.6	12.1	0.348 - 0.75
	C3R2	20.2	9.1	0.343 - 1.00
	All	248.7	58.8	

Table 3.6.: Detector exposures and ROIs in the first two CONUS data collection periods.

basis.[6] In the following, the more phenomenologically oriented analysis routine developed by Dr. T. Hugle and the author is described in detail, before the first spectral CEνNS limits from the CONUS experiments, derived with both analysis routines, are presented.

3.3.1 Conus data collection

After commissioning in the beginning of 2018, the data collection period started with the first collection of reactor Off data within the reactor outage from 31 March to 07 May 2018. Subsequently, the collection of reactor On data started from 8 May 2018 to 07 June 2019 with an additional opportunity to collect more Off data in the outage from 08 June to 09 July 2019. These data sets are split into different periods (from now on called "runs") which was necessary due to different DAQ setting and noise levels. Hereby, each run is attributed its own reactor Off period to ensure most stable environmental conditions at the experimental site. Remember that both data sets of C4 as well as data collection period C2R2 were excluded due to artifacts and incompatible DAQ settings, respectively.

For each detector's minimal energy threshold, three different criteria were applied: trigger efficiencies above 95%, no correlation with (ambient) temperature and a ratio between electron noise and MC background above a factor of 4 to not include data dominated by electronic noise events. The ROIs' higher end was limited to ~ 1 keV due to the L-shell x-ray lines around $1-1.3$ keV and since the CEνNS signal does not reach that far in energy. Since detector C1 exhibits a local artifact an even lower value, i.e. ~ 750 eV, was selected which is still way above the CEνNS signal region. It was tested that the exact choice has no influence on the determined results and an overall energy bin width of about 10 eV was selected. The individual ROIs of each detector are listed in Tab. 3.6.

Although maintaining stable experimental condition so close to a reactor core turned out be quite challenging, "almost-lab" conditions were established, cf. Ref. [82, Table 11]. For instance, power-correlated radiation background (fission neutrons or gamma radiation from ^{16}N decays in primary cooling cycle close to room A-408), vibrations originating from steam generators, rising temperatures and radon level in outages turned out to be most demanding. However, counteraction like careful monitoring of experimental parameters,

---

[6] At this point, the good cooperation and the joint effort during the entire investigation needs to be emphasized!

improvement of environmental conditions and auxiliary measurements, e.g. measurements with seismographs and tests, in which artificial sounds were induced inside room A-408, helped to overcome these issues. Further, stability of detector properties (energy scale and stability) was verified with different methods. Occurring noise-temperature correlations at the noise edge close to the CEνNS ROI were identified and safely removed by excluding such data and establishing more stable temperature conditions. This led to a large loss of exposure, but allowed for stable experimental conditions above 200 eV. In addition, investigation of the time difference distribution between single events turned out to be beneficial in terms of discriminating physics events from noise and further spurious events. Appropriate cuts helped to improve the energy region above the noise edge, cf. Ref. [82, Figure 13]. More details about the data processing can be found in Ref. [239].

In the end, data sets with similar room temperature and detector noise levels between reactor On and Off were selected by our experimental colleagues and are used in the following analysis. The corresponding exposures can be found in Tab. 3.6.

3.3.2 Background contributions and modeling

In our analysis, the theoretical background description is divided into two parts: an experimental fit of the detector noise and a dedicated MC simulation of all important background components. Now, we give an overview of the different background contributions and investigations during its assessment, whereby we point to Ref. [239] for a full background decomposition assisted with MC simulations. The overall background stability is checked in two different energy regions, i.e. $E_1 = [0.4, 1.0]$ keV and $E_2 = [2, 7]$ keV, while we focus here only on E_1 where detector-specific background levels of $5 - 13\,\mathrm{kg}^{-1}\,\mathrm{d}^{-1}$ were obtained [82].

3.3.2.1 Reactor-uncorrelated background contributions

The dominating background component that is uncorrelated to the reactor thermal power are events attributed to the cosmic muon flux. Both at MPIK and KBR interactions of cosmic muon inside the CONUS shield or the surrounding environment induce prompt or delayed background events at a level of 160 ± 10 counts $\mathrm{kg}^{-1}\mathrm{d}^{-1}$. The muon veto exhibits efficiencies of $\sim 97\%$ and thus allows a reduction down to to $5-13$ counts $\mathrm{kg}^{-1}\mathrm{d}^{-1}$. Further, the decay of induced isomeric germanium states contributes additional background at a level of < 0.1 counts $\mathrm{kg}^{-1}\mathrm{d}^{-1}$. Seasonal or barometric variations that affect the cosmic muon flux do not create significant differences between the background levels of reactor On and Off periods.

Further background events originate from the decays of the radioisotope ^{210}Pb which contribute a rather constant contribution due to its long half-live of 22.3 yr. Although within the CONUS shield the radiopurity of the used lead bricks increases towards the detector chamber, a background level of $2 - 7$ counts $\mathrm{kg}^{-1}\mathrm{d}^{-1}$ originates from this component.

Radon and its progenies emanating from the reactor building's concrete walls can penetrate the experimental set-up and decay in its interior. Thus, the radon concentration in room A-408 is permanently monitored and the CONUS detector constantly flushed with breathing air bottles, in which the air has been stored for at least 2-3 weeks. This period is long enough for the radon to decay away (half life $T_{1/2} \sim 5\,\mathrm{d}$). The average radon level of $(175 \pm 35)\,\mathrm{Bq\,m^{-3}}$ results, despite all counteractions, in a background level of $0.9\,\mathrm{counts\,kg^{-1}d^{-1}}$.

The achieved overburden at the CONUS site effectively shields against (almost) all hadronic cosmic ray component, such that associated background events basically reflect each detectors activation history besides small in-situ production rate of ^{71}Ge. The created cosmogenic isotopes (^{71}Ge, ^{68}Ge, ^{3}H) lead to a background component that is expected to decrease over time, but on average induces $0.2 - 0.4\,\mathrm{counts\,kg^{-1}d^{-1}}$.

Further background contributions from natural radioactivity, i.e. gamma rays and (α,n) reactions in the walls, are confirmed to have a negligible impact. In addition, MC simulations confirmed that neutrons or neutrinos emitted from the spent fuel storage pool above the experiment at site, cf. Fig. 3.1, can be neglected as well [244].

3.3.2.2 Reactor-correlated background contributions

Critical events of CEνNS investigations at a reactor site are time-varying and, as CEνNS itself, correlated to the reactor thermal power ("reactor-correlated"). Potential candidates are fission neutrons that can escape the reactor core or gamma radiation from neutron induced-isotopes that decay inside the primary cooling loop in the proximity of room A-408, e.g. ^{16}N. Most critical are reactor-correlated neutrons since they can mimic potential CEνNS signals in the detectors. Hence, a good understanding of such neutron-induced background components is crucial for any CONUS-like experiment located close to a reactor core.

A detailed investigation of reactor-correlated neutron and gamma ray fluxes was performed prior to the experiment's commissioning, cf. Refs. [239, 240]. In cooperation with the Physikalisch-Technische Bundesanstalt (PTB) precision neutron spectroscopy was done at the CONUS experimental site at KBR, which included direct neutron measurements with Bonner spheres, indirect neutron measurements with HPGe detectors (via gamma rays from neutron capture in the shield or the detector and thermal neutrons) in combination with a sophisticated multi-step MC simulation of reactor neutrons as validation. The investigation revealed the presence of a neutron fluence composed of 80% thermal neutrons and 20% neutrons with below-MeV energies. The simulation confirmed an overall neutron suppression (during propagation from the reactor core to the location of the CONUS set-up) of about 20 orders of magnitude [240, Section 5]. Further, no fast neutron emission from the spent fuel storage pool could be confirmed. Since the reactor-correlated neutrons are fully mitigated by the CONUS shield, i.e. the corresponding background level is two orders of magnitude smaller than the muon-induced neutron background, this potentially problematic background component is of negligible impact for the CONUS investigations.

Additionally, gamma rays from ^{16}N decays are almost shielded by the lead layers of the CONUS shield and are of minor importance, i.e. $0.010 \pm 0.005\,\mathrm{counts\,kg^{-1}d^{-1}}$ at full reactor power.

3.3.2.3 Background modeling

Monte Carlo model The CONUS background model is provided by our colleague Dr. J. Hakenmüller, cf. Ref. [239, 244], in such way that we only need to multiply the detector-dependent models with the corresponding detection efficiency. The individual background contributions are simulated via MC techniques which is why we refer to them as MC (background) models. The whole MC background model with its individual components is compared to data in App. C.7. The most relevant contributions for the CEνNS and EνeS (following chapter) analyses are the internal ^{210}Pb contamination of the applied detector and shield materials as well as the cosmic muon-induced events in the shield material. Further, the cosmogenic induced K- and L-shell x-ray transitions at $\sim 10\,\mathrm{keV}$ and $\sim 1\,\mathrm{keV}$ are dominant at their explicit energy values. Cosmic muon-induced neutrons that are produced in the reactor building's concrete rise towards lower energies, though with a background level at least one order of magnitude smaller the corresponding shield events. In general, the provided spectra are in excellent agreement between reactor OFF data for energies $\gtrsim 100\,\mathrm{keV}$. Uncertainties on the MC background model are assumed to be negligible for the CEνNS ROI. For more details related to the background description, we refer to Ref. [239] or Ref. [244].

Threshold description Below 500 eV towards each detector's energy threshold, an additional background component related to electronic noise starts to rise towards lower energies and needs to be considered in our analysis.[7] Generally, the noise that broadens the width of detected lines, i.e. the resolution, influences the achieved detection threshold as well. It consists of several contributions, among others the electronic noise and and environmental vibrations, cf. Ref. [211, Section 5] and Ref. [239, Section 1.4.4.]. The first originates from noise of individual electronics components. The latter can be induced by vibrations of the reactor building, e.g. when cooling pumps are started or stopped, or when the detector cryocoolers compensate for varying environmental conditions. Consequently, avoidable contributions of both origins can be mitigated by guaranteeing cold and stable environmental conditions. As most components contributing to the detector resolution are of statistical origin, a Gaussian distribution can be expected [263], while distortions through the DAQ system might occur, cf. Ref. [239, Section 1.4.4.].

Within our analysis these noise contributions are treated as an individual detector-specific component. As is rises towards the detection threshold, we refer to it as "threshold description". This "threshold description" is assumed to be dependent on the data collection period and parameterized with an exponential function of the form

$$f_{\text{noise}}(E; p_0, p_1) = \frac{10^{p_0}}{p_1^2} \exp\left(-\frac{E}{2p_1}\right), \tag{3.11}$$

with E being the bin energy and the free parameters $p_{0,1}$ which are determined by our ML routines.

---

[7] This small paragraph is based on the content of Ref. [239, Section 1.4.4.].

3.3.2.4 Elastic neutrino-electron scattering (EνeS)

In principle, SM EνeS mediated by Z and W bosons contributes an additional signal that is given by the following cross section, cf. Ref. [1, Chapter 5.1] or Ref. [118],

$$\frac{\mathrm{d}\sigma}{\mathrm{d}T_e}(T_e, E_\nu) = \frac{G_F^2 m_e}{2\pi}\left[(g_V + g_A)^2 + (g_V - g_A)^2\left(1 - \frac{T_e}{E_\nu}\right) + \left(g_A^2 - g_V^2\right)\frac{m_e T_e}{E_\nu^2}\right], \quad (3.12)$$

with $g_V = \frac{1}{2} + 2\sin^2\theta_W$ and $g_A = -\frac{1}{2}$ in the case of electron antineutrino scattering off electrons in the target material. The electron recoil T_e, which does not undergo any signal quenching, can be directly read out with a semiconductor detector as the resulting ionization signal. However, the binding of electrons in the target atoms needs to be considered when the electron recoil energy T_e is of similar size. In doing so, we follow Ref. [264] and multiply Eq. (3.12) with a sum of step functions that accounts for the individual binding energies

$$R(T_e) = \frac{1}{32}\sum_i n_i \Theta(T_e - \epsilon_i)\,, \quad (3.13)$$

with i running over all electron binding levels, while n_i and ϵ_i being the number of electrons and the associated binding energy, respectively. The applied values are taken from Ref. [265]. The prefactor accounts for the total number of electrons in a germanium atom. Note that the formula for the maximum recoil energy (Eq. (2.30)) is also valid in this context when the nucleus mass is exchanged with the electron mass m_e. Compared to reactor antineutrino energies $\lesssim 10\,\mathrm{MeV}$, the electron mass is negligibly small such that the resulting recoil energy is similar to the neutrino energy, i.e. $T_e \sim 9.9\,\mathrm{MeV}$ (compared to a nuclear recoil in germanium of $T_A \sim 3\,\mathrm{keV}$). Moreover, for electron recoil energies in the keV-region that we probe with the CONUS set-up, neutrino-electron scattering is sensitive to similar neutrino energies E_ν, i.e. the lowest energy parts of the antineutrino spectra which we have not yet included, cf. Ch. 4.

However, comparing the cross-sections of CEνNS and EνeS, the latter is orders of magnitude smaller such that explicit event rates in the CONUS detectors are negligibly small cf. Fig. 1.1. For example, we expect about $84\,\mathrm{counts\,kg^{-1}\,yr^{-1}}$ from CEνNS ($k = 0.20$) and $< 1\,\mathrm{count\,kg^{-1}\,yr^{-1}}$ from EνeS in the data collection period C1R1. Thus, we can safely neglect this interaction channel in the following analysis.

3.3.3 Statistical investigation

After a summary of the CONUS data collection periods and the characteristics of the background (model) that we expect at the experimental site, we deal now with the analysis of the assembled data sets. We shortly list the considered experimental uncertainties and illustrate how they are implemented. Further, the technical aspects of the chosen ML approach, i.e. the form of the likelihood function and its numerical implementation, are explained as well as details are given of how the underlying test statistic is obtained. During the development of the analysis scheme, special emphasis was put on compatibility and extensibility, since it was already geared to incorporate further BSM-analyses at this stage of development. In such way, new interaction cross sections can be easily added to our investigation methods and studied with the same uncertainties that underlie the spectral CEνNS investigations.

3.3.3.1 Systematic uncertainties

Besides the parameters of interest, i.e. the signal strength of a CEνNS signal or the background normalization, parameters that have been determined during the experiment's commissioning or by auxiliary measurements are usually treated as nuisance parameters, cf. Sec. 2.3.1.4. Thus, they are determined from data, while they are constrained via a pull-term which incorporates the previously determined parameter with its uncertainty. In doing so, we basically *let the data decide* which value agrees best since, within a Frequentist's point of view, we expect the determined quantity to be itself affected by statistical fluctuations.

In this analysis, such parameters are each detector's active mass (determined at MPIK, cf. Tab. 3.1), the detection efficiencies and energy scale calibration (cf. Sec. 3.2.3) or the detector-specific reduced reactor fluxes (cf. Tab. 3.4). Uncertainties on the detector runtimes are assumed to be negligibly small, cf. Tab. 3.6. The MC background model is attributed with a free parameter b to determine its overall normalization via the fit routine.

In principle, one could also incorporate uncertainties on fundamental constants, such as the Fermi constant G_F or the Weinberg angle $\sin^2\theta_W$, which are currently still subdominant compared to the experimental uncertainties. Also the spectral uncertainties of the constructed antineutrino emission spectra could be implemented via the refined covariance matrix, cf. Sec. 3.2.1. However, as predictions with the achieved experimental specification already indicate only a few number of events, we do not expected strong sensitivity on the individual reactor bin energies. In practice, the 26 additional parameter of the reactor antineutrino spectrum are simply set to their best-fit values within the fitting routine due to the associated pull-term though at the cost of rather high computation time (already in the case of only one detector). At several stages in the development phase of our analysis routine, the impact of spectral uncertainties have been checked for single-detector fits, e.g. C1R1, and found to be of minor importance. We circumvented this issue, by selection of MC-generated test spectra that lead to strong deviations, cf. Fig. 3.4, and verified this by the independent analysis routine of our colleague Dr. J. Hakenmüller. Likelihood fits that used such reactor spectra showed negligible deviation from their best-fit values. Hence, in what follows we neglect uncertainties related to the reactor model and fix corresponding bins to their mean values.

The energy scale calibration, cf. Sec. 3.2.3, was confirmed to be stable within the data collection periods. However, the uncertainties on the energies of the K- and L-shell x-ray lines due to the low count rate, especially at $\sim 1\,\mathrm{keV}$, induce an uncertainty on the energy scale of $\sim 15\,\mathrm{eV}$ in the ROI. As mentioned in Sec. 3.2.3, the electronic detection efficiency is a combination of the efficiencies induced by the muon veto system and the actual trigger efficiency of the DAQ. The dead time induced by efficiencies of the muon veto are determined to be $(5.8 \pm 0.2)\%$ (reactor ON) and $(3.5 \pm 0.2)\%$ (reactor OFF). Further, trigger uncertainties are determined to by 5% in RUN-1 and 1% in RUN-2 [82]. As a consequence overall uncertainties on the efficiency are calculated to be 5% (RUN-1) and 1% (RUN-2), respectively.

Parameter	Uncertainty or related parameter
background MC	b (free parameter)
noise threshold	Θ_{thr_1}, Θ_{thr_2} (free, uncertainty considered via toy MC)
reduced neutrino flux $\Delta\Phi^*$	$\sim$3%
neutrino spectrum	subdominant uncertainty (compared to quenching)
reactor ON and OFF duration	negligible uncertainty
active mass	$< 1\%$
electronic detection efficiency c_{eff}	$\leq 5\%$
energy calibration uncertainty ΔE	15 eV
quenching	k (explicitly included)

Table 3.7.: Overview of the fit parameters that enter the likelihood function with their corresponding uncertainties for the present analysis.

The QF, or correspondingly in our implementation the k-parameter, is the dominating uncertainty of our analysis. Hence, we decided to perform our investigation explicitly for fixed k-values that spread the range of measured quenching values, i.e. $k \in [0.1, 0.3]$ [168, 169, 266–270].[8] On overview of the fit parameters underlying our ML approach with given uncertainties is shown in Tab. 3.7.

3.3.3.2 Likelihood function and implementation

In what follows, we present the technical details of the performed data analysis such as the explicit form of the likelihood function and its numerical implementation. A binned likelihood approach is chosen, in which we assume the number of detected events to follow a Poisson distribution in each bin. The reactor ON data are fitted in a typical “signal + background” fashion, where we extract the amplitude of the CEνNS signal via an unconstrained fit parameter s that represents a signal normalization. A similar (normalization) parameter b is ascribed to the overall MC background model, whereas two additional fit parameters are needed for the effective analytic description of the electronic noise, cf. Eq. (3.11).

In addition, we simultaneously fit the reactor OFF data with a background-only hypothesis which introduces an additional “lever” on parameters solely related to the background description. The previously introduced nuisance parameters are constrained with four Gaussian pull-terms that are added to the likelihood function.

---

[8] Remember that the k-parameter in the energy-dependent description of Lindhard represents the quenching factor QF at nuclear recoil energies of $T_A \sim 1\,\mathrm{keV}$.

In conclusion, the overall likelihood function that is fit to data exhibits the form

$$-2\log\mathcal{L} = -2\log\mathcal{L}_{\mathrm{ON}} - 2\log\mathcal{L}_{\mathrm{OFF}} + 2\sum_i \frac{(\Theta_i - \Theta_i^*)^2}{2\sigma_i^2}\,, \tag{3.14a}$$

$$\text{with } -2\log\mathcal{L}_{\mathrm{ON}}(s, b, \Theta_{\mathrm{thr}_{1,2}}, \Theta_{\mathrm{reactor}}, \Theta_{\mathrm{det}}, \Theta_{\Delta\mathrm{E}})\,, \tag{3.14b}$$

$$-2\log\mathcal{L}_{\mathrm{OFF}}(b, \Theta_{\mathrm{thr}_{1,2}}, \Theta_{\mathrm{det}}, \Theta_{\Delta\mathrm{E}})\,, \tag{3.14c}$$

with the parameters s, b, Θ_{thr_1}, Θ_{thr_2} being non-negative quantities that are determined without any constraints. Here, $\Theta_{\mathrm{reactor}}$ basically are the detector-specific reduced fluxes Φ_x^* and the corresponding pull-term reflects all uncertainties listed in Tab. 3.5 (except the spectral ones as previously explained). Further, Θ_{det} represents all detector-related multiplicative quantities such as its active mass m_x and the combined efficiency induced by the DAQ and the muon veto $\epsilon^{s,b}$ for reactor ON and reactor OFF periods. The uncertainty on the latter are accounted for by introducing an artificial parameter c_x^{eff} which is "pulled" to unity with the respective uncertainties of RUN-1 and RUN-2. The parameter $\Theta_{\Delta\mathrm{E}}$ is attributed to the energy scale uncertainty, which we implement as a shift in energy of the theoretical prediction. Since we assume the number of total events to be affected by statistical fluctuations as well, we are in the case of an extended ML approach, such that the individual likelihood functions in Eqs. (3.14) exhibit the form[9]

$$-2\log\mathcal{L} = 2\sum_i \nu_i - n_i\log\nu_i + \log n_i!\,, \tag{3.15}$$

while n_i being the provided data in bin i and ν_i the corresponding theoretical predictions, cf. Eq. (2.41). Note that the latter term is irrelevant for minimization purposes.

The free parameters mentioned above are incorporated in the theoretical prediction of the expected CEνNS spectrum of detector i

$$\begin{aligned} N_i^{\mathrm{ON}}(E) &= s\cdot N^{\mathrm{CE}\nu\mathrm{NS}}\Big(E - \Delta E_i;\ \Phi_i^*, m_i, t_i, c_i^{\mathrm{eff}}, (dN/dE_\nu)_i\,, k\Big) \\ &\quad + b_i\cdot\left(\frac{t_{\mathrm{ON,i}}}{t_{\mathrm{OFF,i}}}\right) c_i^{\mathrm{eff}}\epsilon_i^s(E)\,\Big(f_i^{\mathrm{noise}}(E; p_{0,1}) + f_i^{\mathrm{mc}}(E - \Delta E_i)\Big)\,, \end{aligned} \tag{3.16}$$

with $N_{\mathrm{CE}\nu\mathrm{NS}}$ being the function that provides the expected CEνNS spectrum with all its functional dependencies. The detector runtime (collected time of reactor ON period) is represented by t_i and detector-specific antineutrino emission model by $(dN/dE_\nu)_i$. The fixed quenching parameter of the modified Lindhard model is indicated with the parameter k. Since the provided background MC simulations f_i^{mc} are designed to describe the reactor OFF data, we have to rescale them to the corresponding reactor ON lifetimes. Note that some energy-dependent functions receive a shift in energy by ΔE, e.g. the electronic noise description f_i^{noise}, while others do not, e.g. the MC background model f_i^{mc}. This depends whether the corresponding quantities are fundamentally determined in terms of the detected energy E or the DAQ's detection channels. Therefore, efficiencies or the noise edges, which are usually obtained in terms of DAQ channels, receive no shift, whereby theoretical predictions are shifted by ΔE as they are generically given in terms

---

[9] This can be easily verified by performing the operation $-2\log$ on Eq. (2.40).

of (detection) energy. The theoretical prediction for the number of expected background counts for detector i is given by

$$N_i^{\text{OFF}}(E) = b_i \cdot c_i^{\text{eff}} \epsilon_i^b(E) \left(f_i^{\text{noise}}(E; p_{0,1}) + f_i^{\text{mc}}(E - \Delta E_i) \right) . \tag{3.17}$$

Note that in the above implementation each detector receives its own background normalization b_i. Statistically significant deviation from unity would be an indicator for not fully covered systematic contributions. However, the CEνNS signal in all detectors share the same s parameter in order to be sensitive for overall systematic deviations from the SM prediction. Otherwise the detector data sets would be independent of each other and could be evaluated separately.

The whole analysis routine is set up within the SciPy framework [271–278] and by the use of the IDE PyCharm [279]. The likelihood minimization is performed by application of the iminuit package [280, 281], whereas the cluster computations are implemented with the message passing interface MPI for Python [282, 283].

For the limit investigation of the CEνNS signal, a (binned) likelihood ratio test is performed, cf. Eqs. (2.44) and (2.45), which exhibits the form

$$-2 \log \lambda(s) = -2 \log \left(\frac{\mathcal{L}(s)}{\mathcal{L}(0)} \right) \to \frac{H_1}{H_0} , \tag{3.18}$$

with H_1 being the conventional choice of (CEνNS) signal plus background and H_0 being the background-only hypothesis. The above likelihood ratio is calculated for a broad range of fixed s parameters in order to subsequently assign them a certain p-value from the underlying distribution of possible likelihood ratios. The chosen test statistic $\lambda(s)$ equals the standard profile likelihood ratio of Eq. (2.45) in the case of $\hat{s} = 0$. As we are, in a first step, mostly interested in showing that there is a non-zero signal, i.e. falsifying the no-signal hypothesis, we fix $\hat{s} = 0$ for our analysis.

3.3.3.3 Simulation of test statistic

In order to link the obtained likelihood ratios to certain p-values, the distribution of the selected test statistic is needed. When the significance of a signal is not high enough to report a discovery, one usually reports a limit on its signal strength μ or an equivalent number of events at a certain C.L. for rejecting the background-only hypothesis. In our case, we want to test for a discovery, i.e. reject the background-only hypothesis, such that we use the test statistic q_0, cf. Eq. (2.47). Further, in our situation the background-only hypothesis ($s = 0$) is a subset of the space of signal hypotheses ($s \geq 0$), i.e. both hypotheses are *nested*. Wilks' theorem, cf. Sec. 2.3.2.3, implies the test statistic q_0 to follow a χ^2-distribution of one DOF. As we allow the signal strength parameter s to fluctuate only in one direction, i.e. CEνNS signal only contributes additional events, we are in the one-sided case and apply the "half χ^2" distribution of Eq. (2.49) with $x \to q_0$.

In fact, we perform a full MC simulation of the test statistic. In order to do that, we sample all experimental parameters according to their underlying (Gaussian) distribution and generate mock data under the assumption of the background-only hypothesis with the provided background description (threshold description and MC model). Special care is taking in the consideration of uncertainties that came along with the analytic threshold description since the corresponding parameter are partially correlated and exhibit asymmetric uncertainty contours. Thus, from the individual best-fits values of each detector the uncertainty contours of the two threshold parameters where extracted and used for sampling. A detailed description of the procedure is given in App. D.1. 10000 data sets are generated with the sampled parameters and fitted with likelihood functions for both, the background-only ($s = 0$) and the "signal+background" hypothesis (free s), to determine the corresponding q-values, i.e. the likelihood ratios of Eq. (2.44). The overall distribution of these values allow the calculation of p-values that are used in the final deduction of exclusion limits on the signal strength parameter, cf. Fig. 3.8.

3.3.4 First spectral CEνNS limits from the CONUS experiment

After all steps and ingredients of the analysis procedure have been outlined, we present and discuss the results that are derived from the combined CONUS data sets. Before dealing with the collaborative results published in Ref. [70], we briefly discuss the obtained ML fits using the example of a single detector, i.e. C1R1.

3.3.4.1 Exemplary single-detector fit: C1R1

The ML fits of the individual data sets were checked for their stability, before the combined fit that includes all data sets, cf. Tab. 3.6, is performed. Fit stability is confirmed for several benchmark k-parameters that we consider within this analysis, i.e. $k \in [0.1, 0.3]$, via the corresponding minuit functions. As previously mentioned, reactor ON and OFF data are fitted simultaneously in order to have an additional handle on the overall background normalization and the noise edge parameter. However, at this point we remark that this lever is limited by the amount of available reactor OFF exposure, which, in the case of C1R1, renders the reactor ON data to have a larger impact of a factor 7. An example fit for data collection period C1R1 is illustrated in Fig. 3.7, where we selected a signal strength parameter s close to the analysis' best-fit value and a k-parameter of $k = 0.20$. The statistical limitation of the data set is evident from the absolute amount of counts in the data and the fact that corresponding reactor OFF data are reduced by another factor of ~ 7. Nevertheless, fit stability is confirmed and the corresponding fit residuals show no indications for significant signals or systematic effects.

After fit stability and residuals of each detector was confirmed, the combined fit is performed. Since the recently achieved CONUS specifications in combination with the gained exposures of reactor ON and OFF periods are not enough to confirm a CEνNS detection at significant C.L., we state limits on the overall number of CEνNS counts in the considered data sets. This is done by determination of the likelihood ratio, cf. Eq. (3.18), for a range of selected signal strength parameters s. From the distribution of the underlying (discovery) test statistic, either via approximate χ^2 distributions according to Wilks' theorem or a MC simulation, on can then determine the value that corresponds to a C.L. of 90%. The resulting limit on the signal normalization s is subsequently converted into a number of CEνNS counts. For collection period C1R1, Figure 3.8 illustrates the calculated $(1 - p)$ values of the scanned s parameters and corresponding CEνNS signal counts, respectively. We use the MC simulation of our test statistic to determine limits at 90% C.L. on s and the number of signal counts, respectively. For illustrative purposes, we

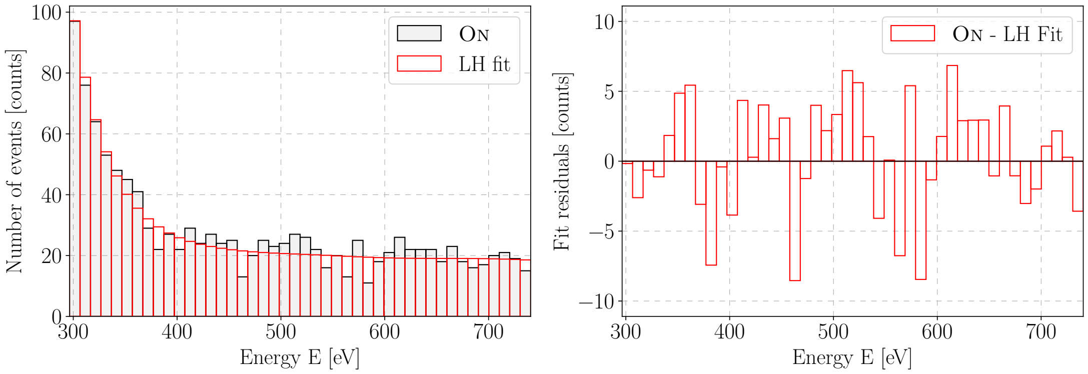

Figure 3.7.: Exemplary fit of reactor On periods belonging to data collection period C1R1. **Left:** Reactor On data (black) compared to the result of a singe-detector fit under the assumption of a quenching parameter $k = 0.20$ (red). **Right:** The corresponding fit residuals show no indications of systematic effects and prove the validity of our fit routine.

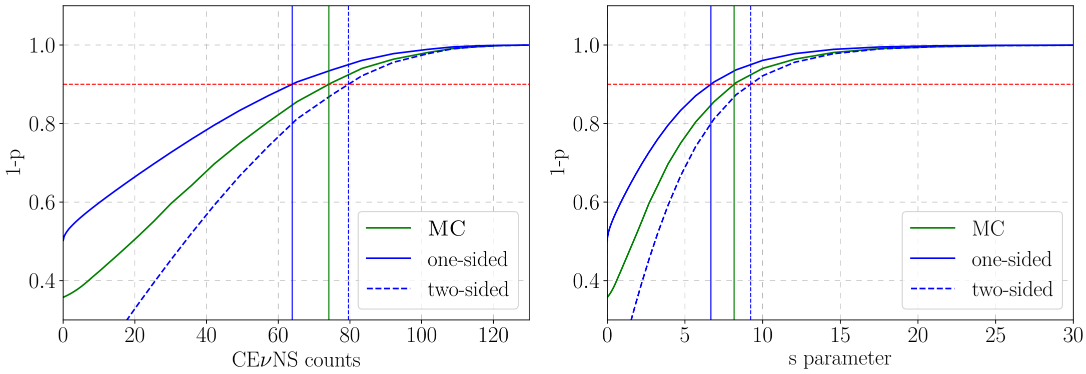

Figure 3.8.: Confidence levels $(1 - p)$ on CEνNS counts and signal strength parameters s for data collection period C1R1. Our limits (at 90% C.L.) are generally determined from a MC simulation of the underlying test statistic (green) and and compared to the approximate test statistics according to Wilks' theorem for both, the one-sided "half χ^2" (blue, solid) and the two-sided χ^2 distribution (blue, dashed), respectively. **Left:** Limits (90% C.L.) for CEνNS counts: 64 (one-sided), 74 (MC), 80 (two-sided). **Right:** Limits (90% C.L.) for the signal strength parameter s: 6.7 (one-sided), 8.2 (MC), 9.2 (two-sided).

list the limits that are obtained via the approximate test statistics according to Wilk's theorem, cf. Sec. 2.3.2.3. Naively, one would expected a one-sided test statistics as the CEνNS signal simply adds up to the background. However, due to the incorporation of the energy scale in our analysis, i.e. by shifting the energy value of the theory prediction, also slight downward fluctuations can occur. Thus, deviations from the approximate "one-sided" case is naively expected as also shown by the simulated test statistic. This procedure is done for a fixed k-parameter and repeated for a selection of parameter on the whole range of considered values, i.e. $k \in [0.1, 0.3]$. Remember that we selected this approach since quenching is the main uncertainty underlying our analysis. With a precise quenching measurement at hand, one can simple determine the valid limit on CEνNS from our results, cf. Ref. [257].

3.3.4.2 CEνNS limits from combined data sets

In the end, we present the results of the first spectral fitCEνNS analysis obtained from the first two CONUS data collection periods, cf. Tab. 3.6. The analysis, illustrated for the case of one detector in the previous section, is extended with the remaining data sets and carried out in a similar way. Since no significant hints for a CEνNS signal can be reported for these data sets as well, upper limits on the CEνNS event of the overall exposure are determined via the binned likelihood ratio test, cf. Eq. (3.18), now under application of the sum of all individual log-likelihood functions. Again, we compare a potential CEνNS signal (of given s parameter) with the null hypothesis H_0 via the ratio of likelihood values. These steps are repeated for a selected range of k-parameters, such that we can deduce explicitly upper limits in terms of it. From a MC simulation that includes now all considered data sets, the *combined* distribution of possible q-values is determined.[10] With this distribution, we determine the upper limits on the signal normalization s (that all data sets have in common) at 90% C.L. and convert it into a corresponding number of CEνNS counts.

The results of this combined investigation and all k-parameters under consideration are summarized in Fig. 3.9 where the individual upper limits on the CEνNS counts are presented in dependence of the k-parameter of the applied modified Lindhard model. For comparison, the combined SM CEνNS prediction is shown as well which allows to disfavor k-parameter larger than $k = 0.27$ with CONUS RUN-(1+2) data and the assumption of a pure SM scenario. Further, for the measured value of $k = 0.18$ [169], an upper limit of 85 counts (at 90% C.L.) is found which corresponds to < 0.34 events $\mathrm{kg}^{-1}\,\mathrm{d}^{-1}$. These obtained results are the collaborative results of two independently developed analysis schemes and represent so far the world's best limits obtained from a CEνNS-investigating reactor experiment. Comparing this to the combined SM expectation of (11.6 ± 0.8), it yields a difference of about a factor of 7.

The current analysis is mainly limited by the amount of reactor OFF time. Thus, in order to shrink the difference between the obtained limits and the SM expectation more data and improved experimental specifications are needed. Improvements on the experimental apparatus, e.g. a new DAQ system and more stable environmental conditions,

---

[10] Since the combined MC simulations are computationally extensive, we checked the dependence of these distributions on the explicit k-parameters with reduced statistics for one detector, i.e. C1R1. The dependence turned out to be mild, such that we selected one representative k-value ($k = 0.20$) and determined the q-value distribution with high statistics, i.e. 10000 samples.

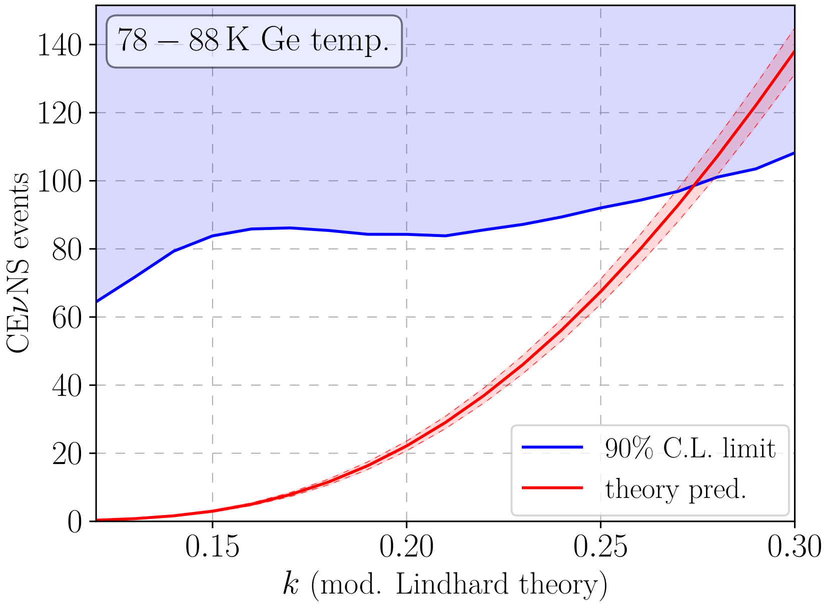

Figure 3.9.: Upper limits at 90% C.L. on the number of CEνNS counts as a function of the quenching parameter k. For comparison, the expected theoretical prediction with uncertainties is indicated in red, cf. Sec. 3.2. The present data sets further allow to exclude quenching parameters larger than $k = 0.27$. The findings of the performed analysis in combination with this figure are reported in Ref. [70].

are already implemented. Further data collection is continuing which will help to improve the obtained limits and eventually detect CEνNS at the KBR site. However, the applied combination of technologies, i.e. a low background HPGe diode in a compact, sophisticated shield design close to a powerful (anti)neutrino source, already revealed its potential for future CEνNS detection as well as investigations of CEνNS-related topics, cf. Ch. 4.

3.4 Summary and outlook

The present chapter deals with the first spectral investigation of SM CEνNS at a reactor site with the CONUS set-up. At first a detailed description of the CONUS experiment and its individual components is given in Sec. 3.1. Characteristics of the experimental site, cf. Fig. 3.1, are presented as well as descriptions of the advanced shield design and the special features of the applied HPGe detectors, cf. Fig. 3.2.

Next, in Sec. 3.2 the individual components needed for a realistic theory prediction of CEνNS that is later applied in the CONUS data analysis are expounded. Special care is taken in assembling the reactor antineutrino spectra, cf. Sec. 3.2.1, since the CONUS Collaboration was granted access to the reactor simulation data, i.e. the time-resolved reactor thermal power, cf. Fig. 3.3 and its fuel composition, cf. Tab. 3.2. The implementation of this information and the assessment of underlying uncertainties allows to provide realistic flux and spectral predictions for the individual CONUS data collection periods, cf. Fig. 3.4 and Tab. 3.4 as well as corresponding uncertainties, cf. Tab. 3.5. Further, the signal's sensitivity to the underlying antineutrino spectra is investigated, cf. Fig. 3.5, and the impact of quenching is discussed, cf. Fig. 3.6. Finally, the implementation of detector-specific responses allows to supply tailored CEνNS predictions for the individual detector collection periods.

Afterwards, Section 3.3 illustrates the analysis procedure for the CEνNS limits from the CONUS experiment. The collection of analyzed data sets is summarized, cf. Tab. (3.6), and details about the background composition, its description and implementation in the analysis chain are discussed, cf. Sec. 3.3.2. For more details on this matter, we refer to Ref. [239]. We continue with a in-depth discussion of the implemented analysis procedure including underlying uncertainties, cf. Tab. 3.7, the form and implementation of the chosen ML approach, cf. Eqs. (3.14),(3.16) and (3.17), as well as the simulation of the underlying test statistic, cf. Eq. (2.44). We close by illustrating the steps of our analysis scheme using the example of one detector, cf. Figs. 3.7 and 3.8, before we present final results, i.e. combined upper limits (at 90% C.L.) in terms of the k-parameter of the applied modified Lindhard theory, cf. Fig. 3.9. The obtained results represent the world's best limits on SM CEνNS in germanium and, moreover, at a reactor site. They are based on CONUS data collection periods which exhibit an overall exposure of 248.7 kg d (reactor On) and 58.8 kg d (reactor Off).

The present CONUS results are limited by the exposure of reactor Off periods, which means that additional data collection, particularly after the reactor shutdown, increases the statistical reach. However, improving the currently achieved detection thresholds is crucial in order to increase the expected number of CEνNS counts. This does not only increase the signal's statistics, but also makes data collection more resilient towards changing environmental conditions like temperature-induced noise fluctuations and consequential loss of exposure. Meanwhile, a lot of effort has been undertaken to stabilize the environmental conditions at site in order to retain more of the original exposure. A new DAQ system, which has recently been installed, might allow to reduce the CONUS detectors' energy threshold even further. At the moment, the electronics noise edge is part of the each detector's ROI and thus introduces additional uncertainties due to the corresponding threshold description, cf. Eq. (3.11). An improved DAQ system with a noise edge at lower energies might provide higher expected CEνNS count rates while at the same time allowing to cut away the electronic noise edge such that corresponding uncertainties vanish.

Moreover, a precise measurement of the QF in CONUS-like detectors and at low nuclear recoils, which are relevant for CEνNS, will be highly beneficial for the present analysis. This external knowledge can be simply accounted for with a nuisance parameter that is attributed with a corresponding pull-term. In doing so, the major uncertainty of our analysis and the resulting scans over still allowed k-parameters then simply reduce to another *pulled* fit parameter. Theoretical predictions and the MC simulation of the test statistic underlying our analysis benefit from a precisely measured k-parameter as well.

Further improvements might be achieved in terms of the detectors' energy scale calibration, which at the moment exhibits an uncertainty of $\sim 15\,\mathrm{eV}$. Irradiation with a ^{252}Cf source is proposed in order to stronger activate the K- and L-shell x-ray lines. It is assumed that the energy scale will become determinable at the $\sim 5\,\text{eV}$-level. Recently, new IBD-based signal spectra have been provided by Ref. [196]. Further, a technique to construct data-based antineutrino spectra has been proposed by Ref. [195] that allows a determination at 2%-precision. This new insights will improve the signal prediction and decrease the corresponding uncertainties. The consideration of all the mentioned potential improvements in combination with the collection of additional exposure both in reactor ON (until the reactor shutdown at the end of 2021) and reactor OFF periods (until the end of 2022) might push the CONUS experiment into a realm where a CEνNS detection with enough significance can be possible.

Although, the current experimental sensitivity is not enough to claim a CEνNS detection, the collected data still provide opportunities for CEνNS-related BSM investigations as shown in the following chapter.

CHAPTER 4

NOVEL CONSTRAINTS ON NEUTRINO PHYSICS BEYOND THE STANDARD MODEL

The following chapter covers BSM investigations based on CONUS RUN-1 and partially RUN-2 data sets. With the analysis procedure introduced on the previous chapter, we investigate potential BSM physics related to the neutrino sector such as NSIs of vector- and tensor-type. Further, we look for new particles in the context of simplified models for new scalar and vector mediators, which interact with neutrinos and the first generation of quarks. In the latter case we additionally test for effects on EνeS at higher energies, i.e. $[2, 8]$ keV. This allows us to use extended data sets with larger exposure. In a second analysis, we search for electromagnetic neutrino properties, mainly in terms of an effective νMM via EνeS in the energy region $[2, 8]$ keV. We use the obtained result to deduce a bound on an effective νMC.

At first, we introduce adjustments that are made in our analysis scheme in order to perform the intended BSM analyses. The consideration of EνeS and the incorporation of extended data sets demand small changes in our routines, which are laid down in more detail. Then, the performed investigations of the mentioned BSM extensions are illustrated in turn, whereby small theoretical introductions are given. We present the corresponding cross sections, which are applied in our analysis, and the obtained results, i.e. limits at 90% C.L.. In the end, we conclude with a small summary of our findings. The present chapter includes the results published in Ref. [225] and Ref. [284].

4.1 Adjustments of the analysis procedure

The BSM extensions to be tested within this chapter are included one after the other into our analysis scheme, while we rely on the same (binned) likelihood ratio as before, cf. Eq. (2.44). The underlying assumption is that SM CEνNS and EνeS are either modified through interference with BSM extensions or, in the case of a different interaction structure, simply can be viewed as background events to the new BSM physics. For CEνNS-related analyses, we use RUN-1 data sets that have already been used in the previous analysis, i.e. at energies below 1 keV, while for EνeS we analyze extended data sets of RUN-1/2 in the energy range of $[2, 8]$ keV. During the BSM analyses, quenching still remained the dominating uncertainty, thus, we continued to state our results in dependence of the QF, i.e. the k-parameter of the modified Lindhard model, cf. Sec. 3.2.2. However, internal investigations of the CONUS Collaboration already indicated k-values below $k = 0.18$, which is favored in Ref. [169]. Therefore, we investigate the individual BSM models in terms of certain benchmark values, i.e. $k \in \{0.12, 0.16, 0.20\}$, which is a representative set of k-values that at the same time reduces necessary computation times. Further, nuclear form factors in the cross section of the models under study are approximated with unity as in Ch. 3. In what follows, the individual adjustments for the performed BSM analyses are illustrated.

4.1.1 Extension of data sets at higher energies

For the investigations of potential BSM signatures in neutrino-electron scatterings, we define a different ROI within the energy interval of $[2, 8]$ keV. This proofs advantageous as the strong criteria on the stability of the CEνNS ROI below ~ 1 keV do not apply, cf. Sec. 3.3.1. Thus, data collection periods that have been excluded by different cuts from the previous analysis, can be retrieved and used within these analyses. The selected energy interval of $[2, 8]$ keV is not arbitrarily chosen. First, this energy region is stable and does not show any noise-temperature correlations. Hence, it is not affected by the corresponding noise-temperature cut. Second, there are almost no lines in the energy range confined by x-ray peaks at ~ 1 keV and ~ 10 keV. These correspond to K- and L-shell transitions in decays of Ge-related isotopes, which have been cosmogenically created during above ground storage in the manufacturing process or are created by in-situ activation of residual cosmogenic background as well as artificial neutron calibrations.

Therefore, in our BSM investigations we use (usual) RUN-1 data sets for CEνNS-related studies, while we make use of extended data sets of RUN-1 in the energy region $[2, 8]$ keV. For the separately performed νMM investigation even more data sets are considered, i.e. RUN-2 data. In the “low energy region” of $[0.5, 1]$ keV background levels of a few 10 counts $\text{kg}^{-1}\text{d}^{-1}\,\text{keV}^{-1}$ [82] are obtained, while at the “high energy region” $[2, 8]$ keV stable background rates of 27-41 counts $\text{kg}^{-1}\text{d}^{-1}\,\text{keV}^{-1}$ [244] are reached. The data sets for both, electron and nucleus scattering, with their corresponding reactor ON and OFF exposures used in the following BSM investigations are listed in Tab. 4.1. All in all, an increase in exposure of about a factor of 3.1 for reactor ON and 2.5 for reactor OFF periods can be achieved with the extended, high energy data sets compared to the energy region below 1 keV. The subsequent inclusion of additional RUN-2 data in the case of the performed νMM investigation yields a factor of 3.3 for reactor ON and 3.5 for reactor OFF periods.

4.1.2 Background modeling and systematic uncertainties

Although the incorporation of data sets at higher energies comes with a significant increase in detector exposures for both, reactor ON and OFF periods, the larger analyzed energy range increases the sensitivity towards small uncertainties in the underlying MC background models, which are therefore now reflected in the analysis. In particular, spectral shape variations in the provided MC background models can occur due to uncertainties in

Analysis	Data set	On [kg d]	Off [kg d]	ROI [keV]
BSM	C1R1	96.7	13.8	0.276 - 0.741
($\bar{\nu}_e + A(Z,N)$)	C2R1	14.6	13.4	0.281 - 0.999
	C3R1	97.5	10.4	0.333 - 0.991
	all	208.8	37.6	
BSM + νMM	C1R1	215.4	29.6	2.013 - 7.968
($\bar{\nu}_e + e$)	C2R1	184.6	32.2	2.006 - 7.990
	C3R1	248.5	31.7	2.035 - 7.989
	all	648.5	93.5	
νMM	C1R2	19.6	18.5	2.010 - 7.955
($\bar{\nu}_e + e$)	C3R2	20.8	19.0	2.007 - 7.991
	all	688.9	131.5	

Table 4.1.: Detector exposures of reactor On and Off periods together with the ROIs of different data sets for both scattering channels. As mentioned in the text, for energies above 2 keV data can be restored since the stricter selection criteria for the CEνNS ROI can be relaxed. For the separate investigation of a finite νMM via EνeS, cf. Sec. 4.4, additional (high-energy) data sets of run-2 are incorporated as well.

the production rates of cosmogenic-induced germanium isotopes and potential surface contamination on the detector diodes. A full description of the refined MC background models is given in Ref. [244].

As a consequence for our analyses, we need to take into account these spectral variations by allowing the provided MC background to vary within their corresponding uncertainty regions. These are provided by our colleague Dr. J. Hakenmüller in addition to the actual simulation data, cf. Sec. 3.3.2. We incorporate these uncertainties by multiplication with a second order polynomial of the form

$$R(E; b_0, b_1, b_2) = b_0 \left(1 + b_1 \cdot E + b_2 \cdot E^2\right) \ , \tag{4.1}$$

where the parameters b_i with $i = 0, 1, 2$ are determined from the combined fit of reactor On and Off data for each data collection period, cf. Sec. 3.3.3.2. In this form, the parameter b_0 retains its interpretation of the previous CEνNS analysis, while the additional background parameters b_1 and b_2 allow for a linear and quadratic tilt of the provided background models, respectively.

In order to properly account for the uncertainties of the rescaled MC background, a specific pull-term is constructed. Within the fit procedure, we square the difference between the rescaled and the original MC background spectra and weight them with the corresponding uncertainty regions of the provided error bands. This procedure is in analogy to the usually applied pull-terms for single parameter, cf. Sec. 2.3.1.4 or Sec. 3.3.3.2. The obtained values already give some indication about the deviation between the fit and the provided spectra. To consider this within the likelihood minimization, we take the mean over all these values in the ROI and add the results as penalty to our likelihood function. In doing so, we allow each bin to contribute equally, while potential deviations are viewed in terms of their impact on the whole background spectrum.

In general, these three background parameters account for the overall background normalization and take care of shape uncertainties that are introduced by cosmic production rates of radioisotopes as well as detector surface effects. The latter are related to the thickness of the detectors' passivation layer and eventual ^{210}Pb decays on its surface. However, the overall spectral uncertainties are less then 5%. To guarantee a similar treatment of these uncertainties throughout our BSM analyses, we apply these methods also for the energy region below 1 keV.

Another modification regarding the background is related to the description of the electronic "noise edge" for energies below 1 keV. In order to guarantee stable likelihood minimization and to eliminate potential parameter correlations in the previous threshold description, cf. Eq. (3.11), we choose a new analytic description with less degeneracy and extend the fit region to slightly lower energy values. Thus, in the investigations regarding nucleus scattering, we apply the following analytic function

$$f_{\text{noise}}(E;p_0,p_1) = \exp\left(-\frac{p_1}{(p_0/450)^4}\,(E-p_0)\right)\,, \tag{4.2}$$

with E being the energy, while the parameters $p_{0,1}$ are determined by the minimization routines. The new and slightly lower energy threshold are listed in Tab. 4.1.

Further, an overview of all uncertainties considered in the refined analysis procedure is given in Tab. 4.2, while we refer to the analysis description of Ch. 3 for their individual implementation.

4.1.3 Refined antineutrino emission spectra

So far, our reactor antineutrino emission model relied on the HMM [247, 248] which has been corrected for the reactor bump by using the corresponding correction factors of the Daya Bay Collaboration [194]. Therefore, the lowest neutrino energy considered is ~ 1.8 MeV. For the (SM) CEνNS investigations performed so far, this is no problem as with the current energy threshold we are only affected by the higher energy part of the reactor antineutrino spectrum ($\gtrsim 5$ MeV), cf. Fig. 3.5. As the BSM investigations now also include EνeS, which is sensitive to the lower neutrino energies, we need to account for the antineutrino emission below the IBD threshold as well. Unfortunately, no direct measurements of this spectral part exist, so we have to rely on ab-initio calculations with their corresponding high uncertainties, cf. Sec. 2.2.1.2. Remember that within our procedure the number of neutrinos per fission is encoded in the combined antineutrino emission spectrum (dN/dE_ν), while all reactor-related quantities are incorporated in the reduced reactor fluxes, cf. Sec. 3.2.1. Thus, by modifications of the isotope-specific spectra $(dN/dE_\nu)_i$, reduced reactor fluxes remain unchanged. However, the extended data sets

Parameter	Uncertainty or related parameters
background MC	Θ_{b_0} (free), Θ_{b_1,b_2} ($\leq 5\%$, uncertainty from background model)
noise threshold (for CEνNS-related analyses)	Θ_{thr_1}, Θ_{thr_2} (free, uncertainty considered via toy MC)
reduced neutrino flux $\Delta\Phi^*$	$\sim 3\%$
neutrino spectrum	subdominant uncertainty (compared to quenching)
reactor On and Off duration	negligible uncertainty
active mass	$< 1\%$
electronic detection efficiency c_{eff}	$\leq 5\%$
energy calibration uncertainty ΔE	15 eV
quenching	k (explicitly included)

Table 4.2.: Overview of nuisance parameters that enter the likelihood function of the performed BSM analyses with their corresponding uncertainties.

exhibit different exposures such that the associated data collection periods affect the reduced reactor fluxes due to changes in the average thermal power $\bar{P}_{\mathrm{th}}$. The corresponding values are listed in Tab. 3.4. Accordingly, the average fission fractions of the extended data sets change as well, cf. Tab. 3.2, and have to be considered in the compilation of the total antineutrino emission spectrum.

For our investigations, we use the simulated, isotope-specific reactor emission spectra of Ref. [187] and weight them with their fission fractions. However, to account for the correct emission of ~ 7.2 neutrino per fission [186], we normalize the combined low-energy part appropriately. In particular, we normalize it to the difference between the overall antineutrino emission per fission and the integrated number of neutrinos already contained in the spectrum of HMM. For uncertainties of the combined low energy antineutrino spectrum we assign a 10% error to the individual bins and ignore potential bin-to-bin correlations. The spectral covariance matrix deduced in Sec. 3.2.1 is extended towards lower energies with these values. However, throughout this analysis we neglect any spectral uncertainties because of practical reasons. Similar to the previous analysis, we do not expect to resolve any spectral features with the current experimental sensitivity, not only from CEνNS but also from the small number of EνeS events. Further, the 39 additional parameters related to the antineutrino emission spectrum (basically for every data collection period), although attributed with a pull-term, would increase computation time to an unacceptable amount. In addition, as we cannot resolve spectral features, the impact on the result plots can be expected to be negligible.

4.1.4 Simulation of test statistic and limit determination of BSM models

In the end, we discuss the consequences of the introduced modifications on the MC generation of the underlying test statistic. Depending in the BSM signal's characteristic, i.e. whether it is purely additive or might affect the SM interactions, SM CEνNS and EνeS are considered as additional background and are sampled in addition to other quantities like background or experimental parameters. For instance, in the case of tensor-type NSIs, the CEνNS interaction is sampled as well, whereas for vector-type NSIs it is not, since it is directly included in the signal expectation. Potential correlations among the threshold parameters are accessed according to the same procedure already applied in the previous CEνNS analysis, cf. App. D.1. Due to the numerically extensive computation, we decide to fix the quenching parameter for the correlation extraction to $k = 0.16$. Thus, we neglect small possible deviations since these are covered by a conservative choice of the error ellipses of the threshold parameters. The obtained uncertainty contours are used for the sampling of these parameters within MC generation of the test statistic.

In addition to correlations among the threshold parameters, we also consider the newly introduced parameters $b_{1,2}$ that take care of potential background shape uncertainties. As test fits revealed slight correlations among them as well, we determined their uncertainty contours in analogy to the threshold parameters. In both cases, we sample the parameter pairs from a two-dimensional Gaussian distribution with means and covariance matrices determined via the procedure described in App. D.1. As in Ch. 3, the obtained distribution of q-values is converted into a CDF from which the explicit parameter bounds at 90% C.L. are determined.

For NSI investigations, we simply fit the associated nuclear charge, determine its limit and convert it into the corresponding ϵ couplings. This has the advantage that only one parameter has to be fitted. The corresponding test statistics also reduces to a one-dimensional case. In the case of simplified light mediators where both couplings and masses are generally free, we decided to determine limits for fixed mediator masses, which again reduce our investigation to a one-dimensional problem. Test statistics are generated for characteristic mass values which represent the models' two characteristic parameter regions, i.e. $m \in \{3, 8\}$ MeV for electron and $m \in \{4, 9\}$ MeV for nucleus scattering. For the investigation of a finite νMM, only the extended RUN-2 data sets need to be incorporated in addition, while the remaining procedure remains the same.

4.2 Non-standard neutrino interactions

In our first BSM investigation we test the CONUS RUN-1 data in a model-independent way via NSIs between neutrinos and the first generation of quarks. In this framework, the NC interaction is extended with further effective four-fermion interactions, cf. Eq. (2.8), where new mediators are generally assumed to be much heavier than the physical scale we are probing such that they can consequently be integrated out. The new couplings, which are usually quantified in terms of the Fermi constant G_F, can be flavor-preserving $\epsilon_{\alpha\alpha}$ or flavor-changing $\epsilon_{\alpha\beta}$ with $\alpha \neq \beta$ and the lepton-flavor indices $\alpha, \beta = e, \mu, \tau$. In the case of $\epsilon_{\alpha\alpha} \neq \epsilon_{\beta\beta}$ for $\alpha, \beta = e, \mu, \tau$, lepton flavor universality is violated and one speaks of non-universal couplings. Additional neutrino interactions have received a lot of attention as they could affect several physical branches, for instance neutrino oscillations [114, 285, 286] as well as astrophysics [29, 30, 287, 288] and cosmology [289]. In their conventional formalism NSI affect CEνNS via a modified weak or an additional nuclear charge [111, 112, 115]. More recently, they have been discussed on a broader framework called general neutrino interactions (GNIs) [290–292].

In the following, we give a short introduction to the broader framework of EFTs and NSIs, before we cover conventional vector-type NSIs as well as the more exotic tensor-type NSIs.

4.2.1 Effective field theory and new neutrino interactions

Low energy effects originating from high scale BSM physics are nowadays commonly investigated by using EFT frameworks [293]. Since the associated heavy particles are non-dynamical, they can simply be integrated out[1] and as a consequence manifest themselves in non-renormalizable operators of higher mass dimensions, i.e. $d \geq 5$. The corresponding effective Lagrangian is then given by [291, 294]

$$\mathcal{L} = \mathcal{L}_{\mathrm{SM}} + \sum_{n \geq 5} \frac{1}{\Lambda^{n-4}} C_i \mathcal{O}_i^{(n)} \,, \tag{4.3}$$

with Λ being the theory's cutoff scale, i.e. the scale at which heavy DOFs become dynamical again and the validity of the effective descriptions breaks down. Frequently, this scale is associated with the mass of a new mediator. The dimensionless Wilson coefficients are denoted by C_i and the n-dimensional, non-renormalizable operators $\mathcal{O}_i$ are in general suppressed by the cutoff scale Λ^{-n}. There is only one dimension-5 operator which is famous for its potential of generating neutrino masses, namely the Weinberg operator [295]. Taking for example the SM and integrating out all heavy DOFs around the electroweak (EW) scale, one arrives at a low energy EFT that respects $SU(3)_{\mathrm{c}} \times U(1)_{\mathrm{em}}$. Thereby, the obtained operators exhibit the symmetries of the low energy theory.

Generally formulated as an EFT, NSIs provide a model-independent way of probing a wide range of BSM scenarios in a description that is valid up to the EW scale. Typically discussed are vector-type NSIs that arise from dimension-6 four-fermion operators [20, 285, 291]:

$$\mathcal{L}_{\mathrm{CC}} = -2\sqrt{2} G_F \sum_{f,P,\alpha,\beta} \epsilon_{\alpha\beta}^{ff',P} \left(\bar{\nu}_\alpha \gamma_\mu P_L l_\beta\right) \left(\bar{f} \gamma^\mu P f'\right) + \mathrm{h.c.} \,, \tag{4.4}$$

$$\mathcal{L}_{\mathrm{NC}} = -2\sqrt{2} G_F \sum_{f,P,\alpha,\beta} \epsilon_{\alpha\beta}^{f,P} \left(\bar{\nu}_\alpha \gamma_\mu P_L \nu_\beta\right) \left(\bar{f} \gamma^\mu P f\right) \,, \tag{4.5}$$

where the sums consider the fermions $f, f' \in \{e, u, d\}$ and the chirality projection operators $P \in \{P_L, P_R\}$. Further, the dimensionless ϵ parameters quantify the new interaction's strength in terms of the weak interaction, since they are conventionally normalized with respect to the Fermi constant. Operators of higher dimension can induce NSIs in similar fashion which are so far less stringently constrained by experimental observations related to

---

[1] This can be done via the formal path integral treatment [160, Section 12.1] or simpler, determining the particle's EOM and inserting it into the Lagrangian while ignoring its kinetic term [152, Section 7.2.3].

$SU(2)_L$ invariant operators [116, Section 1.3], i.e. lepton flavor violation (LFV) and lepton unitarity. Equivalent interactions can be defined also for other Lorentz structures, i.e. scalar or tensor interactions, which are for example discussed in the context of GNIs [291]. However, vector-type NSIs are of special interest to oscillation experiments since these new interactions either affect the production and detection of neutrinos (in the case of CC NSI) or influence their propagation through matter (in the case of NC NSIs) [114, 116, 285]. Note that neutrino oscillations can additionally be altered by (pseudo-)scalar and tensor interactions, but since they couple states of opposite chirality their effect is generally expected to be small. However, in extremely large magnetic fields, e.g. within a supernova, such interactions might become sizable and trigger spin-flips during propagation [296]. Consequently, these interactions might influence the determination of still unknown neutrino parameters by future long-baseline experiments, namely leptonic CP-violation δ_{CP}, the neutrino mass hierarchy $sig(\Delta m^2_{32})$ as well as the octant of the atmospheric mixing angle θ_{23}. Further, NSIs (or more generally GNIs) might leave imprints in colliders and LFV experiments as well as they might modify neutrino cross sections. Moreover, in analogy to the oscillation experiments' insensitivity to the absolute neutrino mass, scattering experiments are needed in order to contribute independent knowledge [116]. The situation is even more complex as the above NSI parameterization exhibits certain degeneracies, which could be partially solved by CEνNS measurements at different neutrino sources [297].

Conclusively, we discuss the energy scale at which NSI-related New Physics (NP) is expected to occur. This can be done since the effective couplings $\epsilon^{f,P}_{\alpha\beta}$ are defined in terms of the Fermi constant G_F. Therefore, the scale where corresponding NP becomes relevant can be approximated by [115]

$$\Lambda \approx \frac{g^{f,P}_{\alpha\beta}}{g} \cdot \frac{m_W}{\sqrt{\epsilon^{f,P}_{\alpha\beta}}} \sim \frac{m_W}{\sqrt{\epsilon^{f,P}_{\alpha\beta}}}\,, \tag{4.6}$$

with $g^{f,P}_{\alpha\beta}$ being the NSI coupling and g the $SU(2)_L$ coupling, respectively. In the last step, we assumed both to be approximately of similar size. Consequently, bounds on the NSI couplings can be translated via the above relation into an approximate energy scale, where related new particles are expected to appear.

4.2.2 Vector-type interactions

We start our investigations by looking at the conventional type of NSIs, i.e. vector-type interactions. After a discussion of the corresponding signal expectation, we present the results from our investigation and compare them with existing bounds.

4.2.2.1 Cross section

We assume vector-type NSIs to be induced by an operator that exhibits the following structure

$$\mathcal{O}^{q\mathrm{V}}_{\mathrm{NSI}} = (\bar{\nu}_\alpha \gamma^\mu P_L \nu_\beta)\,(\bar{q}\gamma_\mu P q) + \mathrm{h.c.}\,, \tag{4.7}$$

with the left-handed and right-handed chirality projection operators $P \in \{P_L, P_R\}$ and the lepton-flavor indices $\alpha, \beta \in \{e, \mu, \tau\}$. Further, coupling only to the first generation of quarks is assumed $q \in \{u, d\}$. The hereby introduced NC vector-type NSIs exhibits a similar structure as the usual SM CEνNS interaction, cf. Eq.(2.31), and consequently the associated couplings can be absorbed into the weak nuclear charge, i.e. $Q^{\mathrm{V}}_W \rightarrow Q^{\mathrm{V}}_{\mathrm{NSI}}$. In general, NSIs can render CEνNS to become flavor-dependent, e.g. when flavor non-universal couplings are allowed. Hence, the weak nuclear charge attributed to vector NSIs in its most general form is given by [111]

$$\begin{aligned} Q^{\mathrm{V}}_{\mathrm{NSI}} = &\left(g^p_V + 2\epsilon^{u\mathrm{V}}_{\alpha\alpha} + \epsilon^{d\mathrm{V}}_{\alpha\alpha}\right) Z + \left(g^n_V + \epsilon^{u\mathrm{V}}_{\alpha\alpha} + 2\epsilon^{d\mathrm{V}}_{\alpha\alpha}\right) N \\ &+ \sum_{\alpha,\beta} \left[\left(2\epsilon^{u\mathrm{V}}_{\alpha\beta} + \epsilon^{d\mathrm{V}}_{\alpha\beta}\right) Z + \left(\epsilon^{u\mathrm{V}}_{\alpha\beta} + 2\epsilon^{d\mathrm{V}}_{\alpha\beta}\right) N\right]\,, \end{aligned} \tag{4.8}$$

where the first line represents flavor-diagonal and usual SM couplings that leave the (anti)neutrino's flavor unchanged. The second line contains couplings that introduce flavor transitions in the interaction. Note that in contrast to the SM CEνNS case, cf. Eq. (2.26), the proton number Z is not necessarily suppressed by a small prefactor. As a consequence, the cross section does not scale with the characteristic dependence on the squared neutron number alone. Although the flavor-changing couplings might in principle appear, we restrict ourselves to the case of flavor-diagonal ones, i.e. $\epsilon^{u\mathrm{V}}_{ee}$ and $\epsilon^{d\mathrm{V}}_{ee}$. This is also motivated by the fact that, if present, flavor-changing couplings can be absorbed together with flavor-diagonal ones in effective couplings that we are able to constrain at reactor-site. However, at π-DAR sources investigations of other coupling types are possible due to the emission of neutrinos with different flavor. Hence, bounds exist from investigations that assume both cases, one flavor coupling to be non-vanishing at a time [90, 91] and the general case also including oscillations data [298].

In the upper plot of Fig. 4.1, we illustrate the effect of selected vector NSI couplings on the expected event spectrum for the data collection period C1R1. Due to the same chiral structure also destructive interference is possible between both signals, SM and the NSI-induced CEνNS. Thus, in the context of vector NSIs, event rates smaller than predicted by the SM interaction might occur. The corresponding cases are indicated by the dashed lines in the upper plot of Fig. 4.1.

Already before the analysis, we can estimate our potential to determine competitive bounds with the CONUS data. Since CEνNS and NSIs share the same kinematics, constraining corresponding couplings is, similar to the CEνNS case, limited by the reached experimental specifications. Additionally, without any sensitivity to an actual CEνNS signal, it is not possible for CONUS to resolve parameter regions of destructive interference. Therefore, we cannot expect to set bounds competitive to the ones obtained from COHERENT data [68, 69].

4.2.2.2 Results

The investigation of the CONUS RUN-1 data sets, cf. Tab. 4.1, relies on the analysis procedure presented in Ch. 3 with adjustments described in Sec. 4.1. The lower plot of Fig. 4.1 shows the obtained results at 90% C.L., i.e. the parameter space of vector NSI couplings that are still in agreement with the analyzed data sets. Further, the exemplary parameter points plotted in upper canvas of Fig. 4.1 are indicated with crosses. Note that normal crosses correspond to regions of destructive interference, while bold ones represent constructive interference between both signals. Assuming a QF of $k = 0.16$, the bold green cross is still in agreement with data unlike the bold red cross that can be excluded.

The limits' strong dependence on the quenching factor, i.e. in our implementation the k-parameter of the modified Lindhard model, is immediately evident from the lower plot of Fig. 4.1, a characteristics that we already encountered in the discussion of quenching and its impact on SM CEνNS, cf. Sec. 3.2.2. This underlines again how crucial precise knowledge about quenching is for our results. For the currently favored value of $k = 0.16$ in germanium, our limits are not competitive to existing bounds from COHERENT (CsI [68] and LAr [69]) data.[2] Note that the COHERENT Collaboration reported a slight excess in their argon measurements that yields limits in a special region of parameter space. In particular, this upward fluctuation already allowed to exclude parts of the parameter region that is affected by destructive interference. Consequently, this leads to a segregation of the still allowed regions [69]. A signal detection in the future is required for the CONUS set-up to be able to resolve this region. In addition, we also indicate the strongest limits on vector NSIs obtained from a DM experiment, i.e. the XENON1T experiment [104]. In their analysis, the XENON1T Collaboration searched for the expected 2.1 CEνNS events in their detector that were induced by the solar ^{8}B neutrino flux, which is expected to be $\phi_\nu^{^8\mathrm{B}} = (5.25 \pm 0.20) \cdot 10^6\,\mathrm{cm}^{-2}\,\mathrm{s}^{-1}$ [31, 104, 302]. Although not sufficient to report a discovery, bounds on the corresponding neutrino flux and, moreover, competitive limits (compared to COHERENT) on vector NSIs of electron-type are reported.

The lower plot of Fig. 4.1 additionally shows allowed regions from the CHARM experiment [299] as well as from Large Hadron Collider (LHC) mono-jet searches [300]. The CHARM experiment [299] determined the ratio of NC and CC cross sections for electron (anti)neutrino scattering off nuclei,[3] from which Ref. [303] extracted limits on potentially involved NSI couplings. The LHC bounds are derived from searches of mono-jets plus missing transverse energy, i.e. from the process $q\bar{q} \to \bar{\nu}_\alpha \nu_\beta j$ with $j \in \{g, q, \bar{q}\}$, using $1\,\mathrm{fb}^{-1}$ data at $\sqrt{s} = 7\,\mathrm{TeV}$. In the end, we use Eq. (4.6) and the obtained limits from CONUS in order to estimate the energy scale the experiment is currently sensitive to. Taking $\epsilon \sim 0.7$,

---

[2] We use the tool WebPlotDigitizer [301] for the extraction of limits from other references throughout this work.

[3] The collaboration determined the quantity $R = \frac{\sigma(\nu_e N \to \nu X) + \sigma(\bar{\nu}_e N \to \bar{\nu} X)}{\sigma(\nu_e N \to e X) + \sigma(\bar{\nu}_e N \to \bar{e} X)} = 0.406 \pm 0.140$.

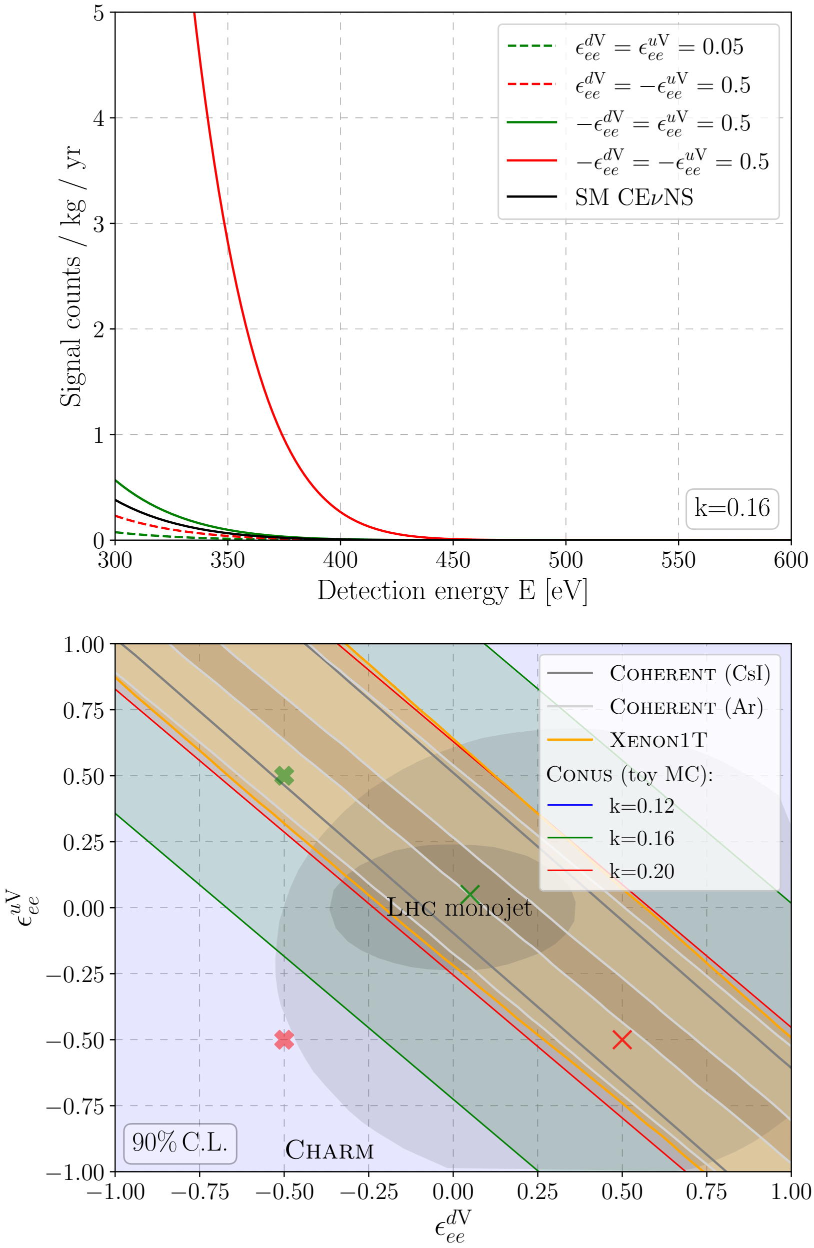

Figure 4.1.: **Top:** Signal expectation of vector NSIs for the data collection period C1R1 under assumption of $k = 0.16$. Coupling values are selected in order to illustrate constructive and destructive interference between the vector NSI and the SM signal. For comparison, the SM CEνNS expectation is shown as well. **Bottom:** Allowed parameter regions (90% C.L.) of vector NSI couplings (ϵ_{ee}^{dV}, ϵ_{ee}^{uV}). The exemplary coupling values of the upper plots are indicated with crosses, while bold crosses mark constructive interference and normal crosses destructive interference between the vector NSI and the SM interactions. In addition, constraints (at 90% C.L.) from other measurements are indicated as well, i.e. COHERENT (CsI [91] and Ar [69]) and XENON1T [104]. Limits from CHARM measurements (90% C.L.) [299] and LHC monojet searches (95% C.L.) [300] are illustrated with gray ellipses. Our results and the corresponding figure are published in Ref. [225].

which is given by the maximal deviation from zero couplings along the diagonal direction for $k = 0.16$, estimates the corresponding NP scale to be $\Lambda_{\text{NP}} \gtrsim 100\,\text{GeV}$.

Although, CONUS limits are not competitive with recent limits on vector NSI couplings, we expect our results to improve with a precise determination of the QF within germanium and a lowered energy threshold. Moreover, as data taking is ongoing with refined environmental conditions and a new improved DAQ system, the CONUS Collaboration is confident that stronger bounds can be contributed in upcoming analyses.

4.2.3 Tensor-type interactions

Besides the conventional vector-type interactions, we also investigate more exotic tensor-type NSIs. In analogy to the previous case, we discuss the corresponding signal expectation at first. In the end, we present the obtained bounds from the CONUS data sets, cf. Tab. 4.1, and deduce the NP scale where related particles might become dynamical again.

4.2.3.1 Cross section

Tensor NSIs can be viewed as a generalization of the conventional vector NSIs [113] such that they naturally occur in the context of GNIs [115, 291]. Their presence would lead to interesting phenomenological consequences, especially in the context of electromagnetic properties of neutrinos [304–306]. In what follows, we assume their existence in terms of the following tensorial operator

$$\mathcal{O}^{q\text{T}}_{\alpha\beta} = \left(\bar{\nu}_\alpha \sigma^{\mu\nu} \nu_\beta\right)\left(\bar{q}\sigma_{\mu\nu} q\right) + \text{h.c.}\,, \tag{4.9}$$

with q representing the first generation of quarks $q \in \{u, d\}$ and $\alpha, \beta \in \{e, \mu, \tau\}$ being the lepton-flavor indices. The induced interaction exhibits a different chiral structure than SM CEνNS and therefore does not interfere with the SM contribution. Hence, in contrast to the vector NSI case of Eq. (4.8), there is only an additive contribution from tensor interactions. Thus, in this investigation, SM CEνNS is considered as a pure background contribution. The resulting quark couplings are absorbed into a new nuclear charge which is, in contrast to vector-type interactions, cf. Eq. (4.8), solely related to tensor-type NSIs:

$$Q^{\text{T}}_{\text{NSI}} = \left(2\epsilon^{u\text{T}}_{\alpha\beta} + \epsilon^{d\text{T}}_{\alpha\beta}\right) Z + \left(\epsilon^{u\text{T}}_{\alpha\beta} + 2\epsilon^{d\text{T}}_{\alpha\beta}\right) N\,, \tag{4.10}$$

with N and Z being the number of neutrons and protons, respectively. Like in the previous case of vector NSIs, the proton number Z is not suppressed by a small prefactor such that the presence of such couplings might break the characteristic N^2-dependence of SM CEνNS.

Although tensor NSIs might in principle trigger lepton-flavor changes, within CONUS we are only sensitive to the sum of such couplings. Analogously to the vector case, we restrict ourselves to diagonal (effective) couplings, i.e. $\epsilon^{u\text{T}}_{ee}$ and $\epsilon^{d\text{T}}_{ee}$. Bounds on muon couplings have been deduced from COHERENT data [88] due to the π-DAR source's muon neutrino content.

In our analysis, we investigate the following cross section, which is expanded with the tensor NSI contribution, cf. Ref. [88, 113],[4]

$$\left(\frac{d\sigma}{dT_A}\right)_{\mathrm{CE}\nu\mathrm{NS}\,+\,\mathrm{tNSI}} = \left(\frac{d\sigma}{dT_A}\right)_{\mathrm{CE}\nu\mathrm{NS}} + \frac{4G_F^2}{\pi} {Q_{\mathrm{NSI}}^{\mathrm{T}}}^2\, m_N \left(1 - \frac{m_A T_A}{4E_\nu^2}\right). \tag{4.11}$$

Here, we point out the difference in kinematic factors between the vector-like interaction of SM CEνNS, cf. Eq. (2.31), and the tensor NSI-induced interactions. This difference in cross sections allows the tensor NSI signal to extend to higher energies, which is advantageous for setting limits on the signal parameters, even in the case where the SM CEνNS signal is not observed. The upper plot in Fig. 4.2 shows the resulting signal expectation of selected coupling values for our benchmark C1R1 in comparison to the SM signal. The signal's extent to higher energies is evident. An additional feature is that the amplitude is significantly higher for same sign couplings than for the case of different signs, a characteristic that is immediately clear from Eq. (4.10).

4.2.3.2 Results

The deduced bounds at 90% C.L. on the parameter space of the tensor NSI couplings $\epsilon_{ee}^{u\mathrm{T}}$ and $\epsilon_{ee}^{d\mathrm{T}}$ are depicted in the lower plot of Fig. 4.2. For comparison, similar bounds obtained from COHERENT CsI data [120] are shown as well. Like in the previous analysis, we indicate the example points of the upper plot in Fig. 4.2 with corresponding crosses. Here, normal crosses indicate points in the parameter space which are still in agreement with the CONUS RUN-1 data sets, whereas coupling values corresponding to bold crosses can already be disfavored.

Although current data sets of the CONUS experiment do not yet allow for the detection of CEνNS, we are able to place world's best limits on the parameter space of tensor NSI interactions, which is due to the signal's extent well above the detector's noise threshold. As a consequence, the dependence of the results on quenching is of minor relevance. Thus, the obtained bounds on this BSM signal are mainly determined by experimental parameters like background and exposure.

As CONUS is able to set competitive bounds, we comment on the degeneracy among the tensor NSI parameter: One can show that the slightly different slopes of the limit bands are due to different target materials (with different neutron and proton numbers, respectively), cf. Eq. (4.10). In principle, this property allows to break the degeneracy among the NSI couplings by using different target materials. This is an argument why CEνNS investigations with several detection technologies is beneficial. Unfortunately, the collected data of CsI and Ge targets are not enough to have a substantial impact on the combined allowed parameter regions.

Finally, we also determine the energy scale at which tensor NSI-related NP is expected to occur. Assuming again a deviation along the diagonal, which is for example motivated by universal couplings to up and down-type quarks, allows a maximal values of $\epsilon \sim 0.05$. Insertion into Eq. (4.6) demands the scale of NP related to tensor NSIs to lie above $\sim 360\,\mathrm{GeV}$. Consequently with improved sensitivity, low threshold experiments like CONUS might be able to probe physics scales comparable to the LHC, i.e. TeV scales.

---

[4] Similar to the SM CEνNS case in Sec. 2.1.2, we ignore negligible terms of the form (T_A/E_{nu}) in the cross section.

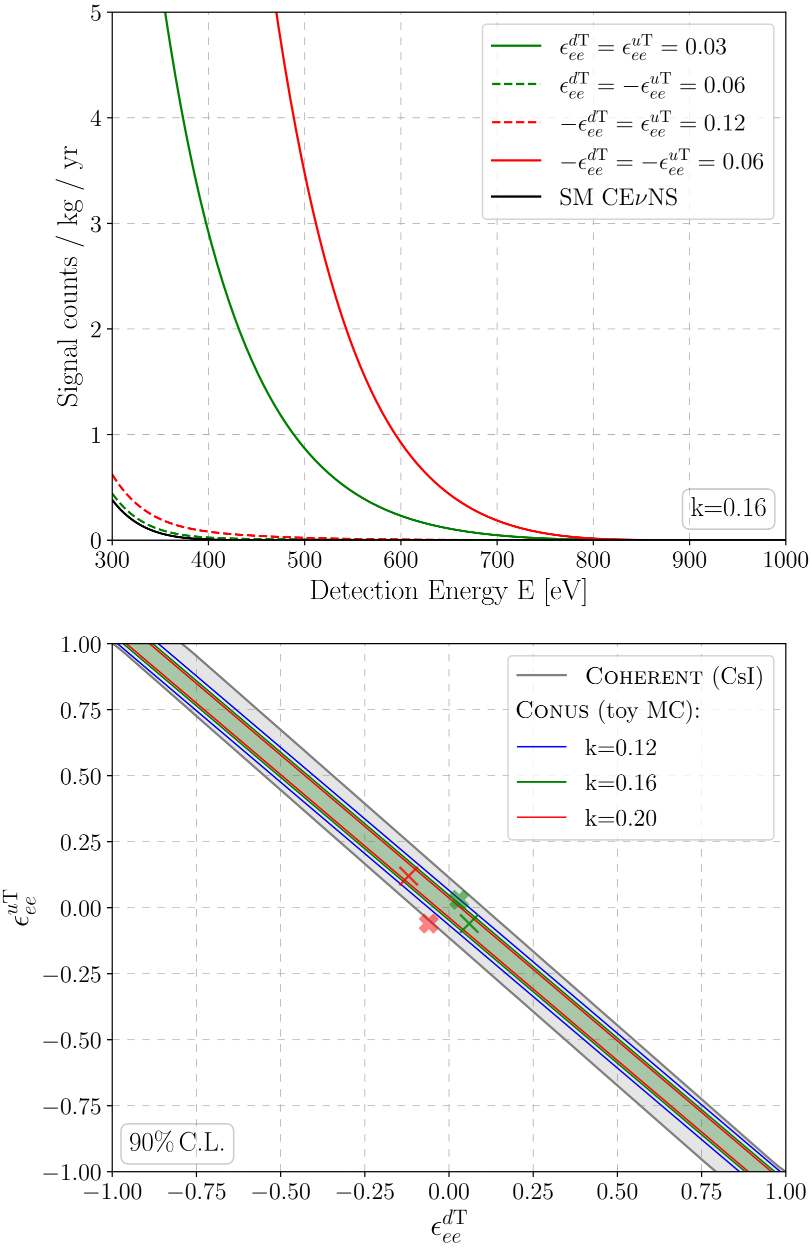

Figure 4.2.: **Top:** Signal expectation of tensor NSIs for the data collection period C1R1 under assumption of $k = 0.16$. Tensor NSI interactions can only contribute with additional events due to their different chiral structure. The SM CEνNS expectation is given for comparison and example couplings are taken from different quadrants in order to illustrate their effect on the overall spectrum. **Bottom:** Allowed parameter regions (90% C.L.) of tensor NSI couplings (ϵ_{ee}^{dT}, ϵ_{ee}^{uT}). The couplings corresponding to the above signal expectations are indicated with crosses, where bold crosses (solid lines from above) represent couplings that are (almost) excluded. Normal crosses (dashed lines from above) refer to signals which are still in agreement with the analyzed data sets. For comparison, bounds at 90% C.L. extracted from COHERENT CsI data are shown as well, cf. Ref. [88]. Our results and the corresponding figure are published in Ref. [225].

This is the case because tensor NSIs extend to higher energies and are therefore less affected by a low QF or low detection thresholds as it is the case for vector NSIs and SM CEνNS. Thus, improving the set-up's overall specifications, e.g. its minimal threshold and the background level, and the addition of further exposure will be beneficial for the deduction of stronger tensor NSI bounds.

4.3 New particle searches in a simplified model framework

The next investigations deal with searches for new light particles that interact with neutrinos. In particular, new interactions with rather weak couplings between neutrinos and quarks can be probed by taking advantage of the coherent enhancement that underlies CEνNS. Of special interest are light mediators with masses in the sub-GeV region, which might be connected to dark sectors, since they are hardly tested by today's collider experiments. In the following, we lay aside explicit aspects of model-building and test the CONUS data sets by application of so-called "simplified models". The popularity of such models can be seen in their increasing application, not only in DM and neutrino physics but also in other contexts such as two Higgs doublet models [307] or testing B-anomalies with leptoquarks [308].

Within this section we investigate the CONUS RUN-1 data sets for light scalar and vector mediators, which is possible since such models would leave imprints on the recorded recoil spectra. Such features are most distinct for mediator masses smaller than the maximum momentum transfer. Therefore, we expect reactor experiments to be particularly sensitive for mediator masses below $\lesssim 10\,\mathrm{MeV}$.

As such models usually allow to incorporate interactions between neutrinos and leptons, we include them as well and investigate both, CEνNS and EνeS. For the latter, we use extended data sets in an energy region of $[2, 8]\,\mathrm{keV}$, cf. Sec. 4.1, while we investigate CEνNS only at energies below $1\,\mathrm{keV}$. The analyzed data sets are listed in Tab. 4.1. However, before we cover the individual models and the obtained results, we give a short introduction into the topic of simplified DM models with special emphasis on their advantages and limitations in the context of SM extensions.

4.3.1 Foundations of simplified DM models

Since simplified models are broadly applied in the context of DM searches (especially at the LHC) [309–311], we approach this framework also from that direction. The following summary of the underlying philosophy, generic models and corresponding problems is mainly based on Refs. [309, 312–314].

In the quest for DM, three types of models are generally under study [309]: EFTs (similar to NSIs in the previous section), so-called simplified models or complete DM models (like the MSSM). While EFTs allow for a simple and model-independent approach, they come with the drawback of relying on non-renormalizable operators that can only be used up to an intrinsic cut-off scale Λ. At energies comparable or above this energy scale, where particles that had been removed from the spectrum become dynamical again, a perturbative description breaks down as contributions of higher-dimensional operators become of similar size. While being a valid description for DD and indirect detection (ID) searches, kinematic features encountered at collider energies might not be captured, e.g. resonant DM production. On the other hand, complete models provide the full spectrum of particles and consistent relations among model parameters, i.e. induced by symmetry principles, but generally exhibit a large number of parameters or particles that might be irrelevant for the process under study. Further, ambiguities in the parameter space complicate the interpretation of data or vice versa prevent clear statements about parameters of interest.

Building bridges between both frameworks, simplified models have become popular [309–311] since they are simple enough to be easily embedded in a more complex content, yet complete enough to describe relevant phenomena and kinematics. In practice, such models incorporate a potential DM candidate χ in addition to a mediating boson between the dark and the SM sector. The corresponding Lagrangian contains renormalizable operators and should respect Lorentz invariance, the SM gauge group and guarantee DM stability. In addition, consistency with the SM's accidental and gauge symmetries is usually required. By inclusion of a propagating mediator, which usually characterizes the model, interaction kinematics are described correctly, i.e. resonant enhancement in DM production, and thus allows a continuous application. In that sense, simplified models are reduced to the minimal set of particles and interactions of a particular selected scenario, e.g. a scalar s-channel mediator (viewed from perspective of DM production). However, they refine the usual EFT approach by describing interactions in terms of a dynamical mediator. The extended behavior of simplified models is also reflected in an enriched phenomenology. While for DM at LHC, mono-X searches are the standard tool for EFT models, additional collider signal can be used to investigate simplified models, e.g. multi-jet+$\not{E}_T$, di-jet and di-lepton resonances [314].

Most relevant to our considerations are the Lagrangians related to s-channel mediators of a (DM) fermion χ,

$$\mathcal{L}_V \supset \frac{1}{2} m_V^2 V_\mu V^\mu - m_\chi \bar{\chi}\chi - g_\chi V_\mu \bar{\chi}\gamma^\mu \chi - g_q^{ij} V_\mu \bar{q}_i \gamma^\mu q_j \,, \tag{4.12}$$

$$\mathcal{L}_S \supset \frac{1}{2} m_S^2 S^2 - m_\chi \bar{\chi}\chi - y_q^{ij} S \bar{q}_i q_j + \text{h.c.} \,, \tag{4.13}$$

with the spin-0 and spin-1 mediators S and V_μ, respectively. Here, we focus solely on pure scalar and pure vector interactions. In general simplified models exhibit more possibilities like more particles and interactions, different kinds of interactions, i.e. (pseudo-)scalar and (axial) vector. Note that these possibilities also depend on the fermionic nature of the DM fermion χ. For example, vector-type couplings for Majorana fermions vanish such that electric and magnetic moments are prohibited, a property that we will also encounter in our discussion of νMMs. For an overview of simplified DM models, we refer to Ref. [315].

In practice, additional assumptions are usually made, e.g. universal couplings to SM particles or only couplings to a preferred quantum number. Nevertheless, interactions that are in conflict with SM symmetries are more delicate as existing bounds are quite strong. Especially, CP as well as baryon and lepton number conservation is usually assumed. In addition, so-called minimal flavor violation is assumed, which demands that the SM flavor interaction structure is to be reproduced.

Simplified models in the limit of heavy mediator masses ($q^2 \ll m^2$) match the usual

EFT framework, i.e. one obtains the effective operators [314], cf. App. A.1,

$$\mathcal{O}_V = \frac{1}{\Lambda^2}\bar{\chi}\gamma_\mu\chi\bar{q}\gamma^\mu q\,, \qquad\qquad \mathcal{O}_S = \frac{m_q}{\Lambda^3}\bar{\chi}\chi\bar{q}q\,. \tag{4.14}$$

However, the obtained limits c due to kinematic differences, i.e. no resonant enhancement or softer missing energy spectrum.

Although, simplified models are a neat tool for investigations, problems arise when it comes to formal aspects [312–314], e.g. consistency, the occurrence of anomalies and perturbativity. The first aspect concerns the SM gauge group, which is to be respected in order to embed the simplified models into a broader framework. From a model-building point of view, anomalies need to cancel for the theory to be valid at quantum level. For simplified models this implies that charge assignment related to potential gauge groups is more involved and/or more fermions are needed. Violation of perturbative unitarity[5] signals either the general break-down of perturbativity or that the underlying theory is incomplete and additional contributions are needed. It can lead to false or diverging predictions [314], e.g. in W boson production, since probabilities are no longer conserved, c.f. Ref. [166, Sec. 15.1]. Due to these issues an explicit realization of a simplified model might not be trivial.

From a bottom-up perspective, simplified models might be viewed as an extended EFT framework which allows to circumvent its intrinsic cutoff while allowing for a richer phenomenology at the same time. Viewed from top-down, complex BSM models are simplified, thus enabling one to focus on the pure DM related interactions. However, the mentioned non-physical results and inconsistencies demand the consideration of additional constraints, couplings or states such that more realistic models need to have a certain degree of complexity.

4.3.2 Light scalar mediators

Now we apply simplified models in the context of neutrino interactions in order to search for corresponding signatures in the CONUS data sets or at least deduce bounds on the corresponding model. Along the lines of previous investigations in the context of solar neutrinos [107] and, moreover, CEνNS investigations [88, 89, 91, 128, 134], we lay aside potential inconsistencies that come along this simplified framework.

We begin with the investigation of a new light scalar boson that mediates scattering between reactor antineutrinos and target nuclei or electrons.

4.3.2.1 Cross sections

In the search for a new light scalar mediator, we select a massive and real boson, even under CP transformation, that couples to the first generation of leptons and quarks. Of course, other SM fermions can be considered as well but since the target material contains mainly up and down quarks, we restrict ourselves to this minimal realization. Thus, the

---

[5] Unitarity of the S matrix is given by $\mathrm{Im}[\mathcal{M}^J_{ii}] = \sum_f |\mathcal{M}^J_{if}|^2 + |\mathcal{M}^J_{ii}|^2 + \sum_{f\neq i}|\mathcal{M}^J_{if}|^2 \geq |\mathcal{M}^J_{ii}|^2$ with $\mathcal{M}^J_{ij}$ being the scattering matrix element between 2-particle initial and final states of the J-th partial wave [312].

Lagrangian of the model under consideration is given by [107]

$$\mathcal{L}_\phi = \phi \left(g_\phi^{q\mathrm{S}} \bar{q} q + g_\phi^{e\mathrm{S}} \bar{e} e + g_\phi^{\nu\mathrm{S}} \bar{\nu}_R \nu_L + \text{h.c.} \right) - \frac{1}{2} m_\phi^2 \phi^2 \,, \tag{4.15}$$

with the scalar couplings $g_\phi^{x\mathrm{S}}$ for $x \in \{\nu, e, q\}$, its mass ϕ and $q \in \{u, d\}$ representing the first generation of quarks. Note that for the Yukawa interaction in the above Lagrangian, a right-handed neutrino ν_R needs to be introduced to the SM such that the neutrino is assumed to be a Dirac fermion. Lepton-number violation can be introduced by assuming the neutrino to be a Majorana fermion and thus introducing a term $\propto \phi \, \bar{\nu}_L^c \nu_L$ [129]. A direct coupling to quarks would imply phenomenological consequences and an explicit low-energy realization consistent with SM symmetries would need a more complex framework in order to meet observations [316]. Following investigations for COHERENT [134] and CONNIE [128], we set aside model-building concerns and phenomenological consequences or constraints for the neutrino sector. The resulting (coherently enhanced) neutrino-nucleus cross section is given by [88, 107]

$$\left(\frac{d\sigma}{dT_A} \right)_{\mathrm{CE}\nu\mathrm{NS} + \phi} = \left(\frac{d\sigma}{dT_A} \right)_{\mathrm{CE}\nu\mathrm{NS}} + \frac{(g_\phi^{\nu\mathrm{S}} Q_\phi)^2 m_A^2 T_A}{4\pi E_\nu^2 (2 m_A T_A + m_\phi^2)^2} \,. \tag{4.16}$$

The Yukawa term in Eq. (4.15) induces a chirality flip which leads to different final states than those in the SM CEνNS case. Consequently, there is no interference and the scalar contribution is simply added to the SM CEνNS cross section, in analogy to the tensor NSI case of Sec. 4.2.3. The corresponding nuclear charge induced by this new boson exchange is given by [107, 156]

$$Q_\phi = \sum_{N,q} g_\phi^{q\mathrm{S}} \frac{m_N}{m_q} f_{T,q}^{(N)} \rightarrow g_\phi (14N + 15.1Z) \,, \tag{4.17}$$

where the last step assumes universal couplings to leptons and quarks $g \equiv g_\phi^{\nu\mathrm{S}} = g_\phi^{e\mathrm{S}} = g_\phi^{u\mathrm{S}} = g_\phi^{d\mathrm{S}}$ and the summation of all nucleon form factors $f_{T,q}^{(N)}$ (taken from Ref. [156]) that incorporate the effective low-energy couplings of the scalar ϕ to nucleons $N \in \{p, n\}$, cf. Sec. 2.1.1.2. Our assumption of universal couplings implies the scalar part of Eq. (4.16) to scale with g_ϕ^4 and reduces the model's parameter space down to only two parameters, i.e. the scalar mass m_ϕ and its coupling g_ϕ to SM fermions. The corresponding signal predictions for data set C1R1 are illustrated in the upper left plot of Fig. 4.3 in comparison to the SM prediction where we have chosen masses for two distinct cases.

Looking at Eq. (4.16), two important kinematic cases can be identified that have direct impact on the cross section's scaling with recoil energy: $q \ll m_\phi^2$ and $q \gg m_\phi^2$. In the first case, where the momentum transfer is much smaller than the scalar's mass m_ϕ, we can neglect it in the denominator. Thus, the scalar part the cross section of Eq. (4.16) scales linearly with nuclear recoil energy T_A (and subsequently with detectable energy E). In the opposite case, $q \gg m_\phi^2$, the mediator mass in the denominator can be neglected and the cross section scales as $1/T_A$, an interesting feature that is different from the case of a light vector mediator.

The Lagrangian of Eq. (4.15) induces an additional interaction between neutrinos and electrons. As before, the Yukawa term induces a chirality flip such that this interaction is simply added to the SM EνeS as well,

$$\left(\frac{d\sigma}{dT_e}\right)_{\mathrm{E}\nu\mathrm{eS}\,+\,\phi} = \left(\frac{d\sigma}{dT}\right)_{\mathrm{E}\nu\mathrm{eS}} + \frac{(g_\phi^{\nu\mathrm{S}} g_\phi^{e\mathrm{S}})^2\, m_e^2 T_e}{4\pi E_\nu^2 (2m_e T_e + m_\phi^2)^2}\,. \tag{4.18}$$

Assuming universal coupling of the scalar yields the same quartic dependence as for neutrino-nucleus scattering: $(g_{\nu\mathrm{S}_\phi} g_{e\mathrm{S}_\phi}) \to g_\phi^4$. Two distinct limits for the momentum transfer can be identified for the cross section in Eq. (4.18) as well, i.e. $2m_eT_e \ll m_\phi^2$ and $2m_eT_e \gg m_\phi^2$. The different behavior of the signal expectation in these regions can be comprehended in the upper right plot of Fig. 4.3, where the expectation of neutrino-electron scattering in C1R1 is illustrated, again for masses that correspond to the two regions of the momentum transfer. Here, the linear scaling for higher mediator masses becomes evident.

Further, by comparing the expressions of Eq. (4.16) and Eq. (4.18), we can estimate bounds from neutrino-electron scattering to be stronger than the ones obtained from neutrino-nucleus scattering. For example, in the case of the light scalar being much lighter than the momentum transfer q, i.e. $m_\phi^2 \ll 2m_{e,A}T_{e,A}$, the scatterer mass in the numerator cancels out and we obtain the term $m_\phi^2 \ll 4m_{e,A}T_{e,A}^2$ in the denominator. By comparing both terms, it is clear that the large nucleus mass suppresses the cross section and leads to weaker limits in comparison to EνeS.

4.3.2.2 Results

The light mediator bounds at 90% C.L. obtained from the analysis of the CONUS RUN-1 data sets are shown in the lower plot of Fig. 4.3. Therein, we state our exclusion limits from CEνNS in the (m_ϕ, g_ϕ)-plane for the three selected benchmark quenching parameters $k \in \{0.12, 0.16, 0.20\}$. As mentioned earlier, the heavier nucleus mass m_A leads to a suppression of the cross section such that EνeS provides stronger limits for low mediator masses, in particular for mediator masses below $\sim$ 100 keV. The characteristic cases previously mentioned correspond to the flat $(q \gg m_\phi^2)$ and rising $(q \ll m_\phi^2)$ regions on the (m_ϕ, g_ϕ)-plane for both interaction channels. We select representative masses for the individual regions and show example coupling values which are still consistent with data (normal crosses) or are already excluded by the analyzed data (bold crosses). The chosen parameter points correspond to the exemplary signal expectations given in the upper plots of Fig. 4.3.

CEνNS allows to probe new couplings as low as $\sim 10^{-5}$ for the most favored quenching value of $k = 0.16$, while EνeS yields coupling bounds down to $\sim 2\cdot 10^{-6}$ for lowest mediator masses under study. For comparison, we also show bounds obtained from COHERENT (CsI and Ar) [134] and CONNIE (Si) [128] data.

Due to the lower neutrino energies, reactor experiments like CONNIE and CONUS allow to set stronger bounds for lower mediator masses, although both experiments have not detected SM CEνNS yet. CONUS reactor bounds exceed π-DAR limits for mediator masses below $\sim$ 10 MeV (assuming $k = 0.16$), while EνeS sets even stronger limits for scalar masses below $\sim$ 1 MeV.

We only present limits of other CEνNS experiments in the lower plot of Fig. 4.3.

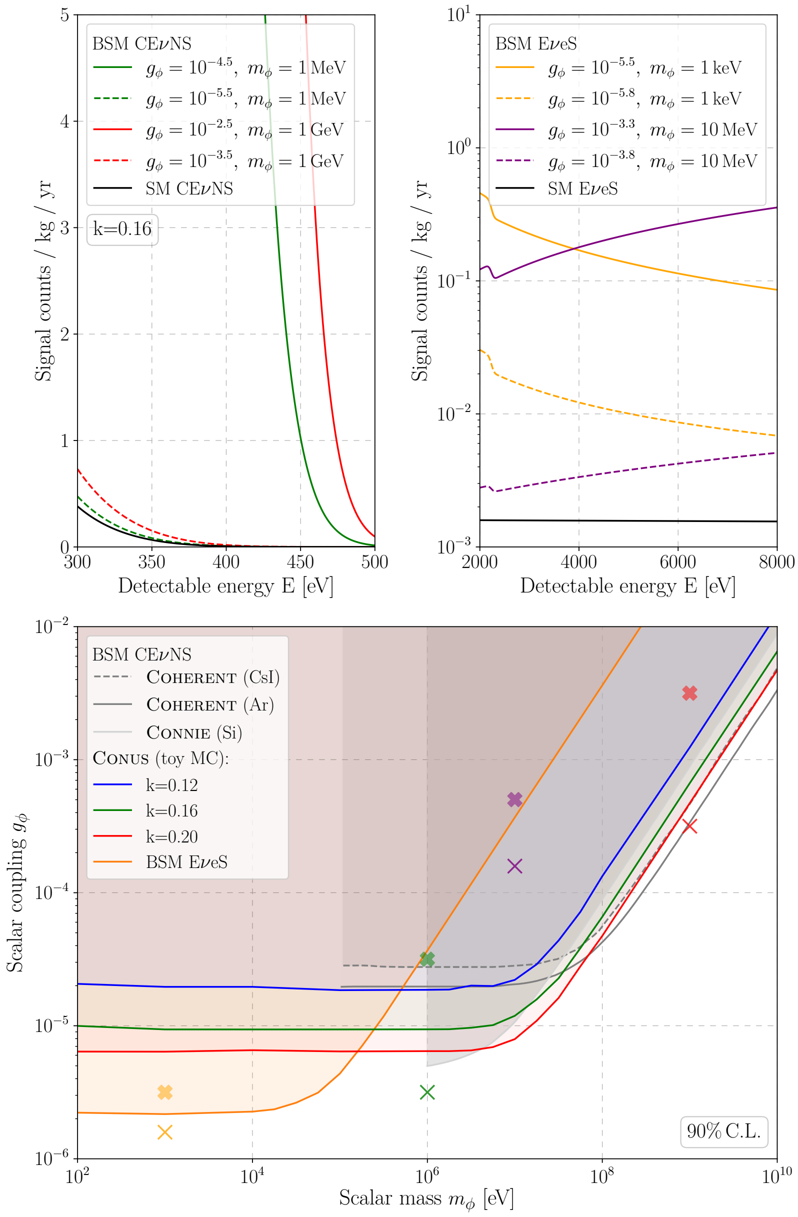

Figure 4.3.: **Top:** Signal expectations of a light scalar mediator for the data collection period C1R1. Spectra related nucleus scattering below 500 eV ($k = 0.16$) are given in the left plot, while spectra for electron scattering between $[2, 8]$ keV are shown in the right plot, both for different couplings and masses. Both interaction channels are compared to their SM equivalent. Note that the wiggles around ~ 2 keV can be related to the applied reactor model. **Bottom:** Exclusion limits at 90% C.L. for the light scalar mediator parameters (m_ϕ, g_ϕ) obtained from both CEνNS and EνeS. The exemplary signal expectations of both plots above are indicated with crosses, where bold crosses mark parameter combinations that can be excluded and regular crosses represent points that still agree with the analyzed data. Limits deduced from Coherent (CsI and Ar) (90% C.L.) [92] as well as Connie (95% C.L.) [128] data are given for comparison. Our results and the corresponding figure are published in Ref. [225].

However, we give a short summary of Ref. [129] in order to show how light scalar particles that couple to neutrinos might be constrained further. For the lepton number conserving interaction of Eq. (4.15), one might use constraints from meson decays like $K^+ \to l^+ \nu \phi$ or $\pi^+ \to l^+ \nu \phi$ with the scalar decaying into neutrinos. In supernovae such new interactions contribute new cooling modes, i.e. ν_R emission in our model, or affect the time of neutrino emission since this new interaction might reduce the neutrino mean free path λ inside the high-density layers of the collapsing star. Further, the new scalar interaction might also affect the number of relativistic degrees of freedom in the early Universe due to additional production of right-handed neutrinos via the t-channel process $\nu_L \bar{\nu}_L \to \nu_R \bar{\nu}_R$.

All in all, even though CONUS has not yet detected CEνNS, already competitive bounds are obtained from the analysis of nucleus scattering. For lowest mediator masses, CONUS bounds are stronger than the ones obtained from π-DAR sources. Although EνeS does not exhibit the same sensitivity to large mediator masses, it remains relevant for low mediator masses.

4.3.3 Light vector mediators

Next, we address a simplified model that enjoyed great popularity in the past because of its easy embedding into broader context via a $U(1)$ extension of the SM gauge group, i.e. a light vector mediator. Vector mediators arising from this simple SM extension have been studied in various scenarios and under assumption of different quantum numbers like gauged $B - L$ [317, 318], $L_\mu - L_\tau$ [319, 320], sequential SM [321] and many others, cf. Ref. [322, 323]. Therefore, we are going to explore the CONUS RUN-1 data sets in terms of vector mediators as well. Working in a simplified model framework, we can again ignore model-building and phenomenological consequences, while searching for spectral distortions due to a mediator in neutrino-nucleus as well as neutrino-electron scattering.

4.3.3.1 Cross sections

Here, we assume a massive Z'-like mediator that couples to leptons and quarks via a pure vector-like interaction. In the spirit of simplified models, we consider only interactions to the first generation of SM fermions. In this way, the model at low energy is described by the following Lagrangian

$$\mathcal{L}_{Z'} = Z'_\mu \left(g_{Z'}^{\nu \mathrm{V}} \bar{\nu}_L \gamma^\mu \nu_L + g_{Z'}^{e \mathrm{V}} \bar{e} \gamma^\mu e + g_{Z'}^{q \mathrm{V}} \bar{q} \gamma^\mu q \right) + \frac{1}{2} m_{Z'}^2 Z'_\mu Z'^\mu \,, \tag{4.19}$$

with the vector couplings $g_{Z'}^{x\mathrm{V}}$ for $x \in \{\nu, e, q\}$, its mass $m_{Z'}$ and $q \in \{u, d\}$ being the first generation of quarks. In contrast to the previous investigation, we do not include any new particles besides the mediator itself. Hence, only interactions of SM fermions, in particular left-handed neutrinos and right-handed antineutrinos, are assumed. Note that in the case of Majorana neutrinos, the vector-interaction term would vanish [1, Section 6.2]. Further, characteristic features of Z' BSM models like kinetic or mass mixing [324–326] are not considered.

In neutrino-nucleus and neutrino-electron scattering induced by Eq. (4.19) initial and final interaction states remain the same. Thus, interference between SM CEνNS and the new vector interaction is possible.

In order to shrink the model's parameter space further, we assume the vector mediator to exhibit universal couplings to the first generation of leptons and quarks, i.e. $g_{Z'} \equiv g_{Z'}^{\nu \mathrm{V}} = g_{Z'}^{e\mathrm{V}} = g_{Z'}^{u\mathrm{V}} = g_{Z'}^{d\mathrm{V}}$. Hence, we are again confronted with a parameter space of only two parameters: $(m_{Z'}, g_{Z'})$.

The cross section of CEνNS under the mediation of a light vector boson can be written as [91]

$$\left(\frac{d\sigma}{dT_A}\right)_{\mathrm{CE}\nu\mathrm{NS}+\mathrm{Z}'} = \mathcal{G}_{Z'}^2(T_A)\left(\frac{d\sigma}{dT_A}\right)_{\mathrm{CE}\nu\mathrm{NS}}, \tag{4.20}$$

with the SM CEνNS cross section given by Eq. (2.31) and the prefactor defined according to

$$\mathcal{G}_{Z'}(T_A) = 1 + \frac{g_{Z'}^{\nu\mathrm{V}}}{\sqrt{2}G_F}\frac{Q_{Z'}}{Q_W^{\mathrm{V}}}\frac{1}{2m_A T_A + m_{Z'}^2}, \tag{4.21}$$

with the weak nuclear charge, cf. Eq. (2.26), the nucleus mass m_A, the nuclear recoil energy T_A and the Fermi constant G_F. Here, the new nuclear charge due to the light vector boson is given by [108]

$$Q_{Z'} = \left(2g_{Z'}^{u\mathrm{V}} + g_{Z'}^{d\mathrm{V}}\right) Z + \left(g_{Z'}^{u\mathrm{V}} + 2g_{Z'}^{d\mathrm{V}}\right) N \to 3\, g_{Z'}\,(Z+N)\ , \tag{4.22}$$

where we used the simplifying assumption of universal vector couplings to quarks and leptons, i.e. $g_{Z'} \equiv g_{Z'}^{\nu\mathrm{V}} = g_{Z'}^{u\mathrm{V}} = g_{Z'}^{d\mathrm{V}}$. Plugging this into Eq. (4.21) yields a dependency on $g_{Z'}^2$, which results in the cross section's scaling of up to $g_{Z'}^4$.

Another feature is related to cross section's quadratic scaling with the prefactor $\mathcal{G}_{Z'}(T_A)$. As the new light vector boson interferes with the SM interaction, we expect constructive and destructive modifications according to the explicit coupling value. The quadratic dependency on the prefactor induces a degeneracy in the parameter space, since values of ±1 appear as SM-like CEνNS interaction. The case of $\mathcal{G}_{Z'}(T_A) = +1$ simply represents the pure SM CEνNS interaction ($g_{Z'} = 0$). In contrast, the case of $\mathcal{G}_{Z'}(T_A) = -1$, which originates from a relative sign between both contributions, yields a situation in which a light vector mediator contribution cannot be distinguished from SM CEνNS. This so-called "island-of-non-exclusion" can be approximated by evaluating the prefactor of Eq. (4.21) for the two kinematic regions,

$$g_{Z'} \simeq \begin{cases} \sqrt{-\frac{2\sqrt{2}G_F Q_W^{\mathrm{V}}}{3(Z+N)}}\, m_{Z'} \sim \sqrt{\frac{G_F}{3}}\, m_{Z'}\ , & \text{for } q \ll m_{Z'}^2\ , \\ \sqrt{-\frac{4\sqrt{2}G_F Q_W^{\mathrm{V}}}{3(Z+N)} m_A T_A} \sim \sqrt{\frac{2\sqrt{2}G_F m_n}{3}}\, T_A\ , & \text{for } q \gg m_{Z'}^2\ , \end{cases} \tag{4.23}$$

where in the last steps, we assumed $Z \approx N$ and $m_p \approx m_n$.

At this point, we point out the connection between vector NSIs, cf. Sec. 4.2.2, and the simplified model considered here: If the vector mediator is very heavy it can be integrated out such that the following mapping between both frameworks is obtained [327]

$$\epsilon^{q\mathrm{V}}_{\alpha\beta} = \frac{\left(g^{\nu\mathrm{V}}_{Z'}\right)_{\alpha\beta} g^{q\mathrm{V}}_{Z'}}{2\sqrt{2}G_F M^2_{Z'}} \,, \tag{4.24}$$

where the couplings $\epsilon^{q\mathrm{V}}_{\alpha\beta}$ depend on the flavor structure in Eq. (4.19). Although this mapping becomes more accurate the heavier the mediator masses are, limits cannot be directly converted into each other, cf. Sec. 4.3.1. For light mediators, especially for $q \sim m^2_{Z'}$, this connection is invalid and, therefore, the mediator's propagators have to be considered as well. This allows to take into account kinematic contributions to the signal's spectral shape, while vector NSIs only modify the CEνNS signal's overall strength.

The simplified Lagrangian of Eq. (4.19) also induces modifications to EνeS, whose combined cross section is now given by [107]

$$\left(\frac{d\sigma}{dT_e}\right)_{\mathrm{E}\nu\mathrm{eS}\,+\,\mathrm{Z}'} = \left(\frac{d\sigma}{dT_e}\right)_{\mathrm{E}\nu\mathrm{eS}} + \frac{\sqrt{2}G_F m_e g_V g^{\nu\mathrm{V}}_{Z'} g^{e\mathrm{V}}_{Z'}}{\pi(2m_eT_e + m^2_{Z'})} + \frac{m_e (g^{\nu\mathrm{V}}_{Z'} g^{e\mathrm{V}}_{Z'})^2}{2\pi(2m_eT_e + m^2_{Z'})^2} \,, \tag{4.25}$$

with the Z boson's vector coupling to electrons $g_V = -\frac{1}{2} + 2\sin^2\theta_W$.

Similar to the case of a light scalar, we expect stronger bounds than from EνeS due to the electron mass in the denominator being much lighter than the nucleus mass, which appears in the denominator of Eq. (4.21).

The event spectra for the data collection period C1R1 are illustrated in the upper plots Fig. 4.4 for both CEνNS and EνeS in comparison to the corresponding SM interactions. Exemplary parameter points are chosen in order to illustrate the two different kinematic regions, $q \ll m^2_{Z'}$ and $q \gg m^2_{Z'}$. Again, each mass is shown with a coupling that still agrees with data and a second one that can already be excluded. Moreover, the spectral behavior of EνeS can be understood by considering the denominators in Eq. (4.25) in the limits $q \ll m^2_{Z'}$ and $q \gg m^2_{Z'}$. While the first condition leads to a constant contribution to the SM cross section that scales only with the new coupling(s), the latter condition leads to a contribution that decreases with rising electron recoil energy T_e.

4.3.3.2 Results

The exclusion limits at 90% C.L. for the light vector parameters $(m_{Z'}, g_{Z'})$ obtained from our investigation are highlighted in the lower plot of Fig. 4.4. We present our results in comparison to limits deduced from data of the CEνNS experiments Coherent [91, 133, 134] and the Connie [128]. As before, we indicate the example parameter values of the upper plots of Fig. 4.4 with crosses in the lower limit plot, where bold crosses represent already excluded values and normal crosses those still compatible with data. While the "island-of-non-exclusion" can be resolved with the Coherent data, both reactor experiments lack sensitivity, necessary to reach this area of the parameter space. At higher mediator masses, $\gtrsim 10\,\mathrm{MeV}$, Coherent data set the strongest bounds due to higher momentum transfers. CONUS limits of $k = 0.16$ almost reach limits obtained from CsI data, while limits from Ar data are still stronger for low mediator masses. Connie limits, however, are about a factor of 2 stronger than the ones of CONUS and are able to set stronger bounds than Coherent. Moreover, our limits from EνeS exceed the ones of

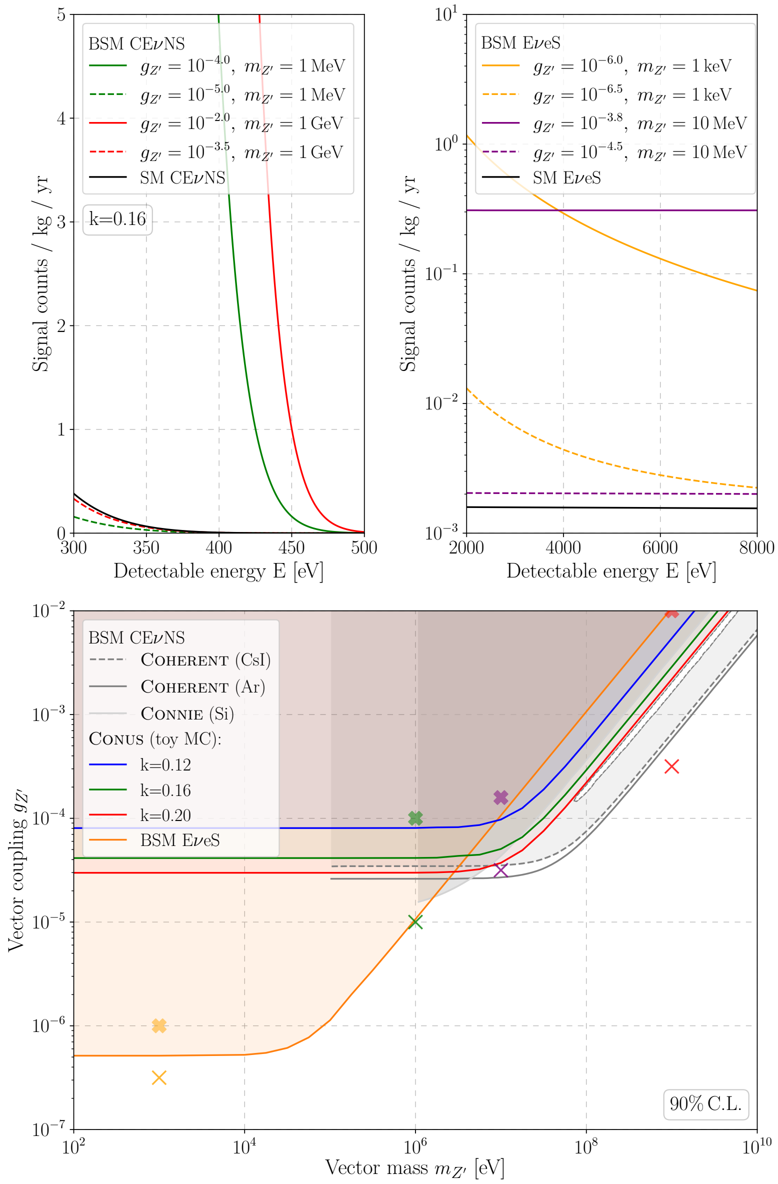

Figure 4.4.: **Top:** Signal expectations of a light vector mediator for the data collection period C1R1. Spectra of nucleus scatterings below 500 eV ($k = 0.16$) are given in the left plot, while spectra for electron scattering between $[2, 8]$ keV are shown in the right plot, both for different couplings and masses. Again, both interaction channels are compared to their SM equivalent. **Bottom:** Exclusion limits at 90% C.L. for the light vector mediator parameters $(m_{Z'}, g_{Z'})$ obtained from both CEνNS and EνeS. The signal expectation for the given couplings and masses are indicated with crosses, where bold crosses refer to parameter points that can be excluded with our analysis and normal crosses being values still in agreement with the analyzed data. Limits extracted from other CEνNS measurements are given for comparison, i.e. Coherent (CsI and Ar) (90% C.L.) [134] and Connie (95% C.L.) [128]. The "island of non-exclusion", where $\mathcal{G}_{Z'} = -1$ is already reached by the Coherent, while reactor experiments still lack sensitivity. Our results and the corresponding figure are published in Ref. [225].

CEνNS for mediator masses $m_{Z'} \lesssim 10\,\mathrm{MeV}$. With the CONUS RUN-1 data sets and assuming $k = 0.16$, we can probe light vector couplings via CEνNS down to $\sim 4 \cdot 10^{-5}$. Bounds from EνeS are even stronger and constrain the vector coupling down to values of $\sim 5 \cdot 10^{-7}$ for lightest masses under consideration.

Finally, we briefly comment on limits obtained from other experiments: Within simplified models the assumption of universal couplings is generic. However, the most popular benchmark model for $U(1)$ extensions of the SM is a gauged $U(1)_{B-L}$ symmetry for which a plethora of bounds exists from various experiments. Bounds on $B - L$ models exist for example from di-electron resonant searches at ATLAS [328] and beam-dump experiments [329, 330]. Investigations of neutrino-electron scattering [326, 331], dark photon searches at BaBar [332, 333] and at LHCb [334] contributed as well. Collections of such bounds can be found, for example, in Refs. [323, 335] for general models and for $B-L$ in Ref. [336]. In order to map our simplified model framework (with universal couplings) to this benchmark, one simply needs to exchange the plus with a minus sign in the prefactor $\mathcal{G}_{Z'}(T_A)$, cf. Eq. (4.21) since this already reflects the $B - L$ charge assignment.

4.4 Neutrino magnetic moment and millicharge

In our last investigation we search for potential signatures of neutrino electromagnetic properties, i.e. a finite νMM as well as a finite νMC. In contrast to the previous investigations, we focus here on EνeS in the energy region of $[2, 8]\,\mathrm{keV}$ and analyze in addition to extended RUN-1 data sets also data of RUN-2. This allows us to work with combined data sets which enlarge the exposure by factors of 3.3 and 3.5 (compared to the exposures below 1 keV) for reactor ON and OFF periods, respectively, cf. Tab. 4.1. In the following, we introduce into the notion of electromagnetic neutrino properties and motivate why such kind of searches are especially interesting in the context of BSM searches at a reactor site. This summary is mainly based on the comprehensive review by C. Giunti and A. Studenikin [119], while additionally Refs. [1, 48] were consulted. After that, we focus on the impact of such properties on EνeS and the corresponding expectation in the CONUS data, before we present our results, i.e. limits on the νMM μ_{ν_e} as well as on the νMC q_{ν_e}.

4.4.1 Neutrino electromagnetic properties

Within the SM, neutrinos are neutral fermions and cannot undergo any classic electromagnetic interaction, i.e. tree-level interactions between the photon and the neutral neutrino are not possible. However, an effective charge radius, cf. Sec. 5.4.2, can be acquired due to radiative corrections, which is the only electromagnetic property they exhibit in the SM. In many BSM models neutrinos can obtain electromagnetic properties through loop processes, usually linked to their masses and mixings. Consequently, they might interact directly with electromagnetic fields or electrically charged particles. Such effects are interesting in astronomical contexts, where neutrinos propagate over long distances in electromagnetic fields or might affect cooling processes of stars. Especially, the neutrino's charge neutrality is a key assumption underlying many high energy astrophysical investigations [337].

For example, in a SM extension with three right-handed neutrinos [338–341] νMMs are typical features. Further, electromagnetic characteristics, if observed, might help in revealing the neutrino's fermionic nature since diagonal dipole moments are forbidden for Majorana neutrinos [342–344].

At loop-level neutrino-photon couplings can be obtained by higher order interactions and in the one-photon approximation it is described for N massive neutrinos by the following effective interaction Hamiltonian

$$\mathcal{H}_{\mathrm{em}}(x) = j_\mu(x) A^\mu(x) = \sum_{k,j=1}^{N} \bar{\nu}_k(x) \Lambda_\mu^{kj} \nu_j(x) A^\mu(x)\,, \tag{4.26}$$

with the effective electromagnetic neutrino four-current $j_\mu(x)$, the photon field $A^\mu(x)$ and Λ_μ being a $(N \times N)$ matrix in neutrino space.[6] The vertex function Λ_μ can be decomposed in a form that is consistent with Lorentz and electromagnetic gauge invariance [343, 344]

$$\Lambda_\mu(q) = \left(\gamma_\mu - q_\mu \not{q}/q^2\right) \left[\mathbb{f}_Q(q^2) + \mathbb{f}_A(q^2) q^2 \gamma_5\right] - i\sigma_{\mu\nu} q^\nu \left[\mathbb{f}_M(q^2) + i\mathbb{f}_E(q^2)\gamma_5\right]\,, \tag{4.27}$$

with the four hermitian $(N \times N)$ matrices of form factors $\mathbb{f}_x$ with $x \in \{Q, M, E, A\}$, i.e. $\mathbb{f}_x = \mathbb{f}_x^\dagger$. The corresponding nomenclature becomes clear when looking at the case of coupling to a real photon, i.e. $q^2 = 0$,

$$\mathbb{f}_Q^{fi}(0) = q_{fi}\,, \qquad \mathbb{f}_M^{fi}(0) = \mu_{fi}\,, \qquad \mathbb{f}_E^{fi}(0) = \epsilon_{fi}\,, \qquad \mathbb{f}_A^{fi}(0) = a_{fi}\,, \tag{4.28}$$

with $q_{fi}, \mu_{fi}, \epsilon_{fi}, a_{fi}$ being the charge, magnetic and electric dipole moment as well as the anapole moment of diagonal $(f = i)$ and transition $(f \neq i)$ type. Below, we will see that the corresponding quantities exhibit different properties whether the neutrino is a Dirac or a Majorana fermion. Up to now, form factors were introduced to account for the internal structure of a nucleon or a nucleus, respectively, cf. Sec. 2.1.3 and Sec. 2.1.1.2. Here, they are introduced to account for different moments of loop-induced electromagnetic interactions of an elementary neutrino.

Assuming CP-invariance and neutrinos to be Dirac fermions allows to deduce further characteristics of the form factor $\mathbb{f}_{Q,M,E,A}$:

$$\begin{aligned}
\nu:&\quad \mathbb{f}^D_{Q,M,A} = \left(\mathbb{f}^D_{Q,M,A}\right)^T = \left(\mathbb{f}^D_{Q,M,A}\right)^*\,, &\quad \mathbb{f}_E &= -\left(\mathbb{f}^D_E\right)^T = -\left(\mathbb{f}^D_E\right)^*\,,\\
\bar{\nu}:&\quad \bar{\mathbb{f}}^D_{Q,M} = -\left(\mathbb{f}^D_{Q,M}\right)^T = -\left(\mathbb{f}^D_{Q,M}\right)^*\,, &\quad \bar{\mathbb{f}}^D_{E,A} &= \left(\mathbb{f}^D_{E,A}\right)^T = \left(\mathbb{f}^D_{E,A}\right)^*\,,
\end{aligned} \tag{4.29}$$

where the expressions for an antineutrino follow the vertex function $\bar{\Lambda}_\mu^{fi} = \mathcal{C}\left[\Lambda_\mu^{if}\right]^T \mathcal{C}^\dagger$, cf. Ref. [119, Section III.A]. Thus, for Dirac neutrinos charge, magnetic dipole and anapole form factors are real and symmetric, while the electric dipole form factor matrix is imaginary and antisymmetric. For Dirac antineutrinos, the properties of the charge, dipole electric and magnetic form factors are changed, while the anapole form factor remains the same. Diagonal entries are real and equal, up to sign shifts due to charge conjugation in the case of charge and both dipole moments.

---

[6] More precisely, $\mathcal{H}_{\mathrm{em}}$ describes an effective electromagnetic interaction vertex with neutrino matrix element $\langle \nu_f(p_f)|\, j_\mu(0)\, |\nu_i(p_i)\rangle = \bar{u}_f(p_f)\Lambda_\mu^{fi}(p_i, p_j) u_i(p_i)$ [119, Section III.A]. One can show that $\Lambda_\mu^{fi}(p_i, p_j)$ only depends on the transferred momentum $q = p_f - q_i$, which relies on a similar reasoning as applied in the description of nucleon currents in Sec. 2.1.1.2.

Majorana neutrinos are their own antiparticles and represent the real solution of the corresponding Dirac equation [345]. Thus, they have only half the DOFs of Dirac neutrinos, which is also reflected in their electromagnetic properties. The effective vertex function of Majorana neutrinos exhibits the form[7]

$$\Lambda_{\mu}^{\mathrm{M}fi}(q^2) = \Lambda_{\mu}^{fi}(q^2) + \mathcal{C}\left[\Lambda_{\mu}^{if}(q^2)\right]^{T}\mathcal{C}^{\dagger}\,, \tag{4.30}$$

and can be cast into the same form as Eq. (4.27). Hermiticity of the form factor matrices and the Majorana condition, i.e. $\nu = \nu^c = \mathcal{C}\bar{\nu}^T$ [345, 346], yields the following properties of the Majorana-type form factors

$$\nu = \nu^c: \qquad \mathbb{f}^{\mathrm{M}}_{Q,M,E} = -\left(\mathbb{f}^{\mathrm{M}}_{Q,M,E}\right)^T = -\left(\mathbb{f}^{\mathrm{M}}_{Q,M,E}\right)^*\,, \qquad \mathbb{f}^{\mathrm{M}}_{A} = \left(\mathbb{f}^{\mathrm{M}}_{A}\right)^T = \left(\mathbb{f}^{\mathrm{M}}_{A}\right)^*\,. \tag{4.31}$$

As a consequence the charge, magnetic and electric form factor matrices are antisymmetric, while the anapole form factor matrix is symmetric. Moreover, this implies that a Majorana neutrino does not have diagonal charge and dipole magnetic and electric form factors! As in the Dirac case, the off-diagonal entries are imaginary and real diagonal anapole form factors are still allowed. Consideration of CP invariance puts further relations among transition form factors, e.g. either electric or magnetic form factors can exist but not both at the same time. In addition, magnetic dipole form factors can only occur together with charge form factors and electric form factors are only accompanied by anapole form factors.

Turning the above statements around, the observation of diagonal electric or magnetic dipole moments for Majorana neutrinos would be an indicator of CPT invariance [343, 344].

4.4.2 Magnetic and electric dipole moments

A generic feature of magnetic and electric dipole moments of neutrinos is their direct proportionality to their mass that leads to a suppression of expected values orders of magnitude below the current experimental limits. Thus, the observation of a νMM above the (extended) SM expectation would be a signature for BSM physics. Here, we briefly discuss νMM values that are expected from Dirac and Majorana neutrinos in the SM extended with three right-handed neutrinos and list generic theory bounds of potential BSM physics.

Calculations of the neutrino electromagnetic dipole moments in the SM extended with three right-handed neutrinos (via loop-diagrams) [338–340] give the following result at leading order in the ratio $\left(\frac{m_l}{m_W}\right)^2$

$$\left.\begin{matrix}\mu^D_{kj}\\ \epsilon^D_{kl}\end{matrix}\right\} \simeq \frac{3eG_F}{16\sqrt{2}\pi^2}\,(m_k \pm m_j)\left(\delta_{kj} - \frac{1}{2}\sum_{l=e,\mu,\tau} U^*_{lk}U_{lj}\frac{m_l^2}{m_W^2}\right)\,, \tag{4.32}$$

---

[7] It is obtained by application of a Fourier transform for Majorana fermions to the matrix element $\langle\nu_f(p_f)|\, j_\mu(0)\,|\nu_i(p_i)\rangle$, cf. Ref. [119, Section III.B].

with the neutrino masses $m_{k,j}$, mixing matrix U and the charged-lepton masses m_l with $l \in \{e, \mu, \tau\}$. Numerical estimates for the diagonal ($k = j$) and off-diagonal ($k \neq j$) dipole moments yield

$$\mu^D_{kk} \simeq 3.2 \cdot 10^{-19} \left(\frac{m_k}{1\,\mathrm{eV}}\right) \mu_B \,, \tag{4.33}$$

$$\left.\begin{matrix} \mu^D_{kj} \\ i\epsilon^D_{kj} \end{matrix}\right\} \simeq -3.9 \cdot 10^{-23} \mu_B \left(\frac{m_k \pm m_j}{1\,\mathrm{eV}}\right) \sum_{l=e,\mu,\tau} U^*_{lk} U_{lj} \left(\frac{m_l}{m_\tau}\right)^2 \,, \tag{4.34}$$

with the neutrino mass $m_{k,j}$, the charged-lepton mass m_l and the Bohr magneton μ_B. There are no diagonal entries for electric dipole moments by virtue of Eq. (4.29), while the transition dipole moments are highly suppressed, a feature analogous to the suppression of flavor-changing NCs in the SM (GIM mechanism). The dependence on the light neutrino mass is evident and the SM limit can be obtained by $m_i \to 0$. However, while in the massless SM, an observed νMM would imply a chirality-flipping interactions, here the dipole moments are generated via radiative correction that do not change chirality!

For Majorana neutrinos, diagonal dipole moments are forbidden due to Eq. (4.31), but the off-diagonal elements can be estimated by

$$\left.\begin{matrix} \mu^M_{kj} \\ \epsilon^M_{kj} \end{matrix}\right\} \simeq \mp i 7.8 \cdot 10^{-23} \mu_B \left(\frac{m_k \pm m_j}{1\,\mathrm{eV}}\right) \sum_{l=e,\mu,\tau} \left(\frac{m_l}{m_W}\right)^2 \left\{\begin{matrix} \mathrm{Im}\Big[U^*_{lk} U_{lj}\Big] \,, \\ \mathrm{Re}\Big[U^*_{lk} U_{lj}\Big] \,, \end{matrix}\right. \tag{4.35}$$

again with the neutrino mass $m_{k,j}$, the charged-lepton mass m_l and the Bohr magneton μ_B. As in the Dirac case, off-diagonal elements are suppressed as they generally imply a flavor-change by a NC. In the Majorana case, the neutrino mixing matrix exhibits two additional phases (the Majorana phases), such that a direct comparison to the Dirac case is not directly possible besides the obvious factor of 2.

The connection between dipole moments and neutrino masses is a frequent features for the simplest SM extensions. In minimal extensions of the SM with massive Dirac neutrinos, νMMs can appear with values of $\mu_\nu < 10^{-15} \mu_B$ [118, 119, 338]. Much weaker constraints up to values of $10^{-7} \mu_B$ are obtained for Majorana neutrinos [342, 347]. “Naturalness upper bounds” have been derived for Dirac and Majorana neutrino and NP arising above the EW scale [119, 347–349]

$$\begin{aligned} \text{Dirac}: \quad & \mu^{\mathrm{D}}_\nu \lesssim 3 \cdot 10^{-15} \mu_B \left(\frac{m_\nu}{1\,\mathrm{eV}}\right) \left(\frac{1\,\mathrm{TeV}}{\Lambda}\right)^2 \,, \\ \text{Majorana}: \quad & \mu^{\mathrm{M}}_{ll'} \lesssim 4 \cdot 10^{-9} \mu_B \left(\frac{M^{\mathrm{M}}_{ll'}}{1\,\mathrm{eV}}\right) \left(\frac{1\,\mathrm{TeV}}{\Lambda}\right)^2 \left|\frac{m_\tau^2}{m_l^2 - m_{l'}^2}\right| \,, \end{aligned} \tag{4.36}$$

where Λ is the scale where new physics is expected to enter. The Dirac limit is presented in the mass basis, i.e. m_ν with $\nu = 1, 2, 3$ being the mass eigenvalues. The Majorana limit is expressed in the flavor basis, i.e. $M^{\mathrm{M}}_{ll'}$ is the Majorana mass matrix in the flavor basis $l, l' = e, \mu, \tau$. For comparison a transformation into the mass basis might be performed via $\mu^{\mathrm{M}}_{kj} = U_{lk} \mu^{\mathrm{M}}_{ll'} U_{l'j}$ [119]. These limits are obtained under the assumption that radiative νMM-contributions to the neutrino mass remain “natural”, i.e. $\delta m_\nu \lesssim m_\nu$.

The general theme in model-building of large νMMs is to obtain large contributions in loop diagrams that are connected to a photon, while at the same time suppressing the corresponding loop (without a photon) contributing to neutrino mass. This is necessary since otherwise large νMM values would be in conflict with neutrino mass measurements. Symmetries generally help in enlarging νMM values while keeping neutrino mass small [350–352], but also suppression mechanisms can be advantageous [353]. A summary of ways to generate large νMMs is given in Ref. [354]. Neutrino magnetic moments have been discussed in frameworks like left-right (parity) symmetric models [355] and the MSSM [356]. Further, more exotic ways have been discussed in the context of extra dimensions [357] or tensor interactions [306], which we encountered already in Sec. 4.2.3.

In general, there is a large gap between experimental limits at $\mathcal{O}(10^{-11})\mu_B$ [119, Table III] and the natural theoretical bounds of Eq. (4.36). For example, a discovery of a (transition) νMM $\mu_\nu > 10^{-15}\mu_B$ might indicate neutrinos to be Majorana particles [348, 349].

Effective magnetic moments In a realistic experimental configuration neutrinos are detected at some distance from their source as flavor states, such that they generally undergo oscillations. As a consequence the measured νMM value incorporates additional neutrino mixing and oscillations parameters [358, 359]. One defines the so-called squared effective magnetic moments for Dirac neutrinos and antineutrinos as[8]

$$\left.\begin{matrix}\mu^2_{\nu_l}(L,E_\nu)\\ \mu^2_{\bar{\nu}_l}(L,E_\nu)\end{matrix}\right\} = \sum_j \left| \sum_k U^*_{lk} \exp\left(\mp i \frac{\Delta m^2_{kj} L}{2E_\nu}\right)(\mu_{jk} - i\epsilon_{jk}) \right|^2 , \tag{4.37}$$

with $j,k = 1,..3$, while an extension to potential existing sterile neutrinos can easily be done. Besides the flavor oscillation parameters, namely propagation length L and mass squared difference Δm^2_{kj}, both electric and magnetic dipole moments contribute to the scattering (detection) process while there is only a oscillation-induced phase difference between the effective magnetic moments of neutrinos and antineutrinos. Fortunately, for very short-baseline experiments such as CONUS, usual oscillations can be neglected and the exponential function is safely approximated with unity. This results in a quantity that is independent of oscillation parameters but still incorporates both electric and magnetic dipole moments, thus for $L \ll 2E/\Delta m^2$ the effective magnetic moment is given by

$$\text{Dirac}: \qquad \mu^2_{\nu_l} \simeq \mu^2_{\bar{\nu}_l} \simeq \Big[U\left(\mu^2+\epsilon^2\right)U^\dagger + 2\,\mathrm{Im}\Big[U\mu\epsilon U^\dagger\Big]\Big]_{ll} , \tag{4.38}$$

$$\text{Majorana}: \qquad \mu^2_{\nu_l} \simeq \sum_{k=1}^{3}\left(\tilde{\mu}^2_k + \tilde{\epsilon}^2_k\right) - \left|\sum_{k=1}^{3} U_{lk}\left(\tilde{\mu}_k - i\tilde{\epsilon}_k\right)\right|^2 , \tag{4.39}$$

with U being the neutrino mixing matrix and $x_{jk} = i\epsilon_{jkm}\tilde{x}_m$ for $x \in \{\mu, \epsilon\}$. Thus, Majorana neutrinos can exhibit an effective νMM to which only transition moments contribute. For solar experiments like Borexino [150], matter effects in neutrino propagation through the Sun have to be considered as well, cf. Ref. [119, Section IV.b]. Of course, the same line of reasoning applies to an effective νMC q_{ν_l}.

---

[8] In literature, the terms “magnetic moment” usually refers to the experimentally accessible squared effective magnetic moment.

4.4.3 Electromagnetic induced EνeS: νMM and νMC

In the following we are going to introduce the electromagnetically induced cross section for EνeS that we are going to cover in our analysis. We perform a full analysis of the extended CONUS RUN-1 and RUN-2 data sets, cf. Tab. 4.1, for the scattering induced by a finite effective νMM. Subsequently, we convert the deduced limit into a limit on an effective νMC by taking advantage of the interactions different behavior.

The interaction induced by a finite effective νMM is chirality-flipping and consequently added to the SM interaction.[9] The EνeS cross section is then given by [118]

$$\left(\frac{d\sigma}{dT_e}\right)_{\mathrm{E}\nu\mathrm{eS}\,+\,\nu\mathrm{MM}} = \left(\frac{d\sigma}{dT_e}\right)_{\mathrm{E}\nu\mathrm{eS}} + \frac{\pi\alpha_{\mathrm{em}}^2}{m_e^2}\left(\frac{1}{T_e}-\frac{1}{E_\nu}\right)\left(\frac{\mu_{\nu_e}}{\mu_B}\right)^2 , \tag{4.40}$$

with the fine-structure constant $\alpha_{\mathrm{em}} \sim 1/137$, the electron mass m_e and recoil energy T_e as well as the energy of the incident neutrino E_ν. Moreover, this interaction exceeds SM EνeS for

$$T_e \lesssim \frac{\pi^2\alpha_{\mathrm{em}}^2}{G_F^2 m_e^3}\left(\frac{\mu_{\nu_e}}{\mu_B}\right)^2 . \tag{4.41}$$

Figure 4.5 illustrates the νMM-induced interactions for selected νMM values in comparison to the SM case in our benchmark C1R1 and is discussed in detail below. Note the characteristic dependence of Eq. (4.40) on T_e^{-1} and the kinematic cut at much higher energies, (cf. Eq. (2.30) with $m_A \rightarrow m_e$), which is advantageous for low threshold detectors and low background as is the case for CONUS. Thus, small values of νMMs can be probed by lowering the energy threshold T_e. However, in the present analysis, we consider only data at higher energies in order to make use of an additional extended data set with larger exposure and to avoid additional uncertainties that occur when entering the energy region below 1 keV, e.g. through the incorporation of the “detection threshold” description, cf. Eq. (4.2).

Further, EνeS can be introduced by a finite effective effective νMC q_{ν_e}, which in contrast is chirality-conserving. Thus, this new contribution is interfering with the SM interaction. The differential cross section for EνeS under consideration of an effective νMC q_{ν_e} is given by [119, 360, 361]

$$\left(\frac{d\sigma}{dT_e}\right)_{\mathrm{E}\nu\mathrm{eS}\,+\,\nu\mathrm{MC}} \simeq \left(\frac{d\sigma}{dT_e}\right)_{\mathrm{E}\nu\mathrm{eS}} + \frac{4\sqrt{\alpha_{\mathrm{em}}}G_F}{\sqrt{2}T_e}\left(\frac{q_{\nu_e}}{e}\right) + \frac{2\pi\alpha_{\mathrm{em}}^2}{m_e T_e^2}\left(\frac{q_{\nu_e}}{e}\right)^2 , \tag{4.42}$$

with the elementary charge e, the Fermi constant G_F as well as the effective νMC q_{ν_e}. The second terms represents the interference between SM and νMC-induced EνeS. In contrast to the νMM case, the interaction via an effective νMC scales as T_e^{-2} in leading contribution, which implies a steeper growth for lower recoil energies compared to the νMM case, cf. Fig. 4.5. Moreover, the different scaling between both reactions can be quantified by taking the ratio of both cross sections (neglecting the interference term and

---

[9] This behavior is due to the presence of $\sigma_{\mu\nu}$ in Eq. (4.27), which couples only two fields of different chirality. This is due to $\bar{v}_{L/R}\,\sigma_{\mu\nu}\,\nu_{L/R}$=0.

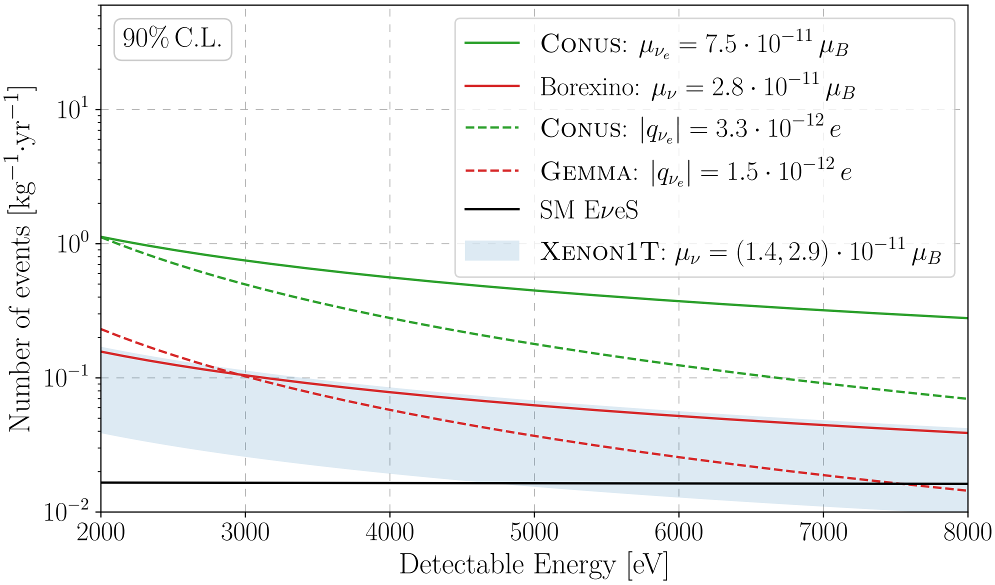

Figure 4.5.: EνeS signal expectation related to the obtained limits of νMM and νMC for data collection period C1R1. We show the event spectra for the obtained limits at 90% C.L. on the effective νMM and effective νMC. For comparison, the current world's best earthbound limits are illustrated as well, i.e. the effective νMM of the Borexino experiment [150] and the bound on the effective νMC deduced from the former world's best νMM of the GEMMA experiments [151, 362]. The signal expectations of νMM values discussed as explanation for the recently measured XENON1T excess [47] are indicated by the light blue band, while the flat spectrum of SM EνeS is represented by the solid black curve. The results of our investigation in addition to a similar figure going to be published as Ref. [284].

the dependency on the neutrino energy E_ν) [151]:

$$R = \frac{(d\sigma/dT_e)_q}{(d\sigma/dT_e)_\mu} \simeq \frac{2m_e}{T_e}\left(\frac{(q_{\nu_e}/e)}{(\mu_{\nu_e}/\mu_B)}\right)^2 . \tag{4.43}$$

Following Ref. [151], this expression can be used to translate an obtained upper limit of the νMM into a limit of the νMC. In particular, by assuming a null result of the νMM investigation and the νMC interaction to be much smaller than the νMM one, i.e. $R \leq 1$, the effective νMC limit is obtained via [151]

$$q^2_{\nu_e} \lesssim \frac{T_e}{2m_e}\left(\frac{\mu_{\nu_e}}{\mu_B}\right)^2 e^2 , \tag{4.44}$$

which corresponds to the procedure we pursue in the next section.

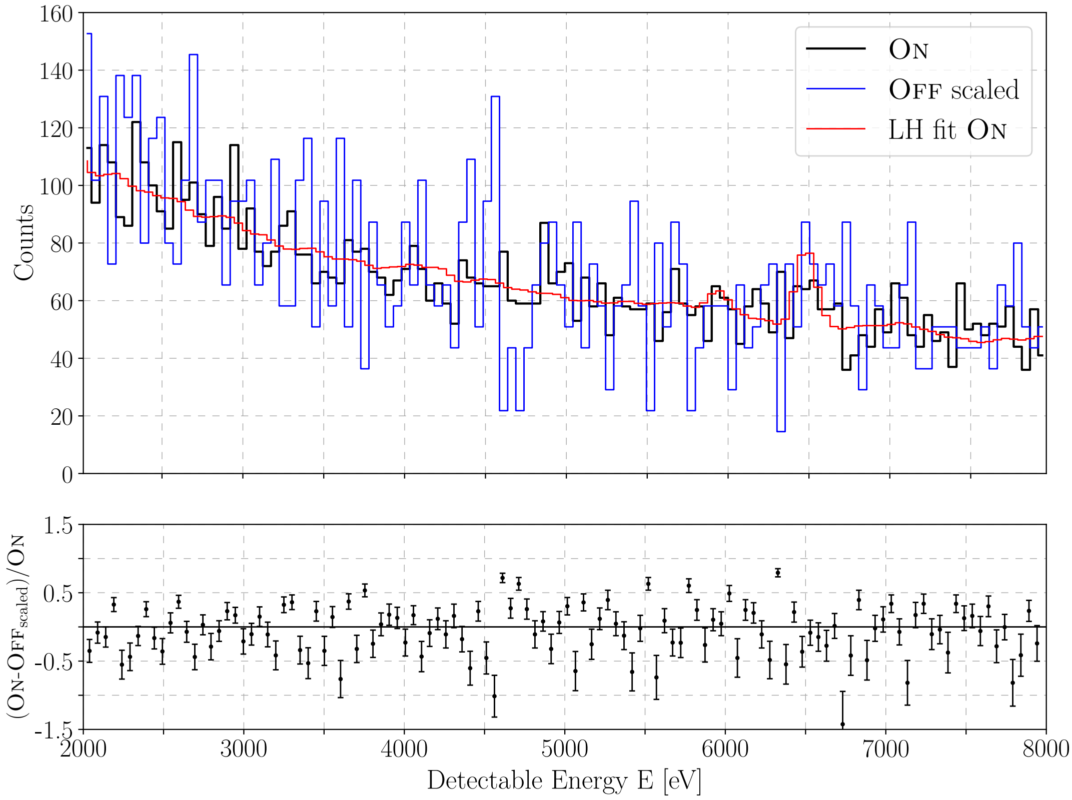

Figure 4.6.: Example fit of the combined νMM investigation in the energy region $[2, 8]$ keV. The performed likelihood fit is shown for data collection period C1R1 and is compared to the obtained data as well as the scaled of reactor Off data set. The results of our investigation in addition to a similar figure are published in Ref. [284].

4.4.4 Results on the effective νMM and νMC

The analysis of the extended run-1 and run-2 data sets in terms of νMM-induced neutrino-electron scatterings shows no indication of a finite effective νMM, c.f. Fig. 4.6. Thus, we report an upper limit of

$$\mu_{\nu_e} < 7.5 \cdot 10^{-11}\,\mu_B \text{ (90\% C. L.)}\,, \tag{4.45}$$

which deviates from the world's best earthbound limit by a factor of ~ 2.7 only. The corresponding event spectrum is illustrated in Fig. 4.5, together with the best earthbound limit of the Borexino experiment ($\mu_\nu < 2.8 \cdot 10^{-11}\mu_B$) [150]. At present, only the Borexino experiment is able to probe possible νMM solutions to the reported Xenon1T excess ($\mu_\nu \in [1.4, 2.9] \cdot 10^{-11}\mu_B$) [47], cf. Fig. 4.5. In comparison to other reactor experiments that searched for finite νMMs, our limit is comparable to the one obtained from the Texono experiment ($\mu_{\nu_e} < 7.4 \cdot 10^{-11}\mu_B$) [363]. The Gemma experiment still provides the strongest limit of $\mu_{\nu_e} < 2.9 \cdot 10^{-11}\mu_B$ [362] obtained from a reactor experiment. Limits from accelerator experiments on the effective muon magnetic moments are about an order of magnitude weaker, i.e. $\mu_{\nu_\mu} < 6.8 \cdot 10^{-10}\mu_B$ [364]. Note that existing bounds are probing "natural" regions of Majorana neutrinos, cf. Eq. (4.36). Here, we highlight the complementary approach between solar and reactor experiments as the solar neutrino flux renders Borexino insensitive to Majorana phases, whereby accelerator and reactor experiments could provide hints for leptonic CP violation [365]. Further, strong bounds exist from astrophysical environments like supernova cooling ($\mu_\nu < (1.1 - 2.7) \cdot 10^{-12}\mu_B$) [123] or from the luminosity of red-giants in globular clusters ($\mu_\nu < 2.2/2.6 \cdot 10^{-12}\mu_B$) [124, 125], which are generally an order of magnitude stronger than laboratory measurements.

Our limit on an effective νMM can be converted via Eq. (4.44) into an upper limit for an effective νMC. Under the assumption of no νMM-related signal being present in our data and a minimal recoil energy of $T_e \sim 2\,\text{keV}$, the CONUS νMM limit constrains an effective νMC to be

$$|q_{\nu_e}| < 3.3 \cdot 10^{-12}\ e\ (90\%\ \text{C.L.})\,. \tag{4.46}$$

An example spectrum of such an effective νMC is indicated in Fig. 4.5 in comparison with the current world's best limit obtained from the GEMMA νMM limit, i.e. $q_{\nu_e} \lesssim 1.5 \cdot 10^{-12}e$ [151, 362]. The strongest laboratory bound on an effective νMC comes from so-called "neutrality of matter" investigations, in which charge conservation in neutron beta decay is tested, i.e. $q_{\nu_e} \lesssim 3 \cdot 10^{-21}e$ [366]. Moreover, bounds are obtained from astrophysical measurements, e.g. solar cooling ($q_\nu \lesssim 6 \cdot 10^{-14}e$), red giant luminosity ($q_{\nu_e} \lesssim 2 \cdot 10^{-14}e$) or from Supernovae (such as SN1987A) ($q_\nu \lesssim 3 \cdot 10^{-17}e$) [366]. From the investigation of cosmological charge asymmetry one can infer information on the individual particle species, which constrains the νMC to be $q_{\nu_l} \lesssim 4 \cdot 10^{-35}e$ [367].

In the end, we would like to mention that νMMs can additionally be constrained via CEνNS with $\mu_\nu \lesssim 10^{-9}\mu_B$ for both ν_e and ν_μ [88, 90, 122]. Although not specifically designed for νMM investigations, CONUS sets a bound in the range of recent limits via EνeS. The obtained νMM limits (and thus the νMC limit) is expected to get stronger with improvements related to the ongoing experiment's CEνNS-measuring campaign. Further investigation possibilities and the signal's scaling with experimental characteristics are discussed in Sec. 5.4.2.

4.5 Summary and outlook

After the SM CEνNS investigation of the previous chapter, we present in this chapter the results of the analysis of several CEνNS-related BSM models, i.e. new interactions due to NSIs or light simplified mediators, and of neutrino electromagnetic properties such as νMMs and νMCs. Besides BSM modification for CEνNS, effects on EνeS are investigated in the context of light mediator searches. For CEνNS-related investigations, the RUN-1 data sets already used in the SM analysis are taken, while EνeS is analyzed at a higher energy range $[2, 8]\,\text{keV}$, which allows to recover data and, thus, gain larger exposure, cf. Tab. 4.1. The performed investigations rely on data sets that exhibit exposures of 209 kg d and 38 kg d for reactor ON and OFF for the analysis of CEνNS below 1 keV, while the extended data sets for EνeS between $[2, 8]\,\text{keV}$ have exposures of 649 kg d and 94 kg d for reactor ON and OFF, respectively.

Minor modifications of our analysis are summarized in Sec. 4.1. For example, systematic uncertainties related to the applied MC background model at higher energies are incorporated (Sec. 4.1.2) and a refined noise edge description is chosen (Eq. (4.2)), which allows to extend the data sets to slightly lower energies. In addition, the investigation of EνeS demands the consideration of low-energy reactor antineutrinos. Thus, the detector-specific antineutrino spectra (Sec. 3.2.1) are combined with simulated antineutrino spectra at energies below the IBD threshold (Sec. 4.1.3). Due to these adjustments, the sampling procedure of our test statistic needs to be adapted as well (Sec. 4.1.4). All uncertainties of the refined analyses procedure are listed in Tab. 4.2.

In the individual BSM analysis, the likelihood function introduced in Sec. 3.3.3.2 is extended with the corresponding cross sections. At the moment of carrying out the analyses, quenching was still subject to high uncertainties and, therefore, it remained the dominating uncertainty also throughout these investigations. In contrast to the previous chapter, we state the limits obtained (at 90% C.L.) in dependence of three benchmark k-parameters which span the range of until mid of 2021 favored quenching factors, i.e. $k \in \{0.12, 0.16, 0.20\}$. Although CONUS could report only bounds on CEνNS at a reactor site, our BSM analyses yield null results in all test cases. The subsequently deduced bounds are competitive with existing bounds from other CEνNS experiments in some region of the parameter space for most models.

In the case of vector NSI (Sec. 4.2.2), our bounds strongly depend on the k-parameter and are at the moment not competitive with existing bounds obtained from COHERENT (CsI and Ar) or XENON1T solar data, cf. lower plot in Fig. 4.1. Here, knowledge of the accurate QF is crucial and competitive limits are expected alongside a CEνNS detection with the CONUS set-up. Especially resolving the regions of destructive interference demands a high-statistics signal detection. Assuming $k = 0.16$, the CONUS set-up with data sets used in this analysis is at the moments able to exclude vector NSI-related physics up to about 100 GeV. For tensor NSIs (Sec. 4.2.3), the signal's extent to higher energies allows to set the world's best limits on electron-type couplings to up and down quarks, cf. the lower plot in Fig. 4.2. Quenching proves to be less relevant such that our limits are determined by the experimental specifications. Moreover, from our limits on tensor NSI couplings, the scale of associated NP is estimated to lie above ~ 360 GeV, cf. Eq. (4.6).

Further, the low energy of reactor antineutrinos revealed their potential in the investigation of simplified mediator models (Sec. 4.3), especially for smallest particle masses. Higher neutrinos energies yield stronger bounds on the coupling strengths for larger mediator masses, as in the case of π-DAR sources. For light scalar mediators (Sec. 4.3.2), CONUS provides stronger bounds for masses below 10 MeV ($k = 0.16$). Under the assumptions of universal couplings, values down to $g_\phi \sim 10^{-5}$ ($k = 0.16$) can be probed, cf. lower plot of Fig. 4.3. Limits for light vector mediators (Sec. 4.3.3) are compatible with limits from COHERENT CsI data, but are weaker than the ones obtained from COHERENT Ar data. Couplings down to $g_{Z'} \sim 4 \cdot 10^{-5}$ ($k = 0.16$) can be probed, again under the assumption of universal couplings to all fermions involved (in the reaction), cf. lower plot of Fig. 4.4. In both simplified models, our limits from EνeS are more restrictive than the ones from CEνNS for mediator masses below $m_\phi \sim 100$ keV and $m_{Z'} \sim 10$ MeV and can probe couplings down to $g_\phi \sim 2 \cdot 10^{-6}$ and $g_{Z'} \sim 5 \cdot 10^{-7}$ in the case of light scalar and vector mediators, respectively. In general, EνeS bounds from a reactor site exceed current CEνNS bounds (independent of the neutrino source) for boson masses of below $m_\phi \sim 100\,\mathrm{keV}$ and $m_{Z'} \sim 1\,\mathrm{MeV}$. The limits and resulting plots of the performed BSM analyses discussed up to now are published in Ref. [225].

The effective νMM is investigated separately via EνeS by consideration of an even larger data set. Furthermore, the obtained limit on the effective νMM is converted into a bound on the effective νMC, cf. Eq. (4.44). With an exposure of 689 kg d reactor ON and 132 kg d reactor OFF, the effective νMM can be constrained with the current CONUS specifications to be $\mu_{\nu_e} < 7.5 \cdot 10^{-11}\ \mu_B$ (at 90% C.L.), which is competitive with the value obtained by the TEXONO [218] and which is a factor of 2.7 above the world's best earthbound limit. The associated effective νMC is limited to $|q_{\nu_e}| < 3.3 \cdot 10^{-12}\ e$ (at 90% C.L.), which deviates by a factor of 2.2 from the current world's best value [151]. Figure 4.5 illustrates the expected signals of both limits for our benchmark case C1R1. The results of this νMM analysis going to be published as Ref. [284].

In the end, we highlight that we are able to present expressive results for most of the investigated models, although a CEνNS measurement with CONUS remains pending. So far, the CONUS data show no indication for any BSM physics related to the neutrino sector. The investigated frameworks have been chosen to be quite general in order to cover a broad class of models, at the price of leaving out questions of model-building or UV completeness. For specific models, the presented contours have to be viewed individually and/or with appropriate corrections.

Nevertheless, in concordance with the results of Ch. 3, the chosen technology has proved to be capable of reaching the specifications that are necessary for potential CEνNS or CEνNS-related investigations. Moreover, this first BSM investigations already indicate the vast potential of CEνNS-measuring experiments. As before, experimental improvements in the near future will be beneficial also for the deduced BSM limits. A measurement of the QF will decrease this uncertainty of our investigations and is going to improve the analysis also in terms of computation time. Investigations within the CONUS Collaboration regarding this matter will settle this issue soon [257]. Being able to pin down CEνNS in an actual measurement will be beneficial in several ways. For example, testing the destructive interference regions for vector NSIs and light vector mediators will become possible. A future high-statistic CEνNS signal exhibits a smaller statistical uncertainty which is going to increase the sensitivity to BSM parameters. Consequently, further BSM phenomena become worthwhile investigating, e.g. sterile eV-mass neutrino and DM searches.

Improved conditions that are necessary for CEνNS measurements with CONUS, will be advantageous for future νMM limits as well, cf. Sec. 5.1. Investigating νMM-induced EνeS below 1 keV would be the next logical step. Constraining the neutrino charge radius via nucleus or electron scattering and investigating νMM-induced CEνNS are further opportunities that might become possible with an improved experimental setting, cf. Sec. 5.4. Some of these near- and far-future CEνNS possibilities are discussed in the next chapter.

Chapter 5

The future of Conus and CEνNS

We close this work by discussing the next stage of the CONUS experiment and an outlook of the general promising future of this newly established interaction channel. The already implemented or planned improvements of the experimental set-up and refinements of the analysis scheme are discussed. After that, further SM and BSM investigation possibilities are covered that might become interesting with an observation of the CEνNS signal. In the end, the importance of complementary CEνNS measurements with different target materials and sources as well as applied astronomical aspects are highlighted.

5.1 Improvements of the Conus set-up

Now we want to discuss experimental improvements that have been implemented stepwise by the CONUS Collaboration since the beginning of data collection at reactor-site. These changes affect the branches environmental stability, data acquisition and background reduction and will improve the quality of the upcoming data sets in several ways which we illustrate in the following.

Environmental stability For the operation of a sensitive experiment like CONUS, special environmental conditions mainly in terms of stable background and noise levels are key for a successful CEνNS detection. It turned out that guaranteeing such demanding laboratory conditions close to an intense reactor core is a challenging task. For example, large temperature fluctuations, especially in outage periods, rising radon concentrations or noise events from steam generators complicated ongoing data collection. An existing noise-temperature correlation in the data led to the loss of large exposure since the strict background criteria for the CEνNS ROI could not be fulfilled anymore. However, site monitoring was improved, background and noise events identified by auxiliary measurements and appropriate mitigation strategies were chosen in order to maintain sufficient and constant environmental conditions. In particular, temperature and radon levels are monitored at several control point at and around the experimental set-up and an air conditioning system in combination with a tent surrounding the apparatus was established to stabilize temperatures. In doing so, the CONUS Collaboration is confident to maintain sufficiently stable experimental conditions and thus to prevent large losses of exposure due to needed cuts for the future data collection periods. Until the reactor shutdown at the end of 2021, the CONUS experiment continues with the collection of reactor ON data. At least one year of pure reactor OFF exposure is planned to be taken in 2022.

Data acquisition system and background reduction Since 20 May 2021 a new DAQ system is used for all CONUS detectors together with the former used Lynx DAQ system. Although not comparable to the Lynx system in terms of trigger efficiency and overall stability, the new established CAEN digitizer system allows recording of waveform information of the detected signals. Further, with carefully chosen settings the system is able to achieve lower noise thresholds. Moreover, a clear separation between electronic noise and physics signals seems achievable, which allows to remove uncertainties related to the detector threshold description from the current analysis scheme, cf. Eq. (4.2). However, being sensitive to such low energy regions puts even stronger requirements on environmental stability in order to guarantee satisfying background conditions below the currently chosen ROIs. Hence, the DAQ response to changing noise levels, e.g. through a spontaneous temperature rise in room A-408, needs to be quantified and is likely to come along with a refined systematic uncertainties related to its trigger efficiency.

Both features of this new DAQ system represent important improvements. Being able to lower the detectable energy threshold, enlarges the expected CEνNS signal and furthermore brings us on comfortable situation of choosing ROIs where the noise edge can safely be excluded. Furthermore, having access to signal waveforms enables the application of PSD techniques [213], which reduce certain background events from the data. In particular, electron-hole pairs that are created in the detector's semi-active layer, close to the detector surface are subject of a weaker drift field than pairs created in the detector bulk. The resulting signals, the so-called "slow pulses", are weaker and slower as a fraction of these pairs immediately recombine again. Consequently, the read-out signal pulses exhibit a reduced number of charges and feature slower rise times [215]. Efficient rejection of such events allows to reduce background events even in the sub-keV region and thus is of special importance for CEνNS investigations. However, since the number of released charges is proportional to the stored energy in the detector, the separation between slow pulses and bulk events becomes more difficult towards lower energies [214, 216]. The TEXONO Collaboration established these techniques for energy values down to $300 - 350\,\text{eV}$ [368]. Investigations of the CONUS Collaboration (with major contribution of Jakob Henrichs) recently proved first successful application of PSD methods in the CEνNS region of interest, i.e. down to $\sim 300\,\text{eV}$) [369].

Quenching factor measurement for germanium In parallel to the main experimental operation the CONUS Collaboration (under the lead of Dr. Aurélie Bonhomme) performed an investigation of the quenching effect within germanium by directly measuring nuclear recoils in a thin low-threshold HPGe detector. The experiment was performed at Physikalisch-Technische Bundesanstalt (PTB) in Germany, which provides a monoenergetic neutron beam [257]. Nuclear recoil energies in the region of $[0.4, 6.2]\,\text{keV}$ are selected via coincidence detection of scattered neutrons in liquid scintillator detectors at different angles. For each selected nuclear recoil energy, the individual QFs are determined at the few percent-level and are compatible with the Lindhard model (without an adiabatic correction factor) for $k = 0.164 \pm 0.004$ (stat. + syst.), cf. Fig. 5.1. Quenching has been assumed to exhibit more dependencies than actually incorporated by Lindhard theory [168]

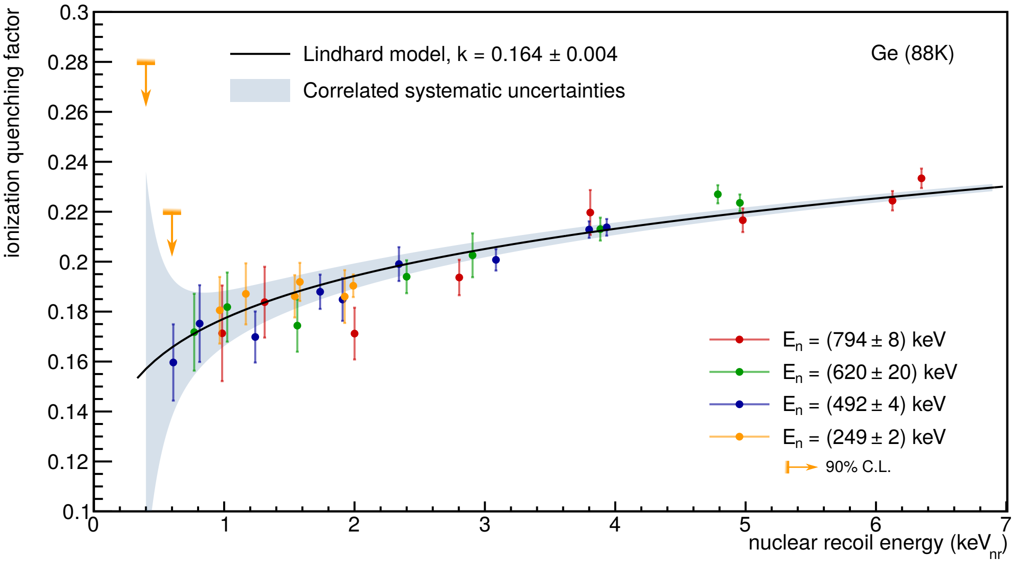

Figure 5.1.: New measurement of the QF in germanium which is performed by the CONUS Collaboration. Neutron beams of different energies were shot on a HPGe target and corresponding nuclear recoils were recorded, while the energy of scattered neutrons was measured with liquid scintillator tube detectors. QFs of the individual energies were determined and fit to the Lindhard model. Figure is published in Ref. [257].

and recent measurements in silicon [370] and germanium [270] also deviate only at very low energies from the Lindhard description, cf. Fig. 5.1. On the contrary other investigations still confirm our conclusions, cf. Refs. [169, 266–269]. Therefore, more investigations at very low recoil energies and at different cryogenic temperatures are needed to settle this issue because of its strong consequences for further CEνNS and light DM investigations.

With this new dedicated measurement for the CONUS detectors at hand, we can now incorporate this knowledge in future analyses. Thus, the k-parameter will be treated as an additional fit parameter that is constrained via a pull-term to the value obtained from our measurement.

Prospects for future data and steps towards CEνNS precision physics Finally, we give a glimpse on what to expect from all the experimental improvements, whereby we point out the estimating character of the following simple counting analysis. Future results might deviate since systematic effects as well as signal shape information are not considered here.

Due to the improved experimental conditions and the reactor shutdown at the end of 2021, we assume new CONUS data sets to have equal reactor ON and OFF runtimes. With the CAEN we are able to collect data of about 250 d (reactor ON) for each detector. Including the detectors C1-C4, an overall exposure of 2.7 kg yr is then achievable, which we assume for both, reactor ON and reactor OFF periods. Further, for the new CAEN DAQ we generally assume an empirical formula of $E_{\mathrm{thr}} \sim 3\Delta E_{\mathrm{P}}$ [368, 371] to be valid, such that for the pulser widths measured at KBR $\Delta E_{\mathrm{P}} \sim 65 - 75\,\mathrm{eV}$, cf. Ref. [82], the energy

$\mathrm{E_{thr}}$ [eV]	CONUS [counts]	Z	V	CONUS-100 [counts]	Z	V
300	30	0.15	42	$5.5 \cdot 10^3$	2.1	$227 \cdot 10^{-3}$
275	49	0.25	16	$9.1 \cdot 10^3$	3.4	$85 \cdot 10^{-3}$
250	99	0.50	4.1	$18 \cdot 10^3$	6.8	$22 \cdot 10^{-3}$
225	178	0.88	1.3	$33 \cdot 10^3$	12.0	$7 \cdot 10^{-3}$
200	286	1.40	0.5	$53 \cdot 10^3$	19.0	$3 \cdot 10^{-3}$

Table 5.1.: Absolute number of CEνNS events for the improved CONUS specifications mentioned in the text together with a potential mass upgrade (CONUS-100). The values represent exposures of 2.7 kg yr (CONUS) and 500 kg yr (CONUS-100) and are given in terms of different energy threshold $\mathrm{E_{thr}}$, while fixing the ROI's upper end to 500 eV. Further, the CEνNS signal significance $Z = s/\sqrt{b}$ and expected variance $V = (s+b)/s^2$ are determined as well, cf. Sec. 2.3.4. Note that these values represent a first simple counting analysis without proper consideration of systematic uncertainties or spectral shape information.

thresholds $E_{\mathrm{thr}} = 195 - 225\,\mathrm{eV}$ are obtained. As detector efficiency, an estimate of the CAEN DAQ of C1R1 is taken. Note that this represents already an optimistic assumption as systematic uncertainties related to the CAEN trigger efficiencies are not included. As background rate we assume a constant contribution of $\sim 40\,\mathrm{kg^{-1}\,d^{-1}}$, which is higher than the background level in the energy region $[0.4, 1]\,\mathrm{keV}$, cf. Sec. 3.3.2. This is due to higher background levels observed after the pressure test of the KBR building at the end of RUN-2 in 2019 [82]. It might be further reduced by application of a PSD cut, for which we assume a background reduction efficiency of $\sim 20\%$ throughout the entire signal region. Finally, a quenching parameter of $k = 0.16$ is assumed, while other experimental parameters, i.e. reactor properties or detector resolution, remain unchanged. The estimated CEνNS events with corresponding signal significance for these improved CONUS specifications are summarized in Tab. 5.1. Additionally, we list values for a potential mass upgrade (CONUS-100) with an exposure of 500 kg yr, while other experimental parameters are assumed unchanged. Here, limitations due to probably less reactor OFF exposure are not considered. From the results of this rough counting analysis, it is evident that by reaching energy thresholds of $\sim 200\,\mathrm{eV}$, the detection of CEνNS is realistic, especially when the detector's energy threshold lies below the ROIs. Unfortunately, the lower energy thresholds obtained with the CAEN DAQ are partially compensated by the loss in detection efficiency. Limited exposure and increased background levels further limit the expected significance However, the experimental improvements will be reflected in results of future data sets.

On the contrary, an experimental upgrade with equal thresholds represents a clear step towards precision CEνNS investigations allowing to probe various BSM models with large accuracy. This step is accompanied with several adaptions in the established analysis routines such as an explicit incorporation of form factors to quantify the *almost* fully coherent situation at a reactor site as well as consideration of radiative corrections [372] and uncertainties of couplings [238, Table 1.1] in the CEνNS cross section. So far, the main uncertainty has been quenching, which is now determined with good precision by our investigation, such that reactor-related quantities, i.e. the reactor antineutrino emission spectra, become the focus of attention, cf. next section. In any case, measuring CEνNS with high precision and high statistics achieved with the next generation of experiments will have significant impact on many SM and further BSM aspects.

5.2 Improved reactor antineutrino spectra

The performed analysis of the previous chapters relied on antineutrino emission spectra provided by the HMM, which are adjusted to the observed "reactor bump" [198, 199] by correction factors taken from Ref. [194]. However, during our investigations new measurements and insights were published, which should be considered in future CONUS data analyses at reactor-sites.

In 2020, a new directly measured IBD antineutrino reactor spectrum was published by the Reno Collaboration, which reflects data taken from August 2011 to March 2020 and is measured via two detectors (with baselines of 419 m and 1447 m, respectively) [196]. Antineutrinos were emitted by six PWRs with maximum thermal power $2.8\mathrm{GW}_{\mathrm{th}}$ with uncertainties on the fission fractions[1] and the reactor thermal powers to be of 0.7% and 0.5%, respectively. Further, a $\sim 6\%$ deviation from HMM clearly visible around 6 MeV was identified as well, cf. left plot of Fig. 5.2. Although compatible in terms of statistics and uncertainties with the used Daya Bay data [194], the spectrum is provided in a smaller energy binning, which might be important when spectral feature are considered in the context of precision measurements. The incorporation of the provided covariance matrix remains unchanged. Hence, the usage of the newer Reno spectrum can be seen as an upgrade of data without changing the general treatment that underlies our analysis.

Furthermore, the Daya Bay Collaboration provided unfolded (IBD-measured) spectra of individual spectral components and, in addition, proposed a method to derive a prediction of the spectral antineutrino emission for other experiments [195], which we will summarize in the following. By unfolding their recorded and converted positron energy data, antineutrino emission spectra are obtained for ^{235}U, the combination of both plutonium isotopes (combo) and the overall spectrum (total) in 25 energy bins with uncertainties estimated to be $\sim 2\%$. Data-based predictions for the antineutrino energy spectrum are then obtained via

$$\begin{aligned}
S_{\mathrm{pred}} &= \mathbf{R} \times \mathbf{S} \\
&\equiv \begin{pmatrix}\mathbf{I}_{25} & \Delta\alpha_{235}\cdot\mathbf{I}_{25} & \Delta\alpha_{239}\cdot\mathbf{I}_{25} & \Delta\alpha_{238}\cdot\mathbf{I}_{25} & (\Delta\alpha_{241}-0.183\Delta\alpha_{239})\cdot\mathbf{I}_{25}\end{pmatrix} \\
&\quad \times \begin{pmatrix}S_{\mathrm{total}} & S_{235} & S_{\mathrm{combo}} & S_{238} & S_{241}\end{pmatrix}^T ,
\end{aligned} \tag{5.1}$$

with $\mathbf{R}$ being a (25×125) matrix and $\mathbf{S}$ being a column vector containing the (5×25) spectral bin values of total, ^{235}U, combined plutonium, ^{238}U and ^{241}Pu spectra. The quantities $\Delta\alpha_i = \alpha_i - \alpha_i^{\mathrm{DB}}$ describe the difference between the Daya Bay fission fractions and the ones of the reactor of interest.[2] Taking spectra for ^{238}U and ^{241}Pu from theoretical

---

[1] The fission fractions of the Reno experiment are (^{235}U, ^{238}U, ^{239}Pu, ^{241}Pu)=(0.57, 0.07, 0.30, 0.06) [196].

[2] The fission fractions of the Daya Bay experiment underlying this methods are (^{235}U, ^{238}U, ^{239}Pu, ^{241}Pu)=(0.564, 0.076, 0.304, 0.056) [195].

models is recommended, e.g. from Ref. [247] (15% bin-to-bin uncorrelated uncertainty) and from Ref. [248] (10% bin-to-bin uncorrelated uncertainty). In general, both spectra are expected to have only a mild impact on the overall result, cf. Ref. [195]. Corresponding uncertainties and correlations, in terms of a covariance matrix, are calculated via $\mathbf{Cov}_{\text{pred}} = R \cdot \mathbf{Cov}_{\text{unfold}} \cdot R^T$ with $\mathbf{Cov}_{\text{unfold}}$ given in Ref. [195]. For other than IBD measurements, the cross section needs to be removed from the provided spectra, a similar procedure we have already used in Sec. 3.2.1. The application of this method allows the incorporation of data-based (measured!) reactor spectra into the CONUS analysis scheme and may be used in order to circumvent potential issues in the theory spectra underlying the HMM.

More recently, interesting results on the side of theoretical calculations appeared. New ab-initio spectra that rely on an updated nuclear database were published, which exhibit only a minor flux deviation compared to the one detected by the Daya Bay experiment, with a remaining shape distortion (the "reactor bump") in the energy region $[5, 7]$ MeV [373]. Further, a refined conversion method including first forbidden transitions of beta decays, cf. Ref. [185], indicating a vanishing "reactor bump", while enhancing the RAA [374]. Moreover, new beta decay measurements of ^{235}U and ^{239}Pu indicate an excess in normalization of old measurements that underlie the HMM. Reevaluation of the uranium antineutrino energy spectra, also by taking into account a newer measurement of the ^{238}U beta decay spectrum [192], points towards a vanishing RAA. All these findings accumulated in a recent evaluation of reactor antineutrino spectra by Ref. [375], which finds the RAA being present only for the HMM and the model of Ref. [374]. The antineutrino spectra of Refs. [373, 376] show only deviations of $\sim 1\sigma$ between data and predictions, with the first being the most favored ab-initio calculation and the latter the most favored conversion method (in terms of goodness-of-fit). If these results persist, the RAA basically diminishes and, with it, a strong motivation for eV-mass sterile neutrinos as potential explanation. However, the still present anomalies seen in gallium experiments [377, 378] as well as short-baseline oscillations experiments [144, 379] leave room for further speculations, but demand more advanced explanations.

Considering these results in the application of the above introduced "Daya Bay method" suggests to use the refined ^{238}U spectra of Ref. [376], while taking ^{241}Pu spectra either from the standard conversion method of HMM [248] or ab-initio calculations [373]. Since Ref. [376] used the unmodified HMM spectrum of ^{241}Pu and obtained agreement between data and predictions, the author tends to use these spectra within future investigations as well.

In the end, we point out the potential of CEνNS as a flavor-independent tool for spectral measurements. As we showed in Fig. 3.5, CEνNS exhibits highest sensitivity to the highest antineutrino energies of the applied spectrum, even for a relatively small parameter value of $k = 0.16$. Thus, a new CEνNS measurement would allow to constrain these spectral parts, which also exhibit the largest uncertainties, cf. left plot in Fig. 5.2. In this way, CONUS can contribute knowledge to the subject of reactor antineutrino emission.

Although, in principle, a detection of the reactor antineutrino spectrum below the IBD threshold is possible, it requires sensitivity to very low recoil energies, which we are going to estimate in the following: Assuming neutrino energies of 2 MeV yields maximum nuclear recoils of ~ 120 eV, cf. Eq. (2.30). With the recently measured QF in germanium ($k = 0.16$, no adiabatic correction assumed), the maximum detection energy is estimated to be ~ 15 eV. Consequently, such endeavors are far from possible with kg-size HPGe

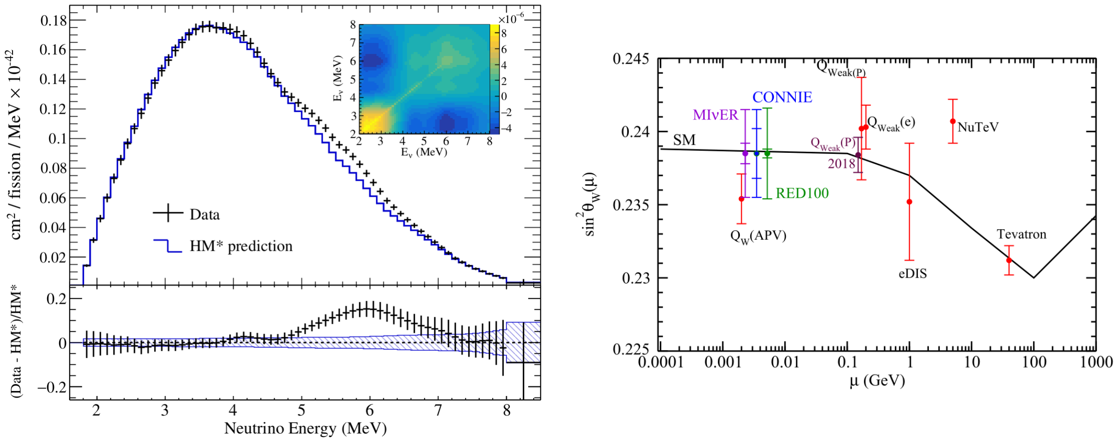

Figure 5.2.: **Left:** New reactor antineutrino spectrum provided by the Reno Collaboration. The unfolded spectrum (crosses) is compared to predictions of the adapted HMM (histogram). Error bars represent their total uncertainty, while a covariance matrix from unfolding is given in the inset. The ratio between the reactor spectrum and the HMM is given below with the blue region representing the uncertainties of the latter. The figure is taken from Ref. [196]. **Right:** Sensitivity of CEνNS experiments to the Weinberg angle compared to the SM prediction indicated by the black line ($\overline{\text{MS}}$ renormalization scheme). The Figure is taken from Ref. [98].

detectors in the near future. On the other side, small-size cryogenic or CCD detectors like the ones used by Miner [72], Connie [71] or ν-cleus [75] might be able to reach these low energy thresholds, however, at the cost of a reduced target mass. The authors of Ref. [87] directly compared CEνNS and IBD in terms of reactor power monitoring and safety and came to the conclusion that for CEνNS detectors detection thresholds below 200 eV are needed to be competitive with current IBD detectors. In particular, CEνNS devices seem more practicable as a complement to IBD detection, in particular by detection of neutrinos emitted from plutonium breeding [87].

5.3 Nuclear form factors

The cross section's dependence on the nuclear form factor, or more precisely the proton and neutron form factors, allows to obtain more insights about nuclear physics from CEνNS measurements. The neutron form factor is of particular interest as it is more difficult to obtain than its proton counterpart that can be probed via electromagnetic interactions in, e.g. proton-electron scattering [166, Section 7]. In principle, neutron form factors are determined in hadron scatterings experiments, whereby their extraction relies on explicit modeling of non-perturbative strong interactions. In contrast, CEνNS allows a model-independent measurement and, thus, complements other measurements even with larger uncertainties [380]. As covered in Sec. 2.1.3, nuclear form factors are basically the Fourier transform of the underlying charge distribution, which allows to determine its root mean square (RMS) $R_{p,n}$. Ref. [93] showed that with CEνNS measurements it is principally possible to probe the neutron's form factor up to its fourth moment at a π-DAR source in a Taylor expansion of the form

$$F_N(q^2) \approx \left(1 - \frac{q^2}{3!}\langle R_n^2\rangle + \frac{q^4}{5!}\langle R_n^4\rangle + \mathcal{O}(q^6)\right) , \tag{5.2}$$

with the momentum transfer q^2 and $\langle R_n^k\rangle = \int \rho_n r^k d^3r / \int \rho_n d^3r$, where ρ_n represents the neutron charge distribution. In these terms, the neutron RMS radius is defined as $R_n = \sqrt{\langle R_n^2\rangle}$. First values have already been obtained form COHERENT data sets [94, 95, 381]. Uncertainties related to different form factor paramterizations are investigated in Ref. [261] and estimated to be negligible for reactor investigations.

Nuclear form factors are most crucial in situations, where a large departure from scattering off a point-like nucleus appears, i.e. large momentum transfers as it is the case at π-DAR sources. So far, we have neglected potential deviations from full coherence, which is only exact for zero momentum exchange $q^2 = 0$, and approximated the nuclear form factor in Eq. (2.31) with unity, a simplification allowed by the low momentum transfers of reactor antineutrinos. In future precision measurements, this factor should be introduced, in order to accurately describe the situation even in *almost* fully coherent circumstances. Here, the complementarity between reactors and π-DAR sources can be advantageous for the overall determination since reactors could provide signals at almost zero momentum transfers that can be compared to deviations from point-like scattering at π-DAR sources.

Such investigations are important as they help to precisely determine the neutron skin $\Delta R_{np} = R_n - R_p$, a quantity that is strongly related to the equation of state of nuclear matter [382–384] and plays an important role in several processes, e.g. nuclear reactions and collisions as well as the behavior of nuclear matter in astrophysical objects like neutron stars [385]. In that sense laboratory CEνNS measurements might complement astrophysical investigations, e.g. via gravitational waves from neutron star mergers [386, 387].

5.4 Further BSM neutrino phenomenology

Now, we discuss a selection of BSM investigations that we have not been considered so far, or which seem suitable with more improved experimental specifications. In particular, we elaborate on further investigations of electromagnetic neutrino properties and discuss the role of CEνNS in searches for new fermions in the context of DM or eV-mass sterile neutrinos. Note that many of them can be addressed at the same time, but degeneracies among them in terms of their impact on CEνNS, i.e. overall normalization or spectral shape, complicate matters. Therefore, comparison with complementary measurements might be considered case by case.

5.4.1 Weinberg angle at low-Q value

The dependence of the CEνNS cross section in Eq. (2.31) on the weak mixing angle is only mild because of appearing couplings in the weak nuclear charge, i.e. $Q_{\mathrm{Q}} \propto Z(1 - 4\sin^2\theta_W)$. However, its scaling with the squared number of proton can still be used to measure it with large precision at very low momentum transfers. Moreover, such a measurement contributes to an energy region where additional measurements are needed and uncertainties are still large. Therefore new precise determinations, especially from a neutrino interaction, is a desired peculiarity. At the moment, the most precise measurements at low energy come from determination of atomic parity violation [388, Section 10.3], and from the determination of the electron's [389] and proton's weak charge [390]. In the future, higher precision is expected from new experiments [391, 392]. However, the strongest bounds are obtained with colliders at the Z-pole with huge statistics [388, Section 10.5].

Because of their lower antineutrino energy, reactor experiments can probe values at even lower momentum transfers than π-DAR sources, whereby complementary measurements at both sites are beneficial in any case. Further, detector materials with higher proton numbers might exhibit stronger sensitivities, if the lower nuclear recoil energies (due to a higher nucleus mass) are compensated in CEνNS detection. A sensitivity study of Ref. [98] showed that competitive results can be gained from CEνNS measurements, if systematic uncertainties become controllable, cf. right plot of Fig. 5.2. Values from π-DAR measurements have already be determined, e.g. from CsI(Na), LAr and a combination of both [99]. Connection to other experiments with same target material is advantageous as proven by Ref. [393], in which inputs from nuclear physics, here the neutron RMS radius are determined by a combined fit of Coherent CsI data and measurements of atomic parity violation in Cs.

Such measurements are not only interesting in order to prove the SM's validity at lowest energies. Moreover, it is interesting as light new physics might reveal itself through a modification of the Weinberg angle at low energy. For example, light (Z'-like) vector bosons, predicted by several theoretical frameworks, can lead to a shift in the measured Weinberg angle [324, 325]. Further, a finite neutrino charge radius could imply a shift in the neutrino's vector-couplings and, thus, might manifest itself in a modified Weinberg angle [88, 118, 394].

5.4.2 νMM and νMC via CEνNS and neutrino charge radius

In Chapter 4, we have only considered electromagnetic neutrino properties via νMM-induced EνeS and investigated potential interactions with data sets of enlarged exposure in the energy region $[2,8]$ keV, cf. Tab. 4.1. However, a finite νMM can also induce CEνNS via an interaction of the νMM with the Coulomb field of the nucleus [118]. The relevant cross section for νMM-induced CEνNS is given by

$$\left(\frac{d\sigma}{dT_A}\right)^{A}_{\nu\mathrm{MM}} = \frac{\pi\alpha_{\mathrm{em}}^2}{m_e^2} Z^2 \left(\frac{1}{T_A} - \frac{1}{E_\nu}\right)\left(\frac{\mu_{\nu_e}}{\mu_B}\right)^2 F^2(T_A)\,, \tag{5.3}$$

with the fine-structure constant α_{em}, the electron mass m_e, the nuclear form factor $F^2(T_A)$ and the number of protons of the target nucleus Z. This cross section is based on the assumption of Dirac neutrinos and a helicity-flipping interaction. Therefore, it just adds up to the usual SM interaction. Note the similarity to the corresponding EνeS interactions, cf. Eq. (4.40), in particular the characteristic dependence on the inverse (nuclear) recoil energy. In contrast, the cross section of νMM-induced CEνNS exhibits a dependence on the squared proton number, which reflects the interaction's coherent nature (similar to the characteristic scaling with N^2 of SM CEνNS). Both νMM interactions feature, in principle, strong potential in limit deduction when looking at energies below 1 keV. However, as long as CONUS is not able to resolve a potential CEνNS signal, such investigations might suffer from degeneracy with the usual SM channel that spoils the analysis. With a CEνNS detection, a combined investigation of a finite νMM via CEνNS and EνeS (in both regions, below 1 keV and within $[2, 8]$ keV) is a promising analysis that has not been done so far and consequently should strongly improve our deduced EνeS-only limit, cf. Eq. (4.45). Without any CEνNS signal, improvements can be achieved by investigating data above the CEνNS ROI with EνeS, e.g. within $[0.4, 1]$ keV. In our analysis in Sec. 4.4, we decided to take advantage of larger exposure (for data within $[2, 8]$ keV) at first. Note that investigation of νMM-induced CEνNS were already performed with COHERENT data and further allow to constrain νMM values due to the source's multi-flavor content [88, 90–92]. Recently, also sensitivities for probing transition magnetic moments with recent and future CEνNS measuring experiments have been published [122].

Finally, we want to comment on the experimental advances for improved νMM limits. This can be qualitatively understood by looking at its scaling with experimental parameters, which is given by [395]

$$\mu_\nu \propto \frac{1}{\sqrt{N_\nu}} \left[\frac{B}{M \cdot t}\right]^{\frac{1}{4}} , \tag{5.4}$$

with the background level B and the detector mass and runtime M and t, respectively. Further, N_ν is the number of signal counts for a reference magnetic moment. This formula explains why νMM limits only improved about one order of magnitude in the last three decades, cf. Ref. [396, Table III]. The scaling of main experimental quantities like exposure and background level with the fourth (inverse) power puts strong requirements on experimental attempts. For example, improving a certain limit by a factor of 2 would require enlarging the experimental exposure by a factor of 16. As Ref. [395] pointed out, the largest improvement would be obtained by increasing the number of expected νMM events N_ν, which scales linearly with the neutrino flux ϕ_ν and inversely with the detectable energy T_e. For setting future competitive bounds, all parameters need to be balanced in order to achieve optimal experimental conditions.

Another interesting topic related to electromagnetic properties is the neutrino charge radius $\langle r^2_{\nu_l} \rangle$.[3] The charge radius $\langle r^2_{\nu_l} \rangle$ is a quantity that describes the spatial extent of a given charge distribution ρ. Even the neutrino as a neutral particle can obtain a charge radius via radiative corrections [119, Section 7.B]. Consequently, the electric form factor $\mathbb{f}_Q$, introduced in Sec. 4.4.1 might contain further information about these processes. Expanding the electric form factor $\mathbb{f}_Q$ in a power series of the momentum transfer q^2, in analogy to Eq. (5.2),

$$\mathbb{f}_Q(q^2) = \mathbb{f}_Q(0) + q^2 \left.\frac{d\mathbb{f}_Q(q^2)}{dq^2}\right|_{q^2=0} + \mathcal{O}(q^4) \,, \tag{5.5}$$

---

[3] The part dedicated to the topic of the neutrino charge radius summarizes content of Ref. [119, Section 7].

the squared neutrino charge radius is defined by the second term, i.e.[4]

$$\langle r^2 \rangle = 6 \left. \frac{d\mathbb{f}_Q(q^2)}{dq^2} \right|_{q^2=0} . \tag{5.6}$$

In the SM, the neutrino is a neutral particle, thus $\mathbb{f}_Q(0) = 0$, while radiative corrections that induce a finite charge radius are calculated to be [397]

$$\langle r^2_{\nu_l} \rangle_{\text{SM}} = \frac{G_F}{4\sqrt{2}\pi^2} \left[3 - 2 \log \left(\frac{m_l^2}{m_W^2} \right) \right] , \tag{5.7}$$

with the lepton and W boson masses m_l for $l \in \{e, \mu, \tau\}$ and m_W, respectively. Note that $\langle r^2_{\nu_l} \rangle$ can be negative depending on the underlying charge distribution. In the SM, the charge radii of all neutrino flavors lie within the same order of magnitude, i.e. $\langle r^2_{\nu_l} \rangle \sim 10^{-33}\,\text{cm}^2$ [119, 398]. The contributions of BSM physics on the charge radius are estimated to be only weak [399], while effects of the neutrino charge radius reflect themselves in a shift of the neutrino vector coupling [118, 119, 394]

$$g_V^{\nu_l} \to g_V^{\nu_l} + \frac{2}{3} m_W^2 \langle r^2_{\nu_l} \rangle + \sin^2 \theta_W . \tag{5.8}$$

Ref. [394] estimated bounds on the neutrino charge radius to be of $\mathcal{O}(10^{-32})\,\text{cm}^2$, which is about an order of magnitude higher than SM predictions. Thus, future measurements might be able to probe the SM prediction. A list of various bounds can be found in Tab. V as well as in the corresponding text of Ref. [119, Section 7].

As previously mentioned, such a shift in the neutrino's vector coupling results also in a shift of the Weinberg angle [88, 394], thus introducing an effective Weinberg angle according to

$$\sin^2 \theta_W \to \sin^2 \theta_W + \frac{\sqrt{2}\pi\alpha_{\text{em}}}{3G_F} \langle r^2_{\nu_l} \rangle , \tag{5.9}$$

which additionally underlines the importance of Weinberg angle investigations by CEνNS experiments. Studies of COHERENT data constrain neutrino charge radii also at the level of $\mathcal{O}(10^{-32})\,\text{cm}^2$. While being slightly weaker than existing bounds, cf. Ref. [119, Tab. 5], a separation into region of positive and negative values is already possible [91, 92].

In the end, we comment also on potentials in improving our stated limit on the νMC, cf. Eq. (4.46). An electromagnetic contribution to the CEνNS cross section can be induced via a finite νMC, which can interfere with the due to the same chiral structure. Thus, the SM cross section is to be augmented with the following terms [361, 396]

$$\left(\frac{d\sigma}{dT_A} \right)^A_{\nu\text{MC}} = \left[\frac{2\pi Z^2}{m_A T_A^2} q^2_{\nu_e} + \frac{\sqrt{8} G_F Q_W Z}{T_A} q_{\nu_e} \right] \left(1 - \frac{2 m_A T_A}{2E_\nu^2} \right) F^2(q^2) , \tag{5.10}$$

with the νMC q_{ν_e} in units of the elementary charge e, Q_W the weak nuclear charge and Z

---

[4] Hereby, the factor 6 originates from Fourier transforming the underlying charge distribution ρ and taking the limit $q^2 \to 0$, cf. Ref. [119, Section 7.B] and Sec. 5.3.

the target proton number. Analogously to the case of a finite νMM such investigations are promising for future CONUS investigations. A dedicated combined investigation of EνeS and CEνNS in both ROIs should improve our current limit on the νMC.

Ref. [361] includes sensitivity studies for both interaction channels at reactor experiments. A conservative estimate of the CONUS potential for a CEνNS-only investigation allows constraints (90% C.L.) of $|q_{\nu_e}| \lesssim 6 \cdot 10^{-13} e$ (assuming a detector mass of 4 kg with a 100 eV-threshold).

5.4.3 Sterile neutrino searches

The coherent enhancement of the CEνNS cross section in principle allows to measure a high-statistics neutrino signal at both, a π-DAR and a reactor site. Thus, via CEνNS a source's (anti)neutrino flux can be measured and constraints on the existence of sterile neutrinos could be drawn [88, 140, 141, 400].

Searches for additional sterile neutrinos are motivated by anomalies reported from short-baseline experiments, i.e. excess neutrinos in the experiments LSND ($\bar{\nu}_e$) [144] and MiniBooNE ($\nu_e, \bar{\nu}_e$) [379], deficits of electron neutrinos in the gallium experiments GALLEX [377]and SAGE [378] as well as the RAA [197, 401, 402]. Although with newest findings of reactor antineutrino spectra, cf. Sec. 5.2, the RAA might loose significance, reactor experiments might still constrain the parameter space connected to the other anomalies. Assuming the existence of only one additional sterile neutrino ("(3+1) scheme") the effective survival probability is given by [120]

$$\begin{aligned} P_{\nu_\alpha \to \nu_\alpha} &= 1 - \sin^2 2\theta_{\alpha\alpha} \sin^2 \left(\frac{\Delta m^2_{41} L}{4 E_\nu} \right) , \\ \sin^2 2\theta_{\alpha\alpha} &= 4 |U_{\alpha 4}|^2 \left(1 - |U_{\alpha 4}|^2 \right) , \end{aligned} \tag{5.11}$$

with the (4×4) neutrino mixing matrix U and the mass squared differences between the lightest and the sterile neutrino $\Delta m^2_{41} = m^2_4 - m^2_1$. At the moment constraints deduced from COHERENT data are not competitive to dedicated experiments at reactor-site, cf. Ref. [197], but might prove as excellent tool in the future [88]. Ref. [403] investigated the discovery potential for TEXONO- and COHERENT-like set-ups. A key message is that reactor experiments are able to probe lower mass squared differences with thresholds of 100 eV and kg-size detectors. However, no sensitivity to sterile neutrino parameters is obtained if energy threshold are at ~ 400 eV. Further, the sensitivities of CEνNS and EνeS is analyzed for several CEνNS measuring reactor experiments in Ref. [141]. While EνeS provides only limited information due to its low statistics, CEνNS measurements might be able to probe important regions of the parameter space, also at different experimental baselines. Hence, CEνNS experiments are able to complement ongoing IBD investigations. For instance, Ref. [142] estimated a 100 kg CsI detector close to a π-DAR source to be capable of probing parameter regions that are related to the anomalies of LSND and MiniBooNE. Additionally, the potential of future π-DAR sources are investigated in terms of their sensitivity to light sterile neutrinos and lepton non-universality in Ref. [143].

As theory does not restrict the number of additional sterile neutrino and their mixing with SM neutrino, more complex scenarios can occur [401]. The only way of proving their existence would be via (anti)neutrino appearance/disappearance and non-unitarity

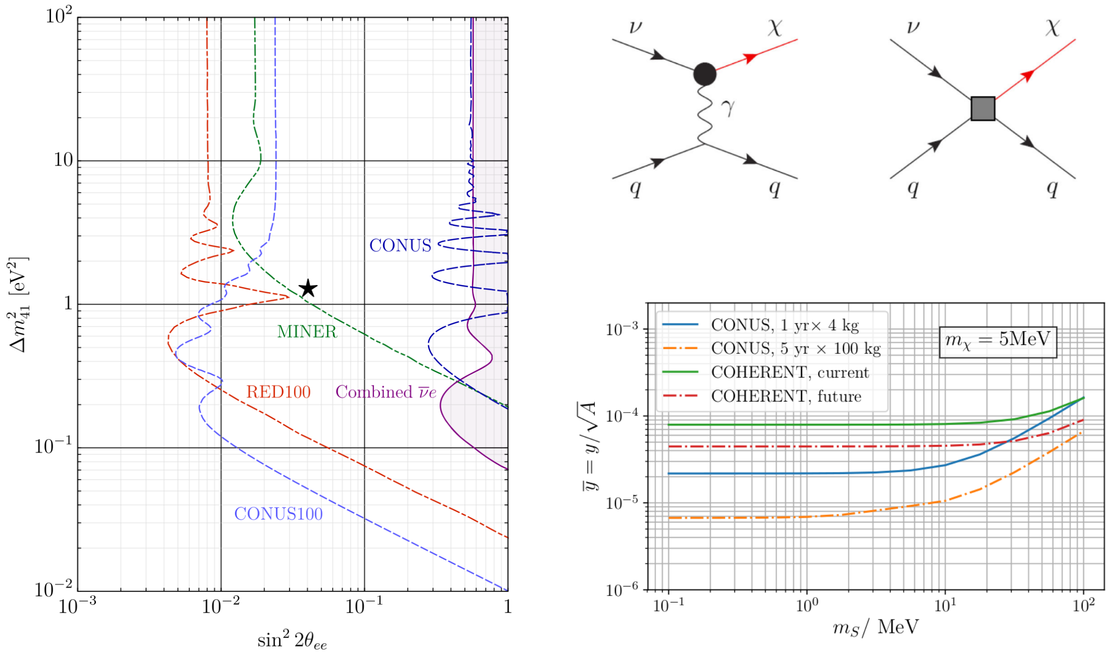

Figure 5.3.: **Left:** Sensitivity (95% C.L.) of CONUS and a potential upgrade on sterile neutrino parameters. For comparison, other CEνNS reactor experiments are shown as well. In addition, 90% C.L. limits from EνeS [141] (purple) and a current best-fit of a global analysis [404] are indicated. Figure taken from Ref. [405]. **Right:** Tree-level diagrams of $\nu A \to \chi A$ with effective dipole and four-fermion interaction (top). Figure taken from Ref. [138]. Sensitivities of COHERENT and CONUS to a new 5 MeV-fermion (mediated by a scalar). Upgrades of COHERENT (statistics ×100) and CONUS ($E_{\text{thr}} = 100$ eV, 500 kg·yr exposure) are given by dashed lines. Figure taken from Ref. [137].

tests (oscillations), beta decays and $0\nu\beta\beta$ (mass effects) as well as cosmological measurements [401, 402]. The potential of CONUS and a related upgrade are deduced in Ref. [405], where also the complementarity between reactor measurements and cosmological observables in terms of sterile neutrino searches is highlighted. The simplified sensitivities of CONUS and CONUS-100 are shown in the left plot of Fig. 5.3.

5.4.4 New Fermions and Dark matter

In the end of this part, we discuss the prospects of CEνNS in terms of measuring effects related to new fermions. When discussing these, the question immediately arises if they can be valid DM candidates and, furthermore, might contribute to light neutrino masses. Refs. [137, 138] considered the coherent interaction $\nu A \to \chi A$, which is possible as long as the nucleon state is not altered. The underlying assumption is a mediating (scalar or vector) particle that interacts with neutrinos and SM fermions. Thus, the production of MeV-scale (related to the occurring momentum transfer) fermions can be investigated.

While Ref. [137] focuses on the fermion's role in neutrino mass generation and as potential DM constituent in context of a singlet scalar mediator, Ref. [138] investigates the occurring interaction in a model-independent effective way, i.e. [5]

$$\mathcal{L} \supset \frac{G_F}{\sqrt{2}}\Bigg(\frac{v_{\mathrm{ew}}}{\sqrt{2}}\left[\bar{\nu}\sigma^{\mu\nu}a_M\chi\right]F_{\mu\nu} + \left[\bar{\nu}\sigma^{\mu\nu}C_T^q\chi\right]\left[\bar{q}\sigma_{\mu\nu}q\right] \\ + \left[\bar{\nu}C_S^q\chi\right]\left[\bar{q}q\right] + \left[\bar{\nu}\gamma^\mu C_V^q\chi\right]\left[\bar{q}\gamma_\mu q\right] + \mathrm{h.c.}\Bigg), \tag{5.12}$$

with the corresponding couplings $C^q_{S,T,V}$ for scalar, tensor or vector interactions and a_M representing a dipole interaction (like the one induced by a finite νMM). Thus, similar channels like the ones investigated in Ch. 4 are possible, "only" with the neutrino being converted into a new fermion, cf. right upper plot in Fig. 5.3. However, the occurrence of a massive final state χ is reflected in the kinematics since now a minimal incident neutrino energy is required in order to produce it: $E_\nu^{\mathrm{min}} = m_\chi(1+\frac{m_\chi}{2m_A})$. Consequently, CE$\nu$NS is most sensitive to probe new fermions with masses below $\sim 40\,$MeV, both at reactors and at π-DAR sources. However, with the antineutrino spectrum rapidly falling above 8 MeV, reactor experiments are most sensitive to lowest masses. This is a behavior we already encountered in the investigation of simplified mediator models, cf. Sec. 4.3. With complementary bounds at higher masses from π-DAR sources, both experimental CEνNS approaches allow for promising investigations, cf. right lower plot in Fig. 5.3. A consideration in the DM context allows to constrain the model's parameter space with further requirements and bounds, e.g. from DD experiments or cosmology [147].

Another possibility for DM searches is to investigate nuclear recoils of sub-GeV DM particles (or byproducts) that have been created in a "portal interaction", i.e. via a particle that bridges between the SM and a dark sector. For example, at a SNS in pion decays in flight ($\pi^0 \to \gamma V^* \to \gamma + \chi^\dagger + \chi$) or π^- captures ($\pi^- + p \to n + V^* \to n + \chi^\dagger + \chi$) DM particles might be created in a vector-portal interactions and subsequently interact with the detector material [126]. Here, the DM particle can be a hidden (SM singlet), scalar or fermion that is charged under a gauged $U(1)$ group. Consequently the associated gauge boson mediates between both sectors. Sensitive CEνNS-measuring devices close to such sources allow investigations without the need of building new dedicated experiments. Ref. [148] presented results of searches for scalar DM mediated through a vector portal at the SNS and pointed out the potential of such searches. Absorption and ionization of bosonic DM χ ($\chi + A \to A^+ + e^-$) has been studied as well [406].

5.5 The future of CEνNS investigations

We have seen that CEνNS provides a large toolbox for various investigations in nuclear physics, within and beyond the SM, astrophysics and cosmology. In addition, more and more experiments are going to measurement this channel and exploit its opportunities within the upcoming years. In the end, we want to address the potential that comes along with CEνNS-sensitive devices measuring this channel with different technologies and different sources.

---

[5] Pseudoscalar and axial vector interactions proportional to γ^5 are omitted, as they experience no coherent enhancement.

5.5.1 Advantages of different target materials

CEνNS investigation with multiple targets are interesting for tests of the interaction's characteristic scaling with the squared neutron number and to reduce systematic effects from the analysis. In order to do this, Ref. [407] proposed to use an array of isotopically enriched targets of a certain detector material but different isotopes. For this purpose, cryogenic detectors would be suitable, e.g. germanium, selenium or zinc. As these detectors would share similar systematic effects, overall uncertainties are smaller then in the case of several individual detector materials and might help to separate these from physics contributions, e.g. to the neutron form factor or the Weinberg angle. Of course, detailed knowledge about the isotopes' nuclear structure and the target material is crucial for precision investigations, cf. Ref. [408].

Further, different target elements are needed in order to break degeneracies among different NSI couplings. Ref. [111] pointed out that the slope of contours in the NSI coupling plain, e.g. $(\epsilon_{ee}^{u\mathrm{V}}, \epsilon_{ee}^{d\mathrm{V}})$, depends on the ratio $k = (A + N)/(A + Z)$. Consequently, at least two target materials with maximally deviating k-value should be chosen together with elements that generally imply large event rates. Two choices could be enough to determine both couplings at the same time. However, this might come with a trade-off in terms of detectable energy, i.e. due to the "push-pull situation" between a large cross section and low thresholds mentioned in Sec. 2.1.4. The impact of target complementarity is shown in more detail by sensitivity studies of Ref. [89], where the individual materials were tested for their potential in investigations of several BSM models. According to their findings, the elements germanium and zinc form a powerful combination in order to break a degeneracy in the NSI parameter space Beyond this, only minor improvements can be achieved with additional elements, while the strongest potential in resolving the parameter region comes from elements with strong deviations in the ratio N/Z, which is a similar statement as the k parameter of Ref. [111].

Conclusively, weighting of interests might become important for individual experimental purposes, but generally the application of a wide range of detection technologies will be beneficial for SM and BSM CEνNS investigations.

5.5.2 Complementarity in CEνNS searches

Now we address the advantages that come along CEνNS investigations with different sources and, further, how their combination can be advantageous for certain topics or other physics branches. Both sources currently relevant for CEνNS investigations have their characteristic features like flavor content and neutrino energy range, cf. Sec. 2.2.1. We have already encountered their complementarity, e.g. in their sensitivity to light mediators of different masses, cf. Sec. 4.3. Moreover, if we take into account detection of astrophysical neutrinos in DM experiments all three neutrino flavors might become accessible for complementary investigations [297]. For NSIs, CEνNS investigations are of general importance as their measurements in neutrino oscillations are limited by several degeneracies. For example, only differences of flavor diagonal NSI elements can be accessed. Couplings to up- and down-quarks cannot be distinguished. Most importantly, the presence of NSIs lead to ambiguities among neutrino mixing parameters that prevent a determination of the neutrino mass ordering via oscillation experiments. Consequently, complementary measurements are needed to solve this issue [409, 410]. Here, CEνNS experiments both at a π-DAR source as well as at reactor-site can contribute in resolving this issue. An extensive study of Ref. [297] showed that precise measurements of electron NSI in reactor experiments allows to separate the effects of electron and muon NSIs at π-DAR sources. Moreover, multi-target approaches at different neutrino sources are needed for breaking the degeneracies that underlie the NSI framework and are valuable ingredients for neutrino oscillation experiments.

Another example for the complementarity between CEνNS and other physics investigations are portal interactions or DM. In the context of a fermionic DM model with a $U(1)$ extension of the SM, Ref. [411] highlighted the complementarity between DM DD and CEνNS experiments in terms of investigating the model's parameter space. In particular, the possibility to simultaneously constrain the model's light portal mediator via CEνNS and the DM candidate via DM DD is beneficial. If the portal mediator exhibits couplings to DM as well as to first-generation quarks (enabling a CEνNS interaction) correlations between both cross section are possible. In that way, one can make use of the full repertoire of bounds that exists for light (portal) DM searches [411] as well as from CEνNS investigations, cf. end of Sec. 4.3.3.

In general, the strict background and threshold requirements for CEνNS detection allow for low-energy investigations of portal interactions independent of the constraint to account for the DM budget of the universe. The general principle relies on the production of a portal mediator in reactions related to the source and their subsequent detection in CEνNS devices. At a SNS, productions would be primarily related to pions, while at reactors the huge photon density in the reactor core is a natural choice. For instance at reactors, Compton-like processes of a dark photon Z' mixing with the photon ($\gamma e^- \to Z' e^-$) [135, 136] (vector portals) can be probed as well as axion portals [412]. In general, investigations of axions and axion-like particles strongly benefit from the experimental condition of CEνNS experiments at a reactor site [131].

5.5.3 Neutrino astronomy

In the end, we mention examples, in which CEνNS interactions can be beneficial for detecting neutrinos of extraterrestrial origin. Its flavor-blind nature allows the detection of all neutrinos flavors independently of any degeneracies or uncertainties related to neutrino oscillations or the unknown light neutrino mass hierarchy. In principle, a threshold-free detection of neutrinos below the IBD threshold is possible, though, this crucially depends on experimental specifications like detectable energy, signal quenching and background contribution of the chosen detection technology.

The recent and future generations of DM DD experiments are going to "probe the neutrino floor", cf. Ref. [104], which refers to the circumstance that with the detection of solar ^{8}B neutrinos a discrimination from a 6 GeV DM particle is limited [107].[6] Basically, separation via complementary targets, annual modulation or much higher energy resolution is possible [107] and directional detectors like CYGNUS [414] will resolve events from different origins. However, it marks the point where DM investigations are strongly altered by

---

[6] Ref. [413] pointed out the dependence of *the* "neutrino floor" on the used target material as well as on the interaction channel. A more independent definition of this term, which actually summarizes several contributions like atmospheric and diffuse supernova remnant neutrinos, was suggested.

neutrino physics. On the contrary, this opens new possibility for neutrino physics as the sun itself becomes a neutrino source that can be probed via CEνNS or EνeS. SM quantities like the Weinberg angle, solar model parameters or even neutrino-related BSM models might become testable [107]. For instance, the amplitude of this "neutrino background" can be affected by neutrino-related BSM phenomena like NSIs or light mediators. In particular, the expected neutrino signal can be increased by orders of magnitude if light mediating particles attribute new interaction channels [109]. Further, the presence of NSIs (within their 3σuncertainties) are able to lift neutrino signals up to a factor of 5 [415]. Consequently, the projected DM sensitivity of new large-scale experiments like Argo [416] or Darwin [417] are modified by the presence of such new contributions, while enabling further investigations within the neutrino sector.

Another topics that comes along this new high-statistics interactions channel is its capability in measuring neutrinos from core-collapse supernova, especially in terms of a potential contribution to the supernova early warning system (Snews) [418]. Since so far electron-type neutrinos are mainly detected via EνeS (SK, Hyper-K), IBD (Juno) or via the CC quasi-elastic process $\nu_e +^{40}\mathrm{Ar} \rightarrow e^- +^{40}\mathrm{K}^*$ (DUNE), a flavor-independent channel is highly valuable for the detection of the overall neutrino signal. As the detected nuclear recoils are directly linked with the incident neutrino energy, CEνNS investigations might be able to reconstruct the average temperature underlying the stellar core-collapse and, thus, be used as a "neutrino thermometer" [419]. While the recent generation of DM detectors would only detect a small number of CEνNS events, e.g. $\mathcal{O}(10)$ within Xenon1T for typical supernovae at 10 kpc-distance [420], future large-scale DM detectors will allow sufficient count rates, e.g. ~ 600 for Darwin [420]. A close, Betelgeuse-like supernova (at 200 pc-distance), could leave $\mathcal{O}(10-100)$ CEνNS events in a $\mathcal{O}(100)$t detector with sub-keV threshold and, thus, trigger a warning alert for the Snews network about 10 h before its explosion [421]. More realistic projections for multi-ton and low-threshold argon experiments claim their potential to detect supernovae occurring throughout the Milky Way (DarkSide-20k) or even up to the Small Magellanic Cloud (Argo) [422]. By detecting direct or diffuse neutrinos from supernovae remnants related to supermassive stars ($M \gtrsim 3 \cdot 10^4 M_\odot$), which are potential seeds for supermassive black holes in galaxy centers, CEνNS might even help to understand the cosmological evolution of galaxies [33].

Laying aside the difficulties that are accompanied by such ambitious endeavors, it is fascinating that with the next generation of experiments DM and neutrino physics well be intertwined and CEνNS will play an important role in bridging these both sectors.

5.6 Summary

In this last chapter we focused on CEνNS in the light of both near and far future investigations. Realized and planned experimental improvements of the CONUS set-up are discussed in Sec. 5.1. Their impact on upcoming CEνNS investigations with the CONUS experiment is highlighted and expected event numbers for the current data collection period are given in combination with estimates of a potential future CONUS upgrade (Conus-100), cf. Tab. 5.1. Adjustments on the analysis scheme related to these improvements are discussed as well, while a dedicated discussion on new measurements and insights of reactor antineutrino spectra can be found in Sec. 5.2. Therein, a new method for compilation of data-based reactor antineutrino spectra is explained, before the impact of CEνNS measurements on this topic is illustrated. After that, new investigation possibilities that come along with an actual signal detection are discussed in the SM and BSM context in Sec. 5.3 and Sec. 5.4, respectively. Highlights are the contributions to weak mixing angle measurements at low energy as well as further opportunities of CEνNS measuring devices for accessing electromagnetic neutrino properties and searching for new fermions. In the end, we point out the impact and complementarity of future multi-target CEνNS investigations at π-DAR sources and reactors, and discuss the impact of CEνNS for neutrino astronomy.

Chapter 6

Conclusions

This work deals with spectral investigations of SM CEνNS and further BSM phenomena based on the first two data collection periods from April 2018 to June 2019 of the CONUS experiment. The experimental set-up is located at the commercial nuclear power plant in Brokdorf (Germany) and uses four kg-size HPGe detectors in an advanced shield in order to measure antineutrinos emitted from the 3.9 $\mathrm{GW_{th}}$ single-unit reactor core at 17 m-distance.

Prior to the analyses of these experimental data, a realistic signal prediction for the CONUS set-up is determined. By incorporating reactor data, i.e. time-averaged fission fractions of the main antineutrino-emitting isotopes as well as thermal power values, for the individual data collection periods, reactor antineutrino emission spectra with corresponding uncertainties are provided. Further, taking into account detector and experimental responses provides tailored CEνNS predictions for each detector in each data collection period. These predictions are used in an analysis scheme, which incorporates all experimental systematic effects together with already existing MC background models in order to investigate the CONUS data for potential (SM and BSM) signals. Using this analysis routine, the world's best limits on CEνNS from a reactor experiments are obtained from data with an overall exposure of 248.7 kg d (reactor On) and 58.8 kg d (reactor Off), respectively. Subsequently, the CONUS run-1 data are tested for several BSM models, i.e. NSIs and simplified mediator models. The inclusion of EνeS at slightly higher energies between $[2, 8]$ keV for the latter requires minor adjustments of the developed analysis routines. In general, the analyses use data sets with exposures of 209 kg d (reactor On) and 38 kg d (reactor Off) for CEνNS-related BSM models below 1 keV, whereas the quest for the corresponding BSM modifications of EνeS relies on extended data sets between $[2, 8]$ keV with exposures of 649 kg d (reactor On) and 94 kg d (reactor On), respectively. Furthermore, for a separate analysis of neutrino electromagnetic properties via EνeS, the data are prolonged with an extended run-2 data set such that the obtained limits on the effective νMM and the effective νMC are based on an exposure of 689 kg d reactor On and 132 kg d reactor Off, respectively. The results obtained in the course of this work are summarized in Tab. 6.1, whereby we refer to the individual summary sections Sec. 3.4 and Sec. 4.5 for detailed discussions.

In the end, undertaken and planned improvements for the CONUS experiment and the set-up's further and future investigation possibilities are discussed, cf. Sec. 5. The potential

Analysis	Interaction	Results (90% C.L.)	Reference
SM	CEνNS	$\lesssim 85$ counts (factor ~ 10 below prediction)	Fig. 3.9
Vector NSI	CEνNS	$\Lambda_{\text{NP}} \gtrsim 100\,\text{GeV}$	Fig. 4.1
Tensor NSI	CEνNS	$\Lambda_{\text{NP}} \gtrsim 360\,\text{GeV}$	Fig. 4.2
Light scalar	CEνNS	$g_\phi \sim 1 \cdot 10^{-5}$	Fig. 4.3
	EνeS	$g_\phi \sim 2 \cdot 10^{-6}$	
Light vector	CEνNS	$g_{Z'} \sim 4 \cdot 10^{-5}$	Fig. 4.4
	EνeS	$g_{Z'} \sim 5 \cdot 10^{-7}$	
νMM	EνeS	$\mu_{\nu_e} < 7.5 \cdot 10^{-11}\,\mu_B$	Fig. 4.5
νMC	EνeS	$\lvert q_{\nu_e} \rvert < 3.3 \cdot 10^{-12}\,e$	

Table 6.1.: Summary of findings obtained in this work. For the performed investigations, we indicate the analyzed interaction, characteristic result and a corresponding reference for more details. All CEνNS channels assume the currently favored QF, i.e. $k = 0.16$. For light mediator models, we list the smallest couplings (in the flat, low-mass region of the parameter space) that can be probed with the current CONUS sensitivity.

of future multi-target CEνNS measurements is highlighted in terms of the complementarity between π-DAR and reactor investigations and further the impact of CEνNS in future large-scale experiments is illustrated.

The first investigations of the CONUS experiment have proven that the chosen technology, i.e. HPGe detectors in a compact onion-like shield close to a strong reactor core, generally fulfills the requirements needed for CEνNS detection. Although reached experimental specifications are not able to claim a successful CEνNS observation at a reactor site yet, the experimental improvements, especially in terms of environmental stability and the improved DAQ system, give us confidence for the currently running data collection period. Still, the data obtained so far allow to set impressive results for most BSM frameworks considered; in the cases of tensor NSIs and light scalar mediators our exclusion power exceeds that of π-DAR sources. However, the repertoire of potential SM and BSM opportunities is still far from being exploited. Future data might allow for further interesting investigations, above all a positive confirmation of CEνNS at reactor-site is crucial. We would like to point out again that any improvement regarding the CEνNS ROIs below 1 keV will generally be beneficial for potential νMM investigations as well.

On more general grounds, the efforts of CEνNS-measuring collaborations and the related community of phenomenologists established this new reaction channel as a very promising neutrino investigation tool. In particular, it is now proven that "car-size" neutrino detectors are feasible! In addition, other detection technologies will tap into this reaction channel in the coming years. By providing a (in principle) high-statistic neutrino signal, CEνNS enables new detection capabilities and opens a new window to neutrino-related BSM physics. It is also noteworthy that small-scale CEνNS experiments in terms of both detector set-up and manpower, might soon probe energy scales comparable to the ones reached by today's collider experiments and, thus, contribute complementary measurements with the advantage of being less time-consuming and less cost-intensive. In any case, the detection of CEνNS, together with the construction of other large-scale neutrino experiments, are important milestones on the path towards an era of precision neutrino physics.

As the present work has shown, close collaboration between experimental and theoretical physicists can be a fruitful combination for both sides, either when theorists learn that it is not "just" taking data or vice versa, when experimentalists learn more about the conceptional context of their measurements.[1] All in all, a promising future for (neutrino) physics may lie ahead of us and there are several reasons to become excited, however the path towards a deeper understanding of nature has always been difficult and arduous. Moreover, confirmations of the SM are still valuable results and not every statistical fluctuation is caused by BSM physics, or spoken in wiser words by S. Weinberg: "There is no principle into the laws of nature that says that theoretical physicists have to be happy" [423].

---

[1] The author himself (theorist) can recommend the sporting activities during an experiment's commission, especially when $\sim 11\,\mathrm{t}$ of lead need to be carried through a nuclear power plant.

APPENDICES

Appendix A

CEνNS fundamentals

A.1 Effective four-fermion interaction of the weak neutral current

In what follows we shortly illustrate how an effective interaction can be obtain from a given theory. In doing so, we summarize content presented in Ref. [322, Section 7.2.3]. Since the weak NC interaction is of main concern throughout this work, we chose this interaction as example. In the limit of small momentum transfer the corresponding effective interaction is given by Eq. (2.8).

In order to obtain the effective description at the (low) energy scale of interest, two approaches are usually chosen: the formal path integral treatment or solving the particle's EOM while ignoring the kinematic term. Here, we only focus on the latter one and refer to the standard literature for the first method, cf. Ref. [160, Section 12].

The weak NC Lagrangian is given by

$$\mathcal{L}_Z = -\frac{1}{4} Z_{\mu\nu} Z^{\mu\nu} + \frac{m_Z^2}{2} Z_\mu Z^\mu - \frac{g}{2\cos\theta_W} Z_\mu J_Z^\mu \,, \tag{A.1}$$

with the Z boson mass m_Z, the weak NC current J_Z^μ given by Eq. 2.6 and the $SU(2)_L$ coupling g as well as the Weinberg angle $\cos\theta_W$. Solving the Euler-Lagrange equation for the Z boson yields its EOM

$$\left(\Box + m_Z^2\right) Z_\mu - \partial_\mu \partial_\nu Z^\nu = \frac{g}{2\cos\theta_W} J_{Z\mu} . \tag{A.2}$$

We now assume to be in an energy regime much lower than the Z boson's mass, i.e. $q^2 \ll m_Z$, with q^2 being the typical momentum transfer of the interactions under consideration. In such cases, the boson is said to be non-dynamical and derivatives in the above EOM are of minor importance. Consequently, the EOM simplifies to

$$Z_\mu = \frac{g J_{Z\mu}}{2 m_Z^2 \cos\theta_W} + \mathcal{O}\left(\frac{E^2}{m_Z^2}\right) . \tag{A.3}$$

Reinserting this into the full Lagrangian $\mathcal{L}_Z$ of Eq. (A.1) leads to a four-fermion operator of the effective low-energy theory

$$\mathcal{L}_{eff}^{\mathrm{NC}} = -\frac{g^2}{8m_Z^2\cos^2\theta_W} J_Z^\mu J_{Z\mu} = -\frac{G_F}{\sqrt{2}} J_Z^\mu J_{Z\mu}\,, \tag{A.4}$$

with $\frac{G_F}{\sqrt{2}} = \frac{g^2}{8m_W^2} = \frac{1}{2\nu^2}$ and $m_W = m_Z\cos\theta$ being used in the last step. The new theory now contains only dynamical, thus only relevant DOFs, which are incorporated in the weak NC current J_Z^μ, cf. Eq. (2.6). However, the obtained operator $J_Z^\mu J_{Z\mu}$ is non-renormalizable as it exhibits mass dimension six. This is of no concern as long as one uses a mass-independent renormalization scheme, e.g. $\overline{\mathrm{MS}}$. The coefficients of the corresponding operators are determined from the underlying theory or by experiments, e.g. for the Fermi constant G_F in muon lifetime measurements. In the general EFT approach, one writes down all possible operators (including derivatives) that can be formed out of dynamical fields and that are in agreement with the symmetries of the energy scale of interest. For more details about EFTs and examples, we refer the reader to Ref. [293].

A.2 Calculation of the CEνNS cross section

In this section we summarize calculations needed to obtain the final expression for the CEνNS matrix elements of Eq. (2.29) as well as corresponding cross section, cf. Eq. (2.31). The following derivations are partially based on the appendices of Ref. [115] and Ref. [153]. Further, the Refs. [164, 166, 265] are used as well.

A.2.1 Lorentz-invariant cross section for $2 \to 2$ scattering

We start with the general expression for the cross section of the process: $p_a + p_b \to \{p_f\}$ [160]

$$d\sigma = \frac{|\mathcal{M}(p_a + p_b \to \{p_f\})|^2}{2E_a 2E_b |v_a - v_b|} \left(\prod_f \frac{d^3p_f}{(2\pi)^3}\frac{1}{2E_f}\right)(2\pi)^4\delta^{(4)}(p_A + p_b - \sum_f p_f)\,, \tag{A.5}$$

which simplifies in the case of $2 \to 2$ scattering $p_a + p_b \to p_1 + p_2$ to the following expression

$$d\sigma = \frac{|\mathcal{M}(p_a + p_b \to p_1 + p_2)|^2}{2E_a 2E_b |v_a - v_b|} \left(\frac{d^3p_1}{(2\pi)^3}\frac{1}{2E_1}\right)\left(\frac{d^3p_2}{(2\pi)^3}\frac{1}{2E_2}\right)(2\pi)^4\delta^{(4)}(p_a + p_b - p_1 - p_2)\,. \tag{A.6}$$

Further, evaluation in the CM frame allows to obtain an even simpler expression for the cross section, cf. Ref. [164, Secton 5.1] or Ref. [166, Section 3.5]. Thus, application of $|v_a - v_b| = \frac{\sqrt{s}p_i^*}{E_a E_b}$ and evaluation of the integrals within the CM frame leads to the following compact form

$$d\sigma = \frac{1}{64\pi^2 s}\frac{p_f^*}{p_i^*}|\mathcal{M}|^2 d\Omega^*\,, \tag{A.7}$$

with the initial and final state momenta p_i^* and p_f^*, the Mandelstam variable $s = (p_a + p_b)^2 = (p_1 + p_2)^2$ as well as the solid angle in the CM frame $d\Omega^*$. In the last expression, a step-function that ensures energy conservation is left out for reasons of brevity, cf. Ref. [164, Secton 5.1]. The initial state momentum in the CM frame is defined as

$$p_i^{*2} = \frac{1}{4s}\left[s-(m_1+m_2)^2\right]\left[s-(m_1-m_2)^2\right] , \tag{A.8}$$

again with the Mandelstam variable s and the masses of the final state particles. Assuming the interaction to be independence of the azimuthal angle ϕ and using $d\Omega^* = \frac{dt d\phi^*}{2p_i p_f}$, which can be derived from the Mandelstam variable $t=(p_a-p_1)^2=(p_b-p_2)^2$ in the CM frame, yields the final form that is applied in the following calculations

$$\frac{d\sigma}{dt} = \frac{1}{64\pi s p_i^{*2}}|\mathcal{M}|^2 . \tag{A.9}$$

Note that this expression is valid in any frame as it contains only Lorentz-invariant quantities. Moreover, the Mandelstam variable represents the momentum transfer in t-channel processes like it is the case for CEνNS. Therefore, we explicitly assume from now on $t=q^2$.

A.2.2 Matrix element evaluation and lab-frame kinematics

Now we calculate the squared matrix element that is needed for the cross section of Eq. (A.9) and start with the matrix element that has already been derived in Sec. 2.1.2,

$$i\mathcal{M} = i\frac{G_F}{\sqrt{2}}Q_W F(q^2) g_L^\nu (k+k')_\mu \bar{v}^s(p)\gamma^\mu(1-\gamma^5)v^{s'}(p') . \tag{A.10}$$

In order to obtain the squared and spin-averaged matrix element $|\mathcal{M}|^2 = \sum_{s,s'}|i\mathcal{M}^{s,s'}|^2$, we multiply with the complex conjugate and sum over the neutrino spins, which yields

$$\begin{aligned}\sum_{s,s'}|i\mathcal{M}^{s,s'}|^2 = \frac{G_F^2}{2}Q_W^2|F(q^2)|\, g_L^{\nu 2}\sum_{s,s'}&(k+k')_\mu \bar{v}^s(p)\gamma^\mu(1-\gamma^5)v^{s'}(p')\\ &\times (k+k')_\nu \bar{v}^{s'}(p')\gamma^\nu(1-\gamma^5)v^s(p) .\end{aligned} \tag{A.11}$$

The neutrino currents can be evaluated by using the trace technique and application of the spinor outer product $\sum_s v^s(p)\bar{v}^s(p) = \not{p} - m$ for antineutrinos. Thus, under assumption of negligible antineutrino mass, the spinor part simplifies to

$$\begin{aligned}&\sum_{s,s'}(k+k')_\mu \bar{v}^s(p)\gamma^\mu(1-\gamma^5)v^{s'}(p')\ (k+k')_\nu \bar{v}^{s'}(p')\gamma^\nu(1-\gamma^5)v^s(p)\\ &\quad = (k+k')_\mu(k+k')_\nu \operatorname{Tr}\left[\not{p}\,\gamma^\mu(1-\gamma^5)\,\not{p}'\gamma^\nu(1-\gamma^5)\right]\\ &\quad = 16\left[(k.p+p.k')(k.p'+k'.p') - (m_A + k.k')p.p'\right] ,\end{aligned} \tag{A.12}$$

where we have used the Mathematica extension “Package-X” for evaluation of the trace and the index contraction [424, 425]. Thus, the squared matrix matrix element is given by

$$|\mathcal{M}|^2 = 8\, G_F^2 Q_W^2 |F(q^2)|\, g_L^{\nu 2}\left[(k.p+p.k')(k.p'+k'.p') - (m_A+k.k')p.p'\right] . \tag{A.13}$$

For further evaluation, we switch to the lab frame, where the occurring momenta are defined as follows

$$p = (E_\nu, \boldsymbol{p}) \,, \qquad k = (m_A, \boldsymbol{0}) \,, \qquad p' = (E_\nu - T_A, \boldsymbol{p'}) \,, \qquad k' = (T_A + m_A, \boldsymbol{k'}) \,, \tag{A.14}$$

with the incident neutrino E_ν, the nucleus mass m_A and the nuclear recoil energy after scattering T_A. Here, the momentum transfer is given by the Mandelstam variable $q^2 = t = (p - p')^2 = (k - k') = -2m_A T_A$. By calculating the products of four-momenta and inserting them in Eq. (A.13), one obtains the final expression for the squared matrix element

$$|\mathcal{M}|^2 = 32 \; G_F^2 Q_W^2 |F(q^2)| \; g_L^{\nu 2} \left(1 - \frac{T_A}{E_\nu} - \frac{m_A T_A}{2E_\nu^2}\right) . \tag{A.15}$$

In the end, we comment on the form the Lorentz-invariant cross section of Eq. (A.9) exhibits in the lab-frame. Assuming a negligible neutrino mass ($m_\nu \ll m_A$) and calculating the Mandelstam variable s in the lab frame, the initial CM momentum in Eq. (A.8) simplifies to $p_i^{*2} \simeq E_\nu^2 m_A^2 / s$. Therefore, the Lorentz-invariant cross section also simplifies to

$$\frac{d\sigma}{dt} = \frac{1}{64\pi E_\nu^2 m_A^2} |\mathcal{M}|^2 \,. \tag{A.16}$$

This can now be transformed into an expression that depends on an actual observable,

$$\frac{d\sigma}{dT_A} = \frac{d\sigma}{dt} \left| \frac{dt}{dT_A} \right| = \frac{|\mathcal{M}|^2}{32\pi m_A E_\nu^2} \,, \tag{A.17}$$

which is the cross section in terms of the nuclear recoil energy T_A.

Another expression that is usually found in literature is the cross section in terms of the scattering angle θ in the lab frame, which is given by [67]

$$\frac{d\sigma}{d\cos\theta} = \frac{G_F^2}{8\pi} \left[N + Z(4\sin^2\theta_W - 1)\right]^2 E_\nu^2 (1 + \cos\theta) \,, \tag{A.18}$$

with the weak nuclear charge Q_W already inserted.

So far, the nucleus has been assumed as a spin-0 particle for reasons of simplicity. Assuming it to be a spin-1/2 target would introduce another vector current in the nuclear matrix element, i.e.

$$\langle A(k', r')| \, J^\mu_{\text{NC}} \, |A(k, r)\rangle = F^2(q^2) \bar{u}^{r'}(k') \gamma^\mu u^r(k) \left[Z g_V^p + N g_V^n\right] . \tag{A.19}$$

The derivation is analogous to the previous one, only with a more complex evaluation of spinor relations. The final result for the squared matrix element is then given by [115]

$$|\mathcal{M}|^2 = \frac{1}{2} \sum_{s,s',r,r'} |i\mathcal{M}^{ss'rr'}|^2 = 32 \; G_F^2 Q_W^2 |F(q^2)| \; g_L^{\nu 2} \left(1 - \frac{T_A}{E_\nu} - \frac{m_A T_A}{2E_\nu^2} + \frac{T^2}{2E_\nu^2}\right) , \tag{A.20}$$

where a factor of $1/2$ is introduced to account for correct spin-averaging. The only difference to the case of a spin-0 target is an additional (T_A/E_ν)-term, which is negligible within our application anyway.

A.3 Form factors

Here we give a short overview of form factor parameterizations commonly used in literature with assumptions on their underlying charge distributions and the resulting RMS radius. Each form factor assumes a certain charge distribution ρ with characteristic parameters that occur in the individual expressions. In the following, we summarize content presented in Ref. [261].

The Helm form factor [426] assumes a uniform density distribution of fixed radius R_0 that is smeared out with a Gaussian distribution of standard deviation s, which in this context is called surface thickness s. The corresponding form factor exhibits the form

$$F_{\mathrm{H}}(q^2) = 3\frac{j_1(qR_0)}{qR_0} e^{-\frac{q^2 s^2}{2}} \,, \tag{A.21}$$

with the spherical Bessel function of first order j_1.

The symmetrized Fermi form factor [427] relies on a generalization of the Woods-Saxon potential with the half-density radius c and a surface diffuseness a, which yields

$$F_{\mathrm{SF}} = \frac{3}{qc}\left[\frac{\sin(qc)}{(qc)^2}\left[\frac{\pi qa}{\tanh(\pi qa)}\right] - \frac{\cos(qc)}{qc}\right] \times \left(\frac{\pi qa}{\sinh(\pi qa)}\right)\frac{1}{1+(\pi a/c)^2} \,. \tag{A.22}$$

Further, the Klein-Nystrand form factor [428] assumes as charge distribution a hard sphere of radius R_A that is convolved with a Yukawa potential of range a_k. This results in the following expression

$$F_{\mathrm{KN}}(q^2) = 3\frac{j_1(q\,R_A)}{q\,R_A}\frac{1}{1+q^2 a_k^2} \,. \tag{A.23}$$

With the definition of the charge radius $\langle r^2\rangle = \int d^3r\rho(r)r^2 / \int d^3r\rho(r)$, the expressions for the corresponding charge distributions lead to the following charge radii,

$$\langle r_{\mathrm{H}}^2\rangle = \frac{3}{5}R_0^2 + 3s^2 \,, \tag{A.24}$$

$$\langle r_{\mathrm{SF}}^2\rangle = \frac{3}{5}c^2 + \frac{7}{5}(\pi a)^2 \,, \tag{A.25}$$

$$\langle r_{\mathrm{KN}}^2\rangle = \frac{3}{5}R_A^2 + 6a_k^2 \,. \tag{A.26}$$

From these expressions, the RMS radii can be calculated via $r_{\mathrm{rms}} \equiv \sqrt{\langle r^2\rangle}$.

Appendix B

Additional tools for maximum likelihood methods

At this point, we elaborate on further important aspects in the context of parameter estimation and statistical inference, which are meant to complement and continue the remarks of Sec. 2.3. For this, we rely on the same references as before [226–229].

B.1 Goodness-of-fit within maximum likelihood methods

One straightforward way of quantifying the "goodness-of-fit" of a likelihood fit is to directly use the maximal likelihood value $\mathcal{L}_{\max}$, which however relies on the underlying PDF, cf. Ref. [227, Section 6.11]. For cases, in which it remains unknown, MC techniques can be used to determine it. Here, the ML estimates of the given data are used as input for the MC simulation's true values. Consequently, a significance level for the performed fit can be derived from the obtained distribution.

Another possibility is to use a data set $\boldsymbol{n}$ and corresponding estimates $\hat{\nu}$ as input for a test statistic that relies on a likelihood ratio, e.g. for a binned likelihood one can use

$$\lambda = \frac{\mathcal{L}(\boldsymbol{n}|\boldsymbol{v})}{\mathcal{L}(\boldsymbol{n}|\boldsymbol{n})} = \frac{f_{\text{joint}}(\boldsymbol{n};\boldsymbol{\nu})}{f_{\text{joint}}(\boldsymbol{n};\boldsymbol{n})}\,. \tag{B.1}$$

In the case of Poisson distributed data this leads to

$$\lambda = e^{n_{\text{tot}}-\nu_{\text{tot}}} \prod_{i=1}^{N} \left(\frac{\nu_i}{n_i}\right)^{n_i}\,. \tag{B.2}$$

Then, in the large sample limit, the test statistic [429]

$$\chi^2 = -2\log\lambda = 2\sum_{i=1}^{N}\left(n_i \log\frac{n_i}{\hat{\nu}_i} + \hat{\nu}_i - n_i\right) \tag{B.3}$$

follows a χ^2 distribution with $(N-m)$ DOFs, with N being the sample size and m the number of estimated parameters.

Note that the denominator of λ does not depend on any unknown parameters. Thus, the parameter set that maximizes λ is equal to the ML estimators that maximize the likelihood function. For this reason, λ can be used as an estimator as well as for testing the goodness-of-fit.

Of course, one can also rely on Pearson's χ^2 test (statistic), which, in the case of a Poisson-distributed total event number n_{tot}, is given by

$$\chi^2 = \sum_{i=1}^{N} \frac{(n_i - \hat{\nu}_i)^2}{\hat{\nu}_i} \,. \tag{B.4}$$

As above, the defined test statistic follows a χ^2 distribution with $(N - m)$ DOFs.

For both test statistics, the approximation of being χ^2-distributed is only valid in the large sample limit. If a histogram contains bins with only a few events, i.e. $n_i < 5$, then it is recommended to perform a MC study in order to obtain the true PDF [227, Chapter 6.11].

B.2 Frequentist confidence intervals

In the context of parameter estimation, one usually reports the best estimate in combination with an estimate on the standard deviation: $\hat{\theta} \pm \hat{\sigma}_{\hat{\theta}}$ or, in the case of multiple estimates, the best estimates together with the corresponding covariance matrix. Moreover, the underlying PDF of most practical estimators can be approximated with a Gaussian in the large sample limit. The standard procedure for determination of Frequentist CIs has been invented by Neyman [236]. Therein, the boundary of the given interval is viewed as a function of the given data and, thus, is expected to fluctuate under inclusion of additional data. Further, the CIs are constructed to have a certain coverage probability with regard to the true parameter value. In that sense, the fraction of intervals that contain the exact parameter is greater or equal to the desired C.L..

The underlying principle is that for a PDF $f(x;\theta)$ and an assumed probability of $(1-\alpha)$ equal for all tested parameters θ, one can construct an interval $[x_1(\theta,\alpha), x_2(\theta,\alpha)]$ with probability

$$P(x_1 < x < x_2; \theta) = \int_{x_1}^{x_2} f(x;\theta)\, dx \geq 1 - \alpha \,, \tag{B.5}$$

which is then inverted into an interval of parameters θ with probability

$$1 - \alpha = P(x_1(\theta) < x < x_2(\theta)) = P(\theta_2(x) < \theta < \theta_1(x)) \,. \tag{B.6}$$

In practice, one scans over all parameter values of the parameter of interest θ and determines for each given value θ_0 the corresponding CI $[x_1(\theta_0,\alpha), x_2(\theta_0,\alpha)]$ under the assumption of a desired C.L. $(1-\alpha)$. Under inversion of the derived intervals, one obtains the CIs on the parameter of interest for the given data, $[\theta_1(x,\alpha), \theta_2(x,\alpha)]$. Note that the interval construction of the first step, cf. Eq. (B.5), depends on the desired intervals and the underlying PDF $f(x;\theta)$. For instance, it changes for one-sided intervals or might be modified in cases of discrete observables x, e.g. into a binomial or Poisson statistic.

Gaussian distributed measurements An important example of the above construction arises in the context of normally distributed measurements, where the underlying PDF $f(x;\theta)$ is a Gaussian with mean $\hat{\theta}$ and standard deviation $\sigma_{\hat{\theta}}$. For known $\sigma_{\hat{\theta}}$, the interval $[a,b]$ is then determined via

$$a = \hat{\theta} - \sigma_{\hat{\theta}}\Phi^{-1}(1-\alpha)\,, \qquad\qquad b = \hat{\theta} + \sigma_{\hat{\theta}}\Phi^{-1}(1+\beta)\,, \tag{B.7}$$

with the inverse of the standard Gaussian CDF Φ^{-1} and the corresponding uncertainties α and β for finding $\hat{\theta} \geq a$ and $\hat{\theta} \leq b$, respectively. The overall coverage probability of the interval is given by $1-\alpha-\beta$.

For example, the standard 1σ intervals with coverage probability of 68.3% are recovered for $\alpha = \beta = \gamma/2$ and $\Phi^{-1}(1-\gamma/2) = 1$. If the standard deviation $\sigma_{\hat{\theta}}$ is not known precisely, the situation is more complicated. In practice, one can still use an estimate from a large enough data set.

B.3 Confidence levels via likelihood functions

In the case of non-Gaussian estimators, the likelihood function itself can be used to obtain (approximate) confidence intervals as it becomes centered about the ML estimate $\hat{\theta}$ in the large sample limit. The obtained expression is similar to Eq. (2.39), but now with the standard deviation $\sigma_{\hat{\sigma}}$ being equal to the one of the underlying PDF. Note that in Sec. 2.3.1.2 the expression is discussed on the context of estimator's variance $\hat{\sigma}^2_{\hat{\theta}}$, which is to be estimated from a data sample. Here, we have to replace $\hat{\sigma}^2_{\hat{\theta}} \to \sigma^2_{\hat{\theta}}$ as we refer to the underlying PDF which is assumed to be known for the moment.

Due to properties of the underlying Gaussian, we can now relate the variance of an estimator to explicit confidence regions. Recall that an estimator's variance is determined by a shift of the maximal likelihood value by $1/2$, cf. Eq. (2.39). It can be shown that even in the case, where the likelihood function is non-Gaussian, central confidence intervals $[a,b] = [\hat{\theta}-c, \hat{\theta}+d]$ can be obtained via

$$\log \mathcal{L}(\hat{\theta}^{+d}_{-c}) = \log \mathcal{L}_{\max} - \frac{N^2}{2}\,, \tag{B.8}$$

with $N = \Phi^{-1}(1-\frac{\gamma}{2})$ being the quantile of the standard Gaussian corresponding to a C.L. of $1-\gamma$. For the case of multidimensional confidence intervals, we refer to the literature, e.g. Ref. [227].

Appendix C

Supplementary plots

C.1 Reactor antineutrino spectrum and uncertainties on CEνNS signal expectation

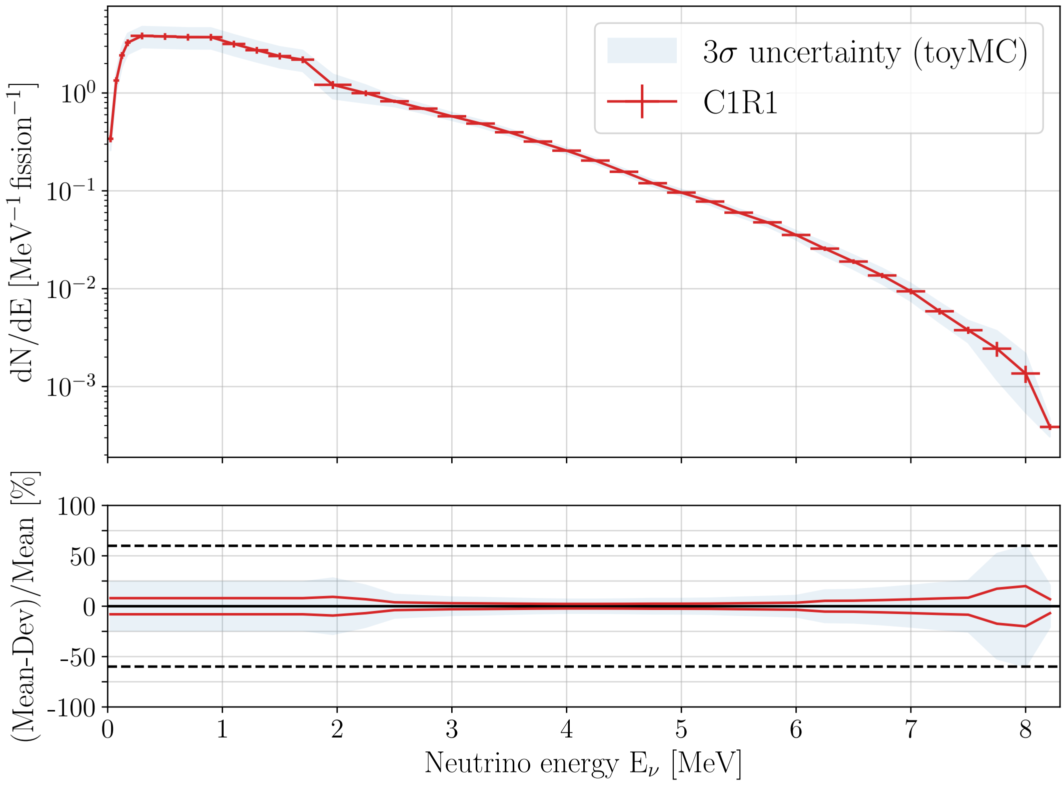

Figure C.1.: Logarithmic reactor antineutrino spectrum for the data collection period C1R1 in order to illustrate the uncertainties induced by the underlying parameters also for the high energy tail.

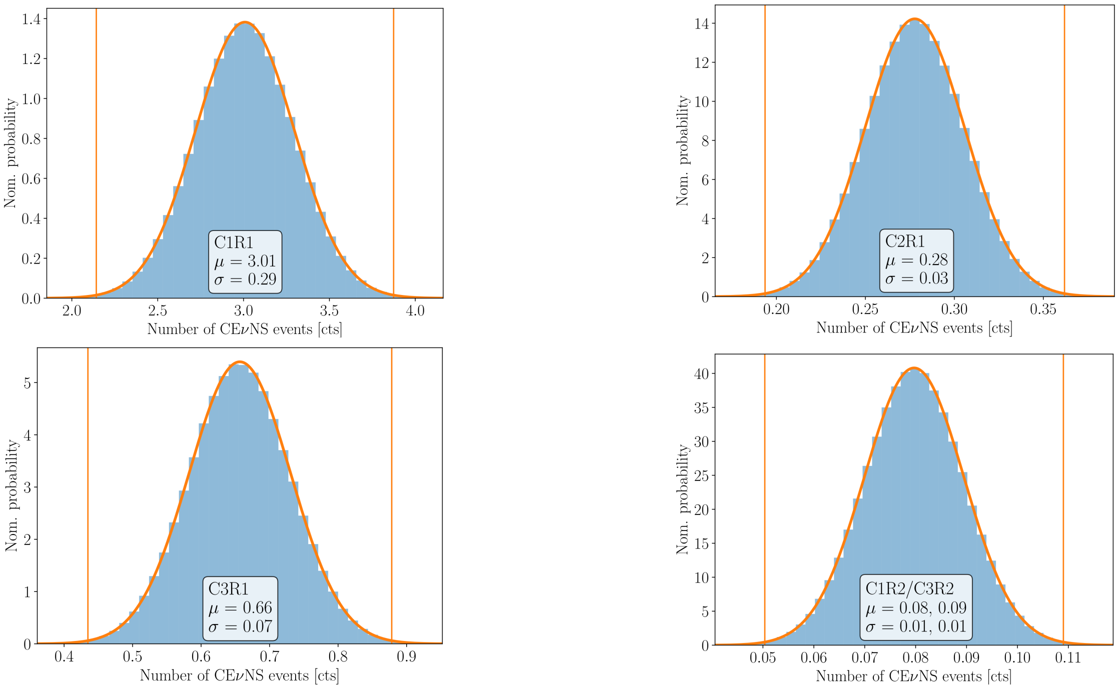

Figure C.2.: Impact of spectral uncertainties on the expected SM CEνNS signal for all data collection periods considered in Ch. 3. Uncertainties are determined from a Gaussian fit to the signal distribution obtained via sampling of reactor spectra and subsequent calculation of the resulting CEνNS events. Orange lines indicate 3σ deviations from the mean value.

C.2 Reactor thermal power for extended data sets

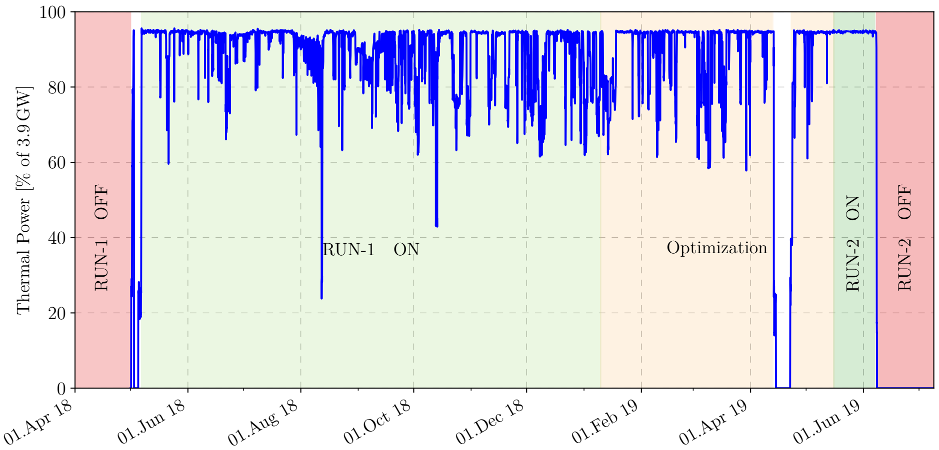

Figure C.3.: Reactor thermal power related to the extended data collection periods used in the BSM analyses of Chapter 4.

C.3 Overview of quenching factor measurements

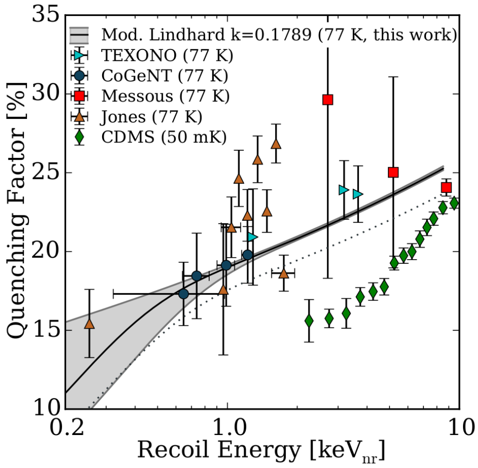

Figure C.4.: Overview of quenching factor measurements in comparison to the prediction of the modified Lindhard model. Figure is taken from Ref. [169]

C.4 CEνNS event spectrum in dependence of different quenching parameters

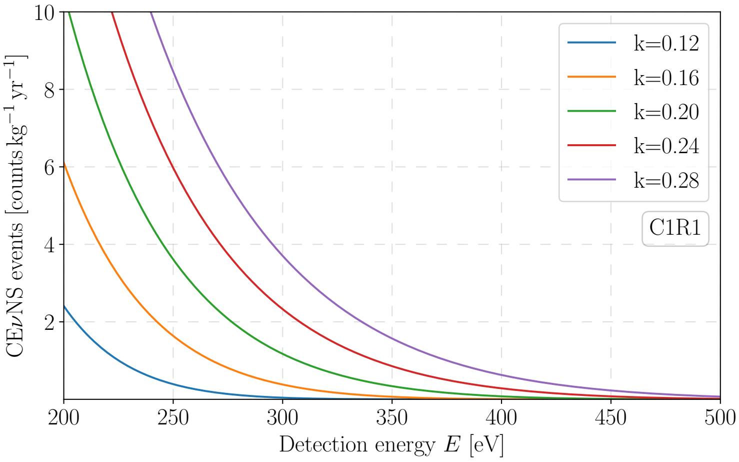

Figure C.5.: CEνNS event spectrum in dependence of the quenching parameter k. The detector response of data collection period C1R1 is assumed and event spectra shown for different k-parameters. Note that the CEνNS analysis of Ch. 3 excluded quenching parameters above $k = 0.27$, while the dedicated measurement of the CONUS Collaboration determined it to be $k = 0.164 \pm 0.004$, cf. Ref. [257].

C.5 Exemplary Conus detector spectrum

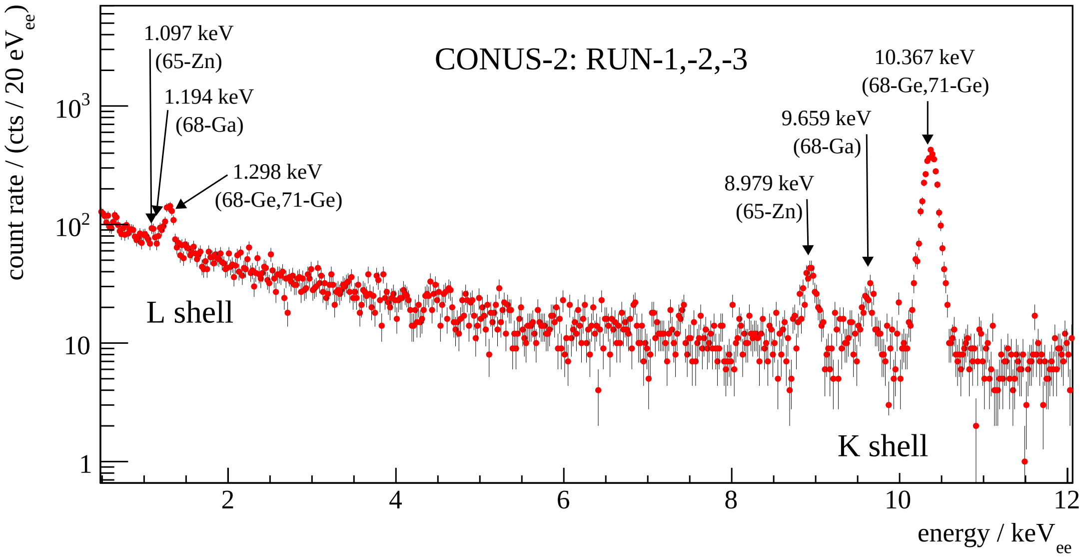

Figure C.6.: Ionization energy spectrum of detector C2 measured in the period of RUN-1 to RUN-3. K- and L-shell x-ray lines are visible due to the achieved low background levels (intrinsic and external). The energy scale calibration and the determination of detector resolution are based on these lines including the corresponding uncertainties. The figure is published in Ref. [82]. For details about the individual lines, we refer to Tab. 7 therein.

C.6 Background suppression of the CONUS shield

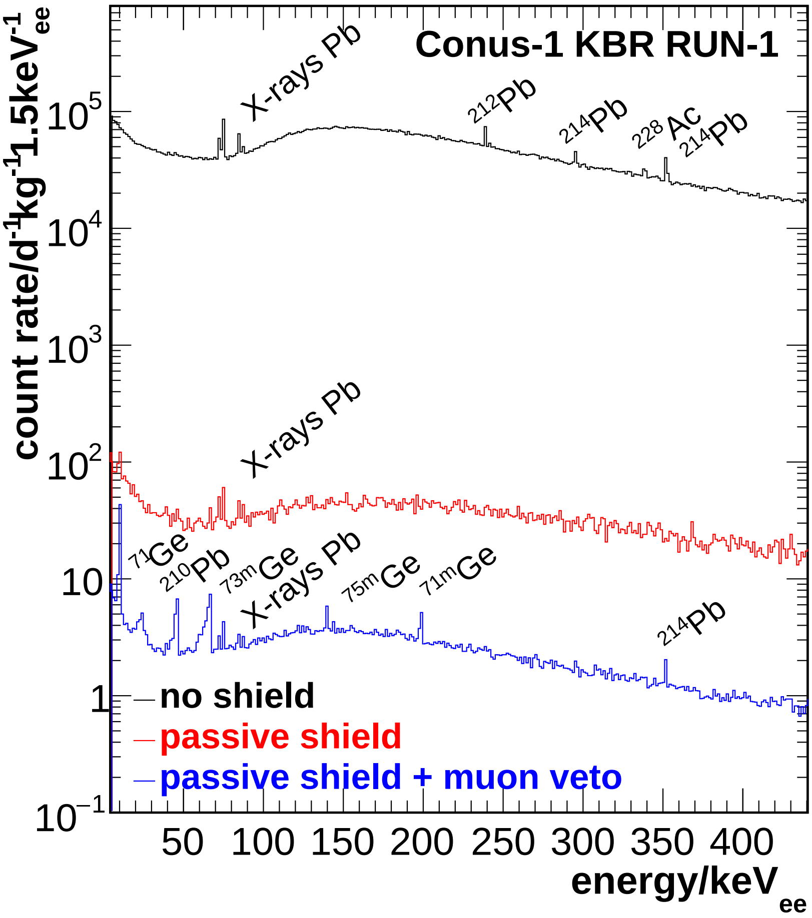

Figure C.7.: Background suppression capability of the CONUS shield illustrated for detector C1. The black spectrum indicates the background level without any shield and consequently lines of natural radioactivity are observed. Background suppression by about 2-3 order of magnitude is already achieved with the passive shield (red), which then shows mainly muon-induced background. The blue curve corresponds to the background level achieved with a muon anticoincidence system (muon veto) in addition to the passive shield. Now, metastable states related to neutron captures in germanium become visible. With the CONUS shield, the overall background level is reduced by about four orders of magnitude. Figure is taken from Ref. [244].

C.7 Monte Carlo background models for CONUS

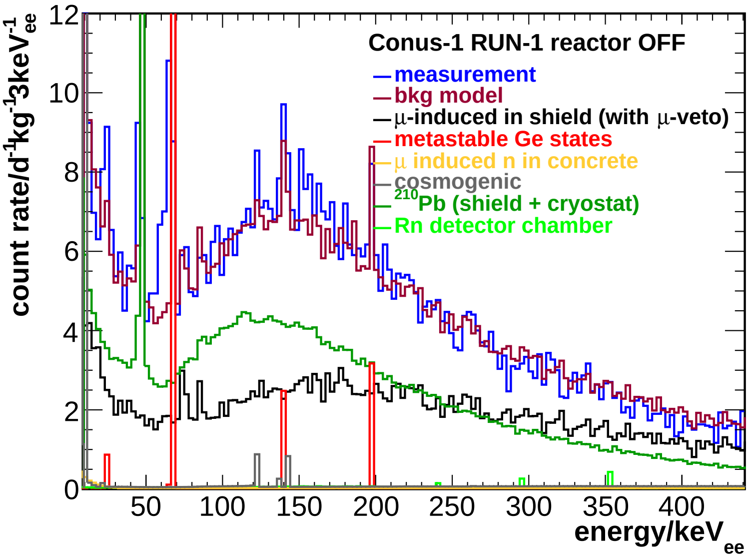

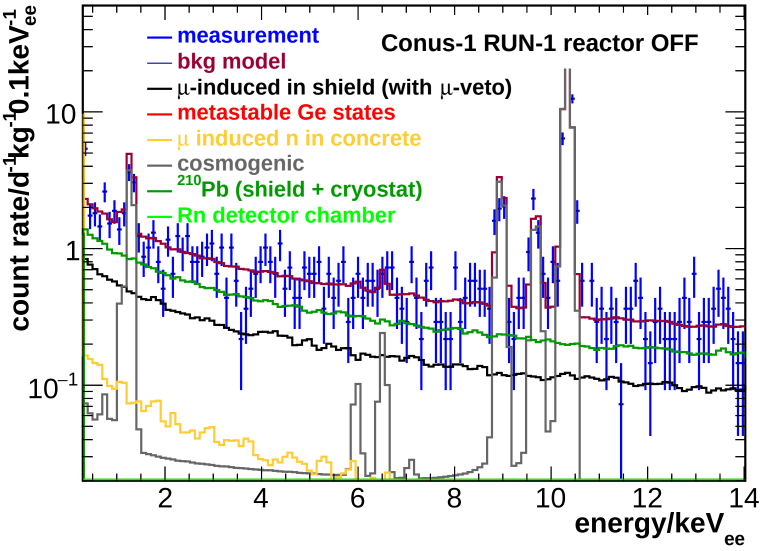

Figure C.8.: CONUS MC background model and its composition for data collection period C1R1 (reactor OFF). Individual background components considered in the performed background simulation are shown in different colors. Further, the sum of all background contributions (*the* MC background model) is given in dark red and compared to the corresponding reactor OFF data in blue. **Top:** The high-energy spectrum shows satisfying agreement between the model and data over a wide energy range, i.e. $[0, 440]$ keV. **Bottom:** The low-energy spectrum is mostly relevant for the analyses of this work. Figures is taken from Ref. [244].

APPENDIX D

MONTE CARLO SIMULATION OF THE TEST STATISTIC

D.1 Parameter correlation of fit parameters

During our analyses we encounter correlated parameters in two key positions, i.e. the parameters of the threshold descriptions of Eq. (3.11) and Eq. (4.2) as well as the background rescaling parameters in Eq. (4.1). Although no problem for the individual fits in our analysis scheme, these parameter correlations need to be taken into account when MC sampling of the underlying test statistic is aimed. In what follows, we illustrate the method that is applied in order to extract two-dimensional Gaussian covariance contours. These contours are used for parameter sampling in order to simulate the underlying test statistics, from which our limits are then extracted.

The applied method relies on an interactive assessment of the individual detector contours within a JupyterLab notebook [278] by using the iminuit package [280, 281] in combination with the SciPy framework [271–274, 276]. Further, knowledge about distance determination in polar coordinates and the Mahalanobis distance is required, which is basically the generalized distance from a distributions mean [430, 431]. The 1σ and 2σ regions correspond to $d^{1\sigma}_{\mathrm{Maha}} = 1.52$ and $d^{2\sigma}_{\mathrm{Maha}} = 2.49$, respectively [431, Table II].

The basic algorithm developed by the author's colleague Dr. T. Hugle is based on the following steps:

1. Determination of individual minos covariance contours for both parameters, e.g. under assumption of certain fixed parameters like quenching, in order to estimate the individual parameter regions

2. Determination and extraction of 1σ and 2σ (covariance) contours via a scan over the parameter space spanned by (x, y), while performing a fit with fixed parameters (x_0, y_0) at each point

3. Rescaling of the obtained contours in order to improve the following fit routines (especially in the case of parameters related to the threshold descriptions)

4. Transformation of cartesian coordinates (x, y) to polar coordinates and sorting according to the polar angle
5. Fitting of polar coordinates with the (Gaussian) Mahalanobis contour functions (underlying assumption: approximate Gaussian distribution), cf. Refs. [431, 432]

$$\text{contour}(\phi, \sigma_1, \sigma_2, \rho) = \frac{d^{1\sigma,2\sigma}_{\text{Maha}}\sqrt{1-\rho^2}}{\sqrt{(\frac{\cos\phi}{\sigma_1})^2 + (\frac{\sin\phi}{\sigma_2})^2 - 2\rho\frac{\sin\phi}{\sigma_2}\frac{\cos\phi}{\sigma_1}}}\,, \tag{D.1}$$

   with $d^{1\sigma,2\sigma}_{\text{Maha}}$ being the Mahalanobis distance for the 1σ or 2σ contour of the two-dimensional Gaussian distribution. In addition, $\sigma_{1,2}$ denote the standard deviation in the corresponding parameter direction.

6. Inversion of scaling for mean values and fitted parameters σ_1, σ_2, ρ
7. Transformation of best-fit values related to the Mahalanobis contours into a covariance matrix of the parameters of interest via

$$\rho_{i,j} = \rho \cdot \sigma_i \cdot \sigma_j\,. \tag{D.2}$$

This procedure is not altered under exchange of the parameters of interest, although a rescaling of contour parameters is not necessary in the case of the background scaling parameters since parameter are by definition of the same order. We apply our procedure to the 1σ- and 2σ-contours determined with the minos routine and chose the covariance matrix that exhibits the best overall coverage, which applies in all cases to the 2σ minos contour. Consequently, the correlation among the two parameters of interest is slightly overestimated, which reflects a conservative treatment of errors and correlations.

D.1.1 Parameter correlation of threshold description

Now we want to illustrate the method's main steps by explicitly showing the determination of a covariance matrix for the parameters of the threshold description, cf. Eq. (4.2). Here we chose the case of vector NSIs for data collection period C1R1.

- Determination of individual minos contours for the individual parameters p_0 and p_1

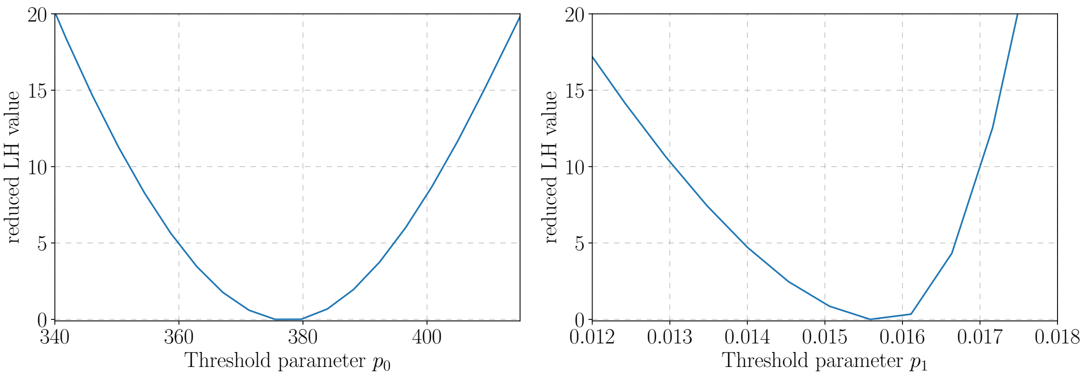

- Determination and extraction of 1σ and 2σ contours in the (p_0, p_1)-plane

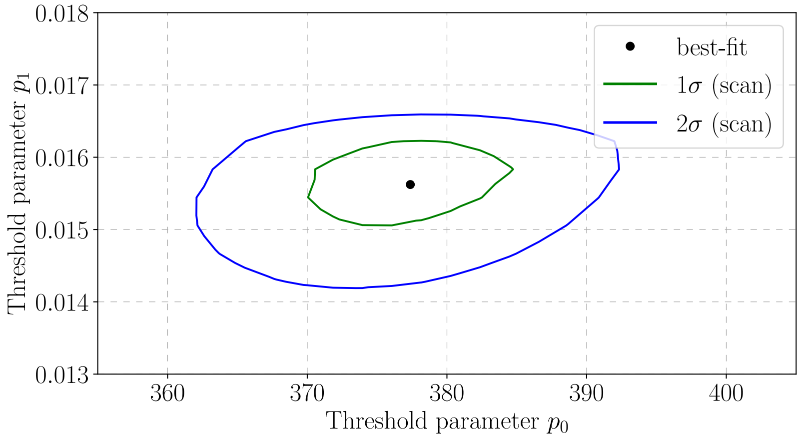

- Polar contour fit of (Gaussian) Mahalanobis contour functions

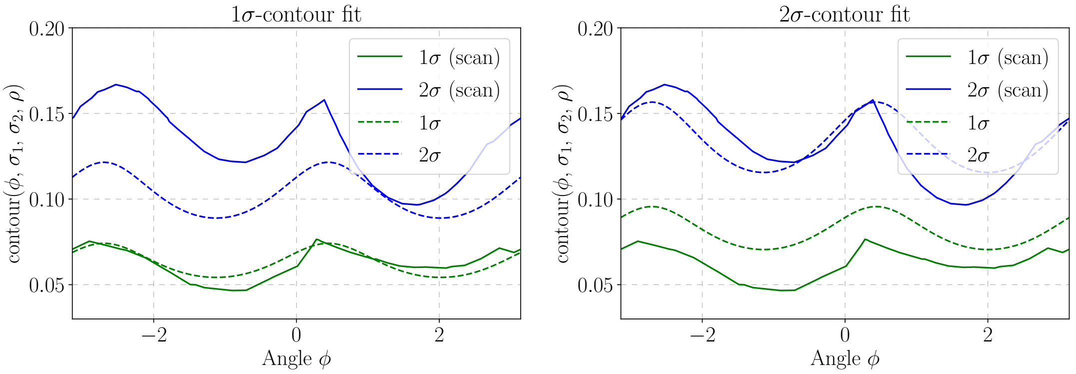

- Covariance contour of the parameters (p_0, p_1) that is used for parameter sampling

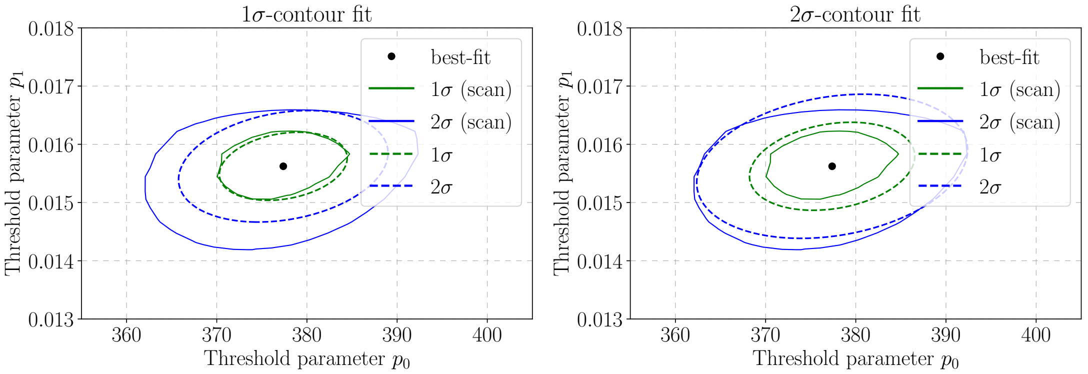

D.1.2 Parameter correlation of background rescaling factors

Further, we show the performance of the developed method for the background rescaling parameters b_1 and b_2, cf. Eq. (4.1). Here we chose the case of a light scalar mediator in the energy region between $[2, 8]$ keV for data collection period C1R1. Again, we restrict ourselves to the important steps.

- Determination of individual minos contours for the individual parameters b_1 and b_2

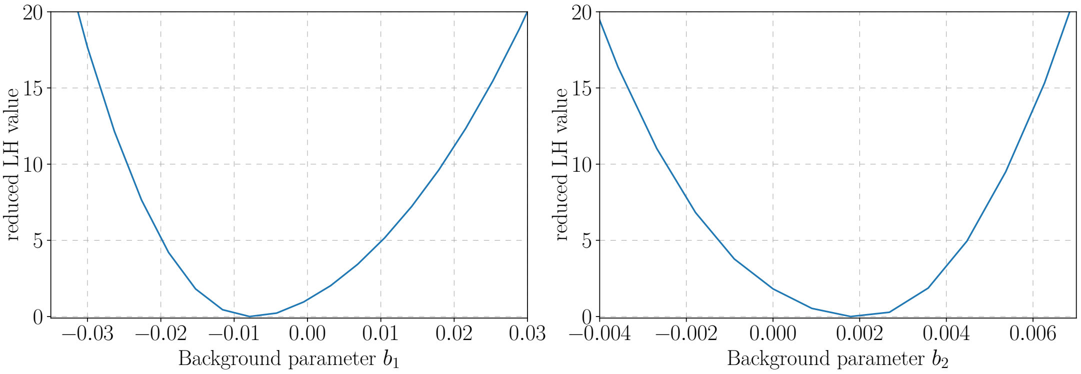

- Determination and extraction of 1σ and 2σ contours in the (b_1, b_2)-plane

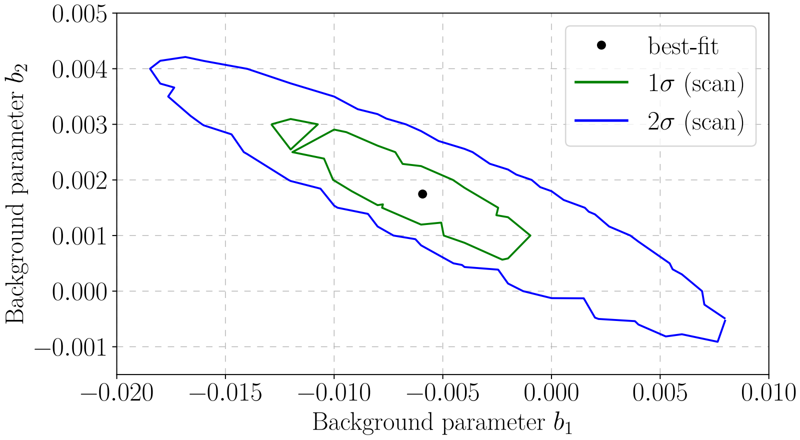

- Polar contour fit of (Gaussian) Mahalanobis contour functions

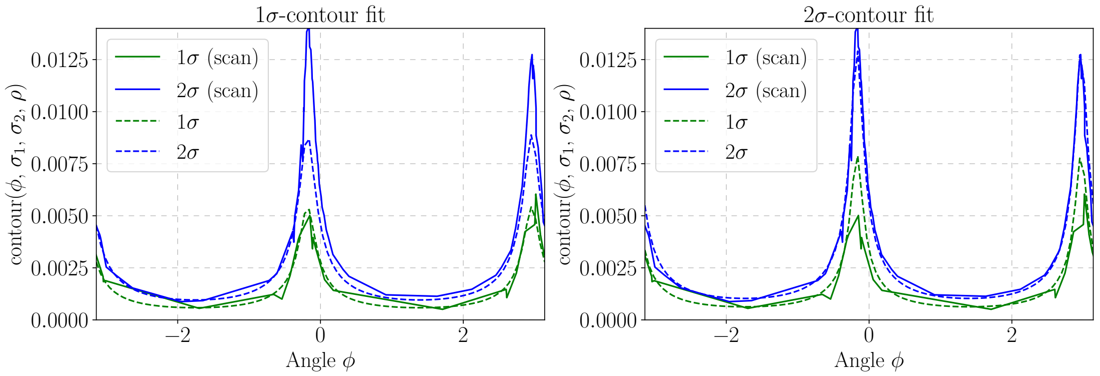

- Covariance contour of the parameters (b_1, b_2) that is used for parameter sampling

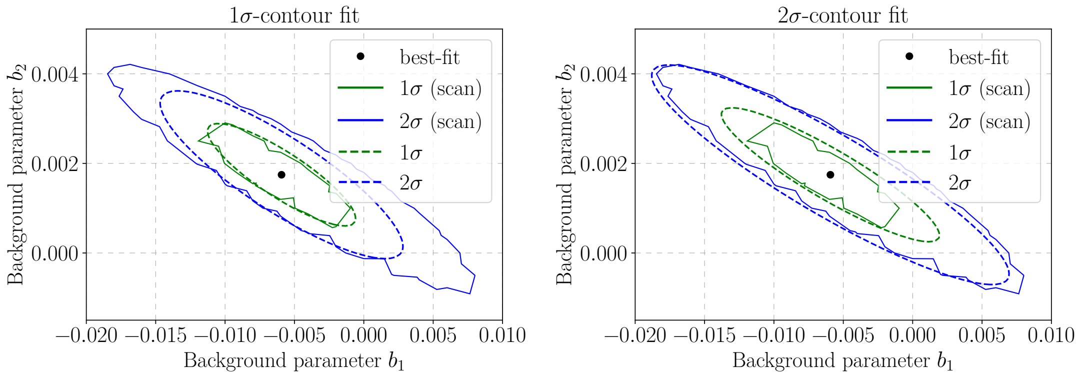

DISCLAIMER

This work was performed as part of the CONUS Collaboration at Max-Planck-Institut für Kernphysik, Heidelberg (Germany). The scientific findings presented in this thesis are based on work done by the author in collaboration with others. The author primarily contributed to Refs. [1–3], which are discussed in the main chapters of this thesis, i.e. Ch. 3 and Ch. 4. In addition, minor contributions were made in the context of Refs. [4, 5]. The author is also listed on the following collaboration papers, cf. Refs. [6–8].

Most of these scientific findings have already been published or are in a collaboration or peer review process at the time of submission of the present work.

In addition to the mentioned scientific works, the author also contributed to the peer-reviewed Ref. [9].

List of publications by Thomas Rink

[1] H. Bonet et al. "Constraints on Elastic Neutrino Nucleus Scattering in the Fully Coherent Regime from the CONUS Experiment". In: *Phys.Rev.Lett.* 126 (4 2021). DOI: `10.1103/PhysRevLett.126.041804`. arXiv: `2011.00210`. URL: `https://inspirehep.net/literature/1827477` (visited on 05/05/2021).

[2] H. Bonet et al. "Novel Constraints on Neutrino Physics beyond the Standard Model from the CONUS Experiment". In: (2021). arXiv: `2110.02174`. URL: `https://inspirehep.net/literature/1938781` (visited on 10/06/2021).

[3] H. Bonet et al. *First limits on neutrino electromagnetic properties from the CONUS experiment.* To be published. 2022.

[4] J. Hakenmüller et al. "Neutron-Induced Background in the CONUS Experiment". In: *Eur.Phys.J.C* 79 (8 2019), p. 699. DOI: `10.1140/epjc/s10052-019-7160-2`. arXiv: `1903.09269`. URL: `https://inspirehep.net/literature/1726342` (visited on 05/06/2021).

[5] H. Bonet et al. "Large-Size Sub-keV Sensitive Germanium Detectors for the CONUS Experiment". In: *Eur.Phys.J.C* 81 (3 2021), p. 267. DOI: `10.1140/epjc/s10052-021-09038-3`. arXiv: `2010.11241`. URL: `https://inspirehep.net/literature/1824413` (visited on 05/06/2021).

[6] C. Buck et al. “A Novel Experiment for Coherent Elastic Neutrino Nucleus Scattering: CONUS”. In: *J.Phys.Conf.Ser.* 1342.1 (2020). DOI: `10.1088/1742-6596/1342/1/012094`. URL: `https://inspirehep.net/literature/1776471` (visited on 05/06/2021).

[7] H. Bonet et al. “Full Background Decomposition of the CONUS Experiment”. In: (2021). arXiv: `2112.09585`. URL: `https://inspirehep.net/literature/1993409` (visited on 12/18/2021).

[8] H. Bonet et al. *Direct measurement of the ionization quenching factor of nuclear recoils in germanium in the keV range*. To be published. 2022.

[9] T. Rink, W. Rodejohann, and K. Schmitz. “Leptogenesis and Low-Energy CP Violation in a Type-II-Dominated Left-Right Seesaw Model”. In: *Nucl.Phys.B* 972 (2021). DOI: `10.1016/j.nuclphysb.2021.115552`. arXiv: `2006.03021`. URL: `https://inspirehep.net/literature/1799478` (visited on 11/28/2021).

Bibliography

[1] C. Giunti and C. W. Kim. *Fundamentals of neutrino physics and astrophysics*. eng. 1. publ. Oxford [u.a.]: Oxford Univ. Press, 2007, XVI, 710 S. ISBN: 0-19-850871-9 and 978-0-19-850871-7.

[2] S. M. Bilenky. “Neutrino. History of a Unique Particle”. In: *Eur.Phys.J.H* 38 (2013), pp. 345–404. DOI: `10.1140/epjh/e2012-20068-9`. arXiv: `1210.3065`. URL: `https://inspirehep.net/literature/1190359` (visited on 12/02/2021).

[3] W. Pauli. “Dear Radioactive Ladies and Gentlemen”. In: *Phys.Today* 31N9 (1978), p. 27. URL: `https://inspirehep.net/literature/45177` (visited on 07/20/2021).

[4] *All Nobel Prizes in Physics*. NobelPrize.org. URL: `https://www.nobelprize.org/prizes/lists/all-nobel-prizes-in-physics` (visited on 12/04/2021).

[5] E. Fermi. “An Attempt of a Theory of Beta Radiation. 1.” In: *Z.Phys.* 88 (1934), pp. 161–177. DOI: `10.1007/BF01351864`. URL: `https://inspirehep.net/literature/3203` (visited on 12/03/2021).

[6] F. Perrin. “Possibilité d’émission de particules neutres de masse intrinsèque nulle dans les radioactivités β”. In: *Comptes rendus* 197 (1933), pp. 1625–1627.

[7] F. Reines and C. L. Cowan. “Detection of the Free Neutrino”. In: *Phys.Rev.* 92 (1953), pp. 830–831. DOI: `10.1103/PhysRev.92.830`. URL: `https://inspirehep.net/literature/40475` (visited on 07/20/2021).

[8] C. L. Cowan et al. “Detection of the Free Neutrino: A Confirmation”. In: *Science* 124 (1956), pp. 103–104. DOI: `10.1126/science.124.3212.103`. URL: `https://inspirehep.net/literature/39882` (visited on 07/20/2021).

[9] B. T. Cleveland et al. “Measurement of the Solar Electron Neutrino Flux with the Homestake Chlorine Detector”. In: *Astrophys.J.* 496 (1998), pp. 505–526. DOI: `10.1086/305343`. URL: `https://inspirehep.net/literature/471829` (visited on 11/16/2021).

[10] J. N. Bahcall and M. H. Pinsonneault. “Standard Solar Models, with and without Helium Diffusion and the Solar Neutrino Problem”. In: *Rev.Mod.Phys.* 64 (1992), pp. 885–926. DOI: `10.1103/RevModPhys.64.885`. URL: `https://inspirehep.net/literature/32101` (visited on 11/16/2021).

[11] S. A. Bludman, D. C. Kennedy, and P. G. Langacker. “Solutions of the Solar Neutrino Problem”. In: *Nucl.Phys.B* 374 (1992), pp. 373–391. DOI: `10.1016/0550-3213(92)90358-I`. URL: `https://inspirehep.net/literature/314961` (visited on 11/16/2021).

[12] W. C. Haxton. “The Solar Neutrino Problem”. In: *Ann.Rev.Astron.Astrophys.* 33 (1995), pp. 459–503. DOI: 10.1146/annurev.aa.33.090195.002331. arXiv: hep-ph/9503430. URL: https://inspirehep.net/literature/393730 (visited on 11/16/2021).

[13] E. K. Akhmedov and J. Pulido. “SNO and the Neutrino Magnetic Moment Solution of the Solar Neutrino Problem”. In: *Phys.Lett.B* 485 (2000), pp. 178–186. DOI: 10.1016/S0370-2693(00)00695-X. arXiv: hep-ph/0005173. URL: https://inspirehep.net/literature/527471 (visited on 11/16/2021).

[14] Q. R. Ahmad et al. “Direct Evidence for Neutrino Flavor Transformation from Neutral Current Interactions in the Sudbury Neutrino Observatory”. In: *Phys.Rev.Lett.* 89 (2002). DOI: 10.1103/PhysRevLett.89.011301. arXiv: nucl-ex/0204008. URL: https://inspirehep.net/literature/585723 (visited on 11/16/2021).

[15] S. Fukuda et al. “Constraints on Neutrino Oscillations Using 1258 Days of Super-Kamiokande Solar Neutrino Data”. In: *Phys.Rev.Lett.* 86 (2001), pp. 5656–5660. DOI: 10.1103/PhysRevLett.86.5656. arXiv: hep-ex/0103033. URL: https://inspirehep.net/literature/554318 (visited on 11/16/2021).

[16] Y. Ashie et al. “A Measurement of Atmospheric Neutrino Oscillation Parameters by SUPER-KAMIOKANDE I”. In: *Phys.Rev.D* 71 (2005). DOI: 10.1103/PhysRevD.71.112005. arXiv: hep-ex/0501064. URL: https://inspirehep.net/literature/675543 (visited on 11/16/2021).

[17] Z. Maki, M. Nakagawa, and S. Sakata. “Remarks on the Unified Model of Elementary Particles”. In: *Prog.Theor.Phys.* 28 (1962), pp. 870–880. DOI: 10.1143/PTP.28.870. URL: https://inspirehep.net/literature/3540 (visited on 11/16/2021).

[18] B. Pontecorvo. “Neutrino Experiments and the Problem of Conservation of Leptonic Charge”. In: *Sov.Phys.JETP* 26 (1968), pp. 984–988. URL: https://inspirehep.net/literature/51319 (visited on 11/16/2021).

[19] S. M. Bilenky and B. Pontecorvo. “Lepton Mixing and Neutrino Oscillations”. In: *Phys.Rept.* 41 (1978), pp. 225–261. DOI: 10.1016/0370-1573(78)90095-9. URL: https://inspirehep.net/literature/135308 (visited on 11/16/2021).

[20] L. Wolfenstein. “Neutrino Oscillations in Matter”. In: *Phys.Rev.D* 17 (1978), pp. 2369–2374. DOI: 10.1103/PhysRevD.17.2369. URL: https://inspirehep.net/literature/122259 (visited on 11/16/2021).

[21] S. P. Mikheyev and A. Yu. Smirnov. “Resonance Amplification of Oscillations in Matter and Spectroscopy of Solar Neutrinos”. In: *Sov.J.Nucl.Phys.* 42 (1985), pp. 913–917. URL: https://inspirehep.net/literature/228623 (visited on 11/16/2021).

[22] P. Vogel and A. Piepke. *Neutrino Properties.* Aug. 2020. DOI: 10.1093/ptep/ptaa104. URL: https://inspirehep.net/literature/1812251 (visited on 07/12/2021).

[23] J.-M. Yang et al. “Constraints on Cosmology and Neutrino Physics from Big Bang Nucleosynthesis”. In: *Astrophys.J.* 227 (1979), pp. 697–704. DOI: 10.1086/156779. URL: https://inspirehep.net/literature/6981 (visited on 12/04/2021).

[24] A. Heger et al. “Neutrino Nucleosynthesis”. In: *Phys.Lett.B* 606 (2005), pp. 258–264. DOI: `10.1016/j.physletb.2004.12.017`. arXiv: `astro-ph/0307546`. URL: `https://inspirehep.net/literature/624671` (visited on 12/04/2021).

[25] K. G. Balasi, K. Langanke, and G. Martínez-Pinedo. “Neutrino–Nucleus Reactions and Their Role for Supernova Dynamics and Nucleosynthesis”. In: *Prog.Part.Nucl.Phys.* 85 (2015), pp. 33–81. DOI: `10.1016/j.ppnp.2015.08.001`. arXiv: `1503.08095`. URL: `https://inspirehep.net/literature/1356761` (visited on 05/05/2021).

[26] J. Lesgourgues and S. Pastor. “Massive Neutrinos and Cosmology”. In: *Phys.Rept.* 429 (2006), pp. 307–379. DOI: `10.1016/j.physrep.2006.04.001`. arXiv: `astro-ph/0603494`. URL: `https://inspirehep.net/literature/712677` (visited on 12/04/2021).

[27] S. Davidson, E. Nardi, and Y. Nir. “Leptogenesis”. In: *Phys.Rept.* 466 (2008), pp. 105–177. DOI: `10.1016/j.physrep.2008.06.002`. arXiv: `0802.2962`. URL: `https://inspirehep.net/literature/779828` (visited on 12/04/2021).

[28] D. Z. Freedman, D. N. Schramm, and D. L. Tubbs. “The Weak Neutral Current and Its Effects in Stellar Collapse”. In: *Annual Review of Nuclear Science* 27.1 (Dec. 1, 1977), pp. 167–207. ISSN: 0066-4243. DOI: `10.1146/annurev.ns.27.120177.001123`. URL: `https://www.annualreviews.org/doi/10.1146/annurev.ns.27.120177.001123` (visited on 02/25/2021).

[29] P. S. Amanik and G. M. Fuller. “Stellar Collapse Dynamics With Neutrino Flavor Changing Neutral Currents”. In: *Phys.Rev.D* 75 (2007). DOI: `10.1103/PhysRevD.75.083008`. arXiv: `astro-ph/0606607`. URL: `https://inspirehep.net/literature/719995` (visited on 05/05/2021).

[30] C. J. Stapleford et al. “Nonstandard Neutrino Interactions in Supernovae”. In: *Phys.Rev.D* 94 (9 2016). DOI: `10.1103/PhysRevD.94.093007`. arXiv: `1605.04903`. URL: `https://inspirehep.net/literature/1459225` (visited on 05/06/2021).

[31] M. Agostini et al. “Comprehensive Measurement of *pp*-Chain Solar Neutrinos”. In: *Nature* 562.7728 (2018), pp. 505–510. DOI: `10.1038/s41586-018-0624-y`. URL: `https://inspirehep.net/literature/1700565` (visited on 12/04/2021).

[32] M. Agostini et al. “Experimental Evidence of Neutrinos Produced in the CNO Fusion Cycle in the Sun”. In: *Nature* 587 (2020), pp. 577–582. DOI: `10.1038/s41586-020-2934-0`. arXiv: `2006.15115`. URL: `https://inspirehep.net/literature/1803362` (visited on 12/04/2021).

[33] V. Munoz et al. “Exploring the Origin of Supermassive Black Holes with Coherent Neutrino Scattering”. In: *JCAP* 11 (2021), p. 020. DOI: `10.1088/1475-7516/2021/11/020`. arXiv: `2102.00885`. URL: `https://inspirehep.net/literature/1844231` (visited on 11/24/2021).

[34] D. L. Tubbs and D. N. Schramm. “Neutrino Opacities at High Temperatures and Densities”. In: *The Astrophysical Journal* 201 (Oct. 1, 1975), pp. 467–488. ISSN: 0004-637X. DOI: `10.1086/153909`. URL: `http://adsabs.harvard.edu/abs/1975ApJ...201..467T` (visited on 02/24/2021).

[35] S. Davidson and A. Ibarra. "A Lower Bound on the Right-Handed Neutrino Mass from Leptogenesis". In: *Phys.Lett.B* 535 (2002), pp. 25–32. DOI: 10.1016/S0370-2693(02)01735-5. arXiv: hep-ph/0202239. URL: https://inspirehep.net/literature/583379 (visited on 12/04/2021).

[36] S. Antusch and S. F. King. "Type II Leptogenesis and the Neutrino Mass Scale". In: *Phys.Lett.B* 597 (2004), pp. 199–207. DOI: 10.1016/j.physletb.2004.07.009. arXiv: hep-ph/0405093. URL: https://inspirehep.net/literature/650163 (visited on 12/04/2021).

[37] T. Hugle, M. Platscher, and K. Schmitz. "Low-Scale Leptogenesis in the Scotogenic Neutrino Mass Model". In: *Phys.Rev.D* 98 (2 2018). DOI: 10.1103/PhysRevD.98.023020. arXiv: 1804.09660. URL: https://inspirehep.net/literature/1670019 (visited on 12/04/2021).

[38] T. Asaka, S. Blanchet, and M. Shaposhnikov. "The nuMSM, Dark Matter and Neutrino Masses". In: *Phys.Lett.B* 631 (2005), pp. 151–156. DOI: 10.1016/j.physletb.2005.09.070. arXiv: hep-ph/0503065. URL: https://inspirehep.net/literature/677890 (visited on 12/04/2021).

[39] E. Ma. "Verifiable Radiative Seesaw Mechanism of Neutrino Mass and Dark Matter". In: *Phys.Rev.D* 73 (2006). DOI: 10.1103/PhysRevD.73.077301. arXiv: hep-ph/0601225. URL: https://inspirehep.net/literature/709378 (visited on 12/04/2021).

[40] M. Drewes et al. "A White Paper on keV Sterile Neutrino Dark Matter". In: *JCAP* 01 (2017), p. 025. DOI: 10.1088/1475-7516/2017/01/025. arXiv: 1602.04816. URL: https://inspirehep.net/literature/1421898 (visited on 12/04/2021).

[41] W. Buchmuller and T. Yanagida. "Quark Lepton Mass Hierarchies and the Baryon Asymmetry". In: *Phys.Lett.B* 445 (1999), pp. 399–402. DOI: 10.1016/S0370-2693(98)01480-4. arXiv: hep-ph/9810308. URL: https://inspirehep.net/literature/477637 (visited on 12/04/2021).

[42] R. N. Mohapatra and A. Y. Smirnov. "Neutrino Mass and New Physics". In: *Ann.Rev.Nucl.Part.Sci.* 56 (2006), pp. 569–628. DOI: 10.1146/annurev.nucl.56.080805.140534. arXiv: hep-ph/0603118. URL: https://inspirehep.net/literature/712568 (visited on 12/04/2021).

[43] Y. Grossman and M. Neubert. "Neutrino Masses and Mixings in Nonfactorizable Geometry". In: *Phys.Lett.B* 474 (2000), pp. 361–371. DOI: 10.1016/S0370-2693(00)00054-X. arXiv: hep-ph/9912408. URL: https://inspirehep.net/literature/511812 (visited on 12/04/2021).

[44] M. Lindner, M. Platscher, and F. S. Queiroz. "A Call for New Physics : The Muon Anomalous Magnetic Moment and Lepton Flavor Violation". In: *Phys.Rept.* 731 (2018), pp. 1–82. DOI: 10.1016/j.physrep.2017.12.001. arXiv: 1610.06587. URL: https://inspirehep.net/literature/1493855 (visited on 12/04/2021).

[45] N. Blinov et al. "Constraining the Self-Interacting Neutrino Interpretation of the Hubble Tension". In: *Phys.Rev.Lett.* 123 (19 2019). DOI: 10.1103/PhysRevLett.123.191102. arXiv: 1905.02727. URL: https://inspirehep.net/literature/1733842 (visited on 12/04/2021).

[46] F. Arias-Aragon et al. “Neutrino Masses and Hubble Tension via a Majoron in MFV”. In: *Eur.Phys.J.C* 81 (1 2021), p. 28. DOI: 10.1140/epjc/s10052-020-08825-8. arXiv: 2009.01848. URL: https://inspirehep.net/literature/1815224 (visited on 12/04/2021).

[47] E. Aprile et al. “Excess Electronic Recoil Events in XENON1T”. In: *Phys.Rev.D* 102 (7 2020). DOI: 10.1103/PhysRevD.102.072004. arXiv: 2006.09721. URL: https://inspirehep.net/literature/1801701 (visited on 11/02/2021).

[48] M. Fukugita and T. Yanagida. *Physics of Neutrinos and Applications to Astrophysics: With 64 Tables.* Physics and Astronomy Online Library. Berlin ; Heidelberg [u.a.]: Springer, 2003. XII, 593 S. ISBN: 978-3-540-43800-7.

[49] K. H. Ackermann et al. “The GERDA Experiment for the Search of $0\nu\beta\beta$ Decay in ^{76}Ge”. In: *Eur.Phys.J.C* 73 (3 2013), p. 2330. DOI: 10.1140/epjc/s10052-013-2330-0. arXiv: 1212.4067. URL: https://inspirehep.net/literature/1207593 (visited on 07/27/2021).

[50] N. Abgrall et al. “The Large Enriched Germanium Experiment for Neutrinoless Double Beta Decay (LEGEND)”. In: *AIP Conf.Proc.* 1894 (1 2017). DOI: 10.1063/1.5007652. arXiv: 1709.01980. URL: https://inspirehep.net/literature/1622264 (visited on 12/04/2021).

[51] N. Abgrall et al. “The Majorana Demonstrator Neutrinoless Double-Beta Decay Experiment”. In: *Adv.High Energy Phys.* 2014 (2014). DOI: 10.1155/2014/365432. arXiv: 1308.1633. URL: https://inspirehep.net/literature/1246934 (visited on 07/27/2021).

[52] M. Pierre. “Neutrinoless Double Beta Decay Search in XENON1T and XENONnT”. In: *PoS* ICRC2021 (2021), p. 540. DOI: 10.22323/1.395.0540. URL: https://inspirehep.net/literature/1928335 (visited on 12/04/2021).

[53] L. Gastaldo et al. “The Electron Capture in ^{163}Ho Experiment – ECHo”. In: *Eur.Phys.J.ST* 226.8 (2017), pp. 1623–1694. DOI: 10.1140/epjst/e2017-70071-y. URL: https://inspirehep.net/literature/1606514 (visited on 12/04/2021).

[54] M. Aker et al. “Improved Upper Limit on the Neutrino Mass from a Direct Kinematic Method by KATRIN”. In: *Phys.Rev.Lett.* 123 (22 2019). DOI: 10.1103/PhysRevLett.123.221802. arXiv: 1909.06048. URL: https://inspirehep.net/literature/1754140 (visited on 12/04/2021).

[55] P. J. Doe et al. “Project 8: Determining Neutrino Mass from Tritium Beta Decay Using a Frequency-Based Method”. In: (Sept. 30, 2013). arXiv: 1309.7093. URL: https://inspirehep.net/literature/1255861 (visited on 12/04/2021).

[56] B. Abi et al. “Deep Underground Neutrino Experiment (DUNE), Far Detector Technical Design Report, Volume I Introduction to DUNE”. In: *JINST* 15 (08 2020). DOI: 10.1088/1748-0221/15/08/T08008. arXiv: 2002.02967. URL: https://inspirehep.net/literature/1779524 (visited on 12/04/2021).

[57] K. Abe et al. “Physics Potential of a Long-Baseline Neutrino Oscillation Experiment Using a J-PARC Neutrino Beam and Hyper-Kamiokande”. In: *PTEP* 2015 (2015). DOI: 10.1093/ptep/ptv061. arXiv: 1502.05199. URL: https://inspirehep.net/literature/1345256 (visited on 12/04/2021).

[58] F. An et al. “Neutrino Physics with JUNO”. In: *J.Phys.G* 43 (3 2016). DOI: 10.1088/0954-3899/43/3/030401. arXiv: 1507.05613. URL: https://inspirehep.net/literature/1384111 (visited on 12/04/2021).

[59] J. Ashenfelter et al. “The PROSPECT Physics Program”. In: *J.Phys.G* 43 (11 2016). DOI: 10.1088/0954-3899/43/11/113001. arXiv: 1512.02202. URL: https://inspirehep.net/literature/1408518 (visited on 12/04/2021).

[60] N. Allemandou et al. “The STEREO Experiment”. In: *JINST* 13 (07 2018). DOI: 10.1088/1748-0221/13/07/P07009. arXiv: 1804.09052. URL: https://inspirehep.net/literature/1669809 (visited on 12/04/2021).

[61] M. Ageron et al. “ANTARES: The First Undersea Neutrino Telescope”. In: *Nucl. Instrum. Meth. A* 656 (2011), pp. 11–38. DOI: 10.1016/j.nima.2011.06.103. arXiv: 1104.1607. URL: https://inspirehep.net/literature/895584 (visited on 12/04/2021).

[62] M. G. Aartsen et al. “Evidence for High-Energy Extraterrestrial Neutrinos at the IceCube Detector”. In: *Science* 342 (2013). DOI: 10.1126/science.1242856. arXiv: 1311.5238. URL: https://inspirehep.net/literature/1265461 (visited on 12/04/2021).

[63] S. Adrian-Martinez et al. “Letter of Intent for KM3NeT 2.0”. In: *J.Phys.G* 43 (8 2016). DOI: 10.1088/0954-3899/43/8/084001. arXiv: 1601.07459. URL: https://inspirehep.net/literature/1417077 (visited on 12/04/2021).

[64] J. A. Aguilar et al. “Design and Sensitivity of the Radio Neutrino Observatory in Greenland (RNO-G)”. In: *JINST* 16 (03 2021). DOI: 10.1088/1748-0221/16/03/P03025. arXiv: 2010.12279. URL: https://inspirehep.net/literature/1826001 (visited on 12/04/2021).

[65] B. P. Abbott et al. “Multi-Messenger Observations of a Binary Neutron Star Merger”. In: *Astrophys.J.Lett.* 848 (2 2017), p. L12. DOI: 10.3847/2041-8213/aa91c9. arXiv: 1710.05833. URL: https://inspirehep.net/literature/1630825 (visited on 12/04/2021).

[66] D. Z. Freedman. “Coherent Neutrino Nucleus Scattering as a Probe of the Weak Neutral Current”. In: *Phys.Rev.D* 9 (1974), pp. 1389–1392. DOI: 10.1103/PhysRevD.9.1389. URL: https://inspirehep.net/literature/85292 (visited on 05/05/2021).

[67] A. Drukier and L. Stodolsky. “Principles and Applications of a Neutral Current Detector for Neutrino Physics and Astronomy”. In: *Phys.Rev.D* 30 (1984), p. 2295. DOI: 10.1103/PhysRevD.30.2295. URL: https://inspirehep.net/literature/13893 (visited on 05/05/2021).

[68] D. Akimov et al. “Observation of Coherent Elastic Neutrino-Nucleus Scattering”. In: *Science* 357 (6356 2017), pp. 1123–1126. DOI: 10.1126/science.aao0990. arXiv: 1708.01294. URL: https://inspirehep.net/literature/1614476 (visited on 05/05/2021).

[69] D. Akimov et al. “First Measurement of Coherent Elastic Neutrino-Nucleus Scattering on Argon”. In: *Phys.Rev.Lett.* 126 (1 2021). DOI: 10.1103/PhysRevLett.126.012002. arXiv: 2003.10630. URL: https://inspirehep.net/literature/1787880 (visited on 05/05/2021).

[70] H. Bonet et al. "Constraints on Elastic Neutrino Nucleus Scattering in the Fully Coherent Regime from the CONUS Experiment". In: *Phys.Rev.Lett.* 126 (4 2021). DOI: 10.1103/PhysRevLett.126.041804. arXiv: 2011.00210. URL: https://inspirehep.net/literature/1827477 (visited on 05/05/2021).

[71] A. Aguilar-Arevalo et al. "The CONNIE Experiment". In: *J.Phys.Conf.Ser.* 761 (1 2016). DOI: 10.1088/1742-6596/761/1/012057. arXiv: 1608.01565. URL: https://inspirehep.net/literature/1479457 (visited on 05/06/2021).

[72] G. Agnolet et al. "Background Studies for the MINER Coherent Neutrino Scattering Reactor Experiment". In: *Nucl.Instrum.Meth.A* 853 (2017), pp. 53–60. DOI: 10.1016/j.nima.2017.02.024. arXiv: 1609.02066. URL: https://inspirehep.net/literature/1485572 (visited on 05/06/2021).

[73] J. Colaresi et al. "First Results from a Search for Coherent Elastic Neutrino-Nucleus Scattering at a Reactor Site". In: *Phys.Rev.D* 104 (7 2021). DOI: 10.1103/PhysRevD.104.072003. arXiv: 2108.02880. URL: https://inspirehep.net/literature/1900982 (visited on 10/28/2021).

[74] J. Choi. "Neutrino Elastic-Scattering Observation with NaI[Tl](NEON)". In: *Proceedings of The 21st International Workshop on Neutrinos from Accelerators — PoS(NuFact2019).* The 21st International Workshop on Neutrinos from Accelerators. Vol. 369. SISSA Medialab, June 11, 2020, p. 047. DOI: 10.22323/1.369.0047. URL: https://pos.sissa.it/369/047 (visited on 10/28/2021).

[75] R. Strauss et al. "The ν-Cleus Experiment: A Gram-Scale Fiducial-Volume Cryogenic Detector for the First Detection of Coherent Neutrino-Nucleus Scattering". In: *Eur.Phys.J.C* 77 (2017), p. 506. DOI: 10.1140/epjc/s10052-017-5068-2. arXiv: 1704.04320. URL: https://inspirehep.net/literature/1591649 (visited on 05/06/2021).

[76] V. Belov et al. "The νGeN Experiment at the Kalinin Nuclear Power Plant". In: *JINST* 10.12 (2015). DOI: 10.1088/1748-0221/10/12/P12011. URL: https://inspirehep.net/literature/1410979 (visited on 05/06/2021).

[77] D. Yu Akimov et al. "First Ground-Level Laboratory Test of the Two-Phase Xenon Emission Detector RED-100". In: *JINST* 15 (02 2020). DOI: 10.1088/1748-0221/15/02/P02020. arXiv: 1910.06190. URL: https://inspirehep.net/literature/1758751 (visited on 05/06/2021).

[78] J. Billard et al. "Coherent Neutrino Scattering with Low Temperature Bolometers at Chooz Reactor Complex". In: *J.Phys.G* 44 (10 2017). DOI: 10.1088/1361-6471/aa83d0. arXiv: 1612.09035. URL: https://inspirehep.net/literature/1507092 (visited on 05/06/2021).

[79] H. T. Wong. "The TEXONO Research Program on Neutrino and Astroparticle Physics". In: *Mod.Phys.Lett.A* 19 (2004), pp. 1207–1214. DOI: 10.1142/S0217732304014574. URL: https://inspirehep.net/literature/658591 (visited on 05/06/2021).

[80] G. Fernandez Moroni et al. "Charge Coupled Devices for Detection of Coherent Neutrino-Nucleus Scattering". In: *Phys.Rev.D* 91 (7 2015). DOI: `10.1103/PhysRevD.91.072001`. arXiv: `1405.5761`. URL: `https://inspirehep.net/literature/1297474` (visited on 05/07/2021).

[81] R. Strauss et al. "Gram-Scale Cryogenic Calorimeters for Rare-Event Searches". In: *Phys.Rev.D* 96 (2 2017). DOI: `10.1103/PhysRevD.96.022009`. arXiv: `1704.04317`. URL: `https://inspirehep.net/literature/1591648` (visited on 05/06/2021).

[82] H. Bonet et al. "Large-Size Sub-keV Sensitive Germanium Detectors for the CONUS Experiment". In: *Eur.Phys.J.C* 81 (3 2021), p. 267. DOI: `10.1140/epjc/s10052-021-09038-3`. arXiv: `2010.11241`. URL: `https://inspirehep.net/literature/1824413` (visited on 05/06/2021).

[83] V. Chepel and H. Araujo. "Liquid Noble Gas Detectors for Low Energy Particle Physics". In: *JINST* 8 (2013). DOI: `10.1088/1748-0221/8/04/R04001`. arXiv: `1207.2292`. URL: `https://inspirehep.net/literature/1121844` (visited on 05/07/2021).

[84] J. J. Choi et al. "Improving the Light Collection Using a New NaI(Tl) Crystal Encapsulation". In: *Nucl.Instrum.Meth.A* 981 (2020). DOI: `10.1016/j.nima.2020.164556`. arXiv: `2006.02573`. URL: `https://inspirehep.net/literature/1799438` (visited on 05/07/2021).

[85] C. Hagmann and A. Bernstein. "Two-Phase Emission Detector for Measuring Coherent Neutrino-Nucleus Scattering". In: *IEEE Trans.Nucl.Sci.* 51 (2004), pp. 2151–2155. DOI: `10.1109/TNS.2004.836061`. arXiv: `nucl-ex/0411004`. URL: `https://inspirehep.net/literature/672791` (visited on 05/05/2021).

[86] A. Bernstein et al. "*Colloquium*: Neutrino Detectors as Tools for Nuclear Security". In: *Rev.Mod.Phys.* 92 (2020). DOI: `10.1103/RevModPhys.92.011003`. arXiv: `1908.07113`. URL: `https://inspirehep.net/literature/1750304` (visited on 05/05/2021).

[87] M. Bowen and P. Huber. "Reactor Neutrino Applications and Coherent Elastic Neutrino Nucleus Scattering". In: *Phys.Rev.D* 102 (5 2020). DOI: `10.1103/PhysRevD.102.053008`. arXiv: `2005.10907`. URL: `https://inspirehep.net/literature/1797440` (visited on 05/05/2021).

[88] D. K. Papoulias and T. S. Kosmas. "COHERENT Constraints to Conventional and Exotic Neutrino Physics". In: *Phys.Rev.D* 97 (3 2018). DOI: `10.1103/PhysRevD.97.033003`. arXiv: `1711.09773`. URL: `https://inspirehep.net/literature/1639033` (visited on 05/05/2021).

[89] J. Billard, J. Johnston, and B. J. Kavanagh. "Prospects for Exploring New Physics in Coherent Elastic Neutrino-Nucleus Scattering". In: *JCAP* 11 (2018), p. 016. DOI: `10.1088/1475-7516/2018/11/016`. arXiv: `1805.01798`. URL: `https://inspirehep.net/literature/1671796` (visited on 05/05/2021).

[90] A. N. Khan and W. Rodejohann. "New Physics from COHERENT Data with an Improved Quenching Factor". In: *Phys.Rev.D* 100 (11 2019). DOI: `10.1103/PhysRevD.100.113003`. arXiv: `1907.12444`. URL: `https://inspirehep.net/literature/1746585` (visited on 05/05/2021).

[91] D. K. Papoulias. “COHERENT Constraints after the COHERENT-2020 Quenching Factor Measurement”. In: *Phys.Rev.D* 102 (11 2020). DOI: 10.1103/PhysRevD.102.113004. arXiv: 1907.11644. URL: https://inspirehep.net/literature/1746478 (visited on 05/05/2021).

[92] O. G. Miranda et al. “Implications of the First Detection of Coherent Elastic Neutrino-Nucleus Scattering (CEvNS) with Liquid Argon”. In: *JHEP* 05 (2020), p. 130. DOI: 10.1007/JHEP05(2020)130. arXiv: 2003.12050. URL: https://inspirehep.net/literature/1788440 (visited on 07/02/2021).

[93] K. Patton et al. “Neutrino-Nucleus Coherent Scattering as a Probe of Neutron Density Distributions”. In: *Phys.Rev.C* 86 (2012). DOI: 10.1103/PhysRevC.86.024612. arXiv: 1207.0693. URL: https://inspirehep.net/literature/1121039 (visited on 05/05/2021).

[94] M. Cadeddu et al. “Average CsI Neutron Density Distribution from COHERENT Data”. In: *Phys.Rev.Lett.* 120 (7 2018). DOI: 10.1103/PhysRevLett.120.072501. arXiv: 1710.02730. URL: https://inspirehep.net/literature/1629155 (visited on 05/11/2021).

[95] P. Coloma et al. “Determining the Nuclear Neutron Distribution from Coherent Elastic Neutrino-Nucleus Scattering: Current Results and Future Prospects”. In: *JHEP* 08 (08 2020), p. 030. DOI: 10.1007/JHEP08(2020)030. arXiv: 2006.08624. URL: https://inspirehep.net/literature/1801419 (visited on 05/05/2021).

[96] N. Van Dessel et al. “Nuclear Structure Physics in Coherent Elastic Neutrino-Nucleus Scattering”. In: (July 8, 2020). arXiv: 2007.03658. URL: https://inspirehep.net/literature/1805471 (visited on 10/29/2021).

[97] H.-S. Lee. “$\mathrm{Sin}^2\theta_W$ Theory and New Physics”. In: *J.Univ.Sci.Tech.China* 46 (6 2016), pp. 470–475. DOI: 10.3969/j.issn.0253-2778.2016.06.004. arXiv: 1511.03783. URL: https://inspirehep.net/literature/1404172 (visited on 05/07/2021).

[98] B. C. Cañas et al. “Future Perspectives for a Weak Mixing Angle Measurement in Coherent Elastic Neutrino Nucleus Scattering Experiments”. In: *Phys.Lett.B* 784 (2018), pp. 159–162. DOI: 10.1016/j.physletb.2018.07.049. arXiv: 1806.01310. URL: https://inspirehep.net/literature/1676467 (visited on 05/05/2021).

[99] M. Cadeddu et al. “Physics Results from the First COHERENT Observation of Coherent Elastic Neutrino-Nucleus Scattering in Argon and Their Combination with Cesium-Iodide Data”. In: *Phys.Rev.D* 102 (1 2020). DOI: 10.1103/PhysRevD.102.015030. arXiv: 2005.01645. URL: https://inspirehep.net/literature/1794089 (visited on 07/02/2021).

[100] G. Fernandez-Moroni et al. “The Physics Potential of a Reactor Neutrino Experiment with Skipper CCDs: Measuring the Weak Mixing Angle”. In: *JHEP* 03 (2021), p. 186. DOI: 10.1007/JHEP03(2021)186. arXiv: 2009.10741. URL: https://inspirehep.net/literature/1818645 (visited on 05/07/2021).

[101] J. Monroe and P. Fisher. “Neutrino Backgrounds to Dark Matter Searches”. In: *Phys.Rev.D* 76 (2007). DOI: 10.1103/PhysRevD.76.033007. arXiv: 0706.3019. URL: https://inspirehep.net/literature/753651 (visited on 05/05/2021).

[102] L. E. Strigari. “Neutrino Coherent Scattering Rates at Direct Dark Matter Detectors”. In: *New J.Phys.* 11 (2009). DOI: 10.1088/1367-2630/11/10/105011. arXiv: 0903.3630. URL: https://inspirehep.net/literature/815958 (visited on 05/05/2021).

[103] A. Gutlein et al. “Solar and Atmospheric Neutrinos: Background Sources for the Direct Dark Matter Search”. In: *Astropart.Phys.* 34 (2010), pp. 90–96. DOI: 10.1016/j.astropartphys.2010.06.002. arXiv: 1003.5530. URL: https://inspirehep.net/literature/850242 (visited on 05/05/2021).

[104] E. Aprile et al. “Search for Coherent Elastic Scattering of Solar ^{8}B Neutrinos in the XENON1T Dark Matter Experiment”. In: *Phys.Rev.Lett.* 126 (2021). DOI: 10.1103/PhysRevLett.126.091301. arXiv: 2012.02846. URL: https://inspirehep.net/literature/1835591 (visited on 07/02/2021).

[105] D. S. Akerib et al. “Projected WIMP Sensitivity of the LUX-ZEPLIN Dark Matter Experiment”. In: *Phys.Rev.D* 101 (5 2020). DOI: 10.1103/PhysRevD.101.052002. arXiv: 1802.06039. URL: https://inspirehep.net/literature/1655569 (visited on 07/28/2021).

[106] E. Aprile et al. “Projected WIMP Sensitivity of the XENONnT Dark Matter Experiment”. In: *JCAP* 11 (2020), p. 031. DOI: 10.1088/1475-7516/2020/11/031. arXiv: 2007.08796. URL: https://inspirehep.net/literature/1807808 (visited on 07/28/2021).

[107] D. G. Cerdeño et al. “Physics from Solar Neutrinos in Dark Matter Direct Detection Experiments”. In: *JHEP* 05 (2016), p. 118. DOI: 10.1007/JHEP09(2016)048. arXiv: 1604.01025. URL: https://inspirehep.net/literature/1442365 (visited on 05/05/2021).

[108] E. Bertuzzo et al. “Dark Matter and Exotic Neutrino Interactions in Direct Detection Searches”. In: *JHEP* 04 (2017), p. 073. DOI: 10.1007/JHEP04(2017)073. arXiv: 1701.07443. URL: https://inspirehep.net/literature/1510885 (visited on 05/05/2021).

[109] C. Bœhm et al. “How High Is the Neutrino Floor?” In: *JCAP* 01 (2019), p. 043. DOI: 10.1088/1475-7516/2019/01/043. arXiv: 1809.06385. URL: https://inspirehep.net/literature/1694491 (visited on 05/05/2021).

[110] J. M. Link and X.-J. Xu. “Searching for BSM Neutrino Interactions in Dark Matter Detectors”. In: *JHEP* 08 (2019), p. 004. DOI: 10.1007/JHEP08(2019)004. arXiv: 1903.09891. URL: https://inspirehep.net/literature/1726486 (visited on 05/05/2021).

[111] J. Barranco, O. G. Miranda, and T. I. Rashba. “Probing New Physics with Coherent Neutrino Scattering off Nuclei”. In: *JHEP* 12 (2005), p. 021. DOI: 10.1088/1126-6708/2005/12/021. arXiv: hep-ph/0508299. URL: https://inspirehep.net/literature/691040 (visited on 05/05/2021).

[112] J. Barranco, O. G. Miranda, and T. I. Rashba. “Low Energy Neutrino Experiments Sensitivity to Physics beyond the Standard Model”. In: *Phys.Rev.D* 76 (2007). DOI: 10.1103/PhysRevD.76.073008. arXiv: hep-ph/0702175. URL: https://inspirehep.net/literature/744791 (visited on 05/05/2021).

[113] J. Barranco et al. “Tensorial NSI and Unparticle Physics in Neutrino Scattering”. In: *Int.J.Mod.Phys.A* 27 (2012). DOI: 10.1142/S0217751X12501473. arXiv: 1108.1220. URL: https://inspirehep.net/literature/922299 (visited on 05/05/2021).

[114] T. Ohlsson. “Status of Non-Standard Neutrino Interactions”. In: *Rept.Prog.Phys.* 76 (2013). DOI: 10.1088/0034-4885/76/4/044201. arXiv: 1209.2710. URL: https://inspirehep.net/literature/1185406 (visited on 10/30/2021).

[115] M. Lindner, W. Rodejohann, and X.-J. Xu. “Coherent Neutrino-Nucleus Scattering and New Neutrino Interactions”. In: *JHEP* 03 (2017), p. 097. DOI: 10.1007/JHEP03(2017)097. arXiv: 1612.04150. URL: https://inspirehep.net/literature/1503169 (visited on 05/05/2021).

[116] P. S. Bhupal Dev et al. “Neutrino Non-Standard Interactions: A Status Report”. In: *SciPost Phys.Proc.* 2 (2019), p. 001. DOI: 10.21468/SciPostPhysProc.2.001. arXiv: 1907.00991. URL: https://inspirehep.net/literature/1742302 (visited on 05/05/2021).

[117] T. Han et al. “Scalar and Tensor Neutrino Interactions”. In: *JHEP* 07 (2020), p. 207. DOI: 10.1007/JHEP07(2020)207. arXiv: 2004.13869. URL: https://inspirehep.net/literature/1793427 (visited on 05/11/2021).

[118] P. Vogel and J. Engel. “Neutrino Electromagnetic Form-Factors”. In: *Phys.Rev.D* 39 (1989), p. 3378. DOI: 10.1103/PhysRevD.39.3378. URL: https://inspirehep.net/literature/25814 (visited on 05/05/2021).

[119] C. Giunti and A. Studenikin. “Neutrino Electromagnetic Interactions: A Window to New Physics”. In: *Rev.Mod.Phys.* 87 (2015), p. 531. DOI: 10.1103/RevModPhys.87.531. arXiv: 1403.6344. URL: https://inspirehep.net/literature/1287034 (visited on 05/05/2021).

[120] T. S. Kosmas et al. “Sensitivities to Neutrino Electromagnetic Properties at the TEXONO Experiment”. In: *Phys.Lett.B* 750 (2015), pp. 459–465. DOI: 10.1016/j.physletb.2015.09.054. arXiv: 1506.08377. URL: https://inspirehep.net/literature/1380205 (visited on 05/10/2021).

[121] M. Cadeddu et al. “Neutrino Charge Radii from COHERENT Elastic Neutrino-Nucleus Scattering”. In: *Phys.Rev.D* 98 (11 2018). DOI: 10.1103/PhysRevD.98.113010. arXiv: 1810.05606. URL: https://inspirehep.net/literature/1698276 (visited on 05/05/2021).

[122] O. G. Miranda et al. “Probing Neutrino Transition Magnetic Moments with Coherent Elastic Neutrino-Nucleus Scattering”. In: *JHEP* 07 (2019), p. 103. DOI: 10.1007/JHEP07(2019)103. arXiv: 1905.03750. URL: https://inspirehep.net/literature/1734043 (visited on 05/05/2021).

[123] A. V. Kuznetsov, N. V. Mikheev, and A. A. Okrugin. “Reexamination of a Bound on the Dirac Neutrino Magnetic Moment from the Supernova Neutrino Luminosity”. In: *Int.J.Mod.Phys.A* 24 (2009), pp. 5977–5989. DOI: 10.1142/S0217751X09047612. arXiv: 0907.2905. URL: https://inspirehep.net/literature/825925 (visited on 05/10/2021).

[124] N. Viaux et al. “Neutrino and Axion Bounds from the Globular Cluster M5 (NGC 5904)”. In: *Phys.Rev.Lett.* 111 (2013). DOI: `10.1103/PhysRevLett.111.231301`. arXiv: `1311.1669`. URL: `https://inspirehep.net/literature/1263637` (visited on 05/10/2021).

[125] S. Arceo-Díaz et al. “Constraint on the Magnetic Dipole Moment of Neutrinos by the Tip-RGB Luminosity in ω -Centauri”. In: *Astropart.Phys.* 70 (2015), pp. 1–11. DOI: `10.1016/j.astropartphys.2015.03.006`. URL: `https://inspirehep.net/literature/1365405` (visited on 05/10/2021).

[126] P. deNiverville, M. Pospelov, and A. Ritz. “Light New Physics in Coherent Neutrino-Nucleus Scattering Experiments”. In: *Phys.Rev.D* 92 (9 2015). DOI: `10.1103/PhysRevD.92.095005`. arXiv: `1505.07805`. URL: `https://inspirehep.net/literature/1373540` (visited on 05/06/2021).

[127] J. B. Dent et al. “Probing Light Mediators at Ultralow Threshold Energies with Coherent Elastic Neutrino-Nucleus Scattering”. In: *Phys.Rev.D* 96 (9 2017). DOI: `10.1103/PhysRevD.96.095007`. arXiv: `1612.06350`. URL: `https://inspirehep.net/literature/1504994` (visited on 05/06/2021).

[128] A. Aguilar-Arevalo et al. “Search for Light Mediators in the Low-Energy Data of the CONNIE Reactor Neutrino Experiment”. In: *JHEP* 04 (2020), p. 054. DOI: `10.1007/JHEP04(2020)054`. arXiv: `1910.04951`. URL: `https://inspirehep.net/literature/1758662` (visited on 05/06/2021).

[129] Y. Farzan et al. “Probing Neutrino Coupling to a Light Scalar with Coherent Neutrino Scattering”. In: *JHEP* 05 (2018), p. 066. DOI: `10.1007/JHEP05(2018)066`. arXiv: `1802.05171`. URL: `https://inspirehep.net/literature/1654924` (visited on 05/06/2021).

[130] J. B. Dent et al. “New Directions for Axion Searches via Scattering at Reactor Neutrino Experiments”. In: *Phys.Rev.Lett.* 124 (21 2020). DOI: `10.1103/PhysRevLett.124.211804`. arXiv: `1912.05733`. URL: `https://inspirehep.net/literature/1770427` (visited on 05/06/2021).

[131] D. Aristizabal Sierra et al. “Axionlike Particles Searches in Reactor Experiments”. In: *JHEP* 03 (2021), p. 294. DOI: `10.1007/JHEP03(2021)294`. arXiv: `2010.15712`. URL: `https://inspirehep.net/literature/1826785` (visited on 05/06/2021).

[132] B. Dutta et al. “Searching for Beyond the Standard Model Physics with COHERENT Energy and Timing Data”. In: *Phys.Rev.Lett.* 123 (6 2019). DOI: `10.1103/PhysRevLett.123.061801`. arXiv: `1903.10666`. URL: `https://inspirehep.net/literature/1726785` (visited on 05/07/2021).

[133] O. G. Miranda et al. “Probing New Neutral Gauge Bosons with CEνNS and Neutrino-Electron Scattering”. In: *Phys.Rev.D* 101 (7 2020). DOI: `10.1103/PhysRevD.101.073005`. arXiv: `2002.01482`. URL: `https://inspirehep.net/literature/1778702` (visited on 05/07/2021).

[134] M. Cadeddu et al. “Constraints on Light Vector Mediators through Coherent Elastic Neutrino Nucleus Scattering Data from COHERENT”. In: *JHEP* 01 (2021), p. 116. DOI: `10.1007/JHEP01(2021)116`. arXiv: `2008.05022`. URL: `https://inspirehep.net/literature/1811403` (visited on 05/07/2021).

[135] S.-F. Ge and I. M. Shoemaker. "Constraining Photon Portal Dark Matter with Texono and Coherent Data". In: *JHEP* 11 (2018), p. 066. DOI: 10.1007/JHEP11(2018)066. arXiv: 1710.10889. URL: https://inspirehep.net/literature/1633428 (visited on 11/23/2021).

[136] H. K. Park. "Detecting Dark Photons with Reactor Neutrino Experiments". In: *Phys.Rev.Lett.* 119 (8 2017). DOI: 10.1103/PhysRevLett.119.081801. arXiv: 1705.02470. URL: https://inspirehep.net/literature/1598457 (visited on 11/27/2021).

[137] V. Brdar, W. Rodejohann, and X.-J. Xu. "Producing a New Fermion in Coherent Elastic Neutrino-Nucleus Scattering: From Neutrino Mass to Dark Matter". In: *JHEP* 12 (2018), p. 024. DOI: 10.1007/JHEP12(2018)024. arXiv: 1810.03626. URL: https://inspirehep.net/literature/1697489 (visited on 05/06/2021).

[138] W.-F. Chang and J. Liao. "Constraints on Light Singlet Fermion Interactions from Coherent Elastic Neutrino-Nucleus Scattering". In: *Phys.Rev.D* 102 (7 2020). DOI: 10.1103/PhysRevD.102.075004. arXiv: 2002.10275. URL: https://inspirehep.net/literature/1781978 (visited on 07/08/2021).

[139] J. A. Formaggio, E. Figueroa-Feliciano, and A. J. Anderson. "Sterile Neutrinos, Coherent Scattering and Oscillometry Measurements with Low-Temperature Bolometers". In: *Phys.Rev.D* 85 (2012). DOI: 10.1103/PhysRevD.85.013009. arXiv: 1107.3512. URL: https://inspirehep.net/literature/918940 (visited on 05/06/2021).

[140] B. Dutta et al. "Sensitivity to Oscillation with a Sterile Fourth Generation Neutrino from Ultra-Low Threshold Neutrino-Nucleus Coherent Scattering". In: *Phys.Rev.D* 94 (9 2016). DOI: 10.1103/PhysRevD.94.093002. arXiv: 1511.02834. URL: https://inspirehep.net/literature/1403556 (visited on 05/06/2021).

[141] B. C. Cañas et al. "The Reactor Antineutrino Anomaly and Low Energy Threshold Neutrino Experiments". In: *Phys.Lett.B* 776 (2018), pp. 451–456. DOI: 10.1016/j.physletb.2017.11.074. arXiv: 1708.09518. URL: https://inspirehep.net/literature/1620907 (visited on 05/06/2021).

[142] C. Blanco, D. Hooper, and P. Machado. "Constraining Sterile Neutrino Interpretations of the LSND and MiniBooNE Anomalies with Coherent Neutrino Scattering Experiments". In: *Phys.Rev.D* 101 (7 2020). DOI: 10.1103/PhysRevD.101.075051. arXiv: 1901.08094. URL: https://inspirehep.net/literature/1716567 (visited on 05/06/2021).

[143] O. G. Miranda et al. "Future CEvNS Experiments as Probes of Lepton Unitarity and Light-Sterile Neutrinos". In: *Phys.Rev.D* 102 (2020). DOI: 10.1103/PhysRevD.102.113014. arXiv: 2008.02759. URL: https://inspirehep.net/literature/1810387 (visited on 05/06/2021).

[144] A. Aguilar-Arevalo et al. "Evidence for Neutrino Oscillations from the Observation of $\bar{\nu}_e$ Appearance in a $\bar{\nu}_\mu$ Beam". In: *Phys.Rev.D* 64 (2001). DOI: 10.1103/PhysRevD.64.112007. arXiv: hep-ex/0104049. URL: https://inspirehep.net/literature/555937 (visited on 05/06/2021).

[145] G. Mention et al. “The Reactor Antineutrino Anomaly”. In: *Phys.Rev.D* 83 (2011). DOI: 10.1103/PhysRevD.83.073006. arXiv: 1101.2755. URL: https://inspirehep.net/literature/884352 (visited on 05/06/2021).

[146] S. Böser et al. “Status of Light Sterile Neutrino Searches”. In: *Prog.Part.Nucl.Phys.* 111 (2020). DOI: 10.1016/j.ppnp.2019.103736. arXiv: 1906.01739. URL: https://inspirehep.net/literature/1738523 (visited on 05/07/2021).

[147] N. Hurtado et al. “Dark Matter-Neutrino Interconversion at COHERENT, Direct Detection, and the Early Universe”. In: *Phys.Rev.D* 102 (1 2020). DOI: 10.1103/PhysRevD.102.015006. arXiv: 2005.13384. URL: https://inspirehep.net/literature/1798035 (visited on 11/16/2021).

[148] D. Akimov et al. “First Probe of Sub-GeV Dark Matter Beyond the Cosmological Expectation with the COHERENT CsI Detector at the SNS”. In: (Oct. 25, 2021). arXiv: 2110.11453. URL: https://inspirehep.net/literature/1950121 (visited on 11/09/2021).

[149] P. Vogel and J. F. Beacom. “Angular Distribution of Neutron Inverse Beta Decay, Anti-Neutrino(e) + p —> e+ + n”. In: *Phys.Rev.D* 60 (1999). DOI: 10.1103/PhysRevD.60.053003. arXiv: hep-ph/9903554. URL: https://inspirehep.net/literature/497639 (visited on 05/06/2021).

[150] M. Agostini et al. “Limiting Neutrino Magnetic Moments with Borexino Phase-II Solar Neutrino Data”. In: *Phys.Rev.D* 96 (9 2017). DOI: 10.1103/PhysRevD.96.091103. arXiv: 1707.09355. URL: https://inspirehep.net/literature/1613521 (visited on 05/10/2021).

[151] A. Studenikin. “New Bounds on Neutrino Electric Millicharge from Limits on Neutrino Magnetic Moment”. In: *EPL* 107 (2 2014). DOI: 10.1209/0295-5075/107/21001. arXiv: 1302.1168. URL: https://inspirehep.net/literature/1217750 (visited on 11/10/2021).

[152] P. Langacker. *The Standard Model and Beyond.* Series in High Energy Physics, Cosmology, and Gravitation. Boca Raton, Fla. [u.a.]: CRC Press, 2010. XII, 663 S. ISBN: 978-1-4200-7906-7.

[153] S. T. Wauthier. “Description of Coherent Elastic Neutrino-Nucleus Scattering Cross Sections”. Master of Physics. KU Leuven. URL: compphys.ugent.be/docs/theses/WauthierSamuelThierry_2016-2017.pdf (visited on 07/08/2021).

[154] E. Del Nobile. “Appendiciario – A Hands-on Manual on the Theory of Direct Dark Matter Detection”. In: (Apr. 28, 2021). arXiv: 2104.12785. URL: https://inspirehep.net/literature/1861022 (visited on 10/29/2021).

[155] E. Del Nobile. “Complete Lorentz-to-Galileo Dictionary for Direct Dark Matter Detection”. In: *Phys.Rev.D* 98 (12 2018). DOI: 10.1103/PhysRevD.98.123003. arXiv: 1806.01291. URL: https://inspirehep.net/literature/1676400 (visited on 10/29/2021).

[156] M. Cirelli, E. Del Nobile, and P. Panci. “Tools for Model-Independent Bounds in Direct Dark Matter Searches”. In: *JCAP* 10 (2013), p. 019. DOI: 10.1088/1475-7516/2013/10/019. arXiv: 1307.5955. URL: https://inspirehep.net/literature/1244066 (visited on 05/11/2021).

[157] M. A. Shifman, A. I. Vainshtein, and V. I. Zakharov. “Remarks on Higgs Boson Interactions with Nucleons”. In: *Phys.Lett.B* 78 (1978), pp. 443–446. DOI: `10.1016/0370-2693(78)90481-1`. URL: `https://inspirehep.net/literature/129398` (visited on 10/29/2021).

[158] H.-Y. Cheng and C.-W. Chiang. “Revisiting Scalar and Pseudoscalar Couplings with Nucleons”. In: *JHEP* 07 (2012), p. 009. DOI: `10.1007/JHEP07(2012)009`. arXiv: `1202.1292`. URL: `https://inspirehep.net/literature/1088241` (visited on 10/29/2021).

[159] J. Ellis, N. Nagata, and K. A. Olive. “Uncertainties in WIMP Dark Matter Scattering Revisited”. In: *Eur.Phys.J.C* 78 (7 2018), p. 569. DOI: `10.1140/epjc/s10052-018-6047-y`. arXiv: `1805.09795`. URL: `https://inspirehep.net/literature/1674710` (visited on 11/30/2021).

[160] M. E. Peskin. *An Introduction to Quantum Field Theory*. Ed. by Daniel V. Schroeder. The Advanced Book Program. Reading, Ma [u.a.]: Addison-Wesley, 1995. ISBN: 978-0-8133-4543-7.

[161] M. Hoferichter, J. Menéndez, and A. Schwenk. “Coherent Elastic Neutrino-Nucleus Scattering: EFT Analysis and Nuclear Responses”. In: *Phys.Rev.D* 102 (7 2020). DOI: `10.1103/PhysRevD.102.074018`. arXiv: `2007.08529`. URL: `https://inspirehep.net/literature/1807717` (visited on 05/07/2021).

[162] T. Lin. “Dark Matter Models and Direct Detection”. In: *PoS* 333 (2019), p. 009. DOI: `10.22323/1.333.0009`. arXiv: `1904.07915`. URL: `https://inspirehep.net/literature/1730217` (visited on 10/29/2021).

[163] J. Engel. “Nuclear Form-Factors for the Scattering of Weakly Interacting Massive Particles”. In: *Phys.Lett.B* 264 (1991), pp. 114–119. DOI: `10.1016/0370-2693(91)90712-Y`. URL: `https://inspirehep.net/literature/323343` (visited on 10/29/2021).

[164] M. D. Schwartz. *Quantum field theory and the standard model*. eng. Cambridge [u.a.]: Cambridge University Press, 2014, XVIII, 850 S. ISBN: 978-1-107-03473-0.

[165] V. A. Bednyakov and D. V. Naumov. “Coherency and Incoherency in Neutrino-Nucleus Elastic and Inelastic Scattering”. In: *Phys.Rev.D* 98 (5 2018). DOI: `10.1103/PhysRevD.98.053004`. arXiv: `1806.08768`. URL: `https://inspirehep.net/literature/1679249` (visited on 05/11/2021).

[166] M. Thomson. *Modern Particle Physics*. Cambridge [u.a.]: Cambridge University Press, 2013. XVI, 554 S. ISBN: 978-1-107-03426-6.

[167] A. Benoit et al. “Measurement of the Response of Heat-and-Ionization Germanium Detectors to Nuclear Recoils”. In: *Nucl.Instrum.Meth.A* 577 (2007), pp. 558–568. DOI: `10.1016/j.nima.2007.04.118`. arXiv: `astro-ph/0607502`. URL: `https://inspirehep.net/literature/722105` (visited on 12/02/2021).

[168] D. Barker and D. M. Mei. “Germanium Detector Response to Nuclear Recoils in Searching for Dark Matter”. In: *Astropart.Phys.* 38 (2012), pp. 1–6. DOI: `10.1016/j.astropartphys.2012.08.006`. arXiv: `1203.4620`. URL: `https://inspirehep.net/literature/1094565` (visited on 05/11/2021).

[169] B. J. Scholz et al. “Measurement of the Low-Energy Quenching Factor in Germanium Using an ^{88}Y/Be Photoneutron Source”. In: *Phys.Rev.D* 94 (12 2016). DOI: `10.1103/PhysRevD.94.122003`. arXiv: `1608.03588`. URL: `https://inspirehep.net/literature/1481014` (visited on 05/06/2021).

[170] J. D. Lewin and P. F. Smith. “Review of Mathematics, Numerical Factors, and Corrections for Dark Matter Experiments Based on Elastic Nuclear Recoil”. In: *Astropart.Phys.* 6 (1996), pp. 87–112. DOI: `10.1016/S0927-6505(96)00047-3`. URL: `https://inspirehep.net/literature/405551` (visited on 05/11/2021).

[171] E. Vitagliano, I. Tamborra, and G. Raffelt. “Grand Unified Neutrino Spectrum at Earth: Sources and Spectral Components”. In: *Rev.Mod.Phys.* 92 (2020). DOI: `10.1103/RevModPhys.92.045006`. arXiv: `1910.11878`. URL: `https://inspirehep.net/literature/1761501` (visited on 10/29/2021).

[172] G. C. McLaughlin and C. Volpe. “Prospects for Detecting a Neutrino Magnetic Moment with a Tritium Source and Beta Beams”. In: *Phys.Lett.B* 591 (2004), pp. 229–234. DOI: `10.1016/j.physletb.2004.02.073`. arXiv: `hep-ph/0312156`. URL: `https://inspirehep.net/literature/635266` (visited on 07/16/2021).

[173] A. Bolozdynya et al. “Opportunities for Neutrino Physics at the Spallation Neutron Source: A White Paper”. In: (Nov. 25, 2012). arXiv: `1211.5199`. URL: `https://inspirehep.net/literature/1203677` (visited on 07/19/2021).

[174] T. Lasserre and H. W. Sobel. “Reactor Neutrinos”. In: *Comptes Rendus Physique* 6 (2005), pp. 749–757. DOI: `10.1016/J.CRHY.2005.08.002`. arXiv: `nucl-ex/0601013`. URL: `https://inspirehep.net/literature/700837` (visited on 07/19/2021).

[175] C. Bellenghi et al. “Coherent Elastic Nuclear Scattering Of ^{51} Cr Neutrinos”. In: *Eur.Phys.J.C* 79 (9 2019), p. 727. DOI: `10.1140/epjc/s10052-019-7240-3`. arXiv: `1905.10611`. URL: `https://inspirehep.net/literature/1736885` (visited on 07/16/2021).

[176] O. G. Miranda, G. Sanchez Garcia, and O. Sanders. “Coherent Elastic Neutrino-Nucleus Scattering as a Precision Test for the Standard Model and beyond: The COHERENT Proposal Case”. In: *Adv.High Energy Phys.* 2019 (2019). DOI: `10.1155/2019/3902819`. arXiv: `1902.09036`. URL: `https://inspirehep.net/literature/1721760` (visited on 05/05/2021).

[177] F. T. Avignone and Yu V. Efremenko. “Neutrino Nucleus Cross-Section Measurements at Intense, Pulsed Spallation Sources”. In: *J.Phys.G* 29 (2003), pp. 2615–2628. DOI: `10.1088/0954-3899/29/11/012`. URL: `https://inspirehep.net/literature/634863` (visited on 07/19/2021).

[178] S. J. Brice et al. “A Method for Measuring Coherent Elastic Neutrino-Nucleus Scattering at a Far off-Axis High-Energy Neutrino Beam Target”. In: *Phys.Rev.D* 89 (7 2014). DOI: `10.1103/PhysRevD.89.072004`. arXiv: `1311.5958`. URL: `https://inspirehep.net/literature/1266049` (visited on 07/19/2021).

[179] S. Ajimura et al. “Technical Design Report (TDR): Searching for a Sterile Neutrino at J-PARC MLF (E56, JSNS2)”. In: (May 25, 2017). arXiv: `1705.08629`. URL: `https://inspirehep.net/literature/1601131` (visited on 07/19/2021).

[180] D. Baxter et al. "Coherent Elastic Neutrino-Nucleus Scattering at the European Spallation Source". In: *JHEP* 02 (2020), p. 123. DOI: 10.1007/JHEP02(2020)123. arXiv: 1911.00762. URL: https://inspirehep.net/literature/1762824 (visited on 05/06/2021).

[181] D. Akimov et al. "The COHERENT Experiment at the Spallation Neutron Source". In: (Sept. 30, 2015). arXiv: 1509.08702. URL: https://inspirehep.net/literature/1395251 (visited on 05/05/2021).

[182] S.-B. Kim, T. Lasserre, and Y. Wang. "Reactor Neutrinos". In: *Adv.High Energy Phys.* 2013 (2013). DOI: 10.1155/2013/453816. URL: https://inspirehep.net/literature/1234475 (visited on 07/20/2021).

[183] X. Qian and J.-C. Peng. "Physics with Reactor Neutrinos". In: *Rept.Prog.Phys.* 82 (3 2019). DOI: 10.1088/1361-6633/aae881. arXiv: 1801.05386. URL: https://inspirehep.net/literature/1648457 (visited on 05/07/2021).

[184] V. I. Kopeikin, L. A. Mikaelyan, and V. V. Sinev. "Inverse Beta Decay in a Nonequilibrium Anti-Neutrino Flux from a Nuclear Reactor". In: *Phys.Atom.Nucl.* 64 (2001), pp. 849–854. DOI: 10.1134/1.1378874. arXiv: hep-ph/0110290. URL: https://inspirehep.net/literature/562109 (visited on 07/20/2021).

[185] A. C. Hayes and P. Vogel. "Reactor Neutrino Spectra". In: *Ann.Rev.Nucl.Part.Sci.* 66 (2016), pp. 219–244. DOI: 10.1146/annurev-nucl-102115-044826. arXiv: 1605.02047. URL: https://inspirehep.net/literature/1456160 (visited on 05/06/2021).

[186] A. G. Beda et al. "First Result for Neutrino Magnetic Moment from Measurements with the GEMMA Spectrometer". In: *Phys.Atom.Nucl.* 70 (2007), pp. 1873–1884. DOI: 10.1134/S1063778807110063. arXiv: 0705.4576. URL: https://inspirehep.net/literature/751858 (visited on 05/10/2021).

[187] V. Kopeikin, L. Mikaelyan, and V. Sinev. "Components of Anti-Neutrino Emission in Nuclear Reactor". In: *Phys.Atom.Nucl.* 67 (2004), pp. 1963–1968. DOI: 10.1134/1.1825513. arXiv: hep-ph/0308186. URL: https://inspirehep.net/literature/626155 (visited on 05/06/2021).

[188] V. I. Kopeikin, L. A. Mikaelyan, and V. V. Sinev. "Spectrum of Electronic Reactor Anti-Neutrinos". In: *Phys.Atom.Nucl.* 60 (1997), pp. 172–176. URL: https://inspirehep.net/literature/457392 (visited on 12/02/2021).

[189] K. Schreckenbach et al. "DETERMINATION OF THE ANTI-NEUTRINO SPECTRUM FROM U-235 THERMAL NEUTRON FISSION PRODUCTS UP TO 9.5-MEV". In: *Phys.Lett.B* 160 (1985), pp. 325–330. DOI: 10.1016/0370-2693(85)91337-1. URL: https://inspirehep.net/literature/221757 (visited on 07/20/2021).

[190] A. A. Hahn et al. "Anti-Neutrino Spectra From ^{241}Pu and ^{239}Pu Thermal Neutron Fission Products". In: *Phys.Lett.B* 218 (1989), pp. 365–368. DOI: 10.1016/0370-2693(89)91598-0. URL: https://inspirehep.net/literature/280774 (visited on 07/20/2021).

[191] N. Haag et al. "Re-Publication of the Data from the BILL Magnetic Spectrometer: The Cumulative β Spectra of the Fission Products of ^{235}U, ^{239}Pu, and ^{241}Pu". In: (May 15, 2014). arXiv: `1405.3501`. URL: `https://inspirehep.net/literature/1296110` (visited on 07/20/2021).

[192] N. Haag et al. "Experimental Determination of the Antineutrino Spectrum of the Fission Products of ^{238}U". In: *Phys.Rev.Lett.* 112 (12 2014). DOI: `10.1103/PhysRevLett.112.122501`. arXiv: `1312.5601`. URL: `https://inspirehep.net/literature/1272925` (visited on 05/06/2021).

[193] A. Strumia and F. Vissani. "Precise Quasielastic Neutrino/Nucleon Cross-Section". In: *Phys.Lett.B* 564 (2003), pp. 42–54. DOI: `10.1016/S0370-2693(03)00616-6`. arXiv: `astro-ph/0302055`. URL: `https://inspirehep.net/literature/612772` (visited on 05/06/2021).

[194] F. P. An et al. "Improved Measurement of the Reactor Antineutrino Flux and Spectrum at Daya Bay". In: *Chin.Phys.C* 41 (1 2017). DOI: `10.1088/1674-1137/41/1/013002`. arXiv: `1607.05378`. URL: `https://inspirehep.net/literature/1477024` (visited on 05/06/2021).

[195] F. P. An et al. "Antineutrino Energy Spectrum Unfolding Based on the Daya Bay Measurement and Its Applications". In: *Chin.Phys.C* 45 (7 2021). DOI: `10.1088/1674-1137/abfc38`. arXiv: `2102.04614`. URL: `https://inspirehep.net/literature/1845578` (visited on 11/19/2021).

[196] Z. Atif et al. "Measurement of Reactor Antineutrino Flux and Spectrum at RENO". In: (Oct. 29, 2020). arXiv: `2010.14989`. URL: `https://inspirehep.net/literature/1826679` (visited on 07/21/2021).

[197] S. Schoppmann. "Status of Anomalies and Sterile Neutrino Searches at Nuclear Reactors". In: *Universe* 7 (10 2021), p. 360. DOI: `10.3390/universe7100360`. arXiv: `2109.13541`. URL: `https://inspirehep.net/literature/1932445` (visited on 11/19/2021).

[198] F. P. An et al. "Measurement of the Reactor Antineutrino Flux and Spectrum at Daya Bay". In: *Phys.Rev.Lett.* 116 (6 2016). DOI: `10.1103/PhysRevLett.116.061801`. arXiv: `1508.04233`. URL: `https://inspirehep.net/literature/1388361` (visited on 11/20/2021).

[199] J. H. Choi et al. "Observation of Energy and Baseline Dependent Reactor Antineutrino Disappearance in the RENO Experiment". In: *Phys.Rev.Lett.* 116 (21 2016). DOI: `10.1103/PhysRevLett.116.211801`. arXiv: `1511.05849`. URL: `https://inspirehep.net/literature/1405297` (visited on 11/20/2021).

[200] J. Holder et al. *Particle Detectors for Non-Accelerator Physics.* Aug. 2020. DOI: `10.1093/ptep/ptaa104`. URL: `https://inspirehep.net/literature/1812251` (visited on 07/12/2021).

[201] G. Heusser. "Low-Radioactivity Background Techniques". In: *Ann.Rev.Nucl.Part.Sci.* 45 (1995), pp. 543–590. DOI: `10.1146/annurev.ns.45.120195.002551`. URL: `https://inspirehep.net/literature/408368` (visited on 05/06/2021).

[202] J. A. Formaggio and C. J. Martoff. “Backgrounds to Sensitive Experiments Underground”. In: *Ann.Rev.Nucl.Part.Sci.* 54 (2004), pp. 361–412. DOI: `10.1146/annurev.nucl.54.070103.181248`. URL: `https://inspirehep.net/literature/670319` (visited on 07/12/2021).

[203] J. Hakenmüller, W. Maneschg, and G. Heusser. “Simulation and Verification of the Cosmogenic Background at the Shallow Depth GIOVE Detector”. In: *J.Phys.Conf.Ser.* 718.4 (2016). DOI: `10.1088/1742-6596/718/4/042028`. URL: `https://inspirehep.net/literature/1468799` (visited on 05/06/2021).

[204] K.-M. Wai et al. “External Cesium-137 Doses to Humans from Soil Influenced by the Fukushima and Chernobyl Nuclear Power Plants Accidents: A Comparative Study”. In: *Scientific Reports* 10.1 (1 May 13, 2020), p. 7902. ISSN: 2045-2322. DOI: `10.1038/s41598-020-64812-9`. URL: `https://www.nature.com/articles/s41598-020-64812-9` (visited on 12/02/2021).

[205] G. Heusser et al. “GIOVE - A New Detector Setup for High Sensitivity Germanium Spectroscopy at Shallow Depth”. In: *Eur.Phys.J.C* 75 (11 2015), p. 531. DOI: `10.1140/epjc/s10052-015-3704-2`. arXiv: `1507.03319`. URL: `https://inspirehep.net/literature/1382558` (visited on 05/06/2021).

[206] L. Baudis and S. Profumo. *Dark matter*. Aug. 2020. DOI: `10.1093/ptep/ptaa104`. URL: `https://inspirehep.net/literature/1812251` (visited on 07/12/2021).

[207] T. Marrodán Undagoitia and L. Rauch. “Dark Matter Direct-Detection Experiments”. In: *J.Phys.G* 43 (1 2016). DOI: `10.1088/0954-3899/43/1/013001`. arXiv: `1509.08767`. URL: `https://inspirehep.net/literature/1395218` (visited on 07/12/2021).

[208] S. N. Ahmed. “6 - Scintillation Detectors and Photodetectors”. In: *Physics and Engineering of Radiation Detection (Second Edition)*. Ed. by S. N. Ahmed. Elsevier, Jan. 1, 2015, pp. 331–433. ISBN: 978-0-12-801363-2. DOI: `10.1016/B978-0-12-801363-2.00006-1`. URL: `https://www.sciencedirect.com/science/article/pii/B9780128013632000061` (visited on 12/03/2021).

[209] R. Bernabei et al. “The DAMA/LIBRA Apparatus”. In: *Nucl.Instrum.Meth.A* 592 (2008), pp. 297–315. DOI: `10.1016/j.nima.2008.04.082`. arXiv: `0804.2738`. URL: `https://inspirehep.net/literature/783645` (visited on 10/29/2021).

[210] J. I. Collar et al. “Coherent Neutrino-Nucleus Scattering Detection with a CsI[Na] Scintillator at the SNS Spallation Source”. In: *Nucl.Instrum.Meth.A* 773 (2015), pp. 56–65. DOI: `10.1016/j.nima.2014.11.037`. arXiv: `1407.7524`. URL: `https://inspirehep.net/literature/1308695` (visited on 10/29/2021).

[211] W. R. Leo. *Techniques for Nuclear and Particle Physics Experiments: A How-to Approach*. 2., rev. ed. Berlin ; Heidelberg [u.a.]: Springer, 1994. XVIII, 378 S. ISBN: 978-3-540-57280-0 978-0-387-57280-2.

[212] G. Gilmore. *Practical Gamma-Ray Spectrometry*. 2. ed. Chichester [u.a.]: Wiley, 2008. XVIII, 387 S. ISBN: 978-0-470-86196-7.

[213] D. Budjas et al. "Pulse Shape Discrimination Studies with a Broad-Energy Germanium Detector for Signal Identification and Background Suppression in the GERDA Double Beta Decay Experiment". In: *JINST* 4 (2009). DOI: `10.1088/1748-0221/4/10/P10007`. arXiv: `0909.4044`. URL: `https://inspirehep.net/literature/831896` (visited on 11/25/2021).

[214] C. E. Aalseth et al. "CoGeNT: A Search for Low-Mass Dark Matter Using p-Type Point Contact Germanium Detectors". In: *Phys.Rev.D* 88 (2013). DOI: `10.1103/PhysRevD.88.012002`. arXiv: `1208.5737`. URL: `https://inspirehep.net/literature/1182215` (visited on 07/27/2021).

[215] H. B. Li et al. "Differentiation of Bulk and Surface Events in P-Type Point-Contact Germanium Detectors for Light WIMP Searches". In: *Astropart.Phys.* 56 (2014), pp. 1–8. DOI: `10.1016/j.astropartphys.2014.02.005`. arXiv: `1311.5957`. URL: `https://inspirehep.net/literature/1266048` (visited on 11/25/2021).

[216] L. T. Yang et al. "Bulk and Surface Event Identification in P-Type Germanium Detectors". In: *Nucl.Instrum.Meth.A* 886 (2018), pp. 13–23. DOI: `10.1016/j.nima.2017.12.078`. arXiv: `1611.03357`. URL: `https://inspirehep.net/literature/1496979` (visited on 11/25/2021).

[217] K.-J. Kang et al. "Introduction to the CDEX Experiment". In: *Front.Phys.(Beijing)* 8 (2013), pp. 412–437. DOI: `10.1007/s11467-013-0349-1`. arXiv: `1303.0601`. URL: `https://inspirehep.net/literature/1222293` (visited on 07/27/2021).

[218] H. B. Li et al. "Limit on the Electron Neutrino Magnetic Moment from the Kuo-Sheng Reactor Neutrino Experiment". In: *Phys.Rev.Lett.* 90 (2003). DOI: `10.1103/PhysRevLett.90.131802`. arXiv: `hep-ex/0212003`. URL: `https://inspirehep.net/literature/603603` (visited on 07/22/2021).

[219] W. E. Ang, S. Prasad, and R. Mahapatra. "Coherent Elastic Neutrino Nucleus Scatter Response of Semiconductor Detectors to Nuclear Reactor Antineutrinos". In: *Nucl.Instrum.Meth.A* 1004 (2021). DOI: `10.1016/j.nima.2021.165342`. URL: `https://inspirehep.net/literature/1862572` (visited on 07/21/2021).

[220] L. Singh and H. T. Wong. "Low Energy Neutrino Physics with Sub-keV Ge-Detectors at Kuo-Sheng Neutrino Laboratory". In: *J.Phys.Conf.Ser.* 888.1 (2017). DOI: `10.1088/1742-6596/888/1/012124`. URL: `https://inspirehep.net/literature/1625548` (visited on 05/06/2021).

[221] E. Armengaud et al. "Constraints on Low-Mass WIMPs from the EDELWEISS-III Dark Matter Search". In: *JCAP* 05 (2016), p. 019. DOI: `10.1088/1475-7516/2016/05/019`. arXiv: `1603.05120`. URL: `https://inspirehep.net/literature/1428644` (visited on 07/28/2021).

[222] G. Angloher et al. "Results on Low Mass WIMPs Using an Upgraded CRESST-II Detector". In: *Eur.Phys.J.C* 74 (12 2014), p. 3184. DOI: `10.1140/epjc/s10052-014-3184-9`. arXiv: `1407.3146`. URL: `https://inspirehep.net/literature/1305879` (visited on 07/28/2021).

[223] R. Agnese et al. "Results from the Super Cryogenic Dark Matter Search Experiment at Soudan". In: *Phys.Rev.Lett.* 120 (6 2018). DOI: 10.1103/PhysRevLett.120.061802. arXiv: 1708.08869. URL: https://inspirehep.net/literature/1620480 (visited on 07/28/2021).

[224] C. Alduino et al. "First Results from CUORE: A Search for Lepton Number Violation via $0\nu\beta\beta$ Decay of ^{130}Te". In: *Phys.Rev.Lett.* 120 (13 2018). DOI: 10.1103/PhysRevLett.120.132501. arXiv: 1710.07988. URL: https://inspirehep.net/literature/1631986 (visited on 07/28/2021).

[225] H. Bonet et al. "Novel Constraints on Neutrino Physics beyond the Standard Model from the CONUS Experiment". In: (2021). arXiv: 2110.02174. URL: https://inspirehep.net/literature/1938781 (visited on 10/06/2021).

[226] R. Barlow. *Statistics: A Guide to the Use of Statistical Methods in the Physical Sciences.* Repr. The Manchester Physics Series. Chichester [u.a.]: Wiley, 1999. XV, 204 S. ISBN: 978-0-471-92294-0 978-0-471-92295-7.

[227] G. Cowan. *Statistical Data Analysis: [With Applications from Particle Physics].* Oxford Science Publications. Oxford: Clarendon Press, 1998. XIV, 197 S. ISBN: 978-0-19-850156-5 978-0-19-850155-8.

[228] L. Lista. "Practical Statistics for Particle Physicists". In: *2016 European School of High-Energy Physics.* Sept. 2016. DOI: 10.23730/CYRSP-2017-005.213. arXiv: 1609.04150. URL: https://inspirehep.net/literature/1486520 (visited on 07/29/2021).

[229] G. Cowan. *Statistics.* Aug. 2020. DOI: 10.1093/ptep/ptaa104. URL: https://inspirehep.net/literature/1812251 (visited on 07/12/2021).

[230] F. James and M. Roos. "Minuit - a System for Function Minimization and Analysis of the Parameter Errors and Correlations". In: *Computer Physics Communications* 10.6 (Dec. 1, 1975), pp. 343–367. ISSN: 0010-4655. DOI: 10.1016/0010-4655(75)90039-9. URL: https://www.sciencedirect.com/science/article/pii/0010465575900399 (visited on 05/11/2021).

[231] L. Lista. *Statistical Methods for Data Analysis in Particle Physics.* Vol. 909. Springer, 2016. ISBN: 978-3-319-20175-7 978-3-319-20176-4. DOI: 10.1007/978-3-319-20176-4.

[232] G. Cowan et al. "Asymptotic Formulae for Likelihood-Based Tests of New Physics". In: *Eur.Phys.J.C* 71 (2011), p. 1554. DOI: 10.1140/epjc/s10052-011-1554-0. arXiv: 1007.1727. URL: https://inspirehep.net/literature/860907 (visited on 05/11/2021).

[233] J. Neyman, E. S. Pearson, and K. Pearson. "IX. On the Problem of the Most Efficient Tests of Statistical Hypotheses". In: *Philosophical Transactions of the Royal Society of London. Series A, Containing Papers of a Mathematical or Physical Character* 231.694-706 (1933), pp. 289–337. DOI: 10.1098/rsta.1933.0009. URL: https://royalsocietypublishing.org/doi/10.1098/rsta.1933.0009 (visited on 08/31/2021).

[234] W. A. Rolke, A. M. Lopez, and J. Conrad. “Limits and Confidence Intervals in the Presence of Nuisance Parameters”. In: *Nucl.Instrum.Meth.A* 551 (2005), pp. 493–503. DOI: 10.1016/j.nima.2005.05.068. arXiv: physics/0403059. URL: https://inspirehep.net/literature/646079 (visited on 10/29/2021).

[235] S. S. Wilks. “The Large-Sample Distribution of the Likelihood Ratio for Testing Composite Hypotheses”. In: *Annals Math.Statist.* 9.1 (1938), pp. 60–62. DOI: 10.1214/aoms/1177732360. URL: https://inspirehep.net/literature/1247197 (visited on 05/11/2021).

[236] J. Neyman. “Outline of a Theory of Statistical Estimation Based on the Classical Theory of Probability”. In: *Phil.Trans.Roy.Soc.Lond.A* 236.767 (1937), pp. 333–380. DOI: 10.1098/rsta.1937.0005. URL: https://inspirehep.net/literature/1510823 (visited on 09/05/2021).

[237] G. J. Feldman and R. D. Cousins. “A Unified Approach to the Classical Statistical Analysis of Small Signals”. In: *Phys.Rev.D* 57 (1998), pp. 3873–3889. DOI: 10.1103/PhysRevD.57.3873. arXiv: physics/9711021. URL: https://inspirehep.net/literature/454197 (visited on 10/29/2021).

[238] Particle Data Group et al. “Review of Particle Physics”. In: *Progress of Theoretical and Experimental Physics* 2020.8 (Aug. 2020). ISSN: 2050-3911. DOI: 10.1093/ptep/ptaa104. URL: https://inspirehep.net/literature/1812251 (visited on 07/12/2021).

[239] J. D. Hakenmüller. “Looking for Coherent Elastic Neutrino Nucleus Scattering with the CONUS Experiment.” In: (2021). DOI: 10.11588/heidok.00029165. URL: https://inspirehep.net/literature/1839748 (visited on 05/06/2021).

[240] J. Hakenmüller et al. “Neutron-Induced Background in the CONUS Experiment”. In: *Eur.Phys.J.C* 79 (8 2019), p. 699. DOI: 10.1140/epjc/s10052-019-7160-2. arXiv: 1903.09269. URL: https://inspirehep.net/literature/1726342 (visited on 05/06/2021).

[241] T. Schierhuber. “Ultra-Low Background Germanium Spectroscopy : Commissioning an Experimental Shielding for a Future Neutrino Experiment”. Ruprecht-Karls-Universität Heidelberg, Sept. 1, 2017. URL: https://pure.mpg.de/pubman/faces/ViewItemOverviewPage.jsp?itemId=item_2486659_1 (visited on 10/10/2021).

[242] *Kernkraftwerk Brokdorf.* URL: https://www.preussenelektra.de/de/unsere-kraftwerke/kraftwerkbrokdorf.html (visited on 10/07/2021).

[243] *Energy Concept for an Environmentally Sound, Reliable and Affordable Energy Supply, Federal Ministry of Economics and Technology.* URL: https://www.osce.org/secretariat/101047 (visited on 10/11/2021).

[244] H. Bonet et al. “Full Background Decomposition of the CONUS Experiment”. In: (2021). arXiv: 2112.09585. URL: https://inspirehep.net/literature/1993409 (visited on 12/18/2021).

[245] *Mirion Technologies (Canberra) SAS, Lingolsheim Office.* URL: https://www.mirion.com/mirion-technologies-canberra-sas-lingolsheim (visited on 10/12/2021).

[246] *Lynx Digital Signal Analyzer*. URL: https://www.mirion.com/products/lynx-digital-signal-analyzer (visited on 10/08/2021).

[247] Th A. Mueller et al. "Improved Predictions of Reactor Antineutrino Spectra". In: *Phys.Rev.C* 83 (2011). DOI: 10.1103/PhysRevC.83.054615. arXiv: 1101.2663. URL: https://inspirehep.net/literature/884183 (visited on 05/06/2021).

[248] P. Huber. "On the Determination of Anti-Neutrino Spectra from Nuclear Reactors". In: *Phys.Rev.C* 84 (2011). DOI: 10.1103/PhysRevC.85.029901. arXiv: 1106.0687. URL: https://inspirehep.net/literature/912553 (visited on 05/06/2021).

[249] I. Endrizzi, M. Beczkowiak, and G. Meier. "Refinement of Siemens Core Monitoring Based on Aeroball and PDD In-Core Measuring Systems Using POWERTRAX TM". In: *Core Monitoring for Commercial Reactors: Improvements in Systems and Methods*. Nuclear Energy Agency (NEA), 2000, pp. 223–234. URL: https://www.oecd-nea.org/jcms/pl_13346/core-monitoring-for-commercial-reactors-improvements-in-systems-and-methods?details=true (visited on 12/01/2021).

[250] Z. Djurcic et al. "Uncertainties in the Anti-Neutrino Production at Nuclear Reactors". In: *J.Phys.G* 36 (2009). DOI: 10.1088/0954-3899/36/4/045002. arXiv: 0808.0747. URL: https://inspirehep.net/literature/792495 (visited on 10/29/2021).

[251] X. B. Ma et al. "Improved Calculation of the Energy Release in Neutron-Induced Fission". In: *Phys.Rev.C* 88 (1 2013). DOI: 10.1103/PhysRevC.88.014605. arXiv: 1212.6625. URL: https://inspirehep.net/literature/1208935 (visited on 05/06/2021).

[252] X. B. Ma et al. "Uncertainty Analysis of Fission Fraction for Reactor Antineutrino Experiments". In: *Mod.Phys.Lett.A* 31 (20 2016). DOI: 10.1142/S0217732316501200. arXiv: 1405.6807. URL: https://inspirehep.net/literature/1298311 (visited on 05/06/2021).

[253] T. Araki et al. "Measurement of Neutrino Oscillation with KamLAND: Evidence of Spectral Distortion". In: *Phys.Rev.Lett.* 94 (2005). DOI: 10.1103/PhysRevLett.94.081801. arXiv: hep-ex/0406035. URL: https://inspirehep.net/literature/652319 (visited on 10/29/2021).

[254] W. Z. Wei, L. Wang, and D. M. Mei. "Average Energy Expended per E-h Pair for Germanium-Based Dark Matter Experiments". In: *JINST* 12 (04 2017). DOI: 10.1088/1748-0221/12/04/P04022. arXiv: 1602.08005. URL: https://inspirehep.net/literature/1424255 (visited on 10/17/2021).

[255] J. Lindhard et al. "INTEGRAL EQUATIONS GOVERNING RADIATION EFFECTS. (NOTES ON ATOMIC COLLISIONS, III)". In: *Kgl. Danske Videnskab., Selskab. Mat. Fys. Medd.* Vol: 33: No. 10 (Jan. 1, 1963). URL: https://www.osti.gov/biblio/4701226-integral-equations-governing-radiation-effects-notes-atomic-collisions-iii (visited on 10/17/2021).

[256] D. J. Ficenec et al. "Observation of Electronic Excitation by Extremely Slow Protons With Applications to the Detection of Supermassive Charged Particles". In: *Phys.Rev.D* 36 (1987), pp. 311–314. DOI: 10.1103/PhysRevD.36.311. URL: https://inspirehep.net/literature/252552 (visited on 10/29/2021).

[257] H. Bonet et al. *Direct measurement of the ionization quenching factor of nuclear recoils in germanium in the keV range.* To be published. 2022.

[258] J. Liao, H. Liu, and D. Marfatia. "Coherent Neutrino Scattering and the Migdal Effect on the Quenching Factor". In: *Phys.Rev.D* 104 (1 2021). DOI: `10.1103/PhysRevD.104.015005`. arXiv: `2104.01811`. URL: `https://inspirehep.net/literature/1856071` (visited on 10/29/2021).

[259] R. M. Gray. *Toeplitz and Circulant Matrices: A Review.* Now Publishers Inc, 2006. ISBN: 978-1-933019-23-9. URL: `https://ee.stanford.edu/~gray/toeplitz.html` (visited on 12/02/2021).

[260] Mathuranathan. *Methods to Compute Linear Convolution.* GaussianWaves. Feb. 18, 2014. URL: `https://www.gaussianwaves.com/2014/02/survey-of-methods-to-compute-convolution/` (visited on 12/02/2021).

[261] D. Aristizabal Sierra, J. Liao, and D. Marfatia. "Impact of Form Factor Uncertainties on Interpretations of Coherent Elastic Neutrino-Nucleus Scattering Data". In: *JHEP* 06 (2019), p. 141. DOI: `10.1007/JHEP06(2019)141`. arXiv: `1902.07398`. URL: `https://inspirehep.net/literature/1720907` (visited on 05/11/2021).

[262] M. Cadeddu et al. "Neutrino, Electroweak, and Nuclear Physics from COHERENT Elastic Neutrino-Nucleus Scattering with Refined Quenching Factor". In: *Phys.Rev.D* 101 (3 2020). DOI: `10.1103/PhysRevD.101.033004`. arXiv: `1908.06045`. URL: `https://inspirehep.net/literature/1749907` (visited on 10/29/2021).

[263] M. Salathe. "Study on Modified Point Contact Germanium Detectors for Low Background Applications". In: (2019). DOI: `10.11588/heidok.00019889`. URL: `https://inspirehep.net/literature/1764828` (visited on 12/05/2021).

[264] L. A. Mikaelyan. "Investigation of Neutrino Properties in Experiments at Nuclear Reactors: Present Status and Prospects". In: *Phys.Atom.Nucl.* 65 (2002), pp. 1173–1187. DOI: `10.1134/1.1495017`. arXiv: `hep-ph/0210047`. URL: `https://inspirehep.net/literature/598696` (visited on 07/04/2021).

[265] S. T. Perkins et al. *Tables and Graphs of Atomic Subshell and Relaxation Data Derived from the LLNL Evaluated Atomic Data Library (EADL), Z = 1–100.* UCRL-50400-Vol.30. Lawrence Livermore National Lab., CA (United States), Oct. 31, 1991. DOI: `10.2172/10121422`. URL: `https://www.osti.gov/biblio/10121422` (visited on 06/16/2021).

[266] K. W. Jones and H. W. Kraner. "Stopping of 1- to 1.8-keV Ge-73 Atoms in Germanium". In: *Phys.Rev.C* 4 (1971), pp. 125–129. DOI: `10.1103/PhysRevC.4.125`. URL: `https://inspirehep.net/literature/72911` (visited on 09/29/2021).

[267] K. W. Jones and H. W. Kraner. "Energy Lost to Ionization by 254-eV Ge-73 Atoms Stopping in Ge". In: *Phys.Rev.A* 11 (1975), pp. 1347–1353. DOI: `10.1103/PhysRevA.11.1347`. URL: `https://inspirehep.net/literature/107898` (visited on 09/29/2021).

[268] Y. Messous. "Calibration of a Ge Crystal with Nuclear Recoils for the Development of a Dark Matter Detector". In: *Astropart.Phys.* 3 (1995), pp. 361–366. DOI: `10.1016/0927-6505(95)00007-4`. URL: `https://inspirehep.net/literature/407387` (visited on 09/29/2021).

[269] P. S. Barbeau, J. I. Collar, and O. Tench. “Large-Mass Ultra-Low Noise Germanium Detectors: Performance and Applications in Neutrino and Astroparticle Physics”. In: *JCAP* 09 (2007), p. 009. DOI: 10.1088/1475-7516/2007/09/009. arXiv: nucl-ex/0701012. URL: https://inspirehep.net/literature/741919 (visited on 10/29/2021).

[270] J. I. Collar, A. R. L. Kavner, and C. M. Lewis. “Germanium Response to Sub-keV Nuclear Recoils: A Multipronged Experimental Characterization”. In: *Phys.Rev.D* 103 (12 2021). DOI: 10.1103/PhysRevD.103.122003. arXiv: 2102.10089. URL: https://inspirehep.net/literature/1847646 (visited on 10/29/2021).

[271] T. E. Oliphant. “Python for Scientific Computing”. In: *Computing in Science Engineering* 9.3 (2007), pp. 10–20. ISSN: 1558-366X. DOI: 10.1109/MCSE.2007.58.

[272] K. J. Millman and M. Aivazis. “Python for Scientists and Engineers”. In: *Computing in Science Engineering* 13.2 (2011), pp. 9–12. ISSN: 1558-366X. DOI: 10.1109/MCSE.2011.36.

[273] P. Virtanen et al. “SciPy 1.0: Fundamental Algorithms for Scientific Computing in Python”. In: *Nature Methods* 17.3 (3 2020), pp. 261–272. ISSN: 1548-7105. DOI: 10.1038/s41592-019-0686-2. URL: https://www.nature.com/articles/s41592-019-0686-2 (visited on 05/11/2021).

[274] J. D. Hunter. “Matplotlib: A 2D Graphics Environment”. In: *Computing in Science Engineering* 9.3 (2007), pp. 90–95. ISSN: 1558-366X. DOI: 10.1109/MCSE.2007.55.

[275] F. Perez and B. E. Granger. “IPython: A System for Interactive Scientific Computing”. In: *Computing in Science Engineering* 9.3 (2007), pp. 21–29. ISSN: 1558-366X. DOI: 10.1109/MCSE.2007.53.

[276] C. R. Harris et al. “Array Programming with NumPy”. In: *Nature* 585.7825 (7825 2020), pp. 357–362. ISSN: 1476-4687. DOI: 10.1038/s41586-020-2649-2. URL: https://www.nature.com/articles/s41586-020-2649-2 (visited on 05/11/2021).

[277] W. McKinney. “Data Structures for Statistical Computing in Python”. In: *Proceedings of the 9th Python in Science Conference* (2010), pp. 56–61. DOI: 10.25080/Majora-92bf1922-00a. URL: http://conference.scipy.org/proceedings/scipy2010/mckinney.html (visited on 02/25/2021).

[278] *JupyterLab Documentation — JupyterLab 3.0.15 Documentation*. URL: https://jupyterlab.readthedocs.io/en/stable/ (visited on 05/11/2021).

[279] *PyCharm: The Python IDE for Professional Developers by JetBrains*. JetBrains. URL: https://www.jetbrains.com/pycharm/ (visited on 05/11/2021).

[280] H. Dembinski et al. *scikit-hep/iminuit: v2.0.0*. Version v2.0.0. Dec. 2020. DOI: 10.5281/zenodo.4310361.

[281] F. James and M. Roos. “Minuit - a System for Function Minimization and Analysis of the Parameter Errors and Correlations”. In: *Computer Physics Communications* 10.6 (1975), pp. 343–367. ISSN: 0010-4655. DOI: 10.1016/0010-4655(75)90039-9. URL: https://www.sciencedirect.com/science/article/pii/0010465575900399 (visited on 05/11/2021).

[282] L. Dalcín, R. Paz, and M. Storti. "MPI for Python". In: *Journal of Parallel and Distributed Computing* 65.9 (2005), pp. 1108–1115. ISSN: 0743-7315. DOI: 10.1016/j.jpdc.2005.03.010. URL: https://www.sciencedirect.com/science/article/pii/S0743731505000560 (visited on 05/11/2021).

[283] L. Dalcín et al. "MPI for Python: Performance Improvements and MPI-2 Extensions". In: *Journal of Parallel and Distributed Computing* 68.5 (2008), pp. 655–662. ISSN: 0743-7315. DOI: 10.1016/j.jpdc.2007.09.005. URL: https://www.sciencedirect.com/science/article/pii/S0743731507001712 (visited on 05/11/2021).

[284] H. Bonet et al. *First limits on neutrino electromagnetic properties from the CONUS experiment.* To be published. 2022.

[285] Y. Farzan and M. Tortola. "Neutrino Oscillations and Non-Standard Interactions". In: *Front.in Phys.* 6 (2018), p. 10. DOI: 10.3389/fphy.2018.00010. arXiv: 1710.09360. URL: https://inspirehep.net/literature/1632454 (visited on 05/06/2021).

[286] I. Esteban et al. "Updated Constraints on Non-Standard Interactions from Global Analysis of Oscillation Data". In: *JHEP* 08 (2018), p. 180. DOI: 10.1007/JHEP08(2018)180. arXiv: 1805.04530. URL: https://inspirehep.net/literature/1672932 (visited on 05/06/2021).

[287] A. Esteban-Pretel, R. Tomas, and J. W. F. Valle. "Interplay between Collective Effects and Non-Standard Neutrino Interactions of Supernova Neutrinos". In: *Phys.Rev.D* 81 (2010). DOI: 10.1103/PhysRevD.81.063003. arXiv: 0909.2196. URL: https://inspirehep.net/literature/830983 (visited on 05/11/2021).

[288] A. Chatelain and M. C. Volpe. "Neutrino Propagation in Binary Neutron Star Mergers in Presence of Nonstandard Interactions". In: *Phys.Rev.D* 97 (2 2018). DOI: 10.1103/PhysRevD.97.023014. arXiv: 1710.11518. URL: https://inspirehep.net/literature/1633615 (visited on 05/11/2021).

[289] Y. Du and J.-H. Yu. "Neutrino Non-Standard Interactions Meet Precision Measurements of N_{eff}". In: *JHEP* 05 (2021), p. 058. DOI: 10.1007/JHEP05(2021)058. arXiv: 2101.10475. URL: https://inspirehep.net/literature/1842893 (visited on 10/30/2021).

[290] D. Aristizabal Sierra, V. De Romeri, and N. Rojas. "COHERENT Analysis of Neutrino Generalized Interactions". In: *Phys.Rev.D* 98 (2018). DOI: 10.1103/PhysRevD.98.075018. arXiv: 1806.07424. URL: https://inspirehep.net/literature/1678635 (visited on 05/06/2021).

[291] I. Bischer and W. Rodejohann. "General Neutrino Interactions from an Effective Field Theory Perspective". In: *Nucl.Phys.B* 947 (2019). DOI: 10.1016/j.nuclphysb.2019.114746. arXiv: 1905.08699. URL: https://inspirehep.net/literature/1735810 (visited on 05/06/2021).

[292] F. J. Escrihuela et al. "Global Constraints on Neutral-Current Generalized Neutrino Interactions". In: *JHEP* 07 (2021), p. 061. DOI: 10.1007/JHEP07(2021)061. arXiv: 2105.06484. URL: https://inspirehep.net/literature/1863312 (visited on 10/30/2021).

[293] A. V. Manohar. "Introduction to Effective Field Theories". In: *Les Houches Lect.Notes* 108 (2020). DOI: 10.1093/oso/9780198855743.003.0002. arXiv: 1804.05863. URL: https://inspirehep.net/literature/1668143 (visited on 11/03/2021).

[294] W. Buchmuller and D. Wyler. "Effective Lagrangian Analysis of New Interactions and Flavor Conservation". In: *Nucl.Phys.B* 268 (1986), pp. 621–653. DOI: 10.1016/0550-3213(86)90262-2. URL: https://inspirehep.net/literature/218149 (visited on 11/03/2021).

[295] S. Weinberg. "Baryon and Lepton Nonconserving Processes". In: *Phys.Rev.Lett.* 43 (1979), pp. 1566–1570. DOI: 10.1103/PhysRevLett.43.1566. URL: https://inspirehep.net/literature/144673 (visited on 11/29/2021).

[296] S. Bergmann, Y. Grossman, and E. Nardi. "Neutrino Propagation in Matter with General Interactions". In: *Phys.Rev.D* 60 (1999). DOI: 10.1103/PhysRevD.60.093008. arXiv: hep-ph/9903517. URL: https://inspirehep.net/literature/497477 (visited on 12/03/2021).

[297] J. B. Dent et al. "Accelerator and Reactor Complementarity in Coherent Neutrino-Nucleus Scattering". In: *Phys.Rev.D* 97 (3 2018). DOI: 10.1103/PhysRevD.97.035009. arXiv: 1711.03521. URL: https://inspirehep.net/literature/1635280 (visited on 05/06/2021).

[298] P. Coloma et al. "Improved Global Fit to Non-Standard Neutrino Interactions Using COHERENT Energy and Timing Data". In: *JHEP* 02 (2020), p. 023. DOI: 10.1007/JHEP02(2020)023. arXiv: 1911.09109. URL: https://inspirehep.net/literature/1766426 (visited on 05/06/2021).

[299] J. Dorenbosch et al. "Experimental Verification of the Universality of ν_e and ν_μ Coupling to the Neutral Weak Current". In: *Phys.Lett.B* 180 (1986), pp. 303–307. DOI: 10.1016/0370-2693(86)90315-1. URL: https://inspirehep.net/literature/231102 (visited on 05/11/2021).

[300] A. Friedland et al. "Probing Nonstandard Standard Model Backgrounds with LHC Monojets". In: *Phys.Lett.B* 714 (2012), pp. 267–275. DOI: 10.1016/j.physletb.2012.06.078. arXiv: 1111.5331. URL: https://inspirehep.net/literature/954987 (visited on 05/27/2021).

[301] A. Rohatgi. *Webplotdigitizer: Version 4.5*. 2021. URL: https://automeris.io/WebPlotDigitizer (visited on 05/27/2021).

[302] B. Aharmim et al. "Combined Analysis of All Three Phases of Solar Neutrino Data from the Sudbury Neutrino Observatory". In: *Phys.Rev.C* 88 (2013). DOI: 10.1103/PhysRevC.88.025501. arXiv: 1109.0763. URL: https://inspirehep.net/literature/926320 (visited on 11/06/2021).

[303] S. Davidson et al. "Present and Future Bounds on Nonstandard Neutrino Interactions". In: *JHEP* 03 (2003), p. 011. DOI: 10.1088/1126-6708/2003/03/011. arXiv: hep-ph/0302093. URL: https://inspirehep.net/literature/613240 (visited on 05/11/2021).

[304] K. J. Healey, A. A. Petrov, and D. Zhuridov. “Nonstandard Neutrino Interactions and Transition Magnetic Moments”. In: *Phys.Rev.D* 87 (11 2013). DOI: `10.1103/PhysRevD.87.117301`. arXiv: `1305.0584`. URL: `https://inspirehep.net/literature/1231953` (visited on 05/06/2021).

[305] D. K. Papoulias and T. S. Kosmas. “Neutrino Transition Magnetic Moments within the Non-Standard Neutrino–Nucleus Interactions”. In: *Phys.Lett.B* 747 (2015), pp. 454–459. DOI: `10.1016/j.physletb.2015.06.039`. arXiv: `1506.05406`. URL: `https://inspirehep.net/literature/1376500` (visited on 05/06/2021).

[306] X.-J. Xu. “Tensor and Scalar Interactions of Neutrinos May Lead to Observable Neutrino Magnetic Moments”. In: *Phys.Rev.D* 99 (7 2019). DOI: `10.1103/PhysRevD.99.075003`. arXiv: `1901.00482`. URL: `https://inspirehep.net/literature/1712702` (visited on 05/10/2021).

[307] G. Arcadi et al. “Comparing 2HDM + Scalar and Pseudoscalar Simplified Models at LHC”. In: *JHEP* 06 (2020), p. 098. DOI: `10.1007/JHEP06(2020)098`. arXiv: `2001.10540`. URL: `https://inspirehep.net/literature/1777752` (visited on 05/21/2021).

[308] N. Vignaroli. “Leptoquarks in B-Meson Anomalies: Simplified Models and HL-LHC Discovery Prospects”. In: *Nuovo Cim.C* 43 (2-3 2020), p. 53. DOI: `10.1393/ncc/i2020-20053-0`. arXiv: `1912.00899`. URL: `https://inspirehep.net/literature/1767975` (visited on 05/21/2021).

[309] J. Abdallah et al. “Simplified Models for Dark Matter Searches at the LHC”. In: *Phys.Dark Univ.* 9–10 (2015), pp. 8–23. DOI: `10.1016/j.dark.2015.08.001`. arXiv: `1506.03116`. URL: `https://inspirehep.net/literature/1375500` (visited on 05/06/2021).

[310] D. Abercrombie et al. “Dark Matter Benchmark Models for Early LHC Run-2 Searches: Report of the ATLAS/CMS Dark Matter Forum”. In: *Phys.Dark Univ.* 27 (2020). DOI: `10.1016/j.dark.2019.100371`. arXiv: `1507.00966`. URL: `https://inspirehep.net/literature/1381178` (visited on 05/06/2021).

[311] A. Boveia et al. “Recommendations on Presenting LHC Searches for Missing Transverse Energy Signals Using Simplified s-Channel Models of Dark Matter”. In: *Phys.Dark Univ.* 27 (2020). DOI: `10.1016/j.dark.2019.100365`. arXiv: `1603.04156`. URL: `https://inspirehep.net/literature/1427412` (visited on 05/06/2021).

[312] F. Kahlhoefer et al. “Implications of Unitarity and Gauge Invariance for Simplified Dark Matter Models”. In: *JHEP* 02 (2016), p. 016. DOI: `10.1007/JHEP02(2016)016`. arXiv: `1510.02110`. URL: `https://inspirehep.net/literature/1396721` (visited on 05/06/2021).

[313] J. Ellis, M. Fairbairn, and P. Tunney. “Anomaly-Free Dark Matter Models Are Not so Simple”. In: *JHEP* 08 (2017), p. 053. DOI: `10.1007/JHEP08(2017)053`. arXiv: `1704.03850`. URL: `https://inspirehep.net/literature/1591329` (visited on 05/06/2021).

[314] E. Morgante. “Simplified Dark Matter Models”. In: *Adv.High Energy Phys.* 2018 (2018). DOI: `10.1155/2018/5012043`. arXiv: `1804.01245`. URL: `https://inspirehep.net/literature/1665857` (visited on 05/06/2021).

[315] G. Arcadi et al. “The Waning of the WIMP? A Review of Models, Searches, and Constraints”. In: *Eur.Phys.J.C* 78 (3 2018), p. 203. DOI: `10.1140/epjc/s10052-018-5662-y`. arXiv: `1703.07364`. URL: `https://inspirehep.net/literature/1518747` (visited on 11/07/2021).

[316] N. F. Bell, G. Busoni, and I. W. Sanderson. “Self-Consistent Dark Matter Simplified Models with an s-Channel Scalar Mediator”. In: *JCAP* 03 (2017), p. 015. DOI: `10.1088/1475-7516/2017/03/015`. arXiv: `1612.03475`. URL: `https://inspirehep.net/literature/1502933` (visited on 09/21/2021).

[317] R. N. Mohapatra and R. E. Marshak. “Local B-L Symmetry of Electroweak Interactions, Majorana Neutrinos and Neutron Oscillations”. In: *Phys.Rev.Lett.* 44 (1980), pp. 1316–1319. DOI: `10.1103/PhysRevLett.44.1316`. URL: `https://inspirehep.net/literature/152192` (visited on 05/06/2021).

[318] S. Khalil. “Low Scale B - L Extension of the Standard Model at the LHC”. In: *J.Phys.G* 35 (2008). DOI: `10.1088/0954-3899/35/5/055001`. arXiv: `hep-ph/0611205`. URL: `https://inspirehep.net/literature/731877` (visited on 05/06/2021).

[319] X.-G. He et al. “Simplest Z-Prime Model”. In: *Phys.Rev.D* 44 (1991), pp. 2118–2132. DOI: `10.1103/PhysRevD.44.2118`. URL: `https://inspirehep.net/literature/315429` (visited on 11/09/2021).

[320] J. Heeck and W. Rodejohann. “Gauged $L_\mu - L_\tau$ Symmetry at the Electroweak Scale”. In: *Phys.Rev.D* 84 (2011). DOI: `10.1103/PhysRevD.84.075007`. arXiv: `1107.5238`. URL: `https://inspirehep.net/literature/920240` (visited on 05/16/2021).

[321] G. Arcadi et al. “Dark Sequential Z Portal: Collider and Direct Detection Experiments”. In: *Phys.Rev.D* 97 (4 2018). DOI: `10.1103/PhysRevD.97.043009`. arXiv: `1708.00890`. URL: `https://inspirehep.net/literature/1614290` (visited on 05/07/2021).

[322] P. Langacker. “The Physics of Heavy Z' Gauge Bosons”. In: *Rev.Mod.Phys.* 81 (2009), pp. 1199–1228. DOI: `10.1103/RevModPhys.81.1199`. arXiv: `0801.1345`. URL: `https://inspirehep.net/literature/777086` (visited on 11/09/2021).

[323] M. Bauer, P. Foldenauer, and J. Jaeckel. “Hunting All the Hidden Photons”. In: *JHEP* 07 (2018), p. 094. DOI: `10.1007/JHEP07(2018)094`. arXiv: `1803.05466`. URL: `https://inspirehep.net/literature/1662673` (visited on 05/06/2021).

[324] K. S. Babu, C. F. Kolda, and J. March-Russell. “Implications of Generalized Z - Z-Prime Mixing”. In: *Phys.Rev.D* 57 (1998), pp. 6788–6792. DOI: `10.1103/PhysRevD.57.6788`. arXiv: `hep-ph/9710441`. URL: `https://inspirehep.net/literature/450102` (visited on 05/11/2021).

[325] J. Heeck and W. Rodejohann. “Kinetic and Mass Mixing with Three Abelian Groups”. In: *Phys.Lett.B* 705 (2011), pp. 369–374. DOI: `10.1016/j.physletb.2011.10.050`. arXiv: `1109.1508`. URL: `https://inspirehep.net/literature/926627` (visited on 05/16/2021).

[326] M. Lindner et al. "Neutrino-Electron Scattering: General Constraints on Z' and Dark Photon Models". In: *JHEP* 05 (2018), p. 098. DOI: `10.1007/JHEP05(2018)098`. arXiv: `1803.00060`. URL: `https://inspirehep.net/literature/1658053` (visited on 05/06/2021).

[327] P. B. Denton, Y. Farzan, and I. M. Shoemaker. "Testing Large Non-Standard Neutrino Interactions with Arbitrary Mediator Mass after COHERENT Data". In: *JHEP* 07 (2018), p. 037. DOI: `10.1007/JHEP07(2018)037`. arXiv: `1804.03660`. URL: `https://inspirehep.net/literature/1667188` (visited on 05/06/2021).

[328] M. Aaboud et al. "Search for High-Mass New Phenomena in the Dilepton Final State Using Proton-Proton Collisions at $\sqrt{s} = 13$ TeV with the ATLAS Detector". In: *Phys.Lett.B* 761 (2016), pp. 372–392. DOI: `10.1016/j.physletb.2016.08.055`. arXiv: `1607.03669`. URL: `https://inspirehep.net/literature/1475476` (visited on 05/06/2021).

[329] B. Batell, M. Pospelov, and A. Ritz. "Exploring Portals to a Hidden Sector Through Fixed Targets". In: *Phys.Rev.D* 80 (2009). DOI: `10.1103/PhysRevD.80.095024`. arXiv: `0906.5614`. URL: `https://inspirehep.net/literature/824478` (visited on 05/06/2021).

[330] J. D. Bjorken et al. "New Fixed-Target Experiments to Search for Dark Gauge Forces". In: *Phys.Rev.D* 80 (2009). DOI: `10.1103/PhysRevD.80.075018`. arXiv: `0906.0580`. URL: `https://inspirehep.net/literature/822131` (visited on 05/06/2021).

[331] S. Bilmis et al. "Constraints on Dark Photon from Neutrino-Electron Scattering Experiments". In: *Phys.Rev.D* 92 (3 2015). DOI: `10.1103/PhysRevD.92.033009`. arXiv: `1502.07763`. URL: `https://inspirehep.net/literature/1346837` (visited on 05/06/2021).

[332] J. P. Lees et al. "Search for a Dark Photon in e^+e^- Collisions at BaBar". In: *Phys.Rev.Lett.* 113 (20 2014). DOI: `10.1103/PhysRevLett.113.201801`. arXiv: `1406.2980`. URL: `https://inspirehep.net/literature/1300153` (visited on 05/06/2021).

[333] J. P. Lees et al. "Search for Invisible Decays of a Dark Photon Produced in e^+e^- Collisions at BaBar". In: *Phys.Rev.Lett.* 119 (13 2017). DOI: `10.1103/PhysRevLett.119.131804`. arXiv: `1702.03327`. URL: `https://inspirehep.net/literature/1513134` (visited on 05/06/2021).

[334] R. Aaij et al. "Search for Dark Photons Produced in 13 TeV *pp* Collisions". In: *Phys.Rev.Lett.* 120 (6 2018). DOI: `10.1103/PhysRevLett.120.061801`. arXiv: `1710.02867`. URL: `https://inspirehep.net/literature/1629161` (visited on 05/06/2021).

[335] P. Ilten et al. "Serendipity in Dark Photon Searches". In: *JHEP* 06 (2018), p. 004. DOI: `10.1007/JHEP06(2018)004`. arXiv: `1801.04847`. URL: `https://inspirehep.net/literature/1648160` (visited on 05/06/2021).

[336] R. Harnik, J. Kopp, and P. A. N. Machado. “Exploring Nu Signals in Dark Matter Detectors”. In: *JCAP* 07 (2012), p. 026. DOI: 10.1088/1475-7516/2012/07/026. arXiv: 1202.6073. URL: https://inspirehep.net/literature/1090939 (visited on 05/06/2021).

[337] A. Palladino, M. Spurio, and F. Vissani. “Neutrino Telescopes and High-Energy Cosmic Neutrinos”. In: *Universe* 6 (2 2020), p. 30. DOI: 10.3390/universe6020030. arXiv: 2009.01919. URL: https://inspirehep.net/literature/1781174 (visited on 11/30/2021).

[338] K. Fujikawa and R. Shrock. “The Magnetic Moment of a Massive Neutrino and Neutrino Spin Rotation”. In: *Phys.Rev.Lett.* 45 (1980), p. 963. DOI: 10.1103/PhysRevLett.45.963. URL: https://inspirehep.net/literature/9503 (visited on 05/10/2021).

[339] P. B. Pal and L. Wolfenstein. “Radiative Decays of Massive Neutrinos”. In: *Phys. Rev. D* 25 (1982), p. 766. DOI: 10.1103/PhysRevD.25.766. URL: https://inspirehep.net/literature/167508 (visited on 11/10/2021).

[340] R. E. Shrock. “Electromagnetic Properties and Decays of Dirac and Majorana Neutrinos in a General Class of Gauge Theories”. In: *Nucl.Phys.B* 206 (1982), pp. 359–379. DOI: 10.1016/0550-3213(82)90273-5. URL: https://inspirehep.net/literature/176797 (visited on 05/10/2021).

[341] S. M. Bilenky and S. T. Petcov. “Massive Neutrinos and Neutrino Oscillations”. In: *Rev.Mod.Phys.* 59 (1987), p. 671. DOI: 10.1103/RevModPhys.59.671. URL: https://inspirehep.net/literature/254332 (visited on 11/10/2021).

[342] J. Schechter and J. W. F. Valle. “Majorana Neutrinos and Magnetic Fields”. In: *Phys.Rev.D* 24 (1981), pp. 1883–1889. DOI: 10.1103/PhysRevD.25.283. URL: https://inspirehep.net/literature/164961 (visited on 05/10/2021).

[343] J. F. Nieves. “Electromagnetic Properties of Majorana Neutrinos”. In: *Phys.Rev.D* 26 (1982), p. 3152. DOI: 10.1103/PhysRevD.26.3152. URL: https://inspirehep.net/literature/168101 (visited on 11/10/2021).

[344] B. Kayser. “Majorana Neutrinos and Their Electromagnetic Properties”. In: *Phys. Rev. D* 26 (1982), p. 1662. DOI: 10.1103/PhysRevD.26.1662. URL: https://inspirehep.net/literature/176509 (visited on 11/10/2021).

[345] P. B. Pal. “Dirac, Majorana and Weyl Fermions”. In: *Am.J.Phys.* 79 (2011), pp. 485–498. DOI: 10.1119/1.3549729. arXiv: 1006.1718. URL: https://inspirehep.net/literature/857504 (visited on 11/29/2021).

[346] E. Majorana. “Teoria Simmetrica Dell’elettrone e Del Positrone”. In: *Nuovo Cim.* 14 (1937), pp. 171–184. DOI: 10.1007/BF02961314. URL: https://inspirehep.net/literature/8251 (visited on 11/29/2021).

[347] S. Davidson, M. Gorbahn, and A. Santamaria. “From Transition Magnetic Moments to Majorana Neutrino Masses”. In: *Phys.Lett.B* 626 (2005), pp. 151–160. DOI: 10.1016/j.physletb.2005.08.086. arXiv: hep-ph/0506085. URL: https://inspirehep.net/literature/684409 (visited on 05/10/2021).

[348] N. F. Bell et al. "How Magnetic Is the Dirac Neutrino?" In: *Phys.Rev.Lett.* 95 (2005). DOI: `10.1103/PhysRevLett.95.151802`. arXiv: `hep-ph/0504134`. URL: `https://inspirehep.net/literature/680709` (visited on 05/10/2021).

[349] N. F. Bell et al. "Model Independent Bounds on Magnetic Moments of Majorana Neutrinos". In: *Phys.Lett.B* 642 (2006), pp. 377–383. DOI: `10.1016/j.physletb.2006.09.055`. arXiv: `hep-ph/0606248`. URL: `https://inspirehep.net/literature/719953` (visited on 05/10/2021).

[350] M. B. Voloshin. "On Compatibility of Small Mass with Large Magnetic Moment of Neutrino". In: *Sov.J.Nucl.Phys.* 48 (1988), p. 512. URL: `https://inspirehep.net/literature/253938` (visited on 11/11/2021).

[351] K. S. Babu and R. N. Mohapatra. "Large Transition Magnetic Moment of the Neutrino from Horizontal Symmetry". In: *Phys.Rev.D* 42 (1990), pp. 3778–3793. DOI: `10.1103/PhysRevD.42.3778`. URL: `https://inspirehep.net/literature/298198` (visited on 11/12/2021).

[352] K. S. Babu, S. Jana, and M. Lindner. "Large Neutrino Magnetic Moments in the Light of Recent Experiments". In: *JHEP* 10 (2020), p. 040. DOI: `10.1007/JHEP10(2020)040`. arXiv: `2007.04291`. URL: `https://inspirehep.net/literature/1805780` (visited on 11/12/2021).

[353] S. M. Barr, E. M. Freire, and A. Zee. "A Mechanism for Large Neutrino Magnetic Moments". In: *Phys.Rev.Lett.* 65 (1990), pp. 2626–2629. DOI: `10.1103/PhysRevLett.65.2626`. URL: `https://inspirehep.net/literature/297760` (visited on 11/11/2021).

[354] M. Lindner, B. Radovčić, and J. Welter. "Revisiting Large Neutrino Magnetic Moments". In: *JHEP* 07 (2017), p. 139. DOI: `10.1007/JHEP07(2017)139`. arXiv: `1706.02555`. URL: `https://inspirehep.net/literature/1603634` (visited on 05/10/2021).

[355] M. Czakon, J. Gluza, and M. Zralek. "Neutrino Magnetic Moments in Left-Right Symmetric Models". In: *Phys.Rev.D* 59 (1999). DOI: `10.1103/PhysRevD.59.013010`. URL: `https://inspirehep.net/literature/480149` (visited on 11/12/2021).

[356] A. Aboubrahim et al. "Large Neutrino Magnetic Dipole Moments in MSSM Extensions". In: *Phys.Rev.D* 89 (5 2014). DOI: `10.1103/PhysRevD.89.055009`. arXiv: `1312.2505`. URL: `https://inspirehep.net/literature/1268330` (visited on 11/12/2021).

[357] R. N. Mohapatra, S.-P. Ng, and H.-B. Yu. "Reactor Searches for Neutrino Magnetic Moment as a Probe of Extra Dimensions". In: *Phys.Rev.D* 70 (2004). DOI: `10.1103/PhysRevD.70.057301`. arXiv: `hep-ph/0404274`. URL: `https://inspirehep.net/literature/649433` (visited on 11/12/2021).

[358] W. Grimus and P. Stockinger. "Effects of Neutrino Oscillations and Neutrino Magnetic Moments on Elastic Neutrino - Electron Scattering". In: *Phys.Rev.D* 57 (1998), pp. 1762–1768. DOI: `10.1103/PhysRevD.57.1762`. arXiv: `hep-ph/9708279`. URL: `https://inspirehep.net/literature/446914` (visited on 11/11/2021).

[359] J. F. Beacom and P. Vogel. "Neutrino Magnetic Moments, Flavor Mixing, and the Super-Kamiokande Solar Data". In: *Phys.Rev.Lett.* 83 (1999), pp. 5222–5225. DOI: 10.1103/PhysRevLett.83.5222. arXiv: hep-ph/9907383. URL: https://inspirehep.net/literature/503951 (visited on 11/11/2021).

[360] M. Cadeddu et al. "Constraints on Neutrino Millicharge and Charge Radius from Neutrino-Atom Scattering". In: *PoS* EPS-HEP2019 (2020), p. 423. DOI: 10.22323/1.364.0423. arXiv: 2001.02278. URL: https://inspirehep.net/literature/1774559 (visited on 11/13/2021).

[361] A. Parada. "Constraints on Neutrino Electric Millicharge from Experiments of Elastic Neutrino-Electron Interaction and Future Experimental Proposals Involving Coherent Elastic Neutrino-Nucleus Scattering". In: *Adv.High Energy Phys.* 2020 (2020). DOI: 10.1155/2020/5908904. arXiv: 1907.04942. URL: https://inspirehep.net/literature/1743572 (visited on 05/10/2021).

[362] A. G. Beda et al. "Gemma Experiment: The Results of Neutrino Magnetic Moment Search". In: *Phys.Part.Nucl.Lett.* 10 (2013), pp. 139–143. DOI: 10.1134/S1547477113020027. URL: https://inspirehep.net/literature/1225418 (visited on 05/10/2021).

[363] H. T. Wong et al. "A Search of Neutrino Magnetic Moments with a High-Purity Germanium Detector at the Kuo-Sheng Nuclear Power Station". In: *Phys.Rev.D* 75 (2007). DOI: 10.1103/PhysRevD.75.012001. arXiv: hep-ex/0605006. URL: https://inspirehep.net/literature/715626 (visited on 11/13/2021).

[364] L. B. Auerbach et al. "Measurement of Electron - Neutrino - Electron Elastic Scattering". In: *Phys.Rev.D* 63 (2001). DOI: 10.1103/PhysRevD.63.112001. arXiv: hep-ex/0101039. URL: https://inspirehep.net/literature/552304 (visited on 05/10/2021).

[365] B. C. Canas et al. "Updating Neutrino Magnetic Moment Constraints". In: *Phys. Lett. B* 753 (2016), pp. 191–198. DOI: 10.1016/j.physletb.2015.12.011. arXiv: 1510.01684. URL: https://inspirehep.net/literature/1396328 (visited on 05/10/2021).

[366] G. G. Raffelt. "Limits on Neutrino Electromagnetic Properties: An Update". In: *Phys.Rept.* 320 (1999), pp. 319–327. DOI: 10.1016/S0370-1573(99)00074-5. URL: https://inspirehep.net/literature/514741 (visited on 05/10/2021).

[367] C. Caprini, S. Biller, and P. G. Ferreira. "Constraints on the Electrical Charge Asymmetry of the Universe". In: *JCAP* 02 (2005), p. 006. DOI: 10.1088/1475-7516/2005/02/006. arXiv: hep-ph/0310066. URL: https://inspirehep.net/literature/629876 (visited on 11/13/2021).

[368] A. K. Soma et al. "Characterization and Performance of Germanium Detectors with Sub-keV Sensitivities for Neutrino and Dark Matter Experiments". In: *Nucl.Instrum.Meth.A* 836 (2016), pp. 67–82. DOI: 10.1016/j.nima.2016.08.044. arXiv: 1411.4802. URL: https://inspirehep.net/literature/1328621 (visited on 11/30/2021).

[369] J. Henrichs. "Development of Pulse Shape Studies for the CONUS Experiment". Master's thesis. Heidelberg University, 2021.

[370] A. E. Chavarria et al. “Measurement of the Ionization Produced by Sub-keV Silicon Nuclear Recoils in a CCD Dark Matter Detector”. In: *Phys.Rev.D* 94 (8 2016). DOI: `10.1103/PhysRevD.94.082007`. arXiv: `1608.00957`. URL: `https://inspirehep.net/literature/1478963` (visited on 11/26/2021).

[371] W. Maneschg. Personal communication. Nov. 26, 2021.

[372] J. Erler and S. Su. “The Weak Neutral Current”. In: *Prog.Part.Nucl.Phys.* 71 (2013), pp. 119–149. DOI: `10.1016/j.ppnp.2013.03.004`. arXiv: `1303.5522`. URL: `https://inspirehep.net/literature/1225117` (visited on 05/11/2021).

[373] M. Estienne et al. “Updated Summation Model: An Improved Agreement with the Daya Bay Antineutrino Fluxes”. In: *Phys.Rev.Lett.* 123 (2 2019). DOI: `10.1103/PhysRevLett.123.022502`. arXiv: `1904.09358`. URL: `https://inspirehep.net/literature/1730487` (visited on 11/20/2021).

[374] L. Hayen et al. “First-Forbidden Transitions in the Reactor Anomaly”. In: *Phys.Rev.C* 100 (5 2019). DOI: `10.1103/PhysRevC.100.054323`. arXiv: `1908.08302`. URL: `https://inspirehep.net/literature/1750681` (visited on 11/20/2021).

[375] C. Giunti et al. “Reactor Antineutrino Anomaly in Light of Recent Flux Model Refinements”. In: (2021). arXiv: `2110.06820`. URL: `https://inspirehep.net/literature/1944147` (visited on 10/29/2021).

[376] V. Kopeikin, M. Skorokhvatov, and O. Titov. “Reevaluating Reactor Antineutrino Spectra with New Measurements of the Ratio between U235 and Pu239 β Spectra”. In: *Phys.Rev.D* 104 (7 2021). DOI: `10.1103/PhysRevD.104.L071301`. arXiv: `2103.01684`. URL: `https://inspirehep.net/literature/1849502` (visited on 11/19/2021).

[377] W. Hampel et al. “Final Results of the Cr-51 Neutrino Source Experiments in GALLEX”. In: *Phys.Lett.B* 420 (1998), pp. 114–126. DOI: `10.1016/S0370-2693(97)01562-1`. URL: `https://inspirehep.net/literature/451948` (visited on 07/21/2021).

[378] J. N. Abdurashitov et al. “Measurement of the Response of the Russian-American Gallium Experiment to Neutrinos from a Cr-51 Source”. In: *Phys.Rev.C* 59 (1999), pp. 2246–2263. DOI: `10.1103/PhysRevC.59.2246`. arXiv: `hep-ph/9803418`. URL: `https://inspirehep.net/literature/468452` (visited on 07/21/2021).

[379] A. A. Aguilar-Arevalo et al. “Significant Excess of ElectronLike Events in the MiniBooNE Short-Baseline Neutrino Experiment”. In: *Phys.Rev.Lett.* 121 (22 2018). DOI: `10.1103/PhysRevLett.121.221801`. arXiv: `1805.12028`. URL: `https://inspirehep.net/literature/1675670` (visited on 11/27/2021).

[380] P. S. Amanik and G. C. McLaughlin. “Nuclear Neutron Form Factor from Neutrino Nucleus Coherent Elastic Scattering”. In: *J.Phys.G* 36 (2009). DOI: `10.1088/0954-3899/36/1/015105`. URL: `https://inspirehep.net/literature/810094` (visited on 05/11/2021).

[381] D. K. Papoulias et al. “Constraining Nuclear Physics Parameters with Current and Future COHERENT Data”. In: *Phys.Lett.B* 800 (2020). DOI: `10.1016/j.physletb.2019.135133`. arXiv: `1903.03722`. URL: `https://inspirehep.net/literature/1724488` (visited on 05/10/2021).

[382] B. A. Brown. “Neutron Radii in Nuclei and the Neutron Equation of State”. In: *Phys.Rev.Lett.* 85 (2000), pp. 5296–5299. DOI: 10.1103/PhysRevLett.85.5296. URL: https://inspirehep.net/literature/537772 (visited on 11/20/2021).

[383] S. Typel and B. A. Brown. “Neutron Radii and the Neutron Equation of State in Relativistic Models”. In: *Phys.Rev.C* 64.2 (2001). DOI: 10.1103/PhysRevC.64.027302. URL: https://inspirehep.net/literature/1475124 (visited on 11/20/2021).

[384] P.-G. Reinhard and W. Nazarewicz. “Information Content of a New Observable: The Case of the Nuclear Neutron Skin”. In: *Phys.Rev.C* 81 (2010). DOI: 10.1103/PhysRevC.81.051303. arXiv: 1002.4140. URL: https://inspirehep.net/literature/846396 (visited on 11/21/2021).

[385] J. M. Lattimer and M. Prakash. “The Physics of Neutron Stars”. In: *Science* 304 (2004), pp. 536–542. DOI: 10.1126/science.1090720. arXiv: astro-ph/0405262. URL: https://inspirehep.net/literature/650294 (visited on 11/20/2021).

[386] B. P. Abbott et al. “GW170817: Observation of Gravitational Waves from a Binary Neutron Star Inspiral”. In: *Phys.Rev.Lett.* 119 (16 2017). DOI: 10.1103/PhysRevLett.119.161101. arXiv: 1710.05832. URL: https://inspirehep.net/literature/1630824 (visited on 11/20/2021).

[387] F. J. Fattoyev, J. Piekarewicz, and C. J. Horowitz. “Neutron Skins and Neutron Stars in the Multimessenger Era”. In: *Phys.Rev.Lett.* 120 (17 2018). DOI: 10.1103/PhysRevLett.120.172702. arXiv: 1711.06615. URL: https://inspirehep.net/literature/1636955 (visited on 11/20/2021).

[388] J. Erler and A. Freitas. *Electroweak Model and Constraints on New Physics.* 2020. DOI: 10.1093/ptep/ptaa104. URL: https://inspirehep.net/literature/1812251 (visited on 07/12/2021).

[389] P. L. Anthony et al. “Precision Measurement of the Weak Mixing Angle in Moller Scattering”. In: *Phys.Rev.Lett.* 95 (2005). DOI: 10.1103/PhysRevLett.95.081601. arXiv: hep-ex/0504049. URL: https://inspirehep.net/literature/681321 (visited on 11/21/2021).

[390] D. Androić et al. “Precision Measurement of the Weak Charge of the Proton”. In: *Nature* 557 (7704 2018), pp. 207–211. DOI: 10.1038/s41586-018-0096-0. arXiv: 1905.08283. URL: https://inspirehep.net/literature/1672659 (visited on 11/21/2021).

[391] J. Benesch et al. “The MOLLER Experiment: An Ultra-Precise Measurement of the Weak Mixing Angle Using M{\o}ller Scattering”. In: (2014). arXiv: 1411.4088. URL: https://inspirehep.net/literature/1328514 (visited on 11/21/2021).

[392] D. Becker et al. “The P2 Experiment”. In: *Eur.Phys.J.A* 54 (11 2018), p. 208. DOI: 10.1140/epja/i2018-12611-6. arXiv: 1802.04759. URL: https://inspirehep.net/literature/1654804 (visited on 11/21/2021).

[393] M. Cadeddu et al. “New Insights into Nuclear Physics and Weak Mixing Angle Using Electroweak Probes”. In: *Phys.Rev.C* 104 (6 2021). DOI: 10.1103/PhysRevC.104.065502. arXiv: 2102.06153. URL: https://inspirehep.net/literature/1846034 (visited on 12/31/2021).

[394] M. Hirsch, E. Nardi, and D. Restrepo. “Bounds on the Tau and Muon Neutrino Vector and Axial Vector Charge Radius”. In: *Phys.Rev.D* 67 (2003). DOI: 10.1103/PhysRevD.67.033005. arXiv: hep-ph/0210137. URL: https://inspirehep.net/literature/599285 (visited on 11/21/2021).

[395] H. T. Wong and H.-B. Li. “Neutrino Magnetic Moments”. In: *Mod.Phys.Lett.A* 20 (2005), pp. 1103–1117. DOI: 10.1142/S0217732305017482. URL: https://inspirehep.net/literature/688996 (visited on 11/30/2021).

[396] C. Giunti et al. “Electromagnetic Neutrinos in Laboratory Experiments and Astrophysics”. In: *Annalen Phys.* 528 (2016), pp. 198–215. DOI: 10.1002/andp.201500211. arXiv: 1506.05387. URL: https://inspirehep.net/literature/1376498 (visited on 11/21/2021).

[397] J. Bernabeu, J. Papavassiliou, and J. Vidal. “The Neutrino Charge Radius Is a Physical Observable”. In: *Nucl.Phys.B* 680 (2004), pp. 450–478. DOI: 10.1016/j.nuclphysb.2003.12.025. arXiv: hep-ph/0210055. URL: https://inspirehep.net/literature/598704 (visited on 07/08/2021).

[398] J. L. Lucio, A. Rosado, and A. Zepeda. “A Characteristic Size for the Neutrino”. In: *Phys.Rev.D* 31 (1985), p. 1091. DOI: 10.1103/PhysRevD.31.1091. URL: https://inspirehep.net/literature/14902 (visited on 11/21/2021).

[399] H. Novales-Sanchez et al. “Effects of Physics beyond the Standard Model on the Neutrino Charge Radius: An Effective Lagrangian Approach”. In: *Phys.Rev.D* 78 (2008). DOI: 10.1103/PhysRevD.78.073014. arXiv: 0805.4177. URL: https://inspirehep.net/literature/786712 (visited on 11/21/2021).

[400] A. J. Anderson et al. “Measuring Active-to-Sterile Neutrino Oscillations with Neutral Current Coherent Neutrino-Nucleus Scattering”. In: *Phys.Rev.D* 86 (2012). DOI: 10.1103/PhysRevD.86.013004. arXiv: 1201.3805. URL: https://inspirehep.net/literature/1084985 (visited on 05/11/2021).

[401] C. Giunti and T. Lasserre. “eV-Scale Sterile Neutrinos”. In: *Ann.Rev.Nucl.Part.Sci.* 69 (2019), pp. 163–190. DOI: 10.1146/annurev-nucl-101918-023755. arXiv: 1901.08330. URL: https://inspirehep.net/literature/1716584 (visited on 05/06/2021).

[402] D. V. Naumov. “The Sterile Neutrino: A Short Introduction”. In: *EPJ Web Conf.* 207 (2019). DOI: 10.1051/epjconf/201920704004. arXiv: 1901.00151. URL: https://inspirehep.net/literature/1712704 (visited on 05/11/2021).

[403] T. S. Kosmas et al. “Probing Light Sterile Neutrino Signatures at Reactor and Spallation Neutron Source Neutrino Experiments”. In: *Phys.Rev.D* 96 (6 2017). DOI: 10.1103/PhysRevD.96.063013. arXiv: 1703.00054. URL: https://inspirehep.net/literature/1515514 (visited on 05/11/2021).

[404] M. Dentler et al. “Updated Global Analysis of Neutrino Oscillations in the Presence of eV-Scale Sterile Neutrinos”. In: *JHEP* 08 (2018), p. 010. DOI: 10.1007/JHEP08(2018)010. arXiv: 1803.10661. URL: https://inspirehep.net/literature/1664547 (visited on 05/11/2021).

[405] J. M. Berryman. “Constraining Sterile Neutrino Cosmology with Terrestrial Oscillation Experiments”. In: *Phys.Rev.D* 100 (2 2019). DOI: `10.1103/PhysRevD.100.023540`. arXiv: `1905.03254`. URL: `https://inspirehep.net/literature/1734009` (visited on 05/11/2021).

[406] M. K. Singh et al. “Constraints on Bosonic Dark Matter with Low Threshold Germanium Detector at Kuo-Sheng Reactor Neutrino Laboratory”. In: *Chin.J.Phys.* 58 (2019), pp. 63–74. DOI: `10.1016/j.cjph.2019.01.006`. arXiv: `1811.11415`. URL: `https://inspirehep.net/literature/1705668` (visited on 11/09/2021).

[407] A. Galindo-Uribarri, O. G. Miranda, and G. S. Garcia. “A Novel Approach for the Study of CEvNS”. In: (2020). arXiv: `2011.10230`. URL: `https://inspirehep.net/literature/1831921` (visited on 07/02/2021).

[408] T. S. Kosmas et al. “Coherent Elastic Neutrino-Nucleus Scattering (CEνNS) Event Rates for Ge, Zn, and Si Detector Materials”. In: *Phys.Rev.C* 104 (6 2021). DOI: `10.1103/PhysRevC.104.064618`. arXiv: `2111.08488`. URL: `https://inspirehep.net/literature/1969366` (visited on 12/31/2021).

[409] P. Coloma et al. “Curtailing the Dark Side in Non-Standard Neutrino Interactions”. In: *JHEP* 04 (2017), p. 116. DOI: `10.1007/JHEP04(2017)116`. arXiv: `1701.04828`. URL: `https://inspirehep.net/literature/1509503` (visited on 05/11/2021).

[410] P. Coloma et al. “COHERENT Enlightenment of the Neutrino Dark Side”. In: *Phys.Rev.D* 96 (11 2017). DOI: `10.1103/PhysRevD.96.115007`. arXiv: `1708.02899`. URL: `https://inspirehep.net/literature/1615211` (visited on 05/06/2021).

[411] L. M. G. de la Vega et al. “Complementarity between Dark Matter Direct Searches and CEνNS Experiments in $U(1)'$ Models”. In: *JHEP* 09 (2021). DOI: `10.1007/JHEP09(2021)146`. arXiv: `2107.04037`. URL: `https://inspirehep.net/literature/1880902` (visited on 11/19/2021).

[412] P. Deniverville, H.-S. Lee, and Y.-M. Lee. “New Searches at Reactor Experiments Based on the Dark Axion Portal”. In: *Phys.Rev.D* 103 (7 2021). DOI: `10.1103/PhysRevD.103.075006`. arXiv: `2011.03276`. URL: `https://inspirehep.net/literature/1828804` (visited on 11/27/2021).

[413] C. A. J. O’Hare. “New Definition of the Neutrino Floor for Direct Dark Matter Searches”. In: *Phys.Rev.Lett.* 127 (25 2021). DOI: `10.1103/PhysRevLett.127.251802`. arXiv: `2109.03116`. URL: `https://inspirehep.net/literature/1918102` (visited on 12/31/2021).

[414] S. E. Vahsen et al. “CYGNUS: Feasibility of a Nuclear Recoil Observatory with Directional Sensitivity to Dark Matter and Neutrinos”. In: (2020). arXiv: `2008.12587`. URL: `https://inspirehep.net/literature/1813839` (visited on 11/30/2021).

[415] M. C. Gonzalez-Garcia et al. “Neutrino Discovery Limit of Dark Matter Direct Detection Experiments in the Presence of Non-Standard Interactions”. In: *JHEP* 07 (2018), p. 019. DOI: `10.1007/JHEP07(2018)019`. arXiv: `1803.03650`. URL: `https://inspirehep.net/literature/1662090` (visited on 05/11/2021).

[416] C. E. Aalseth et al. "DarkSide-20k: A 20 Tonne Two-Phase LAr TPC for Direct Dark Matter Detection at LNGS". In: *Eur.Phys.J.Plus* 133 (2018), p. 131. DOI: `10.1140/epjp/i2018-11973-4`. arXiv: `1707.08145`. URL: `https://inspirehep.net/literature/1611708` (visited on 12/01/2021).

[417] J. Aalbers et al. "DARWIN: Towards the Ultimate Dark Matter Detector". In: *JCAP* 11 (2016), p. 017. DOI: `10.1088/1475-7516/2016/11/017`. arXiv: `1606.07001`. URL: `https://inspirehep.net/literature/1471703` (visited on 12/01/2021).

[418] P. Antonioli et al. "SNEWS: The Supernova Early Warning System". In: *New J.Phys.* 6 (2004), p. 114. DOI: `10.1088/1367-2630/6/1/114`. arXiv: `astro-ph/0406214`. URL: `https://inspirehep.net/literature/652039` (visited on 11/25/2021).

[419] M. Biassoni and C. Martinez. "Study of Supernova ν-Nucleus Coherent Scattering Interactions". In: *Astropart.Phys.* 36 (2012), pp. 151–155. DOI: `10.1016/j.astropartphys.2012.05.009`. arXiv: `1110.3536`. URL: `https://inspirehep.net/literature/940235` (visited on 05/05/2021).

[420] V. Brdar, M. Lindner, and X.-J. Xu. "Neutrino Astronomy with Supernova Neutrinos". In: *JCAP* 04 (2018), p. 025. DOI: `10.1088/1475-7516/2018/04/025`. arXiv: `1802.02577`. URL: `https://inspirehep.net/literature/1653944` (visited on 05/05/2021).

[421] N. Raj, V. Takhistov, and S. J. Witte. "Presupernova Neutrinos in Large Dark Matter Direct Detection Experiments". In: *Phys.Rev.D* 101 (4 2020). DOI: `10.1103/PhysRevD.101.043008`. arXiv: `1905.09283`. URL: `https://inspirehep.net/literature/1736503` (visited on 05/07/2021).

[422] P. Agnes et al. "Sensitivity of Future Liquid Argon Dark Matter Search Experiments to Core-Collapse Supernova Neutrinos". In: *JCAP* 03 (2021), p. 043. DOI: `10.1088/1475-7516/2021/03/043`. arXiv: `2011.07819`. URL: `https://inspirehep.net/literature/1830505` (visited on 05/07/2021).

[423] PBS series NOVA. *The Fabric of the Cosmos: Universe or Multiverse?* Quote by Steven Weinberg, found via [arXiv:2111.00930]. URL: `https://www.pbs.org/wgbh/nova/video/the-fabric-of-the-cosmos/` (visited on 11/18/2021).

[424] Wolfram Research, Inc. *Mathematica 12*. Version 12.2. 2021. URL: `https://www.wolfram.com`.

[425] H. H. Patel. "Package-X: A Mathematica Package for the Analytic Calculation of One-Loop Integrals". In: *Comput.Phys.Commun.* 197 (2015), pp. 276–290. DOI: `10.1016/j.cpc.2015.08.017`. arXiv: `1503.01469`. URL: `https://inspirehep.net/literature/1347391` (visited on 12/04/2021).

[426] R. H. Helm. "Inelastic and Elastic Scattering of 187-Mev Electrons from Selected Even-Even Nuclei". In: *Phys.Rev.* 104 (1956), pp. 1466–1475. DOI: `10.1103/PhysRev.104.1466`. URL: `https://inspirehep.net/literature/45733` (visited on 05/11/2021).

[427] D. W. L. Sprung and J. Martorell. "The Symmetrized Fermi Function and Its Transforms". In: *Journal of Physics A: Mathematical and General* 30.18 (Sept. 1997), pp. 6525–6534. ISSN: 0305-4470. DOI: `10.1088/0305-4470/30/18/026`. URL: `https://doi.org/10.1088/0305-4470/30/18/026` (visited on 09/23/2021).

[428] S. Klein and J. Nystrand. "Exclusive Vector Meson Production in Relativistic Heavy Ion Collisions". In: *Phys.Rev.C* 60 (1999). DOI: `10.1103/PhysRevC.60.014903`. arXiv: `hep-ph/9902259`. URL: `https://inspirehep.net/literature/495018` (visited on 05/11/2021).

[429] S. Baker and R. D. Cousins. "Clarification of the Use of Chi Square and Likelihood Functions in Fits to Histograms". In: *Nucl.Instrum.Meth.* 221 (1984), pp. 437–442. DOI: `10.1016/0167-5087(84)90016-4`. URL: `https://inspirehep.net/literature/193548` (visited on 10/29/2021).

[430] "Reprint of: Mahalanobis, P.C. (1936) "On the Generalised Distance in Statistics."". In: *Sankhya A* 80.1 (2018), pp. 1–7. ISSN: 0976-8378. DOI: `10.1007/s13171-019-00164-5`. URL: `https://doi.org/10.1007/s13171-019-00164-5` (visited on 12/05/2021).

[431] G. Gallego et al. "On the Mahalanobis Distance Classification Criterion for Multidimensional Normal Distributions". In: *IEEE Transactions on Signal Processing* 61.17 (2013), pp. 4387–4396. ISSN: 1941-0476. DOI: `10.1109/TSP.2013.2269047`.

[432] M. Bensimhoun. *N-DIMENSIONAL CUMULATIVE FUNCTION, AND OTHER USEFUL FACTS ABOUT GAUSSIANS AND NORMAL DENSITIES (Reviewed by D. Arnon)*. Corpus ID: 3863837. 2013. URL: `https://www.semanticscholar.org/paper/N-DIMENSIONAL-CUMULATIVE-FUNCTION%2C-AND-OTHER-USEFUL/c653507c6613107f98ada790247697acf25ba1cd` (visited on 12/05/2021).